LUMINESCENCE OF Mn^{2+} IN GLASSES: A SPECTROSCOPIC PROBE FOR THE STUDY OF THERMAL PHASE SEPARATION

by

Pierre-Elie Ménassa

A Thesis Submitted to the Faculty of Graduate
Studies and Research in Partial Fulfillment of
the Requirements for the Degree of
Doctor of Philosophy

McGill University
Department of Chemistry
Montreal, Quebec, Canada

MANGANESE(II) LUMINESCENCE AS A PROBE OF PHASE SEPARATION IN GLASSES

To my mother Claire for her love
and understanding.

and

To the memory of my father Michel

Chemistry Ph.D.

LUMINESCENCE OF Mn^{2+} IN GLASSES: A SPECTROSCOPIC PROBE FOR THE STUDY OF THERMAL PHASE SEPARATION

by

Pierre-Elie Ménassa

ABSTRACT

A new approach for studying thermal phase separation in sodium borosilicate glasses using Mn^{2+} as a luminescent probe is investigated. Seventy-one samples of glasses activated by Mn^{2+} inside and around the $Na_2O \cdot B_2O_3 \cdot SiO_2$ miscibility gaps were prepared. These samples were then phase separated by dry thermal treatment.

It is shown that on addition of MnO, the ternary $Na_2O \cdot B_2O_3 \cdot SiO_2$ system behaved like other quaternary systems of the type $X_2O \cdot MO \cdot B_2O_3 \cdot SiO_2$ (X = Na, K; M = Mg, Ca, Ba, Zn). Scanning electron microscopy and X-ray microanalysis demonstrated that manganese concentrates preferentially in the boron-rich phase. This analysis, in conjunction with a comparison of Mn^{2+} emission spectra of unheated and heat-treated glasses shows that the glasses are submicroscopically phase separated when prepared. The decay-time analysis of Mn^{2+} luminescence indicates that the low energy emission band arises from Mn^{2+} in the boron-rich phase while the high energy emission is due to Mn^{2+} in the silica-rich phase. The difference in the crystal field parameters obtained from the excitation spectra of the two emission bands shows that the high energy emission band is from Mn^{2+} in tetrahedral sites while the low energy emission band is from Mn^{2+} in an octahedral environment.

Chimie Ph.D.

LA LUMINESCENCE DU Mn^{2+} DANS LES VERRES: UNE SONDE SPECTROSCOPIQUES SERVANT A L'ETUDE DES PHENOMENES DE DEMIXTION

par

Pierre-Elie Ménassa

RESUME

Une nouvelle méthode d'étude des phénomènes de démixtion des borosilicates de sodium vitreux, utilisant la luminescence du Mn^{2+}, est examinée. Soixante et onze échantillons de verre activés au Mn^{2+} à l'intérieur et autour des lacunes de miscibilité du $Na_2O\cdot B_2O_3\cdot SiO_2$ ont été préparés. Ces échantillons ont été traités thermiquement à sec jusqu'à démixtion.

Il est montré qu'en ajoutant du MnO au système ternaire $Na_2O\cdot B_2O_3\cdot SiO_2$, ce dernier se comportait comme des systèmes quaternaires du type $X_2O\cdot MO\cdot B_2O_3\cdot SiO_2$ (X = Na, K; M = Mg, Ca, Ba, Zn). La microscopie électronique à balayage et la micro-analyse de rayons X montrent que le manganèse est, essentiellement, concentré dans la phase riche en borate. L'analyse précédente et la comparaison des spectres d'émission, des échantillons sans traitement thermique avec ceux qui ont subit une démixtion, montrent que les verres sont déjà sous-microscopiquement séparés, lors de leur formation, en deux phases non miscibles. L'étude des temps de déclin de la luminescence montre que les bandes d'émission à basse et à haute énergie proviennent respectivement du Mn^{2+} présent dans la phase riche en borate et de celle riche en silicate. La différence, entre les paramètres du champ cristallin obtenus à partir des spectres d'excitation des deux bandes d'émission, montre que la bande à haute énergie provient du Mn^{2+} en coordination tetraédrique tandis que l'autre est associée au Mn^{2+} en coordination octaédrique.

ACKNOWLEDGEMENTS

Throughout the course of this work I have received assistance from various people to whom I shall always remain indebted. I wish to express my gratitude to the following persons:

To Dr. David J. Simkin for his supervision, guidance, patience and encouragement throughout my graduate studies.

To Dr. Peter Taylor, Atomic Energy of Canada Ltd., Pinawa, Manitoba, for giving me a chance to perform part of this work in his laboratory, and for his invaluable help and numerous stimulating discussions.

To all my colleagues and particularly to Drs. K. Oyama-Gannon and J.P. Martin, Mr. J.G. Kang, Mr. W. Lee and Mr. T.F. Belliveau, for helpful discussion and to the latter for proofreading this manuscript.

To Miss D. Wollmann for her help with many drawings and Mr. D. Owen for the micrographs and many slides included in this work.

To Dr. Mona Nemer for her friendship and constant moral support.

To Ms. R. Charron and Mr. F. Kluck for their technical assistance.

To McGill University and Atomic Energy of Canada Ltd. for their financial support.

To all those who helped realise this work, may they forgive me for not mentioning their names.

Finally, special thanks to Mrs. Assunta Cerrone-Mancini for her patience and expertise in typing this manuscript.

TABLE OF CONTENTS

PAGE

PAGE

LIST OF FIGURES

LIST OF TABLES

GLOSSARY OF TECHNICAL TERMS[†]

1. BINARY SYSTEM. A system with two components.

2. BINODAL CURVE. Curve showing compositions of two liquid phases in equilibrium.

3. BOUNDARY LINE (CURVE). The intersection of adjoining liquidus surfaces in a ternary phase diagram. The area enclosed by a series of boundary lines is termed a primary phase area.

4. COMPONENTS (OF A SYSTEM). The smallest number of independently variable chemical constituents necessary and sufficient to express the composition of each phase present in any state of equilibrium. Zero and negative quantities of the components are permissible in expressing the composition of a phase.

5. COMPOSITION (OR COMPATIBILITY) TRIANGLE. In the phase diagram of a condensed ternary system the three joins connecting the composition points of the three primary phases whose liquidus surfaces meet at a point.

6. CONDENSED SYSTEM. One in which the vapor pressures of the solid and liquid phases present are negligible or small in comparison to the atmospheric pressure.

7. CONGRUENT MELTING POINT. At a specified pressure, the temperature at which a solid substance changes to a liquid of identical chemical composition.

8. CONJUGATE PHASE. One of the two phases in equilibrium with each other defining a conode (see (11)).

9. CONSOLUTE COMPONENT. That one which in sufficient amount causes homogenation of two other partially miscible components.

10. CONSOLUTE POINT. Critical point at which two liquids become miscible in all proportions.

11. CONODE (OR TIE LINE). For a particular temperature, the straight line connecting the compositions of two (conjugate) phases in equilibrium with each other.

12. CRITICAL TEMPERATURE. In a one component system, the unique temperature in which the liquid and vapor phases become identical. At the critical temperature the system passes from a heterogeneous state to a homogeneous phase. Above the critical temperature no liquid phase can exist however great the pressure.

13. DEVITRIFICATION. The formation of crystalline material from glass.

14. EUTECTIC. A eutectic represents an invariant (unique temperature, pressure, composition) point for a system at which the phase reaction on the addition or removal of heat results in an increase or decrease, respectively, of the proportion of liquid to solid phases, without change of temperature.

15. GLASS. In ceramic phase equilibria studies glass refers to supercooled liquid.

16. HETEROGENEOUS EQUILIBRIUM. A system is heterogeneous and is in heterogeneous equilibrium when it consists of two or more homogeneous portions (phases) in equilibrium with each other.

17. HOMOGENEOUS EQUILIBRIUM. A system is homogeneous and is in homogeneous equilibrium when it consists of one phase and all processes or reactions occurring within it are in reversible equilibrium.

18. INCONGRUENT MELTING POINT. At a specified pressure the temperature at which one solid phase transforms into another solid phase plus a liquid phase both of different chemical compositions than the original substance.

19. ISOPLETH. A line in a phase diagram of constant composition.

20. ISOTHERM. In a ternary system the locus of all points on the liquidus of constant temperature.

21. ISOTHERMAL STUDY. The method of considering the changes occurring in a system in which the temperature variable is held constant and the composition (or pressure) is varied.

22. JOIN. The region of a phase diagram representing all mixtures that can be formed from a given number of selected compositions. A join may be binary (straight line), ternary (plane), *etc.*, depending on the number of selected compositions, which need not be compounds. Each selected composition, however, must be incapable of formation from the others.

23. LEVER RULE (OR CENTER OF GRAVITY PRINCIPLE). When a particular composition separates into only two phases, the given composition and that of the two phases are colinear; furthermore, the amounts of the two separated phases are inversely proportional to their distances from the given composition. Thus, in the adjacent figure, A and B represent the compositions of two phases formed from composition C: Amt. of A x length AC = Amt. of B x length BC or A/B = BC/AC.

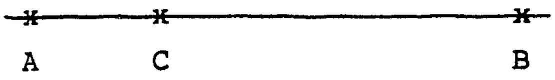

24. LIQUIDUS. The locus of temperature-composition points representing the maximum solubility (saturation) of a solid phase in the liquid phase. In a binary system, it is a line; and in a ternary system, it is a surface, usually curved. At temperatures above the liquidus, the system is completely liquid, and a point on the liquidus represents equilibrium between liquid and, in general, one crystalline phase (the primary one).

25. METASTABLE PHASE. A phase exists metastably in a system if it would not be present at final (thermodynamic) equilibrium, under unchanged conditions, and if the system is not approaching thermodynamic equilibrium at an observable rate.

26. MISCIBILITY GAP. Range of compositions separating into two phases (usually two liquids).

27. MONOTECTIC. Isothermal reversible reaction in a binary system in which a liquid on cooling, decomposes into a second liquid of a different composition and a solid.

28. PHASE. Any portion, including the whole, of a system which is physically homogeneous within itself and bounded by a surface so that it is mechanically separable from any other portions. A separable portion need not form a continuous body, as for example, one liquid dispersed in another.

A system composed of one phase is a homogeneous system; a system composed of more than one phase is heterogeneous.

29. PHASE BOUNDARY CURVE. Curve separating areas of homogeneous compositions from heterogeneous ones (often coincident with a binodal curve).

30. PLAIT POINT. The point on a binodal curve at which the tie line becomes vanishingly short.

31. PSEUDO SYSTEM. It is frequently convenient or necessary to refer to portions of a binary or ternary, *etc.*, system which are not (true) subsystems (see (34)). in such instances the term pseudo binary, or pseudo ternary, *etc.*, is used.

32. SOLID SOLUTION. A single crystalline phase which may be varied in composition within finite limits without the appearance of an additional phase.

33. SOLIDUS. The locus of temperature-composition points in a system at temperatures above which solid and liquid are in equilibrium and below which the system is completely solid. In binary diagrams without solid solutions, it is a straight line, representing constant temperature, and with solid solutions, it is a curved line or combination of curved and straight lines. Likewise, in ternary systems, the solidus is represented by a flat plane or a curved surface, respectively.

34. SUBSYSTEM. Any portion of a binary, ternary, *etc.* system which can be treated as an independent binary or ternary, *etc.* system. The selected substances designating the subsystem must be components for the subsystem (see (4)).

35. TIE LINE. See CONODE (11).

---

†From references 216, 217 and 248.

Science sans conscience n'est
que ruine de l'âme.

Rabelais

CHAPTER 1

INTRODUCTION

1.1 PREFACE

Liquid immiscibility in glass forming systems is a widespread phenomenon. Several reviews have been written on the subject[1-10]. While optical and electron microscopy are the only direct methods used in observing separated phases, small angle X-ray scattering[11], physical property measurements[12] and spectroscopy[13], are some of the various indirect methods capable of detecting phase separation in glasses.

One of the major problems facing the nuclear industry is the permanent safe disposal of radioactive waste arising from nuclear processes in fission reactors. One possibility for the disposal of reprocessed waste is dissolution in a glass (other possibilities are discussed in Ref. 14). After dissolution, these blocks would be contained in metal canisters and then stored in deep rock vaults ($\sim$ 1 km). Among the glass compositions under study is the ternary Na_2O-B_2O_3-SiO_2[15,16]. This system, like many others[1], has miscibility gaps (Fig. 1). That is, two distinct amorphous phases coexist within certain ranges of temperature and composition[17-20]. The temperature and duration of heat treatment, as well as the composition of

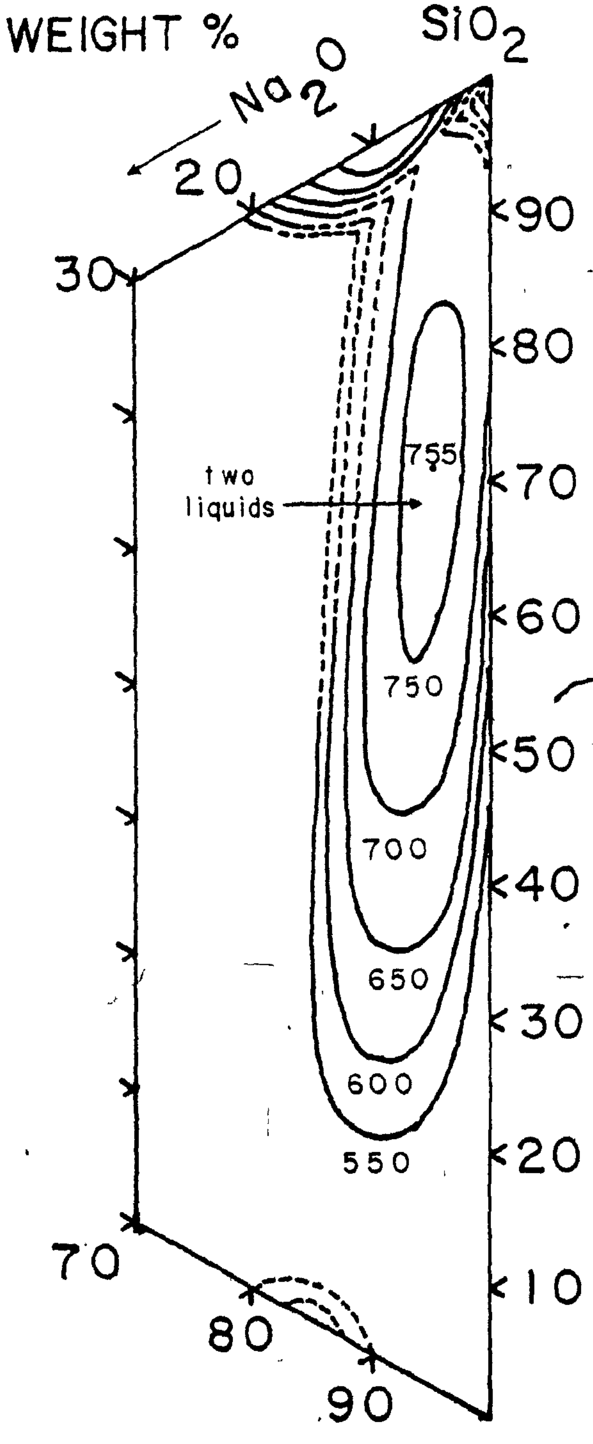

Fig. 1: Ternary plot of immiscibility points in the system $Na_2O \cdot B_2O_3 \cdot SiO_2$ (from Ref. 17).

these phases depends on the composition of the glass within the gap. The only plausible route for escape of radionuclides, after disposal, is by ground water. Since the dissolution behaviour of many glasses is affected by phase separation[21-25], it is important to understand this phenomenon - especially in the early stages - to control or avoid it. One way of better understanding phase separation is to study its effect on a doping material by means of visible spectroscopy. Some attempts have been made to use optical absorption[26-35] or luminescent probes[27,34-41] to study morphological changes in glasses. So far no parallel and comparative studies linking visible spectroscopy and electron microscopy have been made. Although the latter remains for the foreseeable future the most powerful tool for studying morphological changes in glasses, it is highly desirable to complement microscopy with a reliable spectroscopic method. All of the above aspects contributed to the motivation for the present study.

1.2 GLASSES, HISTORICAL AND LITERATURE REVIEWS

1.2.1 The Dark Ages

A detailed study of the history of glass may be found in Ref. 42. We present here a concise summary of its contents. The earliest evidence of glass manufacture comes from Egypt (some 2500 B.C.) and from Babylonia (some 2600 B.C.). Glasses belonging to this era were inhomogeneous and coloured green or blue. It was not until the 6th century B.C. that glasses started to display some homogeneity. Glass markets flourished in the 1st century B.C. with the discovery by the Syrians of glassblowing techniques. This century also saw the beginnings of glass as it is known today. Engraving was performed by the Italians in the 1st century A.D. and was considered an art form. At the same time glassmaking spread to northern Gaul and Britain, while in Egypt glass was commonly used for tableware.

With the fall of the Roman Empire and the conquest of the whole Near East by the Arabs in the 7th century, the evolution of glassmaking was impregnated by Islam. In this period, the Egyptians invented lustre painting, a technique which is not yet fully understood. Meanwhile in Syria two types of glasses, characteristic of two towns, flourished. One belonging to the town of Aleppo characterized by the use of thick enamels, the other belonging to Damascus, notable for its small scale figural decoration. The 12th century saw the introduction of stained glass windows in European Gothic churches. One final note to mention about these middle ages is the invention of the clear "Cristallo" glass by the Venetians.

In the 16th century in Venice a special method to prepare glasses was developed, known as the "façon de Venise". Among the glasses prepared by this method one finds the "latticinio", the "vetro ditrina" and ice glass. The secret of the "façon de Venise" was well protected, and glass workers of the island of Murano were forbidden to leave Venice. Fortunately, near Genoa, at Altare, there existed a second glass centre. Its glass was impossible to differentiate from the one prepared by the "façon de Venise". This second glass centre was not governed by the same restrictions as Venice. Thus, some Altarist and Venetian refugees spread the Italian art of glassmaking to the rest of Europe. It was in England in 1675 that Ravenscroft discovered lead glass. This glass was heavier and more durable but also slower to work than the Venetian glass. In the 18th century a technique special to Bohemia emerged. It consisted of sandwiching a gold leaf between two layers of glass forming beakers or goblets. Glassmaking was imported to the American continent as early as 1535 (in Pueblo Mexico). By the 18th century many glass houses appeared in the U.S. The most important were the Wistar's and the Steigel's. The beginning of the 19th century gave birth, in the U.S., to internationally known glass manufacturers: Libbey's, Pitkin's and Bakewell's. The modern history of glass starts in the mid-19th century where exhibitions were held and glass objects were collected. This century also saw the production of optically reliable glass. This progress was made possible thanks to the collaboration, in Jena, of great scientists like Carl Zeiss, Ernst Abbe and Otto Schott. During all these years (from antiquity to the beginning of the 19th Century) glass science was based on trial and error, without any solid scientific basis.

1.2.2 The Modern History

It was not until the 20th century that some aspects of the properties of glass were elucidated. If the modern history of glass starts with the 20th century, then the number of innovations in glassmaking from 1900 until now outnumber by far what had been achieved in the previous 4500 years.

Among the first to adopt a scientific approach toward the properties and possibilities of glass, was Michael Faraday. He described glass "rather as a solution of different substances one in another than as a strong chemical compound"[43]. He also explained that the red colour of a gold ruby glass was due to small gold particles in the glass[44]. Moreover, he studied the conductivity and electrolysis of various melted glasses[45]. Independently and in the same period Buff conducted similar research[46]. In Jena and around 1880, Otto Schott discovered what seventy years later was to become a major subject of modern glass research: phase separation.

He observed a "milky opacity" when P_2O_5 was added to a mixture of SiO_2 and B_2O_3, and concluded that "phosphoric glass salts are obviously insoluble in a [borosilicate] melt as oil is in water"[47]. In the same period and after a series of experiments, Warburg and Tegetmeier[48,49] concluded that the electrolysis of glass followed Faraday's Law. Diffusion, and exchange of silver ions for sodium ions were studied by Schulz[50]. Meanwhile, Tammann investigated the conditions for glass formation. He also did some work on the glass transition and tried to relate this to crystallization rate and viscosity[51]. The first systematic studies of immiscibility in binary borate glasses were done by Guertler[52] and later on by Greig[53,54] with binary silicates.

In 1930 and with the availability of X-ray diffraction techniques, investigation of oxide glasses began in earnest. Two leading theories emerged, one favouring a crystallite model[55-58], the other a random-network model[59-64]. Later on the crystallite model was dropped in favour of the network model mainly on the basis of arguments proposed by Warren and co-workers[60,64-66]. Warren noted the absence of small-angle X-ray scattering from fused quartz. This indicated that if crystallites were present they must be fused together by a material having the same density. These results were confirmed later on by Weinburg[67] and Levelut[68]. This technique is often used as proof of structural homogeneity of glass, although some authors express reservations[69,70]. Their criticism is based on the fact that small-angle scattering from a liquid is less than that of an isolated molecule, due to the interference effects of molecules in liquids. Similarly, a reduction in low-angle scattering will occur for two neighbouring crystallites. Nonetheless, with the quasi-general acceptance of Warren's arguments, new expressions gained usage in glass science. Cations were classified as "network formers" or "network modifiers" and structural properties of glass were intensively studied. Early in the 1950's a new tool that revolutionized the whole glass science was discovered: the electron microscope.

1.2.3 The Electron Microscope and the "Golden Age" of Glass Science

The first to detect microheterogeneity in glass by electron microscopy was Slayter[71] and later Prebus[72]. On the basis of their results, as well as those of others[73,74], glass scientists concluded that glass cannot be as homogeneous as stated by the random network theorists nor can it be as well organized as postulated by the crystallites group. Furthermore, systematic studies of beryllium fluoride glasses[75-77] led to the conclusion that phase separation was inherent of the general structure-forming process. This subject was intensively covered in the 1960's and over 500 papers were written on this matter. Thus if the 1950's were considered as the "golden age" of metallurgical science, similarly the 1960's might also be considered as the "golden age" of glass science[78]. Among the first in this "golden age" to present theoretical explanations of immiscibility were Cahn[79,80] and Hillert[81]. This phenomenon was observed in many glass-forming oxides. Among the binary systems one finds the alkali borates[†82], the lithium and sodium silicates[84-86], the alkaline earth silicates[53,54,87] and borates[88], SiO_2-B_2O_3[89], PbO-B_2O_3[90-93], Al_2O_3-SiO_2[94,95] and GeO_2-GeO[96]. Phase separation has also been reported for many ternary systems, including Na_2O-B_2O_3-SiO_2[17-20], NaO-CaO-SiO_2[97,98], Li_2O-B_2O_3-SiO_2[99,100], Li_2O-Al_2O_3-SiO_2[100], PbO-Al_2O_3-B_2O_3[92], MgO-Al_2O_3-SiO_2[101], PbO-GeO_2-SiO_2[102]. Phase separation has also been reported in four-component systems by Hummel[103] and more recently by Taylor and co-workers[104-107]. They describe in detail the topography of the miscibility gaps in some complex borosilicate systems.

The properties of glasses and phase separation have been intensively covered by several books and review articles. Further details on the subject may be found in Refs. 1-10. The theoretical aspects of immiscibility will be covered later (*cf*. Chapter 2). Finally, the last dozen years have seen a rapid increase in spectroscopic techniques useful for

---

[†] Some authors[83] question the existence of a subliquidus miscibility gap in the alkali borates except the lithium borate system.

studying structural changes in glass. Among these techniques are E.S.R.[108], N.M.R. and Raman spectroscopy[109-111], X-ray microanalysis[112-114] and finally visible spectroscopy (references cited in Section 1.1).

1.3 GLASSES: VISIBLE SPECTROSCOPY

Among the books and review articles available in the literature dealing with the origin of colours in glasses[13,115-119] we discuss three which complement each other. Certainly the most complete qualitative discussion of the subject was given by Weyl[115] in the early 1950's. It is still considered by many as the "Bible" of coloured glasses. A review article written by Bates[116] discusses the absorption spectra of transition-metal ions in glasses based on ligand-field theory. Finally, a book by Wong and Angell[13] describes quantitatively all aspects of spectroscopy in glass including a broad section on visible spectroscopy.

Visible spectroscopy involves electronic transitions with energies corresponding to frequencies in the visible region of the electromagnetic spectrum. It can be further divided into three major parts: absorption, excitation and emission.

1.3.1 Absorption

Three distinct processes characterize the absorption of visible radiation in glassy materials: interionic and intraionic transitions, and the existence of colour centres.

1.3.1.1 Interionic transitions

Interionic transitions, also commonly called "charge transfer spectra" are those involving the transition of an electron from an orbital located on an atom or an ion to another orbital located on another atom or ion. In chalcogenide glasses, transitions occur to a conduction band as opposed to a localized orbital. When the transition occurs to a localized single level, the absorption band peaks in the U.V. having its tail in the visible region. It is the tail of the band that is responsible for the colouration of the glass. One of the most common impurities in glasses is Fe^{3+}. It is responsible for the green colouration in commercial bottles and can affect glass colouration when present at concentrations as low as 1 ppm[78]. Steele and Douglas[120] studied the spectra of iron in sodium silicate and borate glasses. Their comparison with Fe^{2+} and Fe^{3+} absorption spectra in aqueous solutions led them to the conclusion that Fe^{2+} and Fe^{3+} co-existed in the glasses under study. Thus both ions are responsible for the charge-transfer band centred at *ca.* 210 nm.

1.3.1.2 Intraionic transitions

These occur within the central ion itself or within the ligand orbitals themselves. Transitions within the ligand orbitals result in a redistribution of electrons on the ligand; these transitions are allowed and very intense. Transitions within the central ion are usually forbidden and weak but are responsible for the colour of various glasses. Transitions between the 3d levels are of special interest because they are sensitive to the ion's chemical environment and may therefore be used as indicators on the nature of the environment. A good example is trivalent chromium, the absorption spectrum of which has been interpreted in great detail in terms of ligand field theory[116,117]. Recently, Brawer and White[121] studied the temperature dependence on the absorption of Cr^{3+} ions in silicate glasses. Further optical studies on trivalent chromium in a variety of glasses were carried out by Andrews and co-workers[122]. They concluded that the inhomogeneous broadening of the bands increases along the series phosphate < fluorophosphate ∿ silicate < tellurite ∿ fluorozirconate ∿ phosphotungstate < borate, thus showing that the absorption spectrum of Cr^{3+} in glass is sensitive to its environment.

1.3.1.3 Colour centres in glass

These centres are produced by high energy irradiation (usually a ^{60}Co γ-ray source). Ionizing radiation, on passing through matter, frees bound electrons. This produces both free electrons and positive holes. These are both relatively mobile at room temperature and travel through the material until they are trapped by a defect - an oxygen vacancy will trap an electron, an oxygen atom a hole - or collide with each other and annihilate[123]. It is these species that colour irradiated glasses. Furthermore, the intensity of absorption bands is influenced by the metal alkali cation[124]. The latter factor was studied by Bishay[125]. He found that for the same radiation (2.2×10^{6} R) increasing the alkali content increases the absorbance of the band (centred at *ca.* 625 nm). Thus, although colour centres in glass depend on different factors (as stated above), they can still be induced by radiation damage and contribute to colouring phenomena in glass.

1.3.2 Excitation

Excitation spectra rely on those transitions which are responsible for the luminescence of glasses doped with certain activators. Excitation spectra may be measured conveniently with the apparatus described in Section 3.4.3.3. The excitation spectrum obtained this way is directly related to the absorption spectrum of the activator, but the measurement has some advantages. If the activator has a high luminosity, excitation spectra may be obtained at very low activator concentrations, which do not give observable adsorption spectra. It is not important for the sample to be clear, *i.e.*, to transmit light. This last is a serious problem in absorption particularly in the U.V. ($\nu < 300$ nm) where light is very easily scattered and the glass matrix starts to absorb. Figure 2 shows the absorption, emission and excitation spectra (on a similar scale) of heat-treated sodium borosilicate glass doped with uranium[126] (batch composition $10Na_2O - 27B_2O_3 - 63SiO_2 - 0.07U_3O_8$). Finally, excitation spectra can demonstrate the occurrence of energy transfer between fluorescent centres. Reisfeld and Boehn[127], using excitation spectra showed that the energy absorbed by Sm^{3+} is transferred to Eu^{3+} ions in phosphate glasses. Their conclusion is based on the fact that the difference in excitation between $Eu^{3+} + Sm^{3+}$ and Eu^{3+} corresponds to strong lines in the Sm^{3+} absorption spectrum. Of course excitation spectra can be obtained only from luminescent centres, which can be a serious limitation.

1.3.3 Emission

Emission phenomena including both fluorescence and phosphorescence (or luminescence) result from radiative transitions from higher to lower states. Different processes may promote electrons from ground to

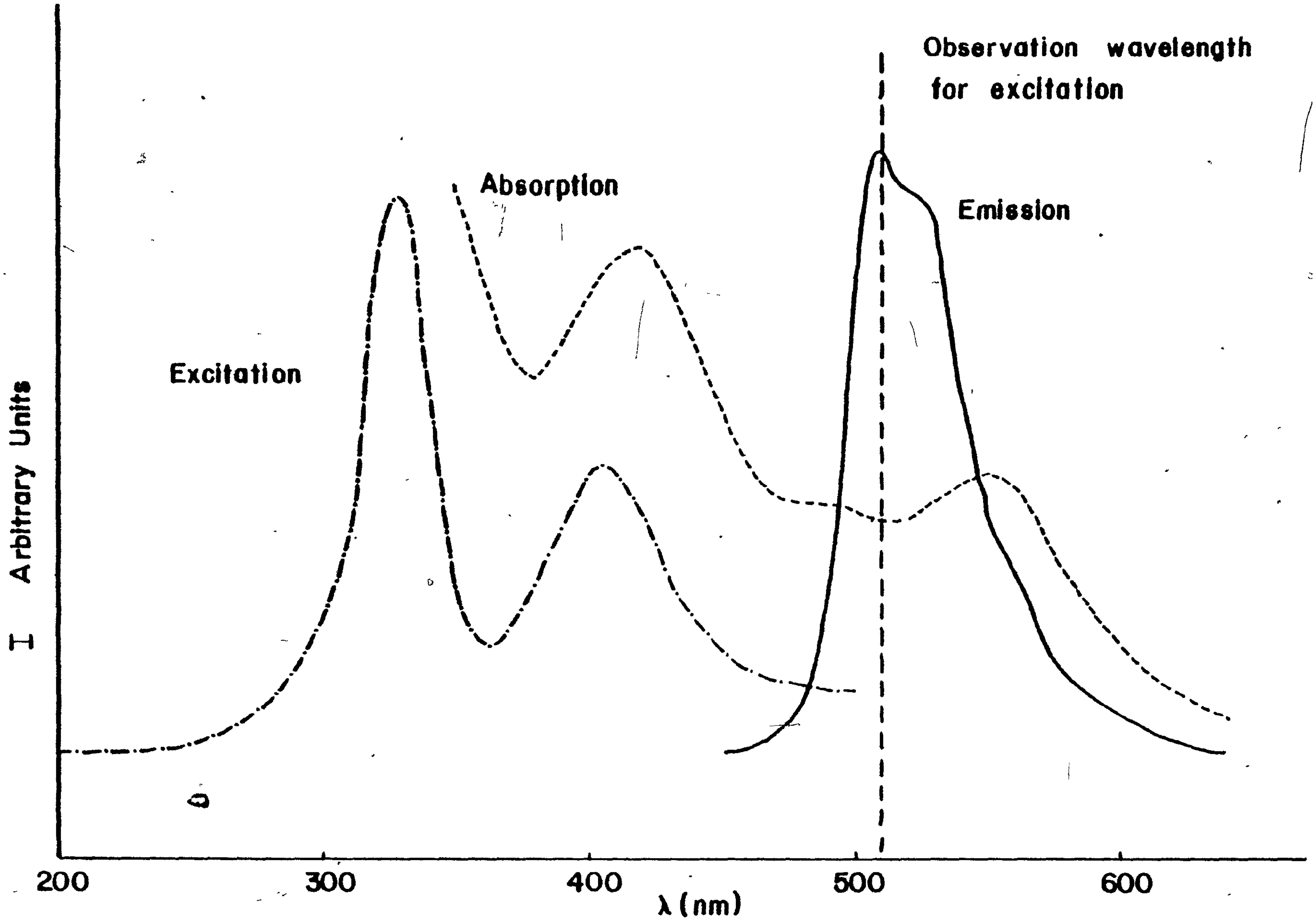

Fig. 2: Excitation, absorption and emission spectra of an uranium doped sodium borosilicate glass (molar composition: $10Na_2O \cdot 27B_2O_3 \cdot 63SiO_2$) after 18 h at 600°C.

excited states. If the luminescent material is bombarded by electrons, the resulting emission is called cathodoluminescent. Electroluminescence follows an excitation by an applied voltage. Irradiation by X-rays produces X-ray luminescence. Chemiluminescence is the term used when the excitation is produced by a chemical reaction. Photoluminescence occurs when the luminescent material is irradiated with electromagnetic radiation. We will be concerned with irradiation by U.V. or visible light. Martin[128] has written a comprehensive review on this subject and its application to alkali halide crystals doped with ns^2 ions. A different approach dealing mainly with glassy materials is presented in the following section.

1.4 FLUORESCENCE AND PHOSPHORESCENCE IN GLASSES

Fluorescence refers usually to allowed transitions where absorption and emission processes are fast. Phosphorescence which occurs on a much longer time scale involves reemission of absorbed energy from levels for which transitions to the ground state are radiatively forbidden. This often results from the trapping of the excited electron in an electronic state having a different multiplicity than the ground state. Such transitions are forbidden by spin selection rules. Weyl[115] classified luminescent centres in glasses into three categories.

1.4.1 Weyl Classification

1.4.1.1 Glasses containing crystalline fluorescence centres

This class consists of glasses containing small luminescent crystals introduced in the host material. These centres may be introduced mechanically or by precipitation from the glass during the cooling process or even by heat treatment (devitrification). Fluorescent enamels belong to this class. They were invented by Sauvagé[129] and Guntz[130] in 1923. Fluorescent enamels found little application and were rapidly replaced by luminous paints. Fluorescence or phosphorescence in these enamels are those of the crystalline phase (*i.e.* glass does not participate in the process). We will not elaborate on this class which is of little interest in the present work.

1.4.1.2 Glasses containing energetically-isolated atoms or molecules

Certain atoms or molecules may be incorporated in a glassy medium. If these atoms or molecules are not strongly bound to their environment, they may be considered as energetically isolated. Weyl[115] describes metal atoms as "frozen in" metal vapour. Silver glasses are a good example. Silver in glass may exist in different forms[131]. Ag^+ ions and $(Ag°)_x$ crystals which do not luminesce (the former is colourless while the latter impart a yellowish colour to the glass) and neutral Ag° atoms which have an absorption band in the U.V. and a white-yellow fluorescence in the visible.

Molecules too can be incorporated in glassy media. Glasses containing cadmium sulfide and cadmium selenide absorb in the ultraviolet and short-wave visible with emission of red to infrared radiation[132]. The introduction of organic molecules in a low temperature molecular glass has also been reported[133]. Certainly the most important class of luminescent glasses are those containing fluorescent ions.

1.4.1.3 Glasses containing fluorescent ions

(i) Rare-earth ions

The luminescence of rare-earth ions in glass has been extensively studied in recent years in view of potential applications as laser materials and solar converters[134] and infrared-to-visible upconvertors[135]. In rare-earth ions the electronic transitions occur within the 4f electrons. These last are well shielded by the outer 5p and 5s electrons. Thus one would not expect the luminescence spectra of these ions to be much affected by environmental changes. Most of the rare-earth optical properties were studied in terms of quantum yield[136,137], radiative lifetimes[138], and fluorescence line-width parameters[139], which are important in laser applications. Despite the fact that the environment has little effect on the absorption and emission spectra of rare-earth ions, successful attempts have been made using spectroscopic observations to draw some conclusions on the symmetry sites of rare-earth ions in glass. This is possible because the transition energies are sharply defined; a concise review on this subject was written by Snitzer[140]. A new powerful technique first recognized by Szabo[141] and applied by Riseberg[142-144] may be used to analyze the inhomogeneous broadening of the bands in a glassy medium. This new technique is referred to as laser-induced fluorescence line-narrowing (FLN). If upon absorption the band is broad due to the distribution of absorbing ion sites, then by exciting with a narrow laser line, it is possible to excite only a fraction or a homogeneous part corresponding to field-split energy-level separation (see Fig. 3). If the temperature is kept low enough the energy redistribution of the absorbed energy is slowed down and FLN is observed. A recent review article on the subject was presented by Yen[145].

(ii) Uranium

The strong luminescence from uranium-doped glasses is due to the U(VI) oxidation state, but only when present

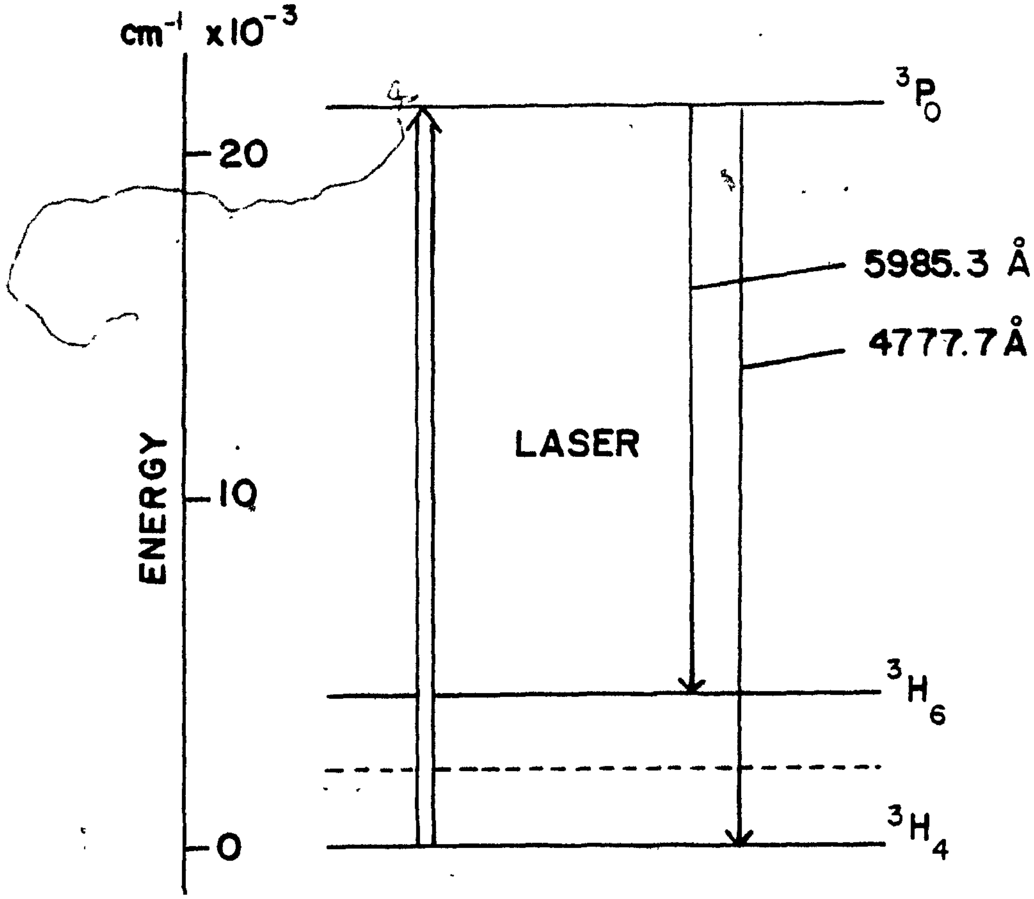

Fig. 3: Laser excitation corresponding to field-split energy-level separation in $LaF_3:Pr^{3+}$ (from Ref. 145).

as the uranyl group UO_2^{2+}[131]. Different bands are present depending on glass composition[146]. Weyl[115] attributed the loss of the luminescence, as a function of glass composition, to the formation of uranate groups UO_4^{2-} or $U_2O_7^{2-}$ which do not fluoresce. Furthermore, glasses containing the glass-former as $(BO_3)^{3-}$ or $(PO_4)^{3-}$ structural units interfere less with uranium luminescence than those containing $(SiO_4)^{4-}$ and $(BO_4)^{5-}$ groups. Moreover, Rodriguez and co-workers[146] showed that substituting Na_2O by K_2O and increasing silica content in a lime silicate glass increases the intensity of uranium fluorescence.

(iii) Transition-metal ions

Transition-metal ions may be dissolved in a glass (at least in small amounts), thus they can be incorporated as part of the glass structure. Certain of these ions will luminesce. We will be interested in the first transition-metal series (3d series). Variations in the interatomic binding forces (changes in the network modifier cations) and their symmetry affects the emission of the activators. Thus some information on the local structure around the transition-metal ion may be obtained.

The fluorescence of pentavalent vanadium ion in silicate glasses has been investigated[115]. Ni^{2+} fluorescence in glasses has also been reported[13]. Glasses containing Cu^+

absorb in the U.V. (238 nm) and fluoresce in the visible (500 nm). Parke and Webb[147] studied Cu^+ luminescence in calcium phosphate glasses. Based on the similarity between excitation and absorption spectra, they concluded that absorption and emission occur between the same two levels. In recent years the luminescence of Cr^{3+} in glasses has been thoroughly investigated[121,122,148]. Brawer and White[121] studied the dependence of the emission on the exciting frequency in silicate glasses. Lunkin and co-workers[148] investigated the luminescence of Cr^{3+} in sodium borosilicate glasses[†]. They observed a quenching of the luminescence when the activator concentration was increased from 0.1 to 0.5 wt%. Furthermore, samples containing 0.1 wt% of the activator and heated for 6 h at 600°C had the same luminescence characteristics as those unheated with 0.5 wt% of the activator. Moreover, studies of heat-treated glasses dissolved in 0.25 N HCl showed that Cr_2O_3 concentrated in the sodium-and-boron rich phase. This concentration-quenching phenomenon has been observed by Andrews and co-workers[122] in soda lime silicate, aluminum phosphate, fluorophosphate, and lithium aluminum borate glasses. Among the 3d transition elements, certainly the luminescent glass activator that has been studied the most remains Mn^{2+} to which we devote a section of its own.

[†] Kindly translated from Russian by Professor Alfred Taurins, McGill University, Department of Chemistry.

1.4.2 Mn^{2+} in Glasses

Since the early work of de Boisbaudran[149] and Urbain[150], the behaviour of Mn^{2+} as an activator in glasses and crystals has been thoroughly investigated. Luminescent studies of glasses doped with Mn^{2+} range from fluoroberyllates[29,34,35,38,39,151,152] to phosphates[29,32,39,41,151-160], silicates[29-31,35,39,40,151-154,161] and borates[30,39,153,154,162]. Mn^{2+} luminescence in glass ranges from green to deep red depending on the glass composition and on the activator concentration[30,39,157]. Although some authors[32,35] attribute this luminescence to the transitions ${}^4A_{1g}\ {}^4E_g(G) \rightarrow {}^6A_{1g}(S)$ and ${}^4T_{2g}(G),\ {}^4T_{1g}(G) \rightarrow {}^6A_{1g}(S)$ (see Fig. 4), there is fair agreement that the electronic transition ${}^4T_1({}^4G) \rightarrow {}^6A_1({}^6S)$ is responsible for both green and/or red luminescence. Unfortunately, some dispute[30,31,35,157] still exists on the factors affecting these frequencies.

Based on the fact that Co^{2+} and Mn^{2+} have the same electric charge and approximately the same ionic radius, Linwood and Weyl[30] compared glasses doped with Mn^{2+} to their counterparts doped with Co^{2+}. They found that whenever the glass composition favoured a tetrahedral coordination for Co^{2+} (silicate glasses) the Mn^{2+} counterpart would luminesce green. Moreover, when an octahedral coordination for Co^{2+} is favoured (in low-melting)

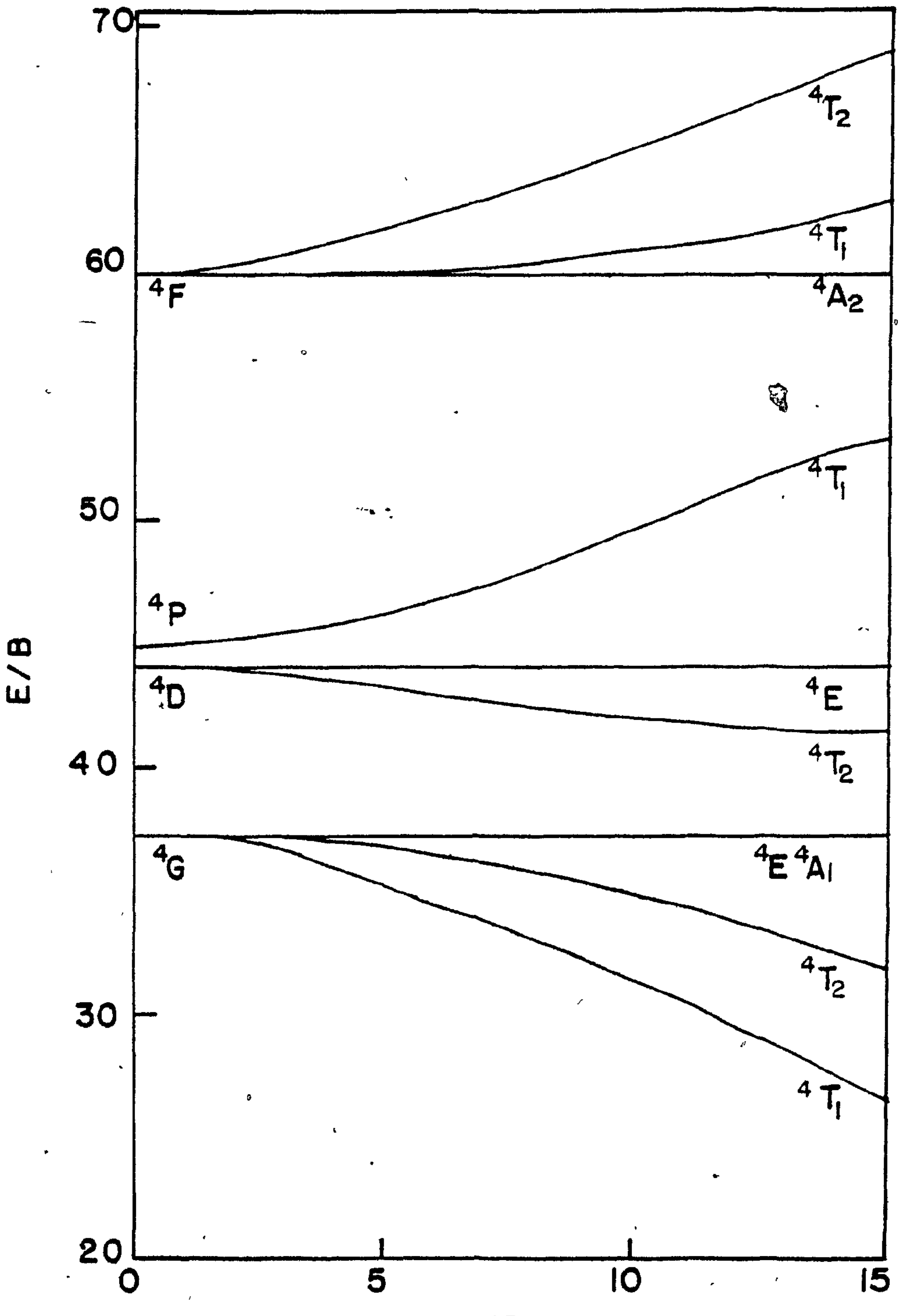

Fig. 4: Energy level diagram for a d^5 configuration (C/B = 5.43). The ground term $^6A_1(^6S)$ is not shown (from Ref. 154).

glasses *i.e.* borates, phosphates), the corresponding Mn^{2+} glass would fluoresce red or orange. From these experiments, they concluded that the green emission was present whenever Mn^{2+} played the role of a network former (tetrahedral coordination) while the orange/red emission occurred when Mn^{2+} occupied interstitial positions (octahedral coordination). Furthermore, they conducted a series of experiments monitoring the fluorescence as a function of the temperature. They found that the green luminescence was less influenced than the red by changes in temperature; these results were confirmed later by Parke[153]. Thus the green emission comes from Mn^{2+} in a rather rigid network and is less influenced by thermal vibration than by Mn^{2+} in interstitial positions (red emission).

Turner and Eastman Turner[31] studied silicate glasses doped with Mn^{2+}. They did not find any experimental evidence in decay time, molar absorptivity, or correlation of luminescence and absorption for a change in coordination number from four to six. Instead, based on luminescence quenching with increasing Mn^{2+} content, they suggested that the green luminescence was due to single ions and the red to pairs or higher groupings. That would explain the quenching of the green emission in favour of the red with increasing Mn^{2+} concentration. Their view was strongly supported by Bohun and Polecha[157]. The latter studied phosphate glasses doped with Mn^{2+} and found two emission bands: one centred at *ca.* 510 nm and the other at *ca.* 590 nm. Their absorption spectrum showed a band at 1.45 μm (6900 cm^{-1}) which corresponds approximately to the value of $\Delta = 6800\ cm^{-1}$ (1.47 μm) chosen by Bates and others[31,116] in fitting the Tanabē Sugano diagram for a d^5 configuration. Furthermore, they did not find any absorption band at *ca.* 3.3 μm (3070 cm^{-1}) corresponding to $\Delta_t = \frac{4}{9}\Delta_o$. They concluded that the band at 1.45 μm determines the value of the crystal field strength for octahedral Mn^{2+}. Moreover, the failure to observe an absorption band at 3.3 μm argues against tetrahedral Mn^{2+}. Thus, the two emissions (green and red) occur with Mn^{2+} in an octahedral coordination. Based on their absorption data and on the fact that luminescence quenching of the green emission occurs with 5 mol% MnO, they concluded that the green emission was due to single ions and the red to dimers or higher groupings.

Lunter and co-workers[35], propose a different explanation for the origins of these bands. They studied fluoroberyllate, phosphate and silicate glasses activated[†] with Mn^{2+}. They observed a dependence of the emission on Mn^{2+} concentration. In potassium cadmium silicate glasses doped with up to 5 wt% of MnO, two bands are present: one is relatively narrow, centred around 522 nm, and another is

---

[†] If 40 or 50 wt% MnO in a glass can be called an "activator". The activator level will be discussed in detail in Chapter 4.

very broad suggesting the presence of two overlapping narrower bands centred around 634 and 658 nm. By increasing Mn^{2+} concentration (30 wt% MnO) only one band centred at *ca.* 710 nm remains. Thus they concluded that the 522 nm band was due to the transition $^4A_{1g}{}^4E_g(G) \rightarrow {}^6A_{1g}(S)$ while the $^4T_{2g}(G)$, $^4T_{1g}(G) \rightarrow {}^6A_{1g}(S)$ transitions were responsible for the 634 and 658 nm bands. Their assignment is based mainly on the fact that increasing Mn^{2+} concentration increases the probability of non-radiative transitions from the $^4A_{1g}{}^4E_g(G)$ to $^4T_{2g}(G)$ and to the $^4T_{1g}(G)$.

Parke, Watson and Webb[158] studied the fluorescence decay time of Mn^{2+} in phosphate glasses. They found it to be exponential in some glasses and non-exponential in others, depending on the glass composition and on MnO concentration. The decay times they found ranged from 2.1 ms in manganese phosphate glasses to 25 ms in sodium manganese phosphate glasses. Other authors studied Mn^{2+} luminescent decay time in glasses[31,40] and also found it to be non-exponential. This suggests the presence of different luminescent centres[159].

As one can see from the preceding discussion, one uncontroversial fact about Mn^{2+} in glasses remains: the luminescence is sensitive to both its environment and its concentration.

1.5 RECENT RESULTS AND STATEMENT OF THE PROBLEM

1.5.1 Recent Results

1.5.1.1 Sodium borosilicate glasses

Liquid immiscibility in glass-forming systems has been thoroughly investigated. A recent review on the subject is given by Tomozawa[10]. The sodium borosilicate system has received particularly close attention[17,18-20,163-167]. Although the boundary of the miscibility gap has been fairly well established, some uncertainty remains about the location of the tie-lines[17,19,20,163,164].

1.5.1.2 Optical properties of doped sodium borosilicate glasses

The use of activators and their spectral properties to study morphological changes in glasses has been rare[26,112,148].

Ehrt, Reiss and Vogel[112] studied some sodium borosilicate glasses doped with Co^{2+}. Using transmission electron microscopy and X-ray microanalysis, they showed that upon phase separation CoO was mainly concentrated in the borate rich phase. Their chemical analysis of separated phases gave 98% of CoO present in the borate rich phase. Their interpretation of optical absorption spectra by ligand-field theory led to the conclusion that Co^{2+} in sodium borosilicate glasses exists in 6-fold and 4-fold coordination.

Furthermore, from the calculated Racah parameters they deduced that the Co-O bond in these sodium borosilicate glasses has an important covalent character.

Toyuki[26] studied phase separation of sodium borosilicate glasses by means of optical absorption of the vanadyl ion[†]. Based on a molecular orbital interpretation of his absorption data, the author concluded that the glass is separated into a SiO_2 phase and a $Na_2O-B_2O_3$ phase from the start (*i.e.* when the glass is formed). Furthermore, he suggested that phase separation of sodium borosilicate glasses caused by heat treatment is due to the development of the separated phases originally existing in the glass.

Lunkin and co-workers[148] studied the spectral and luminescent properties of Cr^{3+} ions in sodium borosilicate glasses. Their work emphasized the effect of heat treatment on the immediate structural surroundings of the activator. From their absorption and luminescence data they concluded that Cr^{3+} ions in sodium borosilicate glasses are in an octahedral coordination and that, upon heat treatment, Cr^{3+} concentrates in the sodium-and-boron rich phase.

[†] This paper was kindly translated from Japanese by Dr. Keiko Oyama-Gannon.

1.5.2 Statement of the Problem

Liquid immiscibility in glass forming systems and optical properties of ions in glasses have both been studied separately for many years (references cited earlier). However, with the exception of the work by Ehrt *et al.*[112], systematic comparative studies linking the morphological changes involved in phase separation with changes in the optical properties of dissolved chromophores are lacking. The primary motivation for the present work was the hope that such a complementary investigation could provide insights into the nature of the phase separation phenomenon which could not be gleaned from either study alone. Morphological studies by the available techniques, *e.g.* electron microscopy and related methods, are inherently limited to the spacial resolution of the instrument (∿ 10 nm), while the spectroscopic properties of a probe chromophore are determined largely by the immediate environment of that species, *i.e.* its neighbours within about ten angstroms. However, the addition of even small amounts of activator may significantly alter the behaviour of the glass system, and hence the need for the parallel morphological study.

The choice of the glass-activator system for the present work was dictated by the requirement of having a system in which the morphology of the glass alone and the spectroscopy of the activator (at least in other similar glasses) were both reasonably well understood. For this reason the sodium borosilicate system was nearly ideal because its immiscibility boundaries have been thoroughly studied and are fairly well established[17,18]. The choice of Mn^{2+} as an activator was based on the sensitivity of its luminescence on its environment in glasses. Both the emission and the luminescent decay times are sensitive to the glass composition and the MnO concentration[30,39,158].

For this investigation, selected samples (doped with different levels of MnO) were prepared with compositions inside and around the immiscibility boundaries of the $Na_2O \cdot B_2O_3 \cdot SiO_2$ system. Morphological studies were conducted using scanning electron microscopy and X-ray microanalysis. Parallel optical studies were carried out using excitation and luminescence spectroscopy as well as decay-time analysis.

Apart from the aforementioned general considerations, the present study also addresses the following particular points. No work has yet appeared on the luminescence, excitation and decay-times of Mn^{2+} in sodium borosilicate glasses. In addition, the assignments of the two emission bands of Mn^{2+} in other glasses are still in doubt, nor has the Mn^{2+} energy level diagram in these glasses been established. The effect of MnO doping level on the process of phase separation and its implications on the position of the immiscibility boundaries and on the possible rotation of the tie-lines of sodium borosilicate glasses have not yet been investigated at all. Finally, the partitioning of Mn^{2+} between the two phases in the phase separated sodium borosilicate glasses is not yet known.

CHAPTER 2

THEORETICAL

2.1 GLASS FORMATION

2.1.1 Definition

The definition of a glass as taken from Webster's dictionary is "Glass: a hard, brittle substance, usually transparent or translucent, made by fusing silicates with soda or potash, lime and sometimes, various metallic oxides: the molten mass is cooled rapidly to prevent crystallization"[168]. This definition agrees with the more scientific definition of a glass given by the ASTM standards for glass: "glass is an inorganic product of fusion which has been cooled to a rigid condition without crystallization"[250]. Two objections to the previous definitions of glasses may be formulated. The first one is that it is not necessary to cool from the liquid state to prepare a glass. Glasses can be formed by vapor deposition onto a cold substrate[169], dehydration[170], and electro deposition[96]. The second objection is that the definition is restricted to inorganic substances. In the technical literature, some glassy organic polymers are called glasses[171]. Based on the previous considerations it seems more appropriate to adopt this general definition of a glass: "glass is an X-ray amorphous solid which exhibits the glass transition[†],[172]. The word "amorphous" is derived from the Greek language and refers to a material with no long-range order, *i.e.* no regularity in molecular arrangement is present on a scale larger than a few times the size of these molecular groups. A material is said to be solid if it does not flow when subjected to small forces. More quantitatively the viscosity value chosen for distinguishing solids from fluids is 10^{15} poise[§]. For comparison the viscosity of air is 10^{-4} poise, that of lubricating oil is 1 poise[173] and that of glycerin at 0°C is 121.10 poise[222]. Often T_g is taken as the temperature at which the viscosity is equal to 10^{13} poise.

2.1.2 Under What Conditions Can A Glass Be Formed?

2.1.2.1 General considerations

A liquid may be transformed into a solid *via* two processes. A discontinuous one leading to crystallization and a continuous one leading to an amorphous solid or vitreous state. Most substances, except helium, may exist in an amorphous form. Turnbull[173] discussed whether a material below its melting point is more stable in its glassy or crystalline form. He did not find any *a priori* evidence that

---

[†] "That phenomenon in which a solid amorphous phase exhibits with changing temperature a more or less sudden change in the derivative thermodynamic properties such as heat capacity and expansion coefficient, from crystal-like to liquid-like values. The temperature of the transition is called the glass (transition) temperature and denoted T_g."[172]

[§] 1 poise = 10^{-1} Ns m^{-2}.

the most stable state of a substance at low temperature is crystalline, but based on experimental evidence it is found that the most stable forms of pure substances are crystalline. Therefore, if glass is to be formed crystallization must be avoided. Whether or not this is possible is determined by a number of factors mainly cooling rates, crystallization constants, nucleation frequency and growth rate of crystals in the supercooled liquid[174].

Wagstaff[175] studied the rate of crystallization of cristobalite[†] as a function of temperature. He found that upon cooling molten silica below the freezing point, 1734°C, the rate of crystallization increases to reach a maximum at 1674°C and then decreases steadily until it reaches 900°C. At this temperature the rate of crystallization becomes so slow that the amount of crystalline material formed (even after keeping the temperature constant for a long period of time) is negligible. Therefore, if glass is to be formed, molten silica must be cooled rapidly to below 900°C. The rate of crystallization of a liquid at a temperature T is given by the following equation[§] from Ref. 78:

$$u = \frac{L(T_m - T)}{3\pi a^2 \eta T_m}. \qquad (1)$$

[†] Cristobalite is a high-temperature crystalline form of SiO_2.

[§] Equations (1), (2) and (3) will be derived in a following section.

where T_m is the melting point, η is the viscosity of the liquid, a is a distance on the order of a lattice spacing and L is the heat of fusion at the melting temperature. The maximum crystallization velocity in cm/s of some glass forming liquids are: vitreous silica SiO_2 $2.2x10^{-7}$ [175], vitreous germania GeO_2 $4.2x10^{-6}$ [176], phosphorous pentoxide P_2O_5 $1.5x10^{-7}$ [177], sodium disilicate $Na_2O\cdot 2SiO_2$ $1.5x10^{-4}$ [178,179], potassium disilicate $K_2O\cdot 2SiO_2$ $3.6x10^{-4}$ [180], barium diborate $BaO\cdot 2B_2O_3$ $4.3x10^{-3}$ [181] and lead diborate $PbO\cdot 2B_2O_3$ $1.9x10^{-4}$ [182]. On the average the maximum rate of crystallization is roughly 10^{-4} cm/s. A simple calculation shows that to prevent the growth of crystals larger than 100 Å, liquids must be quenched in 10^{-2} s. If one is to avoid the growth of crystals larger than 10 Å it is necessary to cool the glass through the maximum range of crystallization in less than 10^{-3} s. This is a relatively short time, nonetheless all the materials cited previously are easily cooled to the glassy state. Therefore other factors seem to interfere in slowing bulk crystallization. The rate of a homogeneous crystal nucleation from a liquid is[78]:

$$I = K \exp\left(\frac{W^*}{RT}\right) \qquad (2)$$

K is specified by the model and its dependence on temperature is neglected, W* is the work needed to form a critical nucleus.

W* may be expressed by the following equation

$$W^* = -\frac{16\pi\gamma^3V^2T_m^2}{3L^2(\Delta T)^2} \tag{3}$$

where γ is the interfacial tension, V is the molar volume of the liquid, T_m is the melting temperature, L is the heat of fusion and ΔT is equal to T_m-T. The principal resistance to nucleation comes from the interfacial tension γ. Equations (2) and (3) are valid for homogeneous nucleation, usually this is not the case and nucleation is heterogeneous. It may start on impurities or on the vessel walls. These impurities lower γ. In condensed systems the nucleation rate may be limited by molecular rearrangement. One way to view this transport limitation is to multiply equation (2) by a factor which is inversely proportional to τ_r (average time for a rearrangement of a molecular position). The latter is roughly proportional to the viscosity[173]. The Fulcher equation[183] describes fairly well the viscosities of some glass-forming liquids[184-186]:

$$\eta = A \exp\left(\frac{b}{T-T_o}\right) \tag{4}$$

where A, b and T_o are constants which depend on the material and T is the actual temperature. It may be seen from equation (4) that the viscosity will increase rapidly with falling temperatures if b >> T or if $T \rightarrow T_o$ when b is small. But even by taking into consideration this transport limitation term, Turnbull and Cohen[187] showed that a low nucleation rate cannot explain glass formation in some glass-forming liquids such as those cited previously. Later Turnbull[173], in a paper entitled "Under What Conditions Can A Glass Be Formed?", discussed conditions for bypassing crystallization. He concluded that for a liquid with a low viscosity, nucleation must be suppressed for crystallization to be bypassed.

2.1.2.2 Oxide systems

Zachariassen[59] studied the atomic arrangement in oxide glasses. He concluded that if a glass is to be formed, the material should be able to form an extended three-dimensional molecular network, lacking periodicity, but having an energy comparable to that of the crystalline form. From these considerations he set up four rules for oxide systems to form a glass. These are:

(1) An oxygen is linked to not more than two atoms A.

(2) The number of oxygen atoms surrounding atoms A must be small.

(3) The oxygen polyhedra share corners with each other, not edges or faces.

(4) At least three corners in each oxygen polyhedron must be shared.

Oxides of the type A_2O or AO (A is a metal atom) do not satisfy these requirements. The rules (1), (3) and (4) are satisfied by oxides of the form A_2O_3 (if the oxygen atoms form triangles around each atom A), AO_2 and A_2O_5 (if the oxygen atoms form tetrahedra around each atom A). Rule (2) apparently excludes higher coordination. Furthermore, he concluded that the following oxides may occur in vitreous forms: B_2O_3, SiO_2, GeO_2, P_2O_5, As_2O_5, P_2O_3, As_2O_3, Sb_2O_3, V_2O_5, Sb_2O_5, Nb_2O_5 and Ta_2O_5. Later Stanworth[188] proposed three conditions for oxides to form glasses:

(1) The cation valence must be three or greater.

(2) The tendency to glass formation increases with decreasing cation size.

(3) The electronegativity should be between about 1.5 and 2.1 on Pauling's scale.

One final note on this subject is to try to relate Zachariassen's rules with crystallization rates as described in the previous section. The criterion that the energy of the glass be comparable with its crystalline form suggests a lower heat of fusion for a glass former as compared to other chemically similar materials[78]. It can be seen from equation (1) and equation (2) that a lower heat of fusion implies lower rates of nucleation and crystallization. Furthermore a relatively difficult viscous flow explains the criterion that the oxides form an extended three-dimensional network (because of the breaking of primary bonds). Unfortunately, Zachariassen's rules can only be applied to oxides. They are not able to predict glass formation in organic liquids.

2.2 PHASE SEPARATION

2.2.1 Stable Immiscibility

When liquid separation occurs at temperatures above the liquidus, it is referred to as stable immiscibility. All systems showing stable immiscibility in a region above and adjoining the liquidus have a region of metastable immiscibility below the liquidus[7] as shown in Fig. 5a. A glass made by cooling melts from above or within the region of stable immiscibility has either a strongly milky appearance or a layered structure[5]. Thus stable immiscibility is a barrier to single-phase glass formation. Figure 5a shows a binary phase diagram with both stable and metastable two-liquid immiscibility regions. In this case the liquidus has a horizontal part corresponding to the invariant (monotectic) temperature (separating the stable region from the metastable one), at which two liquids and one solid, β, co-exist. $PbO \cdot B_2O_3$[90,93] is a good example of a system exhibiting such behaviour. Thermodynamically, the system can exist as two

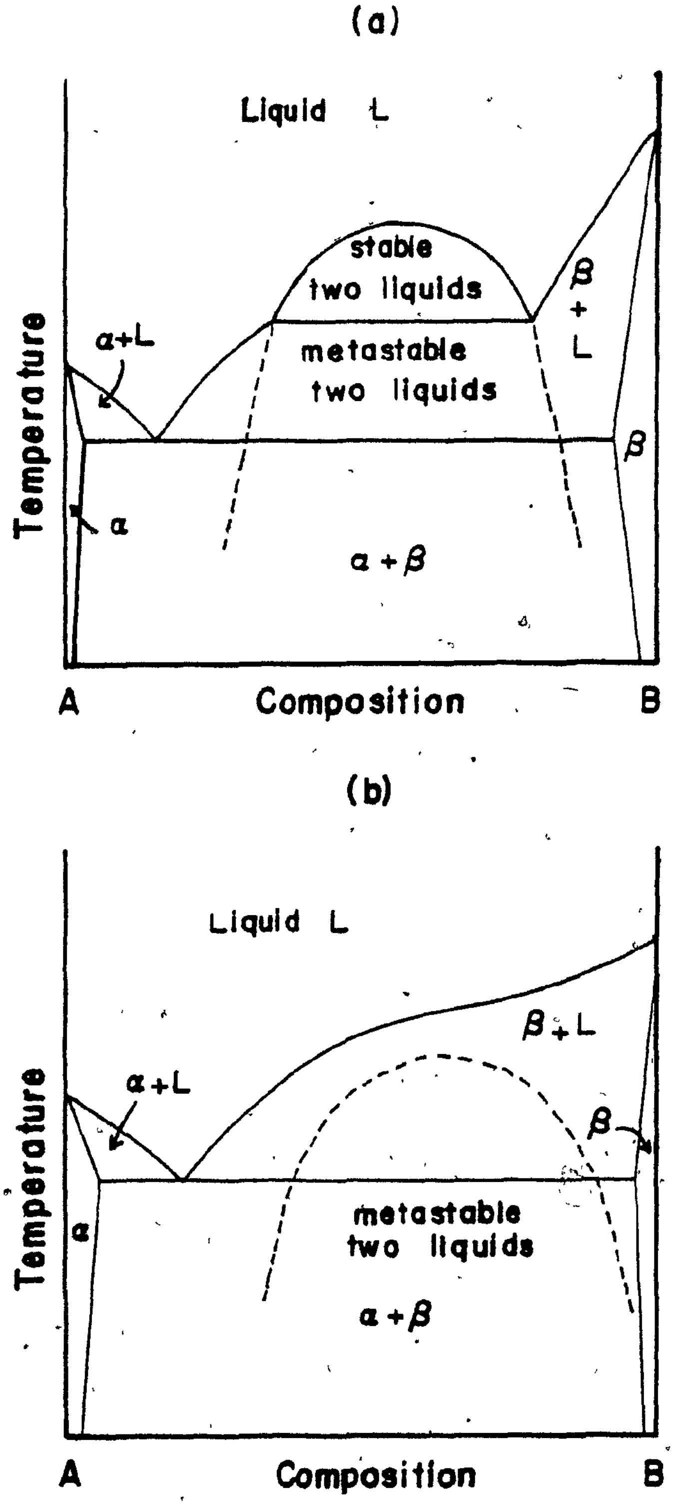

Fig. 5: Binary phase diagrams showing:
(a) Stable and metastable immiscibility;
(b) Metastable immiscibility (from Ref. 5).

liquids for an unlimited length of time (*i.e.* the two liquids comprise an equilibrium phase assemblage). On the other hand in the metastable region glasses evolve toward the more stable crystalline phase(s). This evolution can be stopped by quenching the glass rapidly below its glass transition temperature, thus leading to a kinetically stable phase.

2.2.2 Metastable Immiscibility

2.2.2.1 Experimental evidence

Metastable immiscibility is defined as liquid separation which occurs at subliquidus temperatures. We will be concerned with complete subliquidus immiscibility of the type shown in Fig. 5b. An S-shaped liquidus, as shown in Fig. 5b, is generally an indication of metastable immiscibility. This phenomenon is by far more important than the previous one (stable immiscibility). Metastable immiscibility finds many applications in the glass industry: Vycor® and Pyrex glasses are two of them.

The easiest experimental method to spot metastable phase separation is to heat treat a sample at a given temperature for a certain period of time[†] and to quickly quench the heated sample to room temperature, and observe the opalescence. The latter is in general an indication of phase

---

[†] The time of heat treatment for phase separation to occur usually depends on the temperature and the composition of the glass. A complete account of experimental procedures dealing with sodium borosilicate glasses is given in Section 3.3.2.

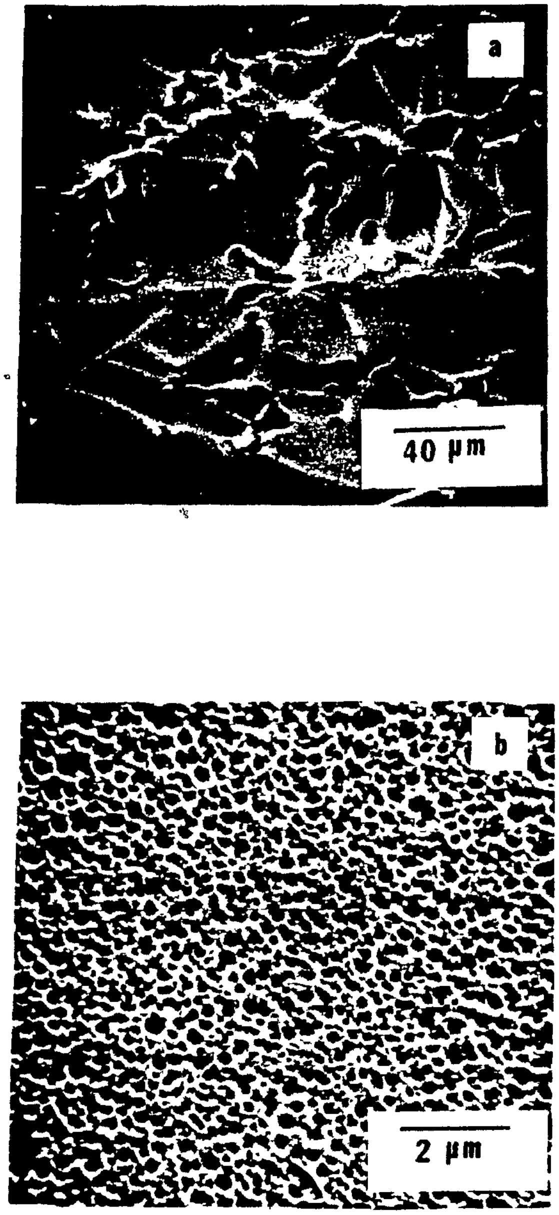

Fig. 6: Electron micrographs of phase separated glasses.
(a) Molar composition: $6.87Na_2O \cdot 48.60B_2O_3 \cdot 44.52SiO_2$, heat treated at 695°C for 16 h. Etching time: 20s/H_2O.
(b) Molar composition: $2.40Na_2O \cdot 34.43B_2O_3 \cdot 63.18SiO_2$, heat treated at 695°C for 16 h. Etching time: 15s/0.5% HF.

separation, but care is necessary because crystallization too produces opalescence[†]. Because of the rapidity of the quenching very little structural rearrangement occurs. Further examination by electron microscopy is needed to determine the extent of phase separation as well as the nature of the phases. Figure 6 shows electron micrographs of phase-separated sodium borosilicate glasses. In Fig. 6a, the fracture surface was etched by water for 20s (to enhance distinction between the phases, due to their different etch rates) while Fig. 6b shows a larger volume fraction of silicate; this latter sample was etched in 0.5% HF for 10s. Both samples were heated for 16 h at 695°C.

2.2.2.2 Thermodynamic considerations

Various theoretical attempts have been made to explain immiscibility boundaries in glasses[64,85,88,189-198] and reviews on the subject may be found in Refs. 5, 10 and 78. The following discussion is in part based on the cited references. Two views have been proposed, one based on thermodynamic principles[85,190,192,193,197], the other on crystal chemistry[64,88,189]. Figure 7a shows the Gibbs energy of two miscible components A and B as a function of composition. With decreasing temperature, the single phase separates into

---

[†] Crystallization can often be recognized visually since it is frequently localized on the glass surface, or is unevenly distributed within the glass.

two phases as shown in Fig. 7b. The molar Gibbs energy of mixing ΔG_m controlling the tendency of a glass to separate into two phases is given by equation (5) from Ref. 192:

$$\Delta G_m = G_{homogeneous} - G_{heterogeneous} \qquad (5)$$

where $G_{homogeneous}$ and $G_{heterogeneous}$ are the Gibbs energies of single-phase and two-phase mixtures. The term ΔG_m may be expressed as a function of the entropy ΔS_m and the enthalpy ΔH_m of mixing by:

$$\Delta G_m = \Delta H_m - T\Delta S_m \qquad (6)$$

For condensed systems it is assumed that the enthalpy change ΔH_m is equal to the energy change ΔE_m[192], thus equation (6) becomes:

$$\Delta G_m = \Delta E_m - T\Delta S_m \qquad (7)$$

For a regular binary solution consisting of two components, A and B, the entropy of mixing is given by equation (8), from Ref. 103:

$$\Delta S_m = -R(X_A \ln X_A + X_B \ln X_B) \qquad (8)$$

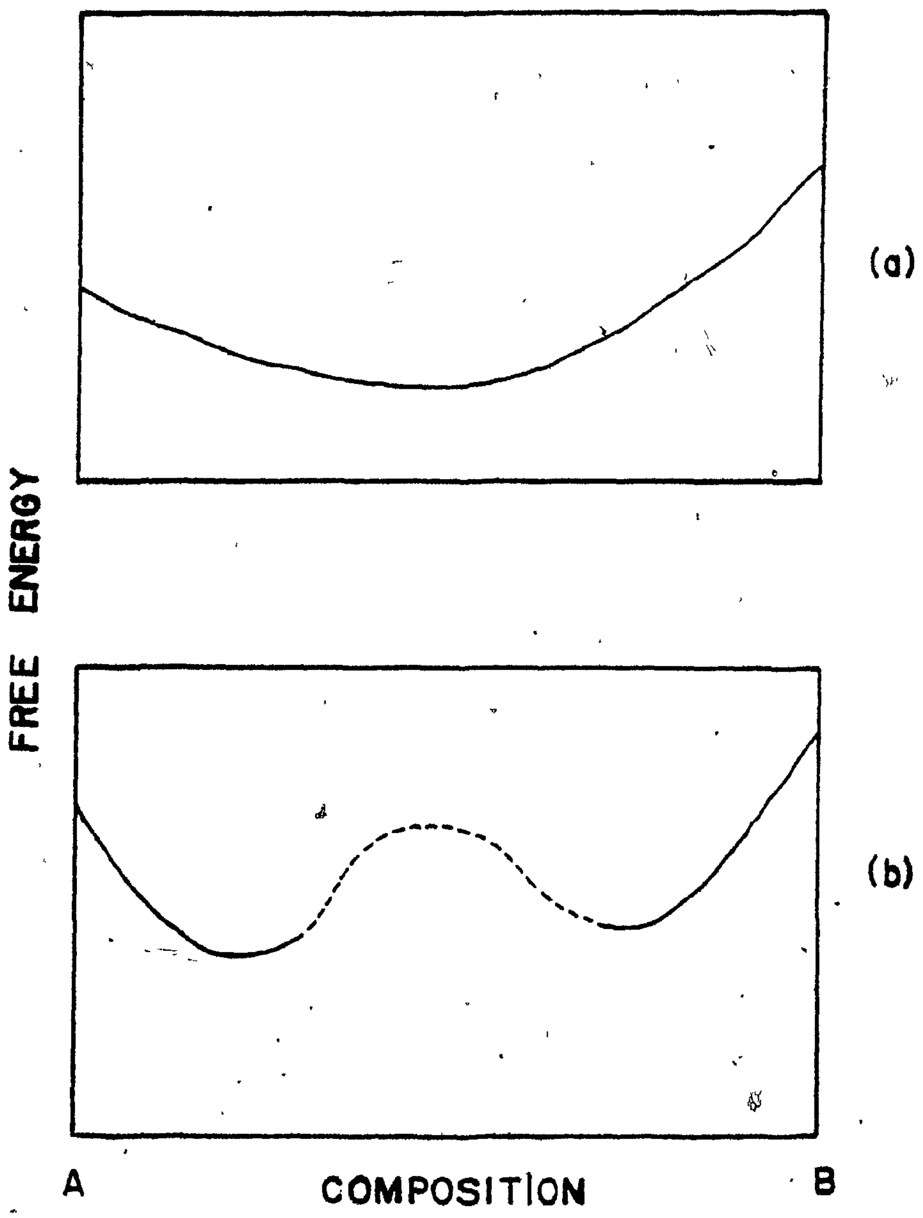

Fig. 7: Gibbs energy as a function of composition: (a) complete miscibility, (b) separation into two phases (from Ref. 78).

where X_A and X_B are mole fractions of components A and B and $X_A + X_B = 1$. The total energy of the system can be calculated from bond energies of nearest neighbours on the assumption that the binding energy is not a function of composition or temperature[78]. In a solution containing A and B molecules each having Z nearest neighbours, one can average ZX_A molecules of A and ZX_B molecules of B around any molecule in the system. Let c be the total concentration of molecules in the solution then $ZX_A^2c/2$ will be the number of A-A pairs per unit volume and similarly $ZX_B^2c/2$ the number of B-B pairs, the number of A-B pairs will be ZX_AX_Bc. The total energy, E, per unit volume may be expressed by:

$$E = -\left(\frac{ZX_A^2cE_A}{2} + \frac{ZX_B^2cE_B}{2} + ZX_AX_BcE_{AB}\right) \tag{9}$$

where $-E_A$, $-E_B$ and $-E_{AB}$ are the respective energies of A-A bonds, B-B bonds and A-B bonds. Keeping in mind that $X_A + X_B = 1$ expression (9) may be rewritten in the following way:

$$E = -\frac{Zc}{2}\left[X_AE_A + X_BE_B + 2X_AX_B\left(E_{AB} - \frac{E_A+E_B}{2}\right)\right] \tag{10}$$

It may be seen from equation (10) that the first two terms in the brackets are the energies of pure A and B, thus the energy of mixing will be:

$$\Delta E_m = - ZcX_AX_B(E_{AB} - \frac{E_A+E_B}{2}) \tag{11}$$

If $E_{AB} > (E_A+E_B)/2$ then ΔE_m is always negative and the two components are completely miscible (Fig. 7a). ΔE_m will be positive for values of $E_{AB} < (E_A+E_B)/2$, below a certain temperature the mixture will separate into two phases (this case is shown in Fig. 7b). Although this model is helpful in discussing some metallic systems[199], it is unrealistic when dealing with silicate solutions. Charles[197] proposes a different model for silicate solutions. He considered the mixing units as being bridging and non-bridging oxygen ions. Here, "bridging" oxygens refer to those linked to two silicons and "non-bridging" oxygens to those linked to one silicon atom. Furthermore, it is supposed that non-bridging oxygen ions occur in pairs. From these considerations Charles deduced the entropy of mixing to be:

$$\Delta S_m = -R[X_A \ln\frac{X_A}{2X_B} + (2X_B-X_A)\ln\frac{2X_B-X_A}{2X_B}] \tag{12}$$

Even though this expression is more realistic than expression (8), there is no direct experimental support for it[78].

A different approach dealing with crystal chemistry and based on the cation field-strength (charge/radius) was proposed[64,88,189] to explain immiscibility. On one hand miscibility is favored when the network former ions bond with all available oxygen in the melt; immiscibility, on the other hand, is favoured in compositions not allowing cations such as Na^+ or Ca^{++} to achieve their favoured coordination with non-bridging oxygen ions. Improved mutual coordination of non-bridging oxygen ions and cations can then be achieved if clusters rich in these ions are formed. These clusters could reach such proportions that two liquid phases would be formed. The number of non-bridging oxygens being somewhat limited and cations being generally surrounded by several non-bridging oxygen ions, it is necessary for a non-bridging oxygen to be bonded to more than one cation. The condition that two cations be bonded to the same oxygen delineates the cation rich limit of the miscibility gap. This last can be calculated by estimating a cation concentration corresponding to the cation-oxygen-cation bond length. Finally, these calculations do not involve any entropy terms, thus the limiting composition referred to previously is valid for 0°K only. However, it seems that below the glass transition temperature, the miscibility gap does not widen by much[10].

2.3 KINETICS OF PHASE SEPARATION

When a homogeneous glass, with a composition inside a miscibility gap, is held at a certain temperature, it starts

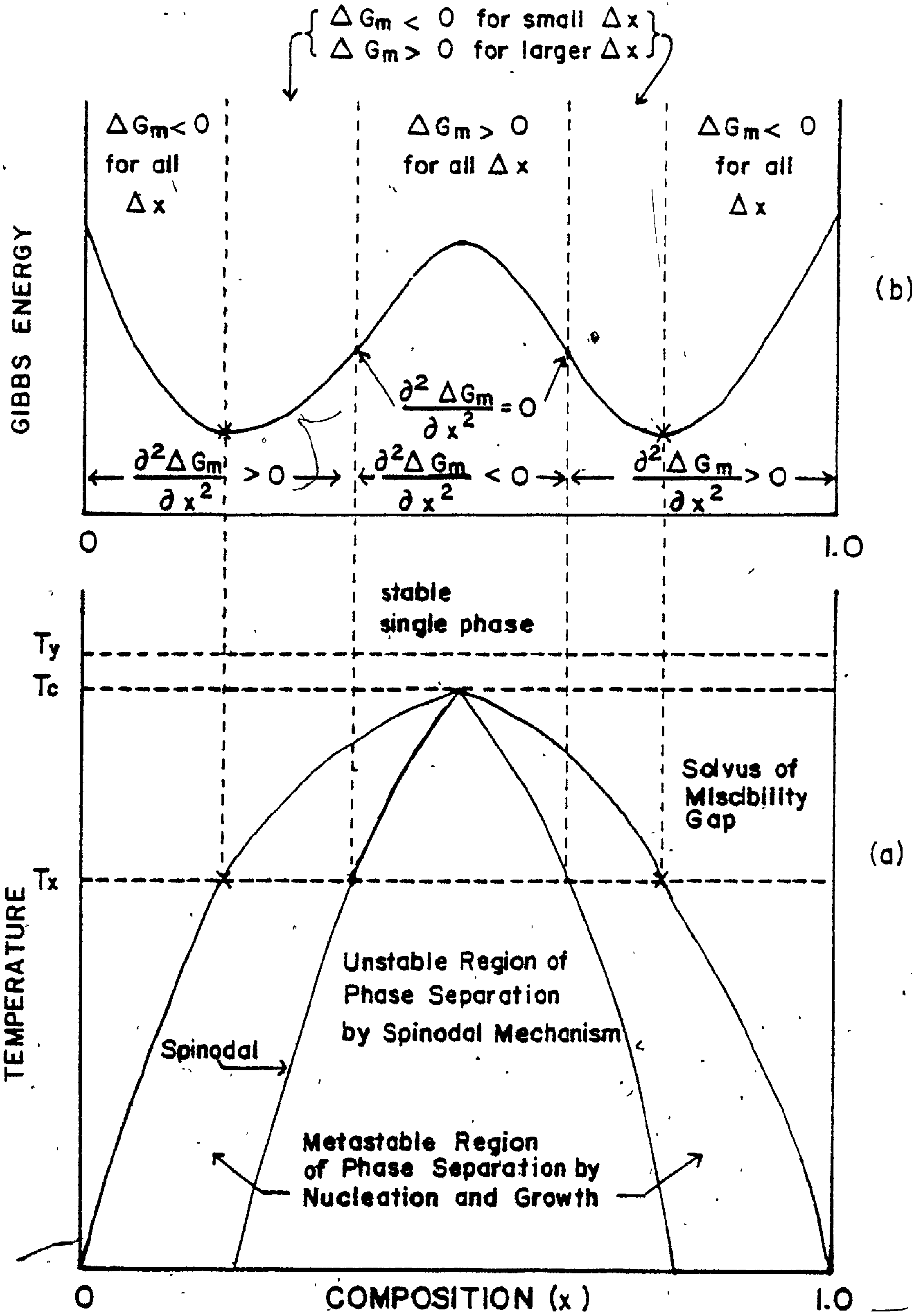

Fig. 8: (a) Schematic diagram of immiscibility boundary and spinodal. (b) Corresponding Gibbs energy of mixing at T = Tx (from Ref. 207).

to separate into two phases. Two mechanisms may be responsible for this phenomenon, one is nucleation and growth, the second is spinodal decomposition. These mechanisms are closely related to the Gibbs energy as may be seen from Figs. 8a and 8b. The spinodal line dividing the unstable region from the metastable one is defined as the locus of points for which:

$$\frac{\partial^2 \Delta G_m}{\partial x^2} = 0 \tag{13}$$

In the unstable[†] region, corresponding to the negative second derivative of the Gibbs energy of mixing with respect to composition, phase separation occurs by a spinodal mechanism. While in the metastable region, corresponding to a positive second derivative of the Gibbs energy of mixing with respect to composition, phase separation occurs by nucleation and growth, (Fig. 8a).

2.3.1 Theory of Nucleation and Growth

The probability of formation of an embryo of a second phase by fluctuation from a liquid is[78]:

[†] In this case, "metastable" and "unstable" refer to the stability of a single liquid towards phase separation, as opposed to the "metastable miscibility gap", which refers to the stability of the two-liquid assemblage towards crystallization.

$$p \propto \exp(\frac{W_r}{kT}) \qquad (14)$$

where W_r is the reversible work done on the surroundings, k is the Boltzman constant and T is the absolute temperature. Thus the rate of formation I of a growing crystalline nucleus will be proportional to the probability of forming a critical nucleus:

$$I = K \exp(\frac{W^*}{kT}) \qquad (15)$$

where K is supposed to be independent of temperature and composition and W* is the work done in forming the critical nucleus and is given by equation (16) from Ref. 200:

$$W^* = -4\pi r^{*2}\gamma + \frac{4\pi r^{*3}\Delta P}{3} \qquad (16)$$

where γ is the interfacial tension, r* the radius of the critical nucleus is given by:

$$r^* = \frac{2\gamma}{\Delta P} \qquad (17)$$

replacing expression (17) in equation (16) yields:

$$W^* = -\frac{16\pi\gamma^3}{3\Delta P^2} \qquad (18)$$

where ΔP is the pressure difference between the inside of the nucleus and the outside and is approximately equal to:

$$\Delta P \approx \frac{L}{vT_m}(T_m - T) \qquad (19)$$

where T_m is the melting temperature, L is the heat of fusion and v is the molar volume of the liquid.

Equation (16) is valid for homogeneous nucleation only. In practice nucleation is rarely homogeneous, but takes place on the vessel walls or on impurity particles, thus lowering the interfacial tension by a factor $f < 1$. Recombining equation (18) and equation (19) gives:

$$W^* = -\frac{16\pi(\gamma f)^3 v^2 T_m}{3L^2(T_m - T)^2} \qquad (20)$$

Fluctuations can be limited by viscous flow, especially in condensed systems like glasses. Taking into consideration this transport term, equation (15) becomes:

$$I = K_1 \exp\left(\frac{W^* - Q}{kT}\right) \qquad (21)$$

where Q is the activation energy for the transport process and K_1 is assumed to be independent of temperature. Two opposing factors exist in equation (21) one being W*, the work done in forming ~~the~~ critical nucleus, which becomes larger at higher temperatures due to the fact that ΔP gets smaller, thus resulting in an increase of nucleation rate with higher temperatures. The other factor is the activation energy for the transport process Q which becomes slower at lower temperatures, thus decreasing the nucleation rate. The balance of these two opposing forces results in a maximum nucleation rate at a given temperature (Fig. 9). Once the critical size is reached, the nuclei can grow by heat treatment. The frequency of jumping from liquid to crystal is:

$$\nu_1 = \nu_o \exp\left(\frac{-Q}{kT}\right) \qquad (22)$$

where ν_o is some vibrational frequency of the molecule and Q is the "activation free energy" required to cross the interface between liquid and crystal. The frequency of jumping from crystal to liquid is:

$$\nu_2 = \nu_o \exp[-(Q-\Delta G)/kT] \qquad (23)$$

where $\Delta G = v\Delta P$ (v and ΔP have been defined earlier). The velocity of crystallization will be:

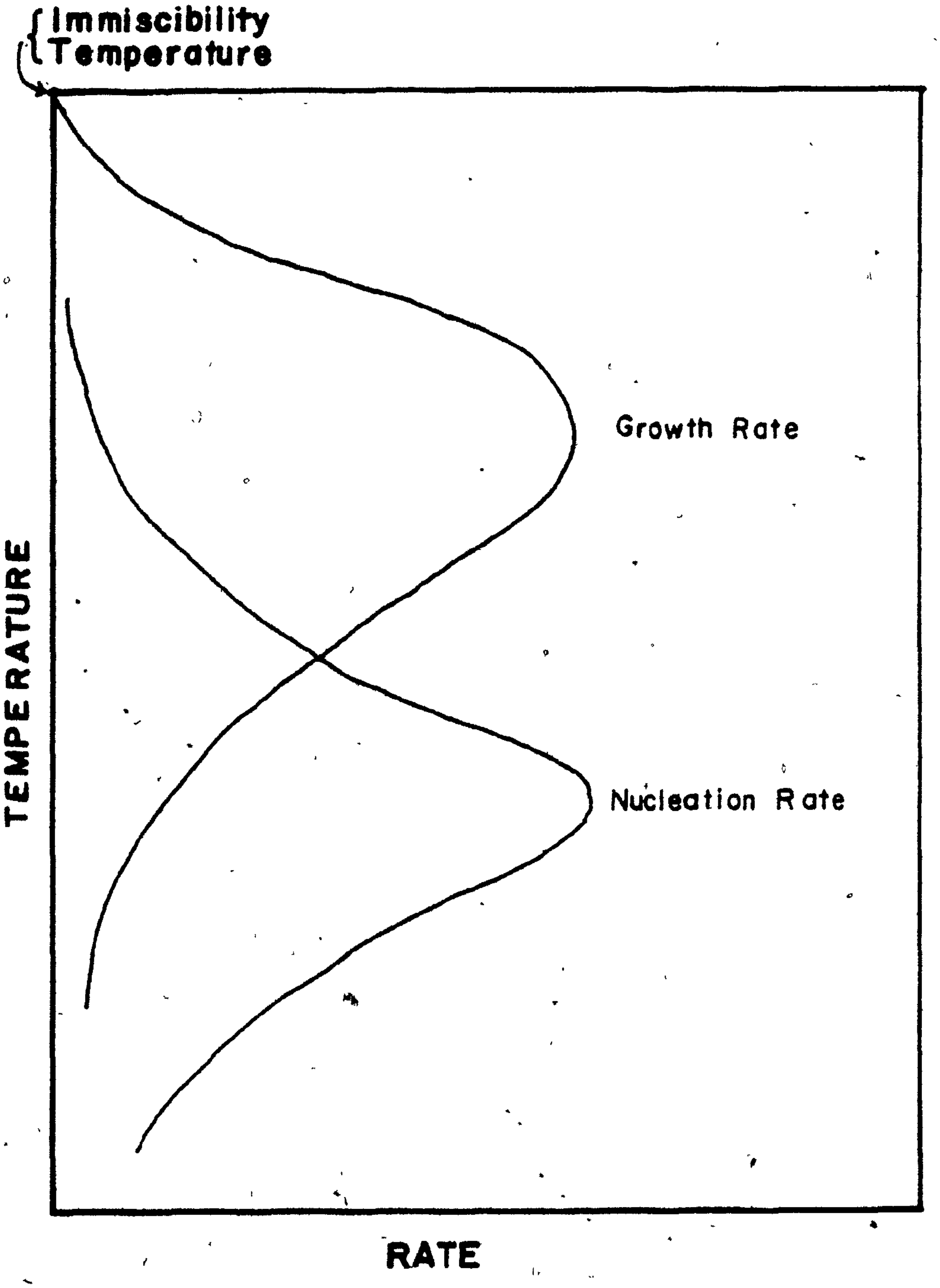

Fig. 9: Schematic diagram of nucleation rate and growth rate.

$$u = \lambda(\nu_1 - \nu_2) \qquad (24)$$

The quantity λ represents the thickness of the transition layer between liquid and crystal. Replacing expressions (22) and (23) in equation (24) yields:

$$u = \lambda v_o \exp\left(\frac{-Q}{kT}\right)\left(1-\exp\frac{\Delta G}{kT}\right) \qquad (25)$$

Here also, because of the two competing factors Q and ΔG, a maximum growth rate is observed at a temperature which is generally different from the one at which the maximum crystallization rate is observed (Fig. 9). Finally, by supposing that the diffusion coefficient in the liquid is equal to:

$$D = \lambda^2 v_o \exp\left(\frac{-Q}{kT}\right) \qquad (26)$$

and that D is also equal to (Stokes-Einstein relation):

$$D = \frac{kT}{3\pi\eta\lambda} \qquad (27)$$

Equation (25) may be rewritten in the following way:

$$u = \frac{1-\exp(\Delta G/kT)}{3\pi\lambda^2\eta} kT \qquad (28)$$

All the above quantities have been previously defined. If $\Delta G/kT$ is small, the exponential may be expanded and equation (28) becomes similar to equation (1).

2.3.2 Experimental Observation of Nucleation and Growth

Nucleation and growth studies of silica-rich particles in a soda lime silicate glass, $13Na_2O \cdot 11CaO \cdot 76SiO_2$, were made by Hammel[97]. He measured both nucleation and growth rates, using electron micrographs and showed that a constant nucleation rate was obtained only after a period of time. Hammel compared his experimental values with theory by calculating the quantities in equation (21). The critical radius, r*, was measured by holding a sample containing silica-rich particles in a temperature gradient and observing the temperature at which the size of the particles remained constant. At this temperature the radius of the particles was considered to be the critical radius r*. At lower temperatures, r* was determined by extrapolating the plot of T *versus* 1/r*. The term ΔP was calculated from miscibility gap data assuming the validity of the Lumsden solution model[201]. A value of 4.6 ergs cm^{-2} for γ was then derived from equation (17). The term ΔQ = 94.5 kcal

mole^{-1} was obtained from Frank's diffusion controlled growth theory[202]. Finally K_1 was calculated from an equation derived by Turnbull[203]. All the quantities needed to calculate nucleation rates from equation (21) were available. The calculated values of nucleation rates agreed fairly well with the experimental ones. Although it is not certain that the diffusion controlled growth theory by Frank can be applied to Hammel's experiments, one can conclude that phase separation in this system probably follows the homogeneous nucleation process.

2.3.3 Theory of Spinodal Decomposition

An alternative to the nucleation and growth mechanism for phase separation is decomposition by a spinodal mechanism. In this mechanism there is no nucleation of the second phase composition. Transformations occur by a continuous change of growing phases with their extent being constant. A comprehensive approach to this theory was proposed by Hillert[204] and Cahn[205]. A concise description of Cahn's analysis is presented here.

The Gibbs energy of the inhomogeneous system is given by[†]:

$$G = \int_V [g(c) + \kappa(\nabla c)^2] \, dv \qquad (29)$$

[†] Cahn used Helmholtz free energy. However, at 1 atm pressure in condensed systems the difference between Helmholtz free energy and Gibbs energy can be neglected.

Where g(c) is the Gibbs energy of a unit volume of homogeneous material of composition c, $\kappa(\nabla c)^2$ the first term of an expansion representing the increase in Gibbs energy due to a gradient of composition and κ a positive quantity called the gradient energy coefficient. Assuming that the molar volume is independent of composition, then g(c) may be expanded around the average composition c_o:

$$g(c) = g(c_o) + (c-c_o)\left(\frac{\partial g}{\partial c}\right) + \frac{1}{2}(c-c_o)^2\left(\frac{\partial^2 g}{\partial c^2}\right) + \ldots \tag{30}$$

and keeping in mind that:

$$\int_V (c-c_o)\, dv = 0 \tag{31}$$

The Gibbs energy difference per unit volume between the homogeneous solution and one with composition fluctuation may be written as:

$$\Delta G = \int_V \left[\frac{1}{2}(c-c_o)^2 \frac{\partial^2 g}{\partial c^2} + \kappa(\nabla c)^2\right] dv \tag{32}$$

Introducing a one-dimensional composition modulation of amplitude A and wavenumber β ($\beta = 2\pi/\lambda$) such as:

$$c-c_o = A \cos \beta x \qquad (33)$$

in equation (32) yields:

$$\frac{\Delta G}{V} = \frac{A^2}{4}\left[\frac{\partial^2 g}{\partial c^2} + 2\kappa\beta^2\right] \qquad (34)$$

From equation (34) it may be seen that if $\partial^2 g/\partial c^2 > 0$, then the solution is stable with respect to infinitesimal sinusoidal fluctuations of all wavenumbers. If $\partial^2 g/\partial c^2 < 0$, then the solution is unstable with respect to infinitesimal sinusoidal fluctuation of wavenumbers less than β_c (critical value of β) given by:

$$\beta_c = \left[- \frac{\partial^2 g}{\partial c^2} \Big/ 2\kappa\right]^{1/2} \qquad (35)$$

or in terms of $\lambda_c = 2\pi/\beta_c$:

$$\lambda_c = \left[- \frac{8\pi^2\kappa}{\partial^2 g/\partial c^2}\right]^{1/2} \qquad (36)$$

A kinetic expression of the initial stages of phase separation by a spinodal mechanism may be obtained by solving a diffusion equation in which the thermodynamic factors are included. This yields for the time-dependent amplitude at a time $\underline{t}$ of a given component with a wavenumber β:

$$\frac{\partial A(\beta,t)}{\partial t} = R(\beta)A(\beta,t) \tag{37}$$

Solving this equation with the initial condition being $t = 0$ gives

$$A(\beta,t) = A(\beta,0)\exp[R(\beta)t] \tag{38}$$

where $A(\beta,0)$ is the amplitude of the initial composition fluctuation and $R(\beta)$ is the amplitude factor given by:

$$R(\beta) = -M\beta^2\left[\frac{\partial^2 g}{\partial c^2} + 2\beta^2\kappa\right] \tag{39}$$

The quantity M is a mobility related to the interdiffusion coefficient $\tilde{D}$ by:

$$M = \frac{\tilde{D}}{\partial^2 g/\partial c^2} \tag{40}$$

It may be seen from equation (38) that an amplitude of composition fluctuation with a wavenumber β changes exponentially with time, this change being governed by $R(\beta)$. In the spinodal region $R(\beta)$ is positive for wavenumbers less

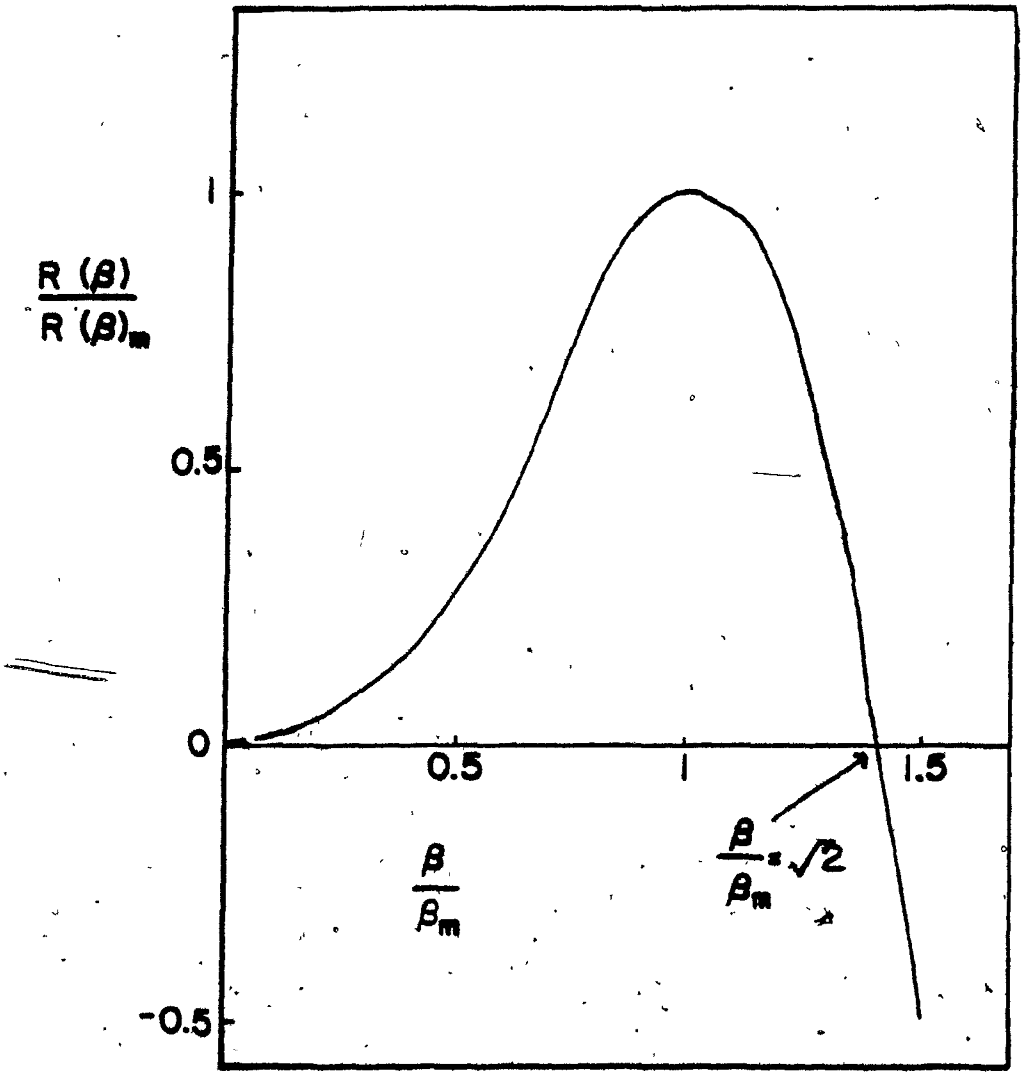

Fig. 10: Amplification factor $R(\beta)$ in Cahn's theory *versus* wavenumber β (from Ref. 5).

than β_c and the maximum amplification occurs at $\beta_m = \beta_c/\sqrt{2}$ (Fig. 10). This particular wavenumber will grow at the fastest rate. Considering only this wavenumber Cahn obtained interconnected phases by computer mixing the sinusoidal composition fluctuation in three dimensions[206]. Further details on spinodal decomposition may be found in Refs. 207-211.

2.3.4 Experimental Observation of Spinodal Decomposition

Cahn's theory was tested by small-angle X-ray scattering (SAXS). This technique is very convenient for investigating the early stage kinetics in the unstable region[212]. The diffracted intensity $I(h,t)$ is proportional to $|A(\beta,t)|^2$ where $A(\beta,t)$ is the amplitude of the Fourier component of wavenumber β at time t (equation 38) and $h = 4\pi/\lambda \sin \theta$, θ being the scattering angle and λ the wavelength (h is the scattering vector in reciprocal space). Thus any change in the amplitude in spinodal decomposition can be studied by following the scattered intensity. Identifying the scattering vector with β yields:

$$I(\beta,t) = I(\beta,0)\exp[2R(\beta)t] \qquad (41)$$

where $I(\beta,0)$ is the scattering intensity at $t = 0$ corresponding to the wavenumber $\beta = 2\pi/\lambda$. From equation (41) $R(\beta)$ can be evaluated by measuring I(β,t) as a function of time of heat treatment. Neilson[213] measured the effect of heat treatment on the scattered intensity in 12.6 $Na_2O \cdot 87.4\ SiO_2$ and 13.2 $Na_2O \cdot 86.8\ SiO_2$ glasses. The times of heat treatment ranged from 0 to 4 h and the heating temperatures from 450 to 650°C. The plot of the scattered intensity *versus* the scattering angle for the 12.6 Na_2O glass showed a common cross-over point† corresponding to a particular β (at least for heat treatment up to 1 h). Moreover, there is a particular wavelength that grows the fastest. These results are consistent with Cahn's prediction of spinodal decomposition. No common cross-over point was detected for the 13.2 Na_2O glass (even in the early stages of heat treatment). Neilson concluded that nucleation and growth is probably responsible for the phase separation in the 13.2 Na_2O glass, while the 12.6 Na_2O glass undergoes spinodal decomposition.

Srinivasan *et al.*[214] studied the time evolution of volume fraction of the minor phase in an alumina doped sodium borosilicate glass inside the miscibility gap. They claimed that a distinction could be made between the two mechanisms of phase separation (*i.e.* nucleation and growth and spinodal decomposition). Their assumption was based on the fact that for spinodal decomposition the volume fraction of the minor phase decreases initially with heat treatment,

---

†The cross-over point comes from the fact that R(β) = 0 for a particular wavenumber and is positive for $\beta < \beta_c$ and negative for $\beta > \beta_c$.

whereas for nucleation and growth it increases. It is not clear if 2°C can distinguish between the two mechanisms of phase separation. Furthermore, etching conditions influence volume fraction determination by replica electron microgroscopy[98].

Recently Tomozawa[215] attributed the gradual change in chemical durability (HF etch rate or HCl leaching rate) and viscosity of heat treated sodium borosilicate (600°C) to gradual composition variation of separated phases. Thus he concluded that phase separation in these glasses when heated at low temperatures (600°C) takes place by spinodal decomposition. The main points of this section are summarized in Table 1 which lists the major differences between the two mechanisms of phase separation.

2.4 INTERPRETATION OF DIAGRAMS

2.4.1 Binary Systems

Books and reviews on the interpretation of phase diagrams may be found in Refs. 1, and 216-218. Figure 11 shows a typical phase diagram for a binary oxide system with a two-liquid region. The line KK' which passes through the two liquid region is an isopleth. Following this line of constant bulk composition, different changes in the phases occur which are described in the following paragraph.

Table I[†]

Difference between nucleation and growth and spinodal mechanisms during isothermal phase separation.

Nucleation and growth	Spinodal decomposition
Invariance of second-phase composition to time at constant temperature	Continuous variation of both extremes in composition with time until equilibrium compositions are reached
Interface between phases is always same degree of sharpness during growth	Interface between phases initially is very diffuse, eventually sharpens
Tendency for random distributions of particle sizes and positions in matrix	Regularity of second-phase distribution in size and position characterized by a geometric spacing
Tendency for separation of second-phase spherical particles with low connectivity	Tendency for separation of second-phase, non-spherical particles with high connectivity

---

[†] From Ref. 210.

Above the temperature T_K the two components are miscible in all proportions. On cooling along KK', the melt begins to separate into two liquids, L_1 and L_2 at T_K. At T_1 a melt of bulk composition a is formed of two liquids L_1 and L_2 of respective compositions a_1 and a_2. The amounts of which are given by the lever rule:

$$L_1 = \frac{a_2-a}{a_2-a_1} \qquad L_2 = \frac{a-a_1}{a_2-a_1}$$

On further cooling the compositions of L_1 and L_2 alter along the immiscibility boundary K-a_1-b_1 and K-a_2-b_2, respectively. At T_2 (monotectic temperature) and when the first crystal of A has formed[†], the amounts of the two liquids b_1 and b_2 in equilibrium with solid A are:

$$\text{Liquid } b_1 = \frac{b_2-b}{b_2-b_1} \qquad \text{Liquid } b_2 = \frac{b-b_1}{b_2-b_1}$$

At this point the temperature remains constant while heat is removed from the system and solid A is formed at the expense of liquid b_2. When the last drop of liquid b_2 has crystallized a solid A is in equilibrium with a liquid b_1[§].

[†] This situation is referred to as maximum heat content.

[§] This situation is referred to as minimum heat content.

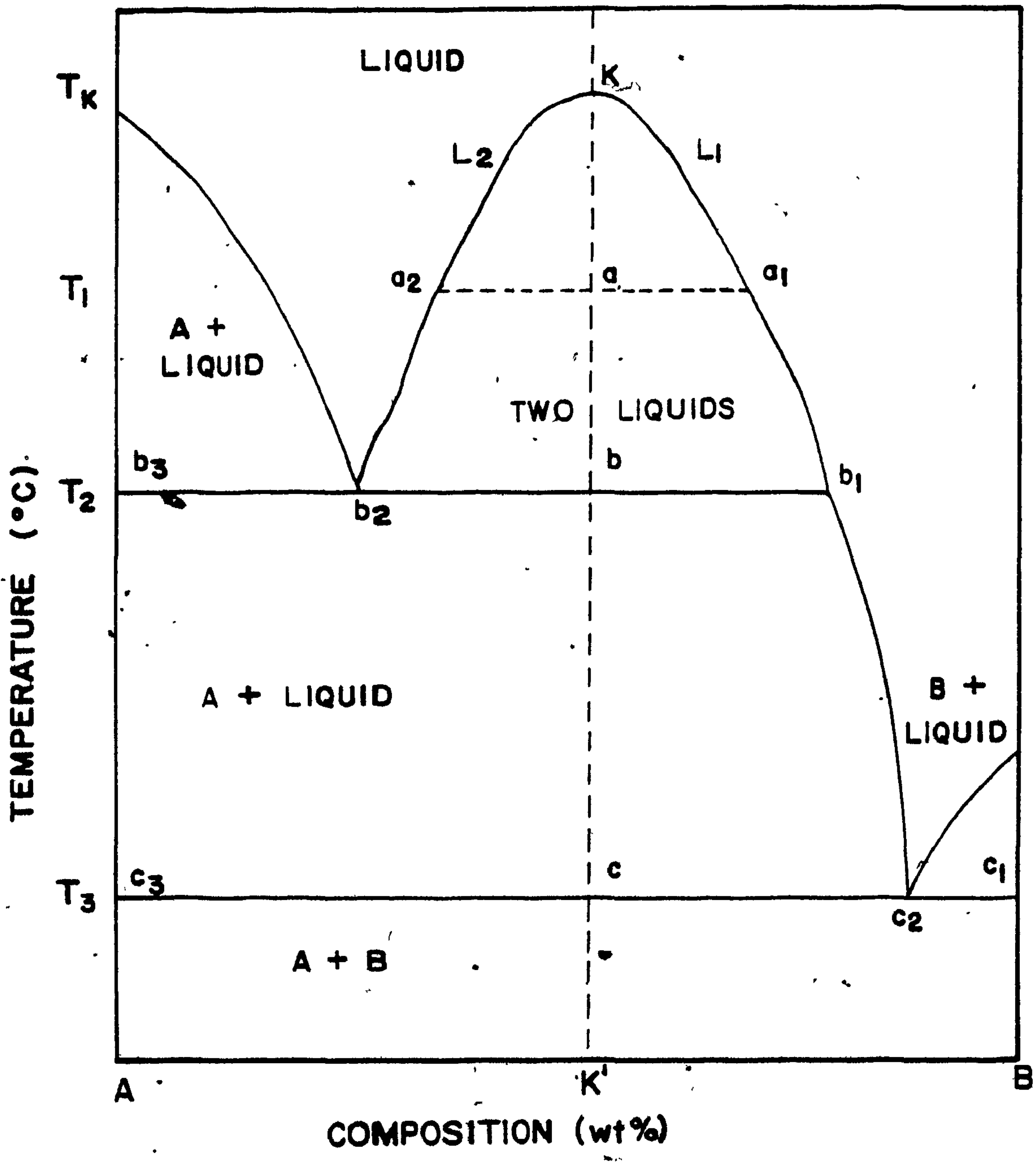

Fig. 11: Phase diagram of a two component system with conjugate liquid phases (from Ref. 1).

Again the amounts present are given by the lever rule:

$$\text{Liquid } b_1 = \frac{b_3-b}{b_3-b_1} \qquad \text{Solid A} = \frac{b-b_1}{b_3-b_1}$$

Upon further cooling the percentage of liquid b_1 decreases as solid A crystallizes. At T_3 (eutectic temperature) crystallization of solid B starts and the amounts of the phases present at maximum heat content are:

$$\text{Liquid } b_1 = \frac{c_3-c}{c_3-c_2} \qquad \text{Solid A} = \frac{c-c_2}{c_3-c_2}$$

When crystallization is complete at minimum heat content the amount of the two solid phases A and B are:

$$\text{Solid A} = \frac{c-c_1}{c_3-c_1} \qquad \text{Solid B} = \frac{c_3-c}{c_3-c_1}$$

Finally, the line connecting the two co-existing liquid phases L_1 and L_2 is called a conode or a tie-line ($a_2\,a\,a_1$, Fig. 11). This line is isothermal and parallel to the composition axis (in binary systems). On going from T_1 to T_K this tie-line decreases in length and transforms to a point K at T_K. T_K is called the consolute temperature and the corresponding point K is the consolute composition. At this point the composition of the two liquids L_1 and L_2 is identical.

2.4.2 Ternary Systems

The compositions of a ternary mixture for a given temperature and pressure can be represented by triangular coordinates (Fig. 12.2 and 12.3). The total composition of the three components is 100%. This restriction reduces the dimensions by one. Each side of the triangle may be considered to be a binary system and the letters A, B and C represent pure components. These triangles are usually equilateral and each side is divided into 100 parts with 10 subdivisions (Fig. 12.3). The composition at point b (Fig. 12.2) represents a binary mixture of 40% A and 60% C; that at point c 55% A and 45% B; and that at point a 65% C and 35% B. Any point inside the triangle is composed of a mixture of A, B and C. One method of estimating the amounts of the mixture for a particular point (P for example, Fig. 12.2) is to draw perpendiculars to the three sides of the triangle. The length of each perpendicular represents the relative amount of the component represented by the apex opposite to the side to which the perpendicular was drawn. Thus point P is a ternary mixture of 50% C, 20% B and 30% A. A more convenient method of estimating the relative composition of a ternary

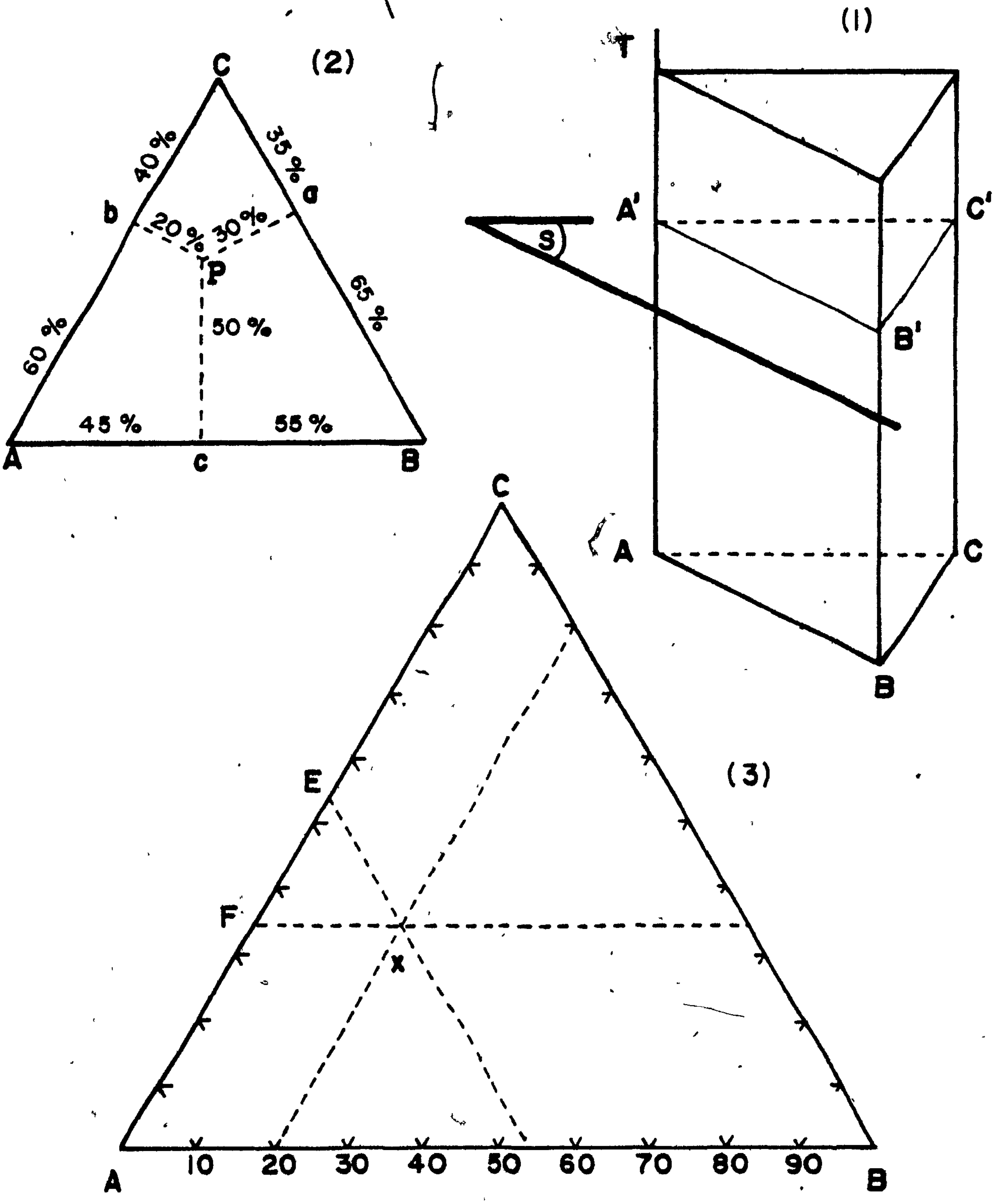

Fig. 12: Graphic representation of a three component system (from Refs. 216 and 217).

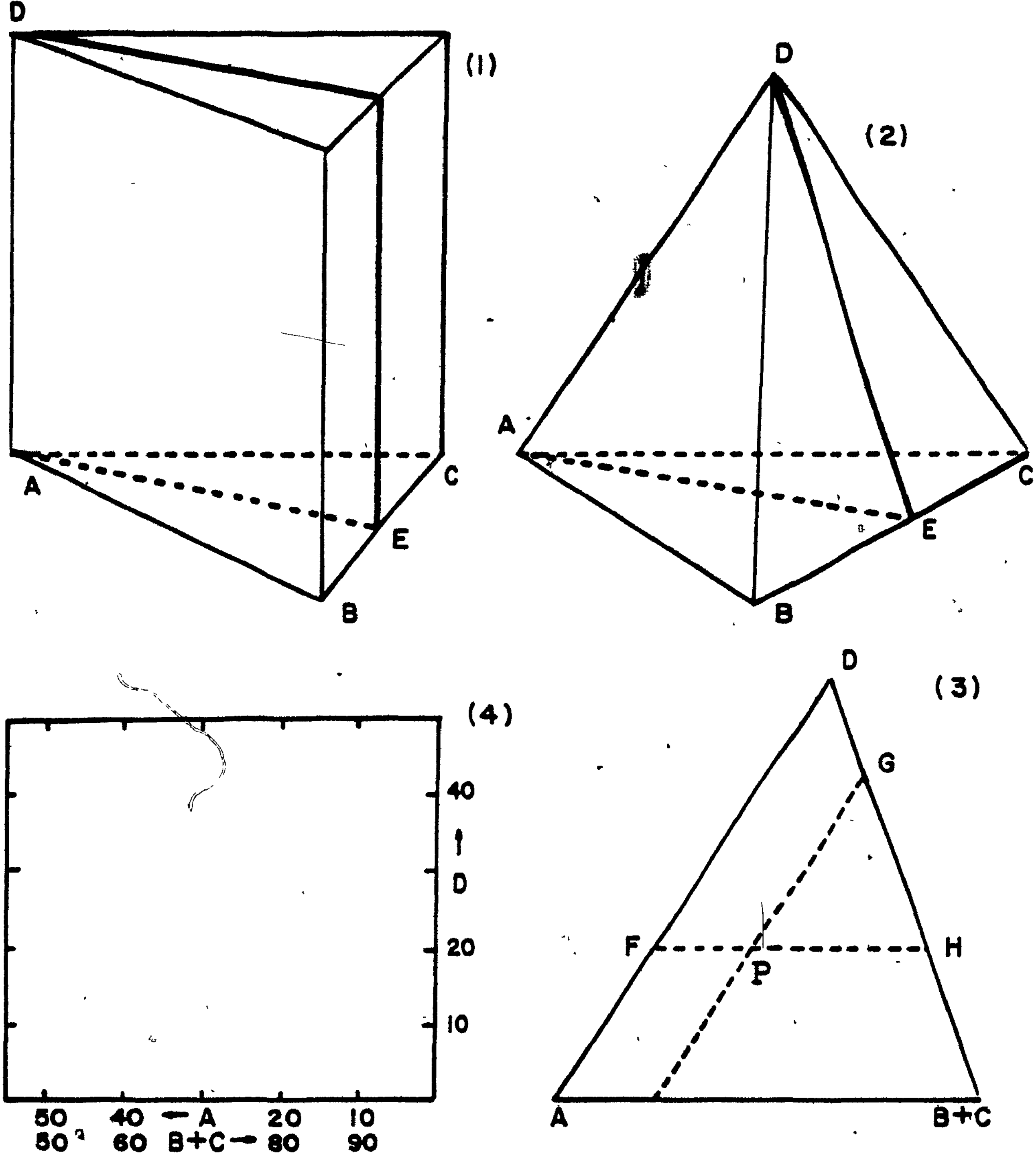

Fig. 13: Graphic representation of a quaternary system.

mixture is to construct parallels to the three sides of the triangle (point X, Fig. 12.3). The length CE represents 45% of A in X, the length AF 35% of C and the length of FE 20% of B. The same procedure could be applied to the other two sides and would yield the same results.

Temperatures can be represented by a perpendicular to the triangular composition section (Fig. 12.1) and phase boundary isotherms by contours within such a triangular composition diagram (Figs. 1 and 14).

2.4.3 Quaternary Systems

A quaternary system is usually represented by a triangular prism (Fig. 13.1) or a regular tetrahedron[†] (Fig. 13.2), the former being more convenient when only small quantities of the fourth component are under study. Each edge of the prism or the tetrahedron represents a binary system, and each face a ternary system. Any point inside the tetrahedron or the prism represents a quaternary mixture of components A, B, C and D. A simplified representation of quaternary systems is obtained by considering pseudo binary systems (Figs. 13.3 and 13.4). Such systems are obtained by drawing a cross-section through one face of the prism or tetrahedron. The join AE represents a fixed ratio of C/B. The corresponding pseudo binary systems (Figs. 13.3 and 13.4) represent phase diagrams for a fixed

---

[†] For a given temperature and pressure.

ratio of two components C and B while the remaining amounts of A and D change. The relative amount of the four components at point P (Fig. 13.3) may be expressed as a function of A, D and the mixture (B+C). The percentage of D = HB/DB x 100; that of A = GH/DB x 100; and that of (B+C) = DG/DB x 100. Thus any quaternary system may be represented in two dimensions as a pseudo binary[†] system.

2.5 SODIUM BOROSILICATE GLASSES

2.5.1 Phase Diagrams

Phase separation in sodium borosilicate glasses has been thoroughly studied[17-20,163-167,219]. The topography of the miscibility gap in this system is generally fairly well established. Two versions of the immiscibility perimeters have been published, one by Haller *et al.*[17] (Fig. 1) and the other by Galakhov and Alekseeva[18] (Fig. 14). Haller's phase diagram is drawn on a weight basis while Galakhov's is on a molar basis. However, some serious discrepancies exist between the two phase diagrams[163]. In Haller's version the 700°C miscibility gap is a dome adjoining the binary $B_2O_3 \cdot SiO_2$ system, while in Galakhov's version it is an elongated dome running roughly parallel to the $B_2O_3 \cdot SiO_2$ binary. Further differences are found in the extent

---

[†] Although the pseudo-binary system can represent all overall compositions in a section of a quaternary system, in general it cannot represent the compositions of the individual phases (*i.e.* tie-lines do not, in general, lie within the pseudo-binary plane).

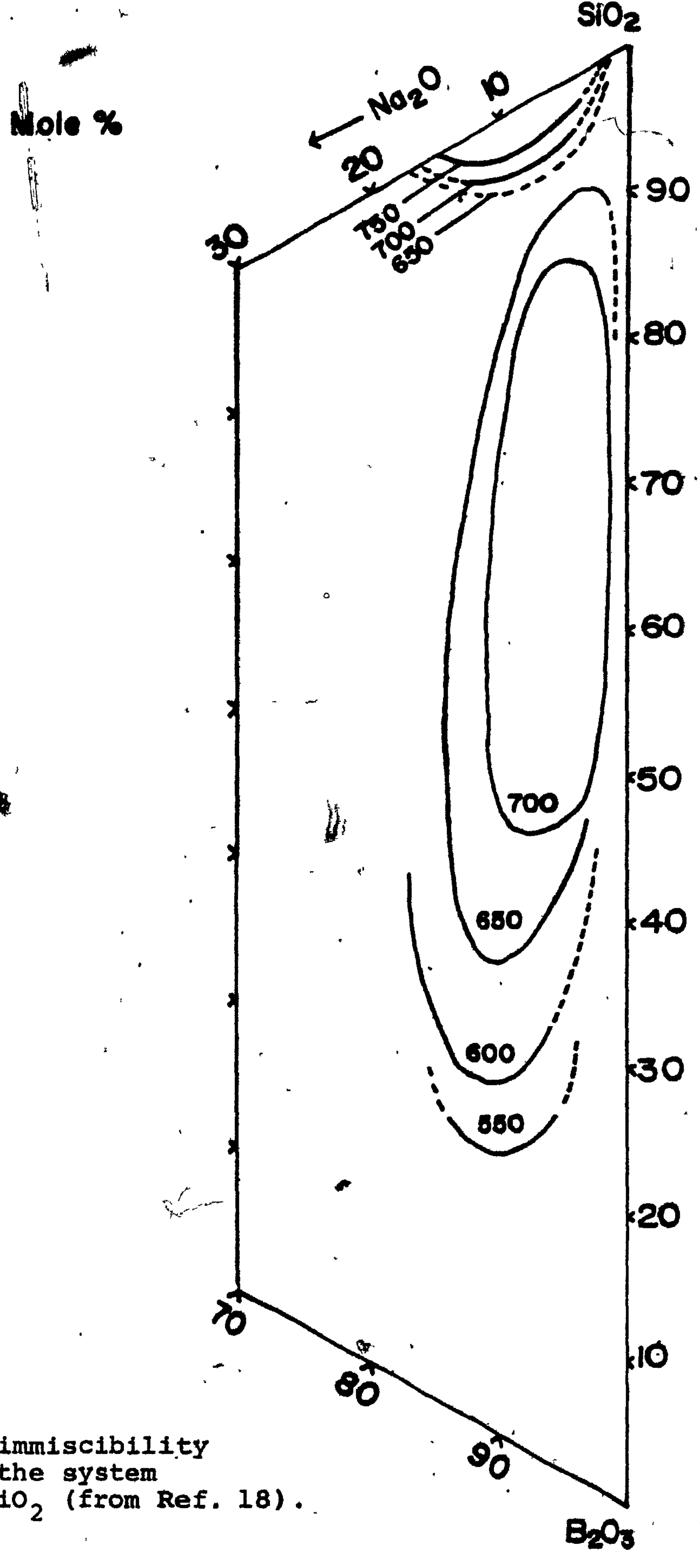

Fig. 14: Metastable immiscibility surface in the system $Na_2O \cdot B_2O_3 \cdot SiO_2$ (from Ref. 18).

of the overlap between the immiscibility area close to the binary $Na_2O \cdot SiO_2$ side. Finally, even if one converts mole% to weight% and brings the two phase diagrams to the same basis, some minor differences still exist in the network former ends of the isotherms. The two versions agree on the general form of the immiscibility boundaries, that is elongated domes one inside another with the lowest immiscibility temperature belonging to the largest dome.

2.5.2 Tie-Lines (or Conodes)

2.5.2.1 Definition

"For a particular temperature, the straight line connecting the compositions of two (conjugate) phases in equilibrium with each other"[216]. Thus any composition on a particular tie-line of an isotherm consists of two phases with compositions represented by the ends of the tie-line. Furthermore, the amounts of the two phases are given by the lever rule.

2.5.2.2 Determination

Several attempts were made to determine the tie-lines in sodium borosilicate glasses. Srinivasan *et al.*[19] examined the volume fraction of separated phases by electron microscopy. However, this method is subject to large error due to variations of etching conditions[98]. Another technique is to use an electron microprobe analyzer[162,163]. Thus the composition of the phases can be determined directly (assuming large separated particles ∿ 1 μm). Chemical analysis of the solvent after leaching the phase separated glasses[220] has also been used. Since direct analysis of phases is generally not feasible, the most reliable method appears to be the determination of the glass-transition temperature of phase-separated glasses. All composition along one tie-line when melted will separate into identical phases. Thus, a line of equal properties of any separable phase must coincide with the appropriate tie-line. Based on the fact that the glass transition temperature T_g is determined solely by one of the separated phases and is independent of its volume fraction[221], Mazurin and Streltsina[20] estimated the positions of the tie-lines in the ternary sodium borosilicate system. One of their tie-lines corresponding to T_g = 400°C is shown in Fig. 31.

2.6 LUMINESCENCE AND RELATED PHENOMENA

2.6.1 Introduction

A free ion with a d^5 electronic configuration gives rise to terms whose separation from the ground state (^6S) depends on the two electron repulsion parameters (Racah parameters) B and C. The electrostatic perturbation caused by a crystal field further splits these terms[249]. As the ratio of the crystal field strength (Δ) to the inter-electron interaction (B) increases, this crystal field splitting increases, giving rise to the energy level diagram. For a point charge model, the magnitude of the splitting within the field depends on the symmetry of the field (octahedral or tetrahedral) surrounding the central ion. For a d^5 configuration (Mn^{2+}), the same terms arise for both fields yielding identical energy level diagrams for either symmetry. Although the energy level diagrams are the same for both symmetries, the crystal field parameter Δ_t for tetrahedral symmetry can be related quantitatively to the crystal field parameter Δ_o for octahedral symmetry by:

$$\Delta_t = -\frac{4}{9}\Delta_o \qquad (41)$$

This relation assumes all ligands have equal point charges and are equidistant from the central ion[244]. Figure 4 shows the energy level diagram of a d^5 configuration at a given C/B.

2.6.2 Absorption

Electronic transitions[†] from the ground state ($^6A_1$) to one of the excited levels of Fig. 4 are governed by the following selection rules: the spin selection rule forbidding transitions between states of different multiplicity, and symmetry selection rules which in O_h forbid transitions between states of the same parity (*i.e.* Laporte selection rule, $g \not\rightarrow g$ and $u \not\rightarrow u$). Spin-orbit coupling, spin exchange or superexchange (*via* oxygen ions) may relax the spin selection rule while vibronic coupling can help overcome the Laporte selection rule. Thus forbidden transitions can still be observed but are generally orders of magnitude weaker than allowed transitions. Since d-d transitions of a given d^5 ion in an octahedral site are forbidden by both selection rules while those of the same ion in a tetrahedral site are only spin forbidden, one would expect higher absorption intensities from the tetrahedral ions than from the octahedral ones. This is indeed the case, and Bingham and Parke[154] reported that Mn^{2+} in sodium silicate glasses (tetrahedral environment) has an extinction coefficient three times that of Mn^{2+} in sodium borate glasses (octahedral environment).

[†] We are interested in those transitions which occur by an electric dipole process. Transitions may also occur by magnetic dipole or electric quadrupole processes but are orders of magnitude weaker in intensity.

2.6.3 Luminescence

The absorption of a quantum of light with a frequency corresponding to the energy separation between any given excited state and the ground state of Fig. 4 causes that particular excited state to be populated. There are two processes which compete to depopulate that excited state: radiationless processes whereby the excited state loses its excess energy through means other than the emission of light (usually as heat), and radiative processes by which the excited state emits photons to dissipate its excess energy. Depending on the position of the populated state with respect to other lower excited states and to the ground state, one of the two processes may prevail. If for example the $^4T_2$ (D) level of Fig. 4 is populated it will probably lose its energy non-radiatively by cascading to the $^4T_1$ (G) level. From that level the excess of energy may then be lost by a radiative process. Although this scheme is likely to occur it is not a general rule. For example radiative emission from the $^4T_2$ (G) to the $^6A_1$ (S) level has been reported by Medlin[243] in anhydrite activated with Mn^{2+}.

In condensed phases, the width of emission (or absorption) bands is due to the slope of the energy parameter of the state (E/B) with respect to the crystal field parameter (Δ/B) and to fluctuations of Δ/B in the particular environment. In crystals these fluctuations (Δ/B) are due primarily to lattice vibrations, and the broadening is temperature dependent because more lattice vibrations are excited at higher temperature. However, in glasses the broadening due to the random nature of the environment (and hence the large spread of crystal fields) is larger than that due to vibrations, therefore little temperature dependence of the emission (or absorption) is expected.

The intensity of the luminescence is related to the concentration of the activator. By increasing the activator concentration, the intensity may initially increase until a critical value is reached and then decrease beyond this value. This phenomenon, known as concentration quenching results from an increase in non-radiative energy dissipation at the expense of the radiative process. Higher concentrations of activator increase the probability of energy transfer (of the excitation energy) to impurities (such as Fe^{3+} ions in the glass) which can then act as trapping sinks that dissipate the excitation energy non-radiatively as heat.

2.6.4 Excitation

The crystal field strength Δ can be determined by fitting absorption data to the corresponding energy level diagram. A value of Δ/B is estimated from these diagrams and Δ can then be calculated. Unfortunately, the absorption spectra of certain glass compositions doped with

MnO are weak and poorly resolved[154]. Furthermore, in phase separated glasses light is badly scattered and absorption spectroscopy is impossible. Excitation spectroscopy is an alternative, the advantages of which have been previously discussed (Section 1.3.2).

In sodium borosilicate glasses Mn^{2+} luminescence consists of a high energy band believed to originate from Mn^{2+} in tetrahedral sites and a low energy one believed to arise from Mn^{2+} in an octahedral environment (this will be discussed in further detail in Chapter 4). It is possible to measure the transitions of Mn^{2+} in each of the two sites by using the corresponding emission band to measure the excitation spectrum. Bingham and Parke[154] measured the excitation spectra of divalent manganese in calcium borate and sodium borate glasses. They reported that the excitation spectra of these doped glasses correlated well with their corresponding (weak) absorption spectra. In the present work excitation spectroscopy is used to locate the corresponding absorption bands.

2.6.5 Energy Level Diagrams

Two approaches are commonly used to calculate the energy level diagrams for a d^n configuration. The weak field scheme of Orgel[246] and the strong field approximation of Tanabé and Sugano[245]. Both calculations give equivalent results. The following method of calculation is from Ref. 154 and is used in Section 4.5 to calculate the energy diagram of Mn^{2+} in sodium borosilicate glasses.

The weak field matrices of the quartet levels of a d^5 configuration are given by:

$^4A_1(^4G)$

$$10B + 5C$$

$^4A_2(^4F)$

$$22B + 7C$$

$^4E(^4G, ^4D)$

$$\begin{array}{c|cc} & ^4D & ^4G \\ \hline ^4D & 17B + 5C & 0 \\ ^4G & 0 & 10B + 5C \end{array}$$

$^4T_1(^4G, ^4P, ^4F)$

$$\begin{array}{c|ccc} & ^4F & ^4P & ^4G \\ \hline ^4F & 22B + 7C & 0 & -0.44722\Delta \\ ^4P & 0 & 7B + 7C & -0.89444\Delta \\ ^4G & -0.44722\Delta & -0.89444\Delta & 10B + 5C \end{array}$$

$^4T_2(^4G,^4D,^4F)$

$$\begin{array}{c|ccc} & {}^4F & {}^4G & {}^4D \\ \hline {}^4F & 22B + 7C & -0.65466\Delta & -0.75591\Delta \\ {}^4G & -0.65466\Delta & 10B + 5C & 0 \\ {}^4D & -0.75591\Delta & 0 & 17B + 5C \end{array}$$

Since the ^4E levels are independent of the field strength (Δ), they give rise to narrow excitation bands which are thus relatively easy to assign. The levels differ in energy by 7B so B can be determined directly from the excitation spectrum. The $^4E(^4G)$ level lies 10B + C above the ground state, so knowing B, C may be calculated. With the values of B and C, the two $^4T_1$ and $^4T_2$ matrices can be solved (diagonalized) for various values of Δ and hence the energy level diagram is obtained.

2.6.6 Luminescent Decay-Time

2.6.6.1 Introduction

The decrease with time of the number of emitted photons from an excited state is related to the Einstein spontaneous transition probability by:

$$\frac{dN_i}{dt} = -N_i A_{fi} \qquad (42)$$

where dN_i/dt is the rate of change with time of the number of ions (or atoms) in a given excited state and N_i is the number of ions in that state. Integrating expression (42) with the initial condition that at time $t = 0$, $N_i = N_o$ yields:

$$\ln \left| \frac{N_i}{N_o} \right| = - A_{fi}t \tag{43}$$

Expression (43) may be rewritten as:

$$N(t) = N_o e^{-A_{fi}t} \tag{44}$$

The spontaneous transition probability A_{fi} is related to the radiative lifetime τ of the transition by[247]:

$$\frac{1}{\tau} = A_{fi} \tag{45}$$

Replacing expression (45) in equation (44) yields:

$$N(t) = N_o e^{-t/\tau} \tag{46}$$

Since the intensity of the luminescence varies as the number of ions in the excited state expression (46) may be rewritten as:

$$I(t) = I_o e^{-t/\tau} \qquad (47)$$

If the emitting activators are in different environments then I(t) will equal:

$$I(t) = I_o e^{-t/\tau_o} + I_1 e^{-t/\tau_1} + I_2 e^{-t/\tau_2} + \ldots \qquad (48)$$

A decrease in decay time τ may result from increasing activator concentrations. Different phenomena may be responsible for this behaviour. A higher activator level can facilitate transfer of excitation energy from a Mn^{2+} ion to a sink (impurity) that can trap the excitation and eventually dissipate it as heat. This leads to a non-radiative decay (which is usually very fast) thus shortening the observed radiative decay-time. Another reason for a decrease of τ in the case of spin forbidden transitions is that spin exchange or superexchange between neighbouring ions is enhanced at increased activator levels, these processes help to overcome the spin selection rule.

2.6.6.2 Analysis

Non-exponential decay in glasses activated with MnO[31,40,158] and Cr_2O_3[122] has been reported. Such behaviour is not surprising since glass has a random network leading to a random distribution of environments for the emitting species. Thus to compare different non-exponential decay-curves, a quantity inherent to these decay-curves must be defined. Andrews *et al.*[122] studying the radiative lifetimes of Cr^{3+} in glasses defined an average decay as:

$$\bar{\tau} = \int_0^\infty t\ I(t)\ dt / \int_0^\infty I(t)\ dt \qquad (49)$$

where $I(t)$ is the experimental decay-curve. $\bar{\tau}$ of expression (49) is actually the average time $\bar{t}$ of a distribution $I(t)$. Thus it would perhaps be appropriate to refer to this parameter as $\bar{t}$ rather than $\bar{\tau}$. It is interesting to consider this parameter for a single exponential. In this case $I(t)$ is equal to:

$$I(t) = I_o e^{-t/\tau} \qquad (50)$$

Replacing expression (50) in equation (49) and dividing by I_o yields:

$$\bar{t} = \int_0^\infty t\ e^{-t/\tau}\ dt / \int_0^\infty e^{-t/\tau}\ dt \qquad (51)$$

Integrating expression (51) by parts gives:

$$\bar{t} = \frac{-t\tau e^{-t/\tau}\Big|_0^\infty - \tau^2 e^{-t/\tau}\Big|_0^\infty}{-\tau e^{-t/\tau}\Big|_0^\infty} \qquad (52)$$

The limit of the first term in the numerator is zero while the limit of the second term is τ^2. The limit of the denominator is τ. Thus for a single exponential decay-curve expression (49) yields:

$$\bar{t} = \tau \qquad (53)$$

And for this special case the average time $\bar{t}$ is indeed the decay time τ. Although the quantity $\bar{t}$ defined in this way does not represent the usual average ($\bar{\tau}$) of the decay-times in a multi-component decay, it is a useful parameter for comparing different decay-curves.

For calculation purposes, equation (49) was necessarily approximated by a discrete expression and the summation was carried out over a finite interval [1.25 ms, 27.5 ms]. The lower boundary of which was chosen as close as possible to zero and the upper one as far as the experimental data permitted. Although this introduces an unavoidable error in the calculated value of $\bar{t}$, it is reasonable to suppose this would be a systematic one as long as the integrating interval was the same for all experimental curves. In other words, the error introduced by performing a finite summation should not affect the *comparison* between different decay-curves. The integration was carried out using Simpson's discrete approximation[†].

[†] Texas Instrument, Model TI59, built-in program, Lubboch, Texas.

CHAPTER 3

EXPERIMENTAL

3.1 SAMPLE PREPARATION

A large number of sodium borosilicate glass samples were prepared in 5-6 g batches, with compositions lying in and near the miscibility gap as determined by Haller *et al.*[17] (weight percent) and by Galakhov and Alekseeva[18] (mole percent). As mentioned in Section 2.5.1 some discrepancies exist between the two phase diagrams. Glass compositions[†] were initially selected on the basis of the tie-line orientation proposed by Haller *et al.*[17]. Subsequent work led us to believe that Mazurin and Streltsina[20] offer a more accurate representation of the tie-lines, and later glass compositions were selected on the basis of their work[20].

Analytical reagent grade materials (Fisher Chemicals) were used. The different chemicals were weighed using a Mettler analytical balance (10^{-2} mg precision). However, due to the volatilization of the materials at high temperatures and/or their water content[223,224], a correction

---

[†] These samples were kindly prepared by D.G. Owen, Atomic Energy of Canada Ltd., Pinawa, Manitoba.

was made to the weighed starting batches, on the basis of weight losses of the pure components, and chemical analyses of previously-prepared glasses. A typical yield at 1300°C is shown in Table II.

Table II

Sodium Borosilicate Starting Material and Yield at 1300°C

Starting Material	Yield After Glass Formation
Na_2CO_3:112.0 g	Na_2O:1 mole
B_2O_3:75.0 g	B_2O_3:1 mole
SiO_2:60.2 g	SiO_2:1 mole

For glasses having a high silica content (above 60 mol%) a melting temperature of 1400°C was required to obtain a macroscopically homogeneous product. In these cases, the quantity of sodium carbonate starting material was raised by 10%, to compensate for increased volatilization. Finally, MnO was introduced by adding manganese sulfate ($MnSO_4 \cdot H_2O$) or manganous acetate ($Mn(C_2H_3O_2) \cdot 4H_2O$) to the mixtures. The acetate generally gave better products, as indicated by less intense discolouration, perhaps because decomposition of the anion provided a reducing environment in the melt thus inhibiting oxidation of Mn^{2+} to Mn^{3+}. The mixtures were then transferred to 95Pt-5Au crucibles (10 cm^3 capacity). Batches were sintered, at 1000°C for 1/2 hour, using a rapid-heating electric furnace[†]. Temperature was controlled by a Pt V.S. Pt-Rh thermocouple. The mixtures were then fused at 1200°C for 1 h before air cooling them to room temperature. The products were then crushed, with a tungsten carbide lined ball mill (∿ 10 minutes), and returned to the crucibles. Carbon powder (0.035 g), acting as a reducing agent, was then added either by sprinkling on the surface of the batch or by mixing. Better quality glasses were obtained when the carbon was sprinkled, since a carbon residue remained after melting when it was mixed with the batch.

The materials were then remelted at 1200°C[§] for 1 h. The samples were then quenched by dipping the crucible into water without immersing the glass. Prepared glasses were cut with an electric saw. They were then cleaned by immersion in acetone in an ultrasonic bath.

3.2 SCANNING ELECTRON MICROSCOPE

3.2.1 Introduction and Basic Principles

The scanning electron microscope (SEM) was proposed by Knoll[225] as early as 1935. The first commercial one was

---

[†] Model 1500A, CM Mfg. and Machine Co., Bloomfield, N.J.

[§] In high silicate glasses a third melt at 1400°C, was required to obtain a homogeneous glass. For such samples, carbon was added only before the third melt.

developed in 1965 by Stewart and Snelling[226] using an electron detector proposed by Everhart and Thornley[227]. Figure 15 shows the block diagram of a SEM. The SEM used in this work was one of the first on the market[†], although the basic principles are the same for almost all SEM's[228-233], the following description applies specifically to this one.

Electrons from a gun (a hairpin tungsten filament) are accelerated to an energy between 1 and 30 kV. These electrons pass through three magnetic lenses and three spray apertures. The first two lenses act as condensers and the third as an objective. The condensers demagnify the image of the gun cross-over and the spray apertures remove stray electrons. Furthermore, a final aperture after the objective reduces the final solid angle of the beam. The objective brings the electron beam to focus at the specimen surface. A number of electromagnetic coils placed above the objective control the position of the beam on the sample. The beam is scanned on the specimen in an X-Y grid pattern. The signal driving the beam is used to scan the cathode-ray tube (CRT) in the same X-Y pattern so as to produce a similar but larger raster on the viewing screen. Magnification in SEM is defined as the ratio V:S, where V and S are the dimensions of the image on the viewing screen and the region scanned,

---

[†] Mark II Stereoscan, Kent-Cambridge Scientific, Inc., Morton Grove, Ill.

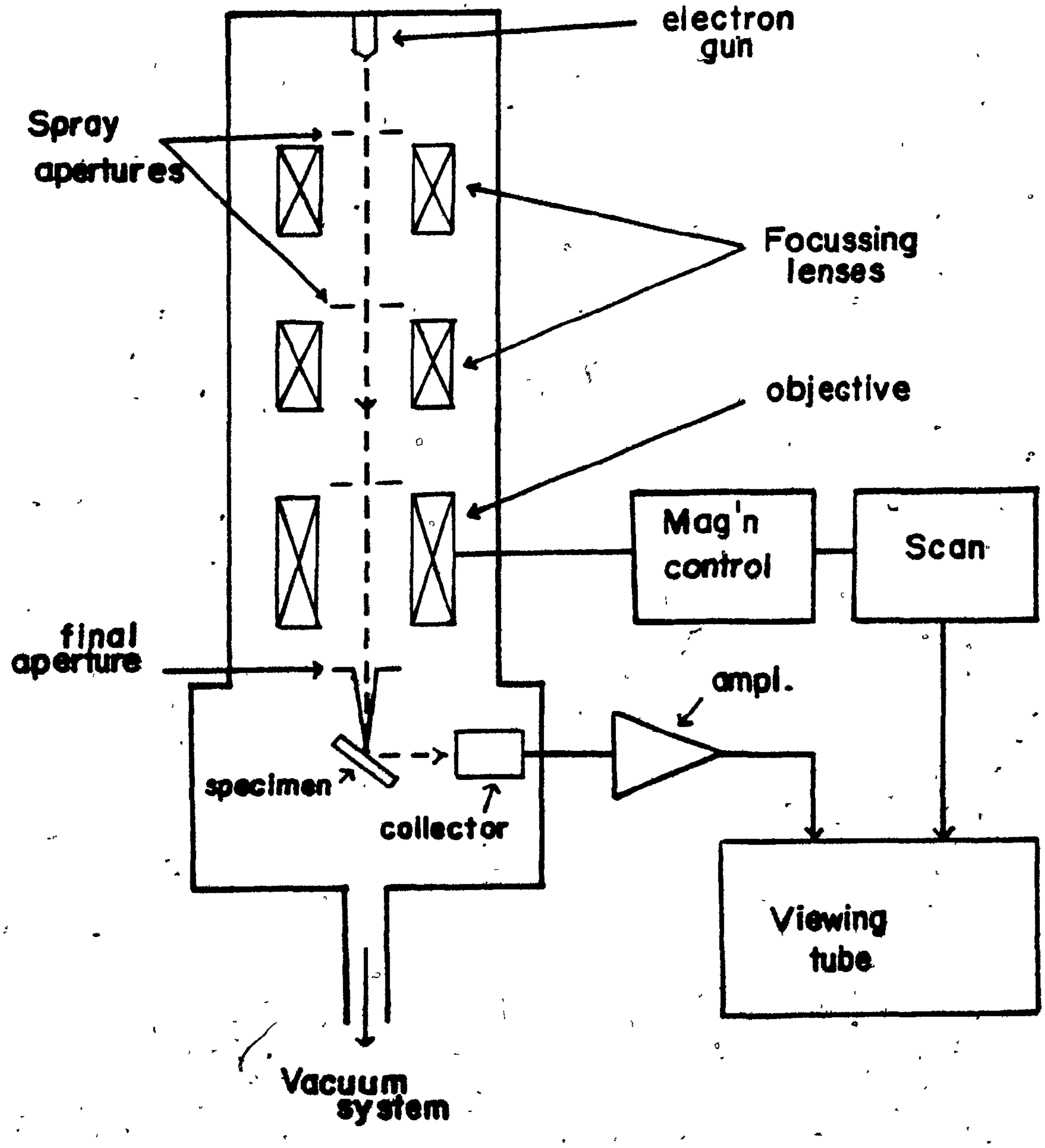

Fig. 15: Block diagram of a SEM. Modified after Ref. 231.

respectively. Actually there are two screens: one with a long persistence phosphor for viewing areas under study and one with a short persistence phosphor for taking pictures.

3.2.2 Types of Signals Available

When a specimen is bombarded by electrons, different effects occur (Fig. 16). The most important are the production of X-rays, Auger electrons, light, backscattered electrons and secondary electrons. Depending on the detector used, the microscope is said to be operating in a certain mode. Two modes are of interest in this work: the emissive mode and the X-ray microanalysis mode.

3.2.2.1 The emissive mode

The detector used in the emissive mode was developed by Everhart and Thornley[227] (Fig. 17). It detects secondary electrons (energy 3-5 ev) which are attracted toward a Faraday cage held at a positive potential ($\sim$ +250 V). Once inside the cage, they are accelerated toward a scintillator, by a potential of 12 kV. The light produced (upon striking the scintillator) proceeds through a perspex light guide to a photo-multiplier tube (PMT) situated outside the vacuum chamber. The current produced by the PMT controls the brightness on the CRT and thus the image is formed by different contrasts.

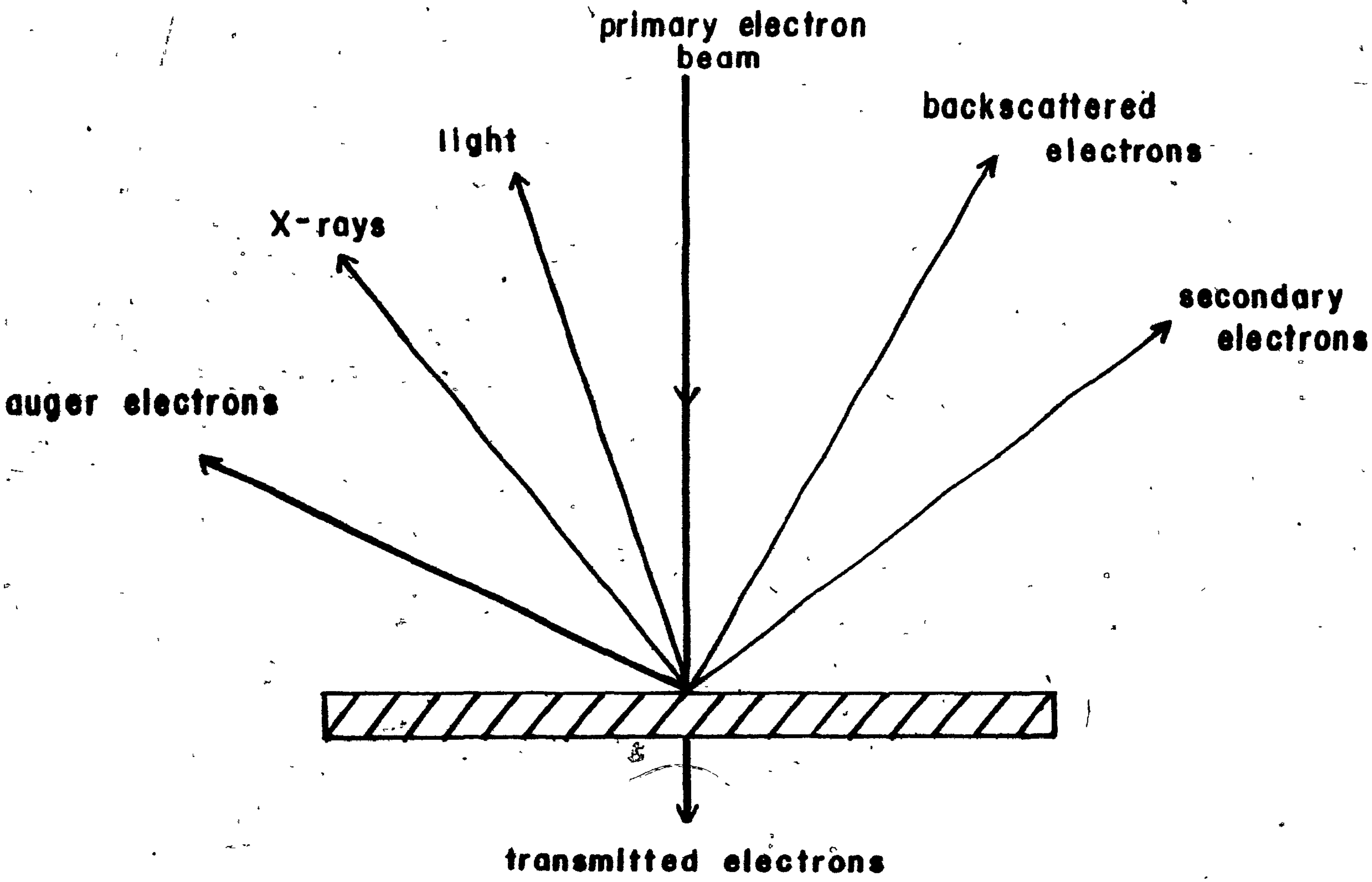

Fig. 16: Different effects that occur when a specimen is bombarded by electrons. Modified after Ref. 228.

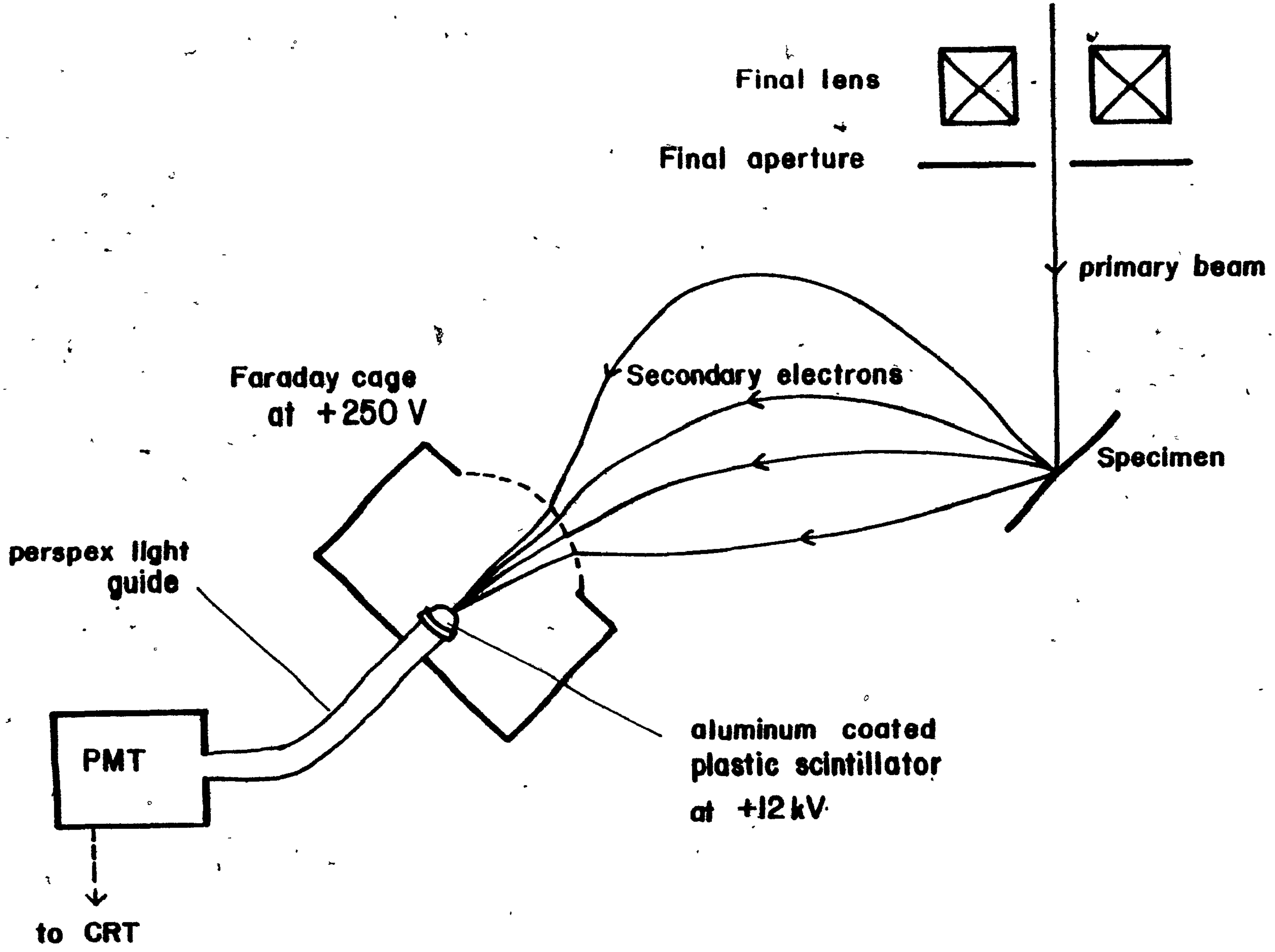

Fig. 17: Everhart and Thornley detector. Modified after Ref. 228.

3.2.2.2 Energy dispersive analysis of X-rays (EDAX[†]).

X-ray production

Electron beam-solid interactions lead to the production of X-rays by two different processes. The first process, resulting from core scattering, leads to the formation of a continuous spectrum of X-ray energies from zero up to the energy of the incident electron beam. The second, resulting from inner shell ionization, leads to the formation of the characteristic spectrum. The continuum is subtracted from the characteristic in the spectral manipulation.

The EDAX detector is a lithium-drifted silicon crystal with a beryllium window. Figure 18 shows the schematic of an energy-dispersive spectrometer. X-ray signals are transformed to charge pulses by the bias applied to the detector then to voltage pulses by the preamplifier. The signal is then amplified and fed to a multichannel analyzer (MCA) where the pulses are sorted by voltage. They are then displayed on a CRT. The sample can be analyzed in three different ways:

(i) Spot analysis

The electron beam is focused and held on one single spot. The generated X-rays are processed in the way described above. The spectrum of all the detected elements is viewed

---

[†] Model 801A, EDAX International, Inc., Prairie View, Ill.

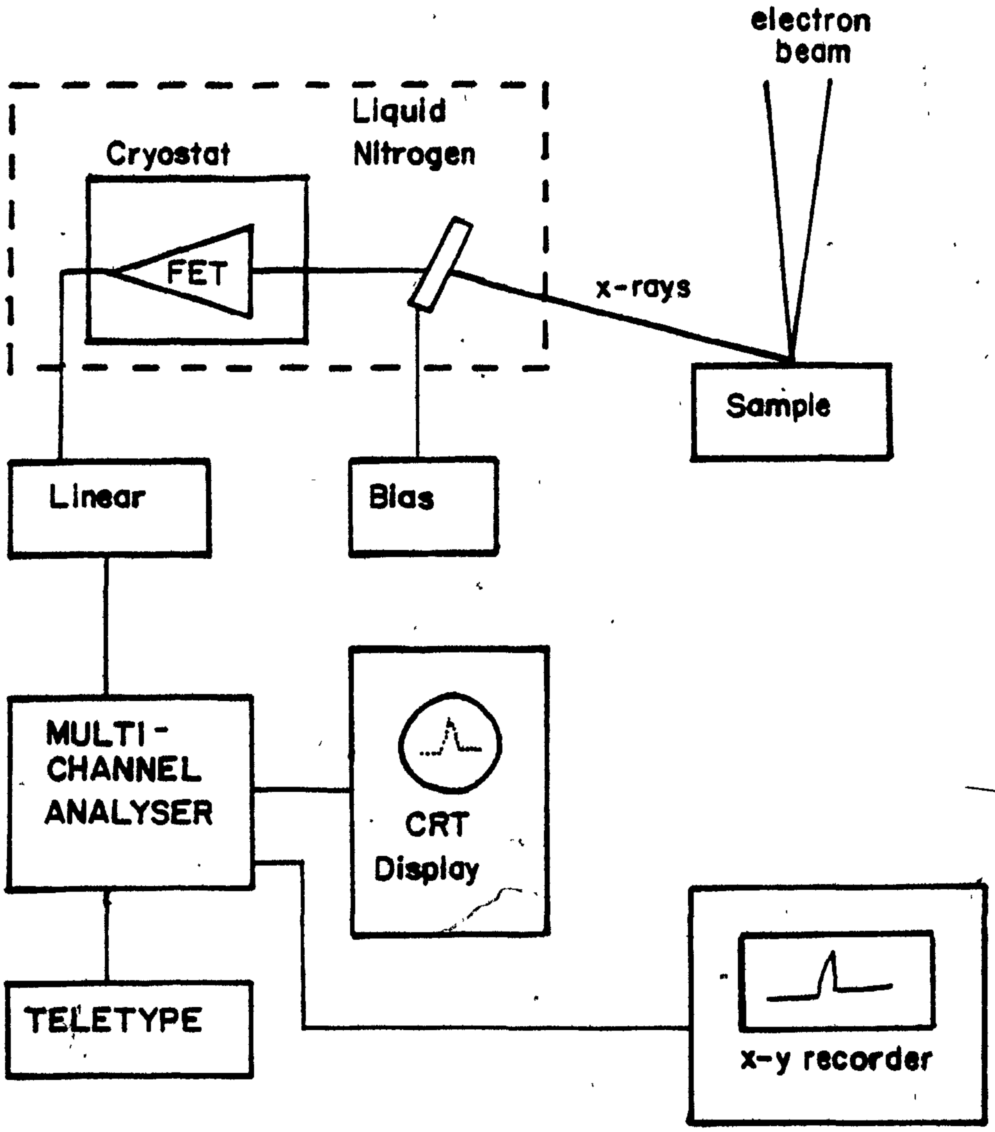

Fig. 18: Schematic of an energy dispersive spectrometer (from Ref. 230).

on the CRT screen. The spectrum obtained is usually stored in the MCA memory. The electron beam is then moved to another spot and another spectrum is obtained. The energies of the bands as well as their intensities may be compared by simultaneously viewing the two spectra. One can also print the position of the peaks as well as their intensities. The scale on the screen may be expanded for better comparison of two superimposed peaks. The count is done for a fixed time (generally 100 s is enough). A chart (usually provided by the manufacturer) gives all the characteristic energy lines.

(ii) Line scan

The focused electron beam is scanned along a line (X or Y direction). In this mode the detector window is set to analyze only a certain characteristic X-ray energy. The final signal seen on a micrograph is superimposed with a trace of the scanned line and a background scan. The latter confirms that the signal is not due to any topographical features.

(iii) Mapping

The electron beam is scanned on the specimen in an X-Y grid pattern. The detector is set up to detect the characteristic X-ray energy of interest. The domains analyzed should be large enough and their concentration above the noise level (usually 4 wt% is enough for a good mapping). Here also a background mapping is required to ensure that the patterns observed are not due to any topographical effects. Every time a characteristic X-ray is detected a bright spot appears on the CRT. The superimposition of all the spots form the image.

3.2.3 Major Factors Affecting the Resolving Power of SEM

"The resolution of SEM is the smallest distance between two separate features of the specimen which permits these features to be reliably distinguished in the image"[229]. While this definition lacks precision it emphasizes the dependence of resolution on both the specimen and the instrument.

3.2.3.1 Emissive mode

Spot size and depth of field

The resolving power of SEM cannot be better than the diameter of the electron beam spot size. Furthermore, when the incident beam strikes the sample, the electrons are scattered within the sample thus making the effective area, from which the secondary electrons are collected, larger than the physical size of the beam. Moreover, the penetration of the beam inside the sample depends on the accelerating voltage and the nature of the specimen. It would be very realistic to put the beam size between 10 and 20 nm and the resolution typically $\sqrt{2}$ times the beam diameter[230].

Astigmatism and aberrations

Astigmatism is the result of asymmetry in the pole pieces of the objective. This will give an elliptical final spot. This defect can be minimized by ensuring that the final aperture is maintained clean.

Aberrations can be divided in two groups: spherical and chromatic. Chromatic aberration is due to the energy spread of the electrons. The focal length of the objective is shorter for electrons of lower energy. This produces a blurred electron spot. This type of aberration is mainly due to change in the accelerating voltage in the electron gun and to current-variation in the electromagnetic lenses. Spherical aberration is the major factor limiting the electron beam diameter. Electrons passing through the axis of the lens are brought to focus in a different plane than those off the axis. This defect cannot be avoided but is minimized by ensuring that the final aperture (Fig. 15) is set to give a small final solid angle.

Charging on specimen and noise

If the sample to be studied is a non-conducting sample, it must be coated with a conductive material to avoid any electrostatic charging on the specimen. Even in so doing, one cannot entirely eliminate this effect. Because the image is time-resolved, a distortion is observed only in the final image.

The main source of noise in SEM operating in the emissive mode is caused by the secondary electrons produced by backscattered primaries. This unwanted background affects the contrast and therefore the resolution.

3.2.3.2 EDAX mode

Resolution in the EDAX mode performing a spot analysis (spectral resolution) is defined as the full width at half maximum peak intensity (FWHM). However, this definition no longer holds when an X-ray mapping or a line scan are performed (spatial resolution). Rather than discussing resolution itself it would be more appropriate; in a qualitative analysis, to comment on the detection limit of the instrument. When sampling over a wide energy interval (spot analysis) a characteristic energy peak is detected if the peak to background ratio is high enough. Usually 4 wt% of an element with atomic number $\geq$ 11[†] gives a peak to background ratio of three. Furthermore, if domains are to be examined they must be large enough ($\sim$ 1 μm across) since the intensity of X-rays produced is determined by electron beam scattering and penetration rather than by the beam diameter. Therefore, areas below 1 μm in diameter cannot be successfully analyzed. Moreover, the beam diameter is increased in size (by changing the spray apertures) to allow an optimum count rate (between 2000 and 3000 over the whole range). When performing a line scan the island under study must be separated (to avoid any interaction) from other particles by at least 1 μm. The same remarks apply also for X-ray mapping.

3.2.4 Specimen Preparation

One of the great advantages of SEM is that specimens can be examined with little or no preparation (compared to TEM where extremely thin samples are needed). Therefore, bulk samples can be studied as long as they do not exceed the maximum specimen size suggested by the manufacturer (12 mm in diameter).

Phase-separated glass samples were etched in two different ways to enhance distinction between the phases, due to their different etch rates[98]: with water (5 or 20 s) for X-ray microanalysis or with 0.5% HF (10 or 15 s) for SEM.

[†] Elements with $Z < 11$ cannot be detected because their X-ray photons are absorbed by the beryllium window of the detector.

The samples were then glued to specimen holders (aluminum stubs) with a conductive carbon paint (Aquadag). The specimens were then sputtered with a thin layer of gold (200 Å) - to avoid charging problems when dealing with insulating samples - in an ionized argon atmosphere (0.1 Torr). They were then transferred to the specimen chamber of the SEM.

Finally, the optical column was evacuated in stages by rotary and diffusion pumps, to an operating pressure of 10^{-5} - 10^{-6} Torr.

3.3 HEAT TREATMENT

3.3.1 Ovens and Temperature Controllers

A cylindrical oven was used for thermal treatment experiments. The heating element (nichrome[†], R = 52 Ω) is wound on a ceramic tube having an outside diameter of 7.07 cm and an inside diameter of 5.14 cm. With good insulation, temperatures of 1000°C are easily reached. The ceramic bore can accommodate a quartz tube, thus allowing control of the sample atmosphere. Dry nitrogen was used in most experiments. The oven is powered by a single phase silicon controlled rectifier (SCR) power package[§]. The latter uses a separate 240 V line capable of delivering a current

---

[†] Kindly provided by the Physics Department of McGill University.

[§] Model LN1-2430 Halmar Electronics, Inc., Columbus, Ohio.

of 30 A. A controller[†] (using a Pt *vs* 10% Pt-Rh thermocouple having its junction placed at the hottest point) controls the oven power supply. Since the controller has a linear set-point potentiometer for temperature ranges, counter settings do not agree with temperature over the entire range. A second thermocouple (chromel *vs* alumel), with one junction placed near the sample and the reference in ice, measures the temperature. To avoid any unwanted junctions, thermocouple alloy wire[§] was used as an extension wire to connect thermocouple sensors to the instrumenation. The accuracy of the measurements with this arrangement is typically ± 1°C at 700°C.

3.3.2 Clearing Temperature Determination

The oven was heated gradually to the required temperature. Samples, placed in platinum boats (typically 0.81 cm^3) were introduced in the quartz tube. The latter was pumped down and then flushed with nitrogen. This procedure was repeated 4 or 5 times to ensure a nitrogen atmosphere inside the tube which was then introduced into the oven. After the heating time was elapsed[¶], the samples were quenched as fast as possible to room temperature. They

---

[†] Electromax III model 6435 Leeds and Northurp Company, North Wales, PA.

[§] All thermocouple materials are from "Omega Engineering, Inc." Stamford, CT.

[¶] Heating periods ranged from 15 min (above 900°C) up to 10 days (at 600°C).

were then visually examined for phase separation (cloudy appearance). If the samples were phase separated, we could conclude that the heating temperature T was below the clearing temperature T_c. Samples with the same composition were then subjected to successive heating, at $T_1, T_2, T_3, \ldots T_n$ with $\Delta T = 10°C$, until the quenched samples appeared clear. At that point, the heating temperature T_n was above T_c and the clearing temperature was determined by $T_c = (T_{n-1}+T_n)/2 \pm 5°C$. On the other hand if upon the first heat treatment the samples were clear, the oven temperature was lowered by decrements of 10°C, until phase separation was observed. Although visual examination was usually adequate for clearing temperature determination, selected samples were also examined by SEM. This is because long heat treatment periods could crystallize the glass surface, giving the glass an opaque or opalescent appearance. In such cases a confirmation of phase separation by SEM was recommended. Between samples the platinum boats were cleaned with a concentrated solution of HF.

3.4 LUMINESCENCE

3.4.1 Sample Preparation

Samples (typically 1 mm x 0.4 mm x 0.8 mm) were polished manually with silicon carbide sandpaper (240, 320, 400 and 600 grit) and then with diamond compound (3,000 mesh equivalent). Polishing movement was done in a figure eight pattern. This movement gives flat surfaces because the pressure on the sample is equally distributed over the whole polished face. Samples having two faces polished at right angles were then cleaned with a solution of carbon tetrachloride. They were then glued[†] to a sample holder. The latter could be moved up or down, backward or forward and from right to left.

3.4.2 Light Sources

3.4.2.1 Xenon arc

A high-pressure xenon arc[§] (1000 W) was used as a wide band light source. Its spectral irradiance is fairly smooth except for a small region near 465 nm (Fig. 19). It is a practical, high-intensity light source (20 μw/cm^2-nm at 50 cm, in the visible) that allows the selection of any wavelength over a large spectral range.

3.4.2.2 Nitrogen laser

The nitrogen laser is a practical excitation source for Mn^{2+} in glasses. The Mn^{2+} absorption spectrum in sodium

---

[†] Gum base, Life Savers Ltd., Ontario, Canada.

[§] Model C-60-50 Oriel Optics Corporation, Stamford, Conn.

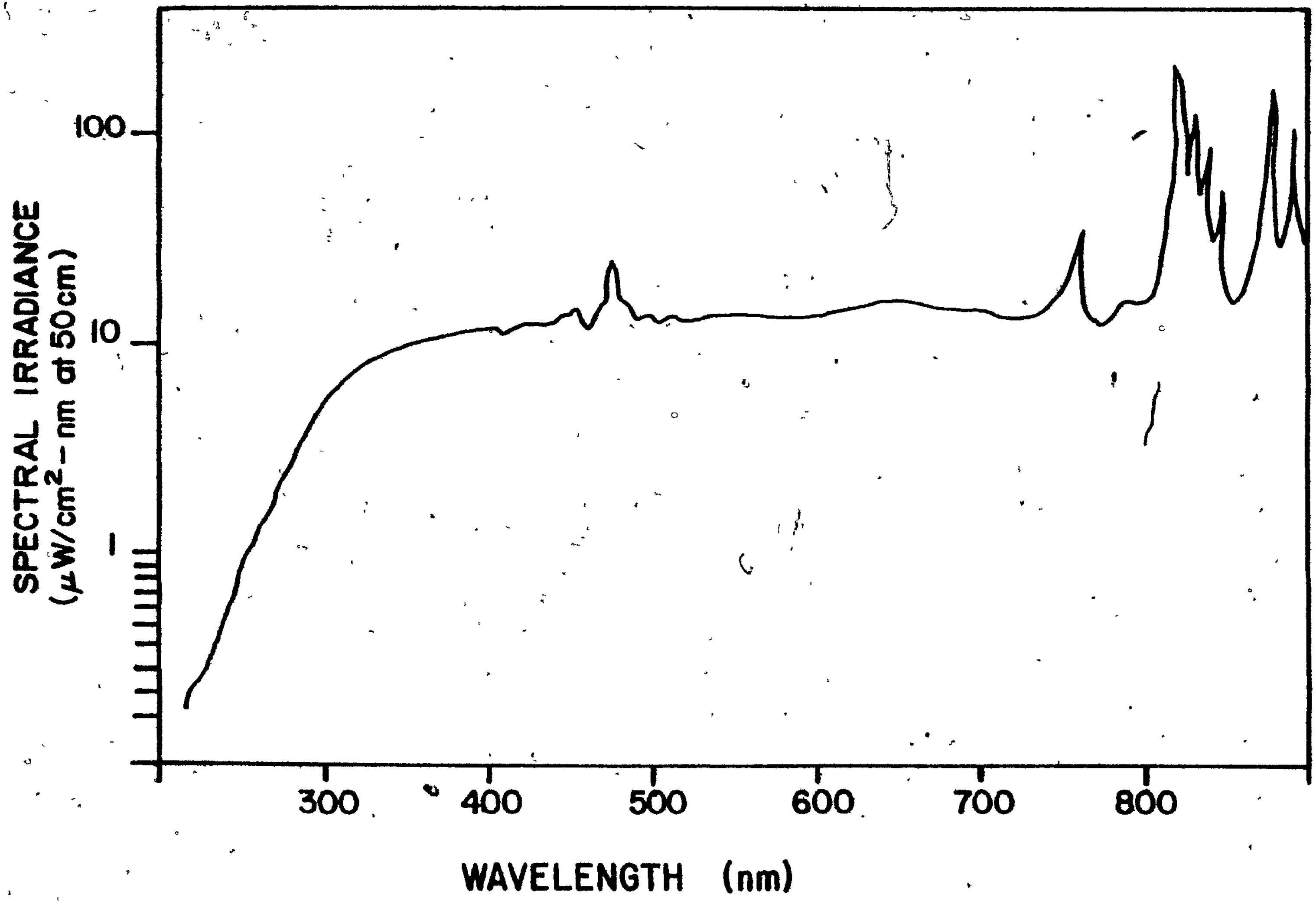

Fig. 19: Spectral distribution of a 1000 Watt Xe arc. From Oriel catalogs.

borosilicate glasses has its high energy absorption band centred at 355 nm. Therefore, the emitted light of the N_2 laser (337.1 nm) excites the shoulder of the high energy absorption band. A commercial nitrogen laser[†] (capable of delivering flashes of 68 μJ when operating at 18 kV with a frequency of 20 Hz) was used. Because the emission of Mn^{2+} comes from the lowest energy level, it was necessary (for the purpose of comparison) to have a pulsed light source capable of exciting the lowest energy level of Mn^{2+} (420 nm). For this purpose a dye laser[§] was used.

3.4.2.3 Dye laser

The dye laser components (Fig. 20) are mainly two mirrors M_1 and M_2 (M_2 being a semi reflective mirror), one dye cell C and a spectrosil B lens L. The dye cell C and the lens L can move backwards and forwards on a small optical bench (rail). Two screws S_1 and S_2 fix the position of L and C on the rail. Three small screws behind the mirrors can tilt them upward or downward and from left to right. Furthermore, the distance of the mirrors to the dye cell can be changed. The two tubes T_1 and T_2 are used to fill the cell with the appropriate dye or to circulate the latter in order to avoid any overheating. Finally, three

---

[†] Model LN100 Photochemical Research Associates Inc., London, Ontario, Canada.

[§] Designed in our laboratory, the necessary pieces were made by Mr. F. Kluck, machine shop, Chemistry Department, McGill University.

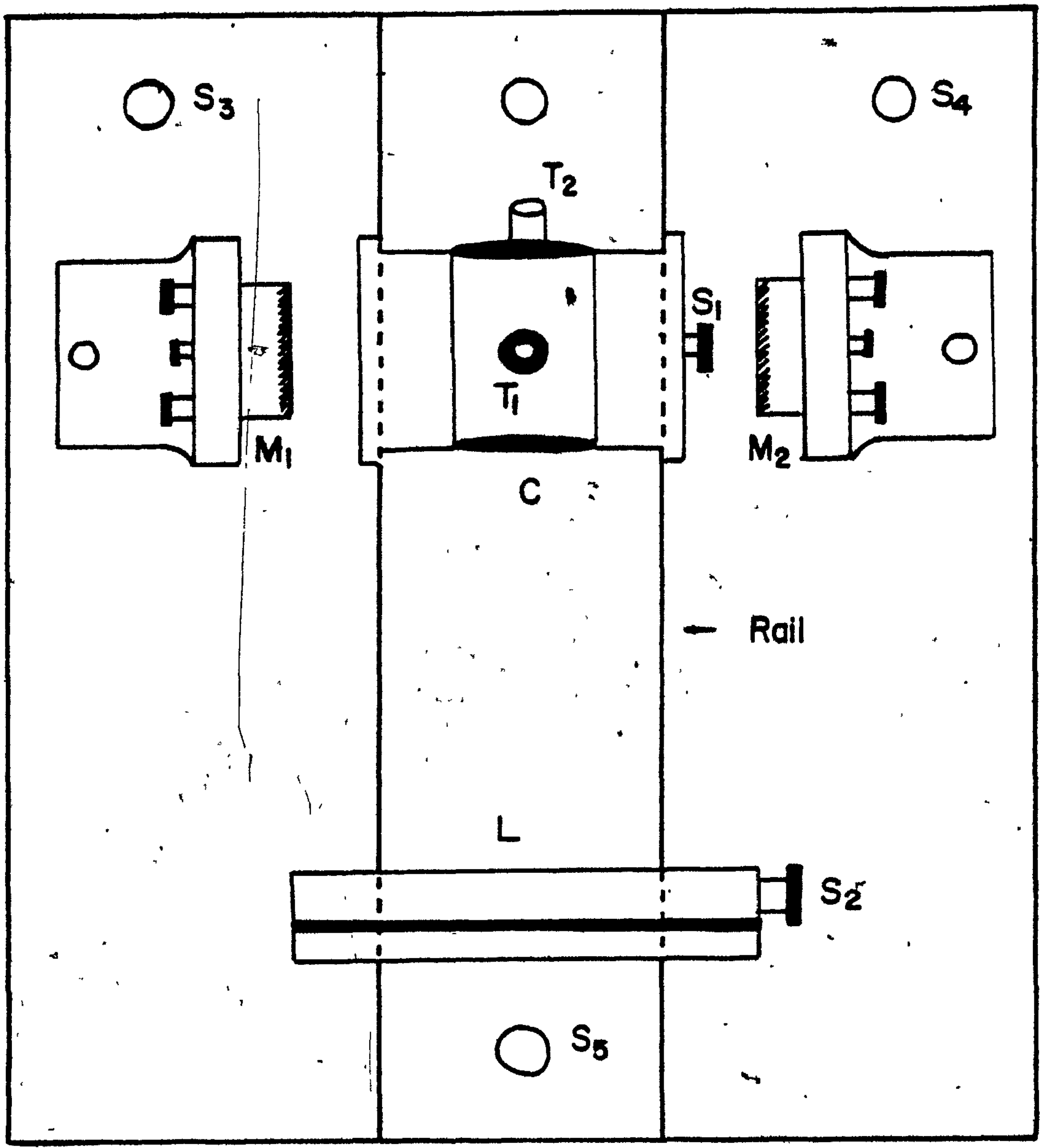

Fig. 20: Dye laser, top view.

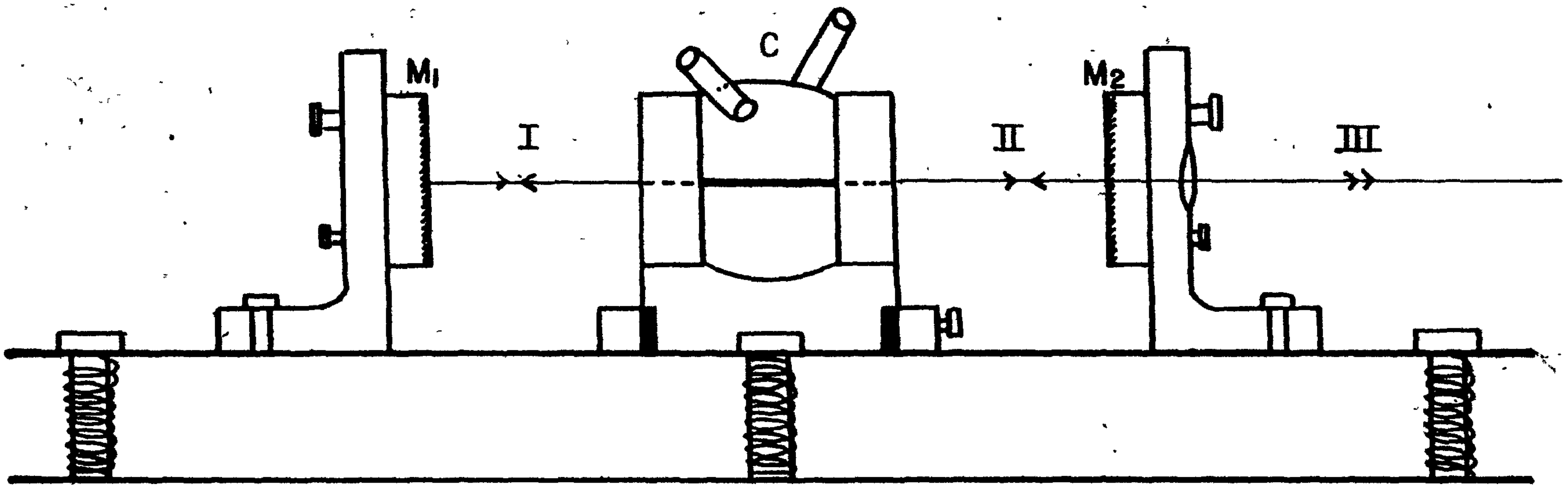

Fig. 21: Dye laser, side view.

screws S_3, S_4 and S_5 control the position of the whole dye laser with respect to the incident beam. The latter, focused by L, strikes C (Fig. 21), the dye lases and the emitted light follows path I. The rays reflected by M_1 cross C and follow path II. Part of the rays follow path III while the other part is reflected by M_2, crosses C again and so on until good light amplification is obtained. A part of the amplified light follows Path III and so on.

A number of organic dyes lase in the 420 nm region (when pumped by a N_2 laser). Among them are Bis-MSB[234,235] Carbostyril 124[236], Popop[237-239] and finally Coumarin 120[240]. The most convenient dye with its lasing band centered at *ca*. 420 nm and having a relatively low threshold is Popop C_6H_4-1,4-[C:NCH:C(C_6H_5)O]$_2$. Scintillation grade Popop

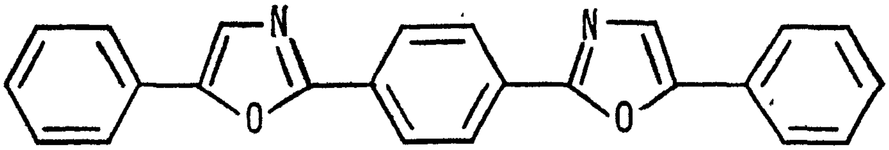

(Kodak Chemicals) was dissolved in spectroscopic-grade toluene (Popop concentration 3.41×10^{-4} M). Before being filled the dye cell was rinsed twice with the solution. A monochromator was set to measure the lasing wavelength. It was found to be between 411 nm and 428 nm, with a peak at 419 nm.

3.4.3 Experimental Arrangement

3.4.3.1 Fluorescence

Figure 22 shows the experimental arrangement used in luminescence emission spectroscopy. The exciting light obtained from a 1000 W Xe arc is filtered by a water filter (mainly to remove high intensity I.R. generated by the Xe arc) and focused on a monochromator[†]. Two band-pass filters, F_1 and F_2, decrease the spectral range of the exciting light to the area of interest (*ca.* 420 nm). The monochromator selects a particular wavelength which is focused on the sample by L_2. The emitted light is collected at right angle by L_3 and focused on the slits of a spectrometer[§] by L_4. Two U.V. cut-off filters eliminate unwanted stray light reflected by the sample. A photomultiplier tube (PMT)[¶], powered by a high voltage power supply[††], transforms the light signal into an electrical signal. The latter is then transmitted to a preamplifier. After amplification the signal is recorded on a strip chart-

---

[†] Model 27180 Bausch and Lomb Opt. Co., Rochester, N.Y.

[§] Model 1702 Spex Industries Inc., Metuchen, N.J.

[¶] Three PMT's were used:

1. EMI 9558QB (response from 200 to 850 nm) EMI Gencom Inc., Plainview, N.Y.
2. Hamamatsu multialkali R928 (response from 180 to 950 nm).
3. Hamamatsu GaAs R943-02 (response from 180 to 920 nm). Hamamatsu Corporation, Middlesex, N.J.

[††] Hewlett Packhard, model 6516 A, Berkeley Heights, N.J.

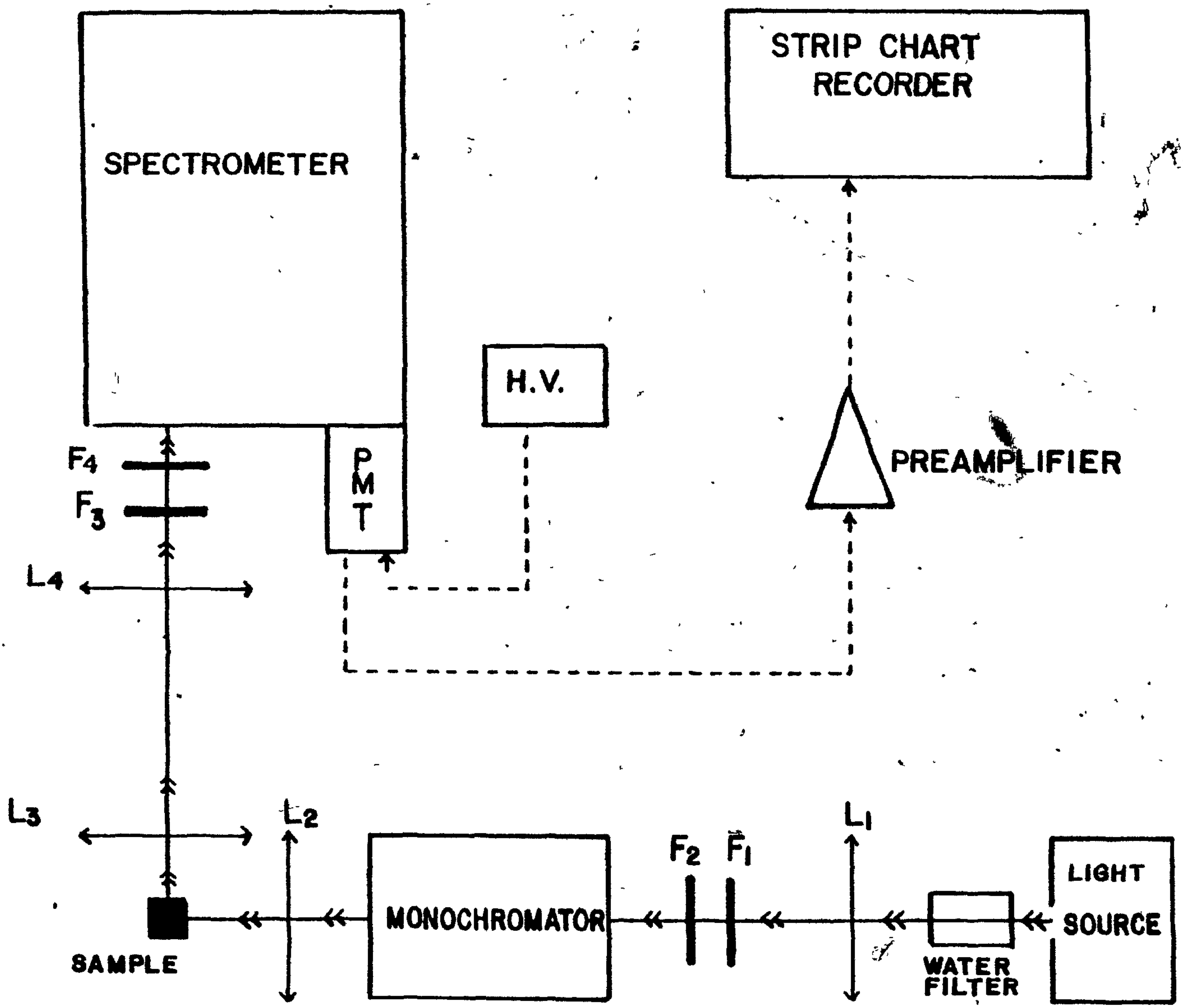

Fig. 22: Luminescence experimental arrangement.

recorder[†]. When low-temperature measurements were required, the sample was mounted in a cryostat[§] (for more details on the cryostat consult Ref. 128). Various optical elements were shielded with cardboard and covered with black cloth. Furthermore, the experiments were done in a dimly lit room. All these precautions were necessary in order to eliminate all possible sources of stray light. The same precautions apply for the different experimental arrangements (decay time and excitation).

3.4.3.2 Decay time

Most of the contents of this paragraph have been extensively covered[128]. We present here a concise description of the experimental set-up. Exciting light from a pulsed source is focused on the sample by L_1 (Fig. 23). A filter, F_1, eliminates the stray light coming from the source. The emitted light from the sample is collected at right angles by L_3, and then filtered by F_3 and F_4. A PMT transforms the collected light to an electrical signal. The latter is amplified and fed to a transient digitizer[¶]. The signal is then transferred to a computer time averager[††]

[†] Moseley 710113 Hewlett Packhard/Moseley Division, Pasadena, California.

[§] Oxford Instruments Model CF-100, Annapolis, MD.

[¶] Biomation model 610B, Cupertino, California.

[††] CAT model C1024 Varian Associates, Palo Alto, California.

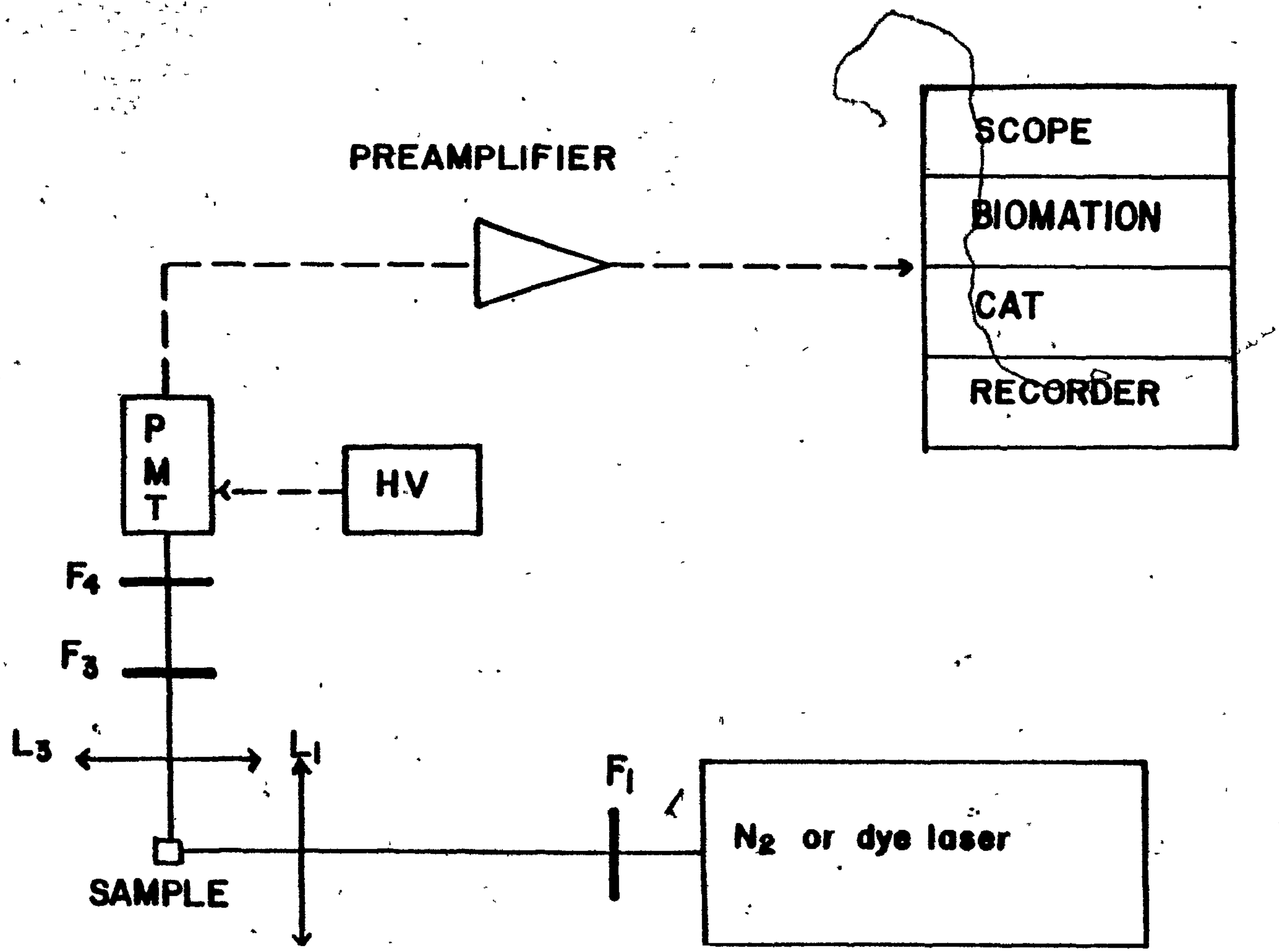

Fig. 23: Luminescent decay-time experimental arrangement.

(CAT). The latter will store and average a certain number of spectra. This procedure improves the signal to noise ratio. Finally, the signal is recorded on a strip chart recorder. An oscilloscope[†] coupled to the biomation allows the viewing of each spectrum transmitted by the biomation to the CAT.

3.4.3.3 Excitation

Figure 24 shows the experimental arrangement of the apparatus for recording excitation spectra. The exciting light from the Xe arc is filtered by a water filter and focused on the slits of a monochromator. The scanning device of the latter has a potentiometer attached to it *via* a cogwheel. The potentiometer drives the X axis of an X-Y recorder[§]. Any change in the monochromator setting will change (in synchronism) the pen's position on the X axis of the recorder. The exciting beam coming out of the monochromator is split in two by a quartz window, W. Approximately 10% of the intensity is used as a reference and processed by a PMT to a divider. The rest of the intensity (90%) is used to excite the sample. The emitted light is collected as described previously (*cf.* Section 3.4.3.1). The signal coming out of the spectrometer's

---

[†] Tektronix model 475A, Beaverton, Oregon.

[§] Model 2000 Omnigraphic Houston Instrument, Austin, Texas.

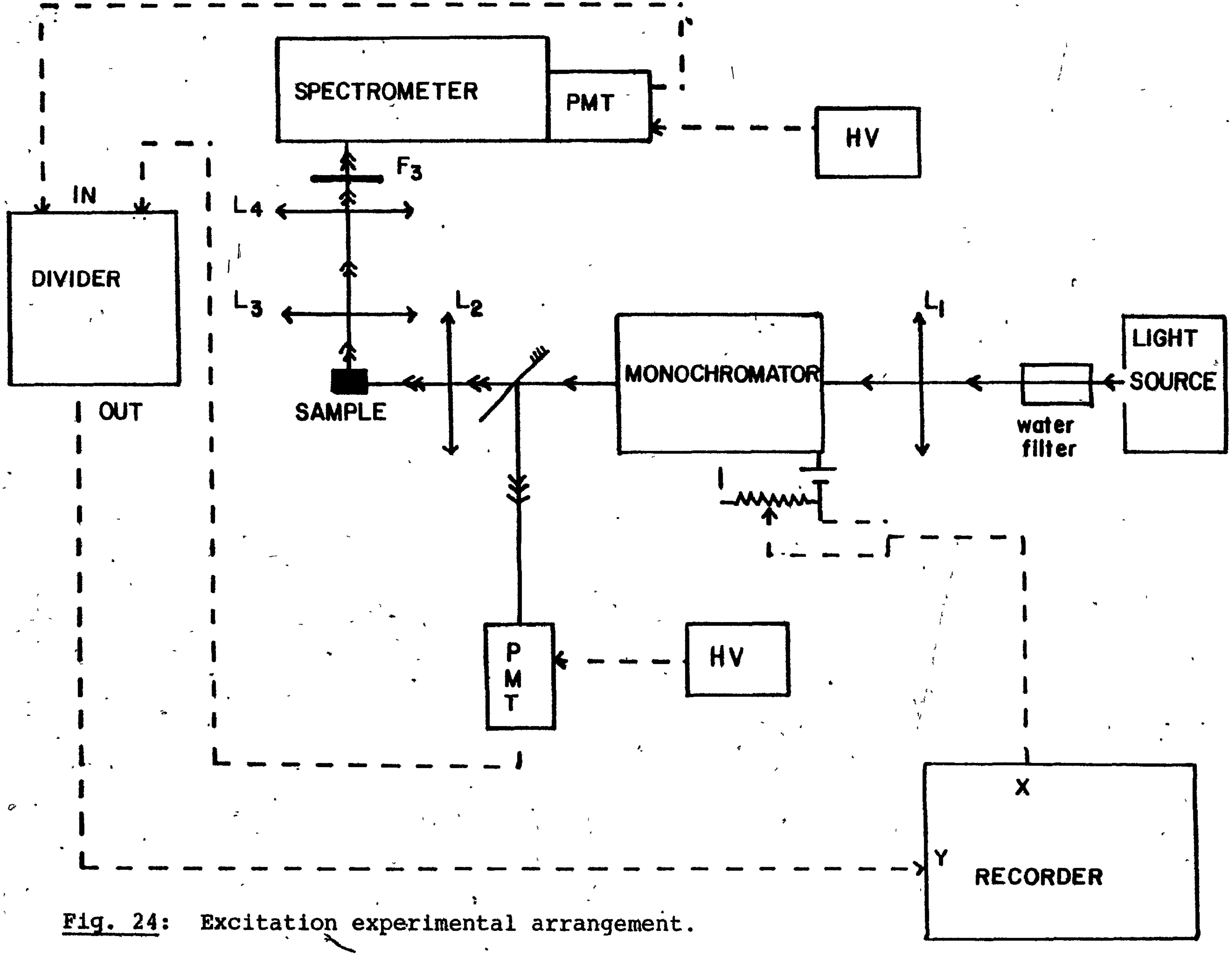

Fig. 24: Excitation experimental arrangement.

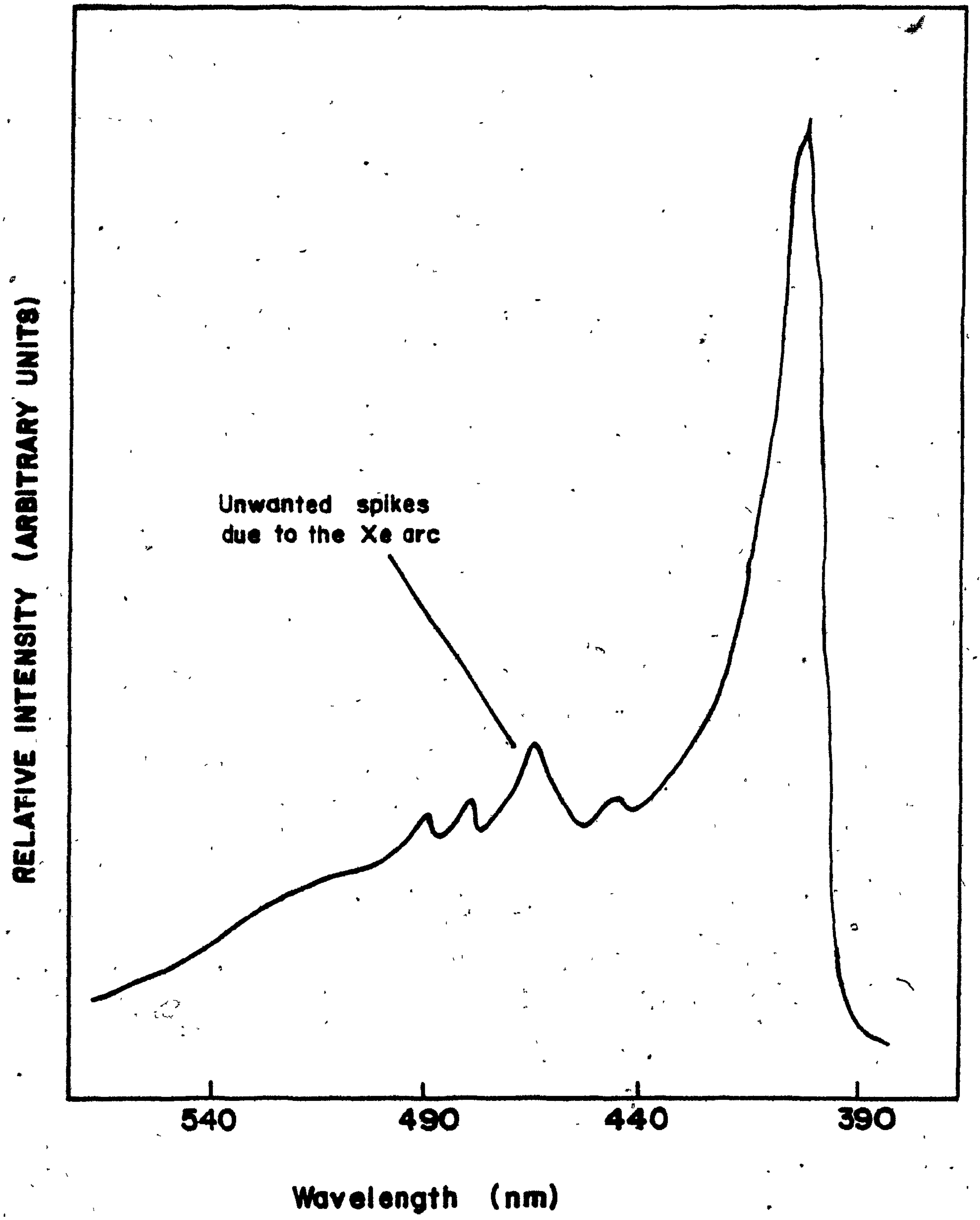

Fig. 25: Unwanted spikes in the excitation spectrum of MnO-doped glasses.

PMT is fed to a divider. The latter divides the sample's signal by the reference signal. This dividing procedure was necessary because the Xe arc has spikes in the 465 nm region (Fig. 19). These spikes contribute to unwanted bands (Fig. 25). Finally the signal coming out of the divider is used to drive the Y axis of the recorder.

3.4.4 Lenses and Filters

All the lenses used in these experiments were made from spectrosil B and have a diameter of 50 mm and a focal length of 50 or 75 mm. The filters used were made by Corning[†] (C), Melles-Griot[§] (M) or Balzers[¶] (B). Balzers and Melles-Griot filters are interference band-pass filters. Their passing bands are respectively 50 and 10 nm. The following table summarizes the different filters used in different arrangements.

[†] Corning Glass Works, Corning, N.Y.

[§] Melles-Griot, Irvine, California.

[¶] Balzers, Toronto, Ontario.

TABLE III

Filters Used in Different Experimental Arrangements

Figures	Exc	Filters			
		F_1	F_2	F_3	F_4
Fig. 22	λ = 355 nm	(B) UG-11	-	(B) 1163/890	-
Fig. 22	λ = 420 nm	(C) 7-59	(C) 5-59	(C) 3-73	(C) 3-73
Fig. 23	λ = 337.1 nm	(M) λ = 337.1 nm	-	(B) λ = 550 nm	(M) λ = 550 nm
Fig. 23	λ = 337.1 nm	(M) λ = 337.1 nm	-	(B) λ = 640 nm	(M) λ = 650 nm
Fig. 23	λ = 420 nm	(J.Y.) λ = 420 nm	-	(B) λ = 550 nm	(M) λ = 550 nm
Fig. 23	λ = 420 nm	(J.Y.) λ = 420 nm	-	(B) λ = 650 nm	(M) λ = 650 nm
Fig. 24	-	-	-	(B) λ = 550 nm or λ = 650 nm	-

J.Y. is a Jobin Yvon monochromator model H.10, Instrument S.A., Inc., Metuchen, N.J.

Chapter 4

RESULTS AND DISCUSSION

4.1 MANGANESE(II) A SPECTROSCOPIC PROBE

4.1.1 Introduction

Although Mn^{2+} luminescence in glasses has been widely studied (*cf.* Chapter 1), so far no work on the optical properties of Mn^{2+} in sodium borosilicate glasses has come to our attention. Bingham and Parke[154] studied the fluorescence spectra of sodium borate and sodium silicate doped with Mn^{2+}. They reported that sodium borate glasses exhibit only red fluorescence, while only the green is present in the silicate. Thus one might expect both red and green emissions from Mn^{2+} in sodium borosilicate glasses. This indeed proves to be the case. In other types of glasses some authors[30,39,157] describe the colours of the two characteristic Mn^{2+} emissions as varying from green to dark red. In the present work these two bands will be labelled H band (for high energy "green" band) and the L band (the low energy "red" band). This avoids the difficulties inherent in using colours to describe bands, especially when there are shifts which can send a green band into the red region of the spectrum.

4.1.2 Dependence of Mn^{2+} Luminescence Spectra on MnO Concentration

A glass of the consolute composition in the sodium borosilicate system (molar composition $6.3Na_2O \cdot 23B_2O_3 \cdot 70.7SiO_2$) was chosen for this study. The samples prepared had MnO concentrations ranging from 0.02 wt% to 5.33 wt% (Table IV). Luminescence spectra were obtained by excitation at 355 or 420 nm, both of which correspond to strong absorption bands of Mn^{2+} in silicate and borate glasses[162]. For a given sample the same luminescence spectrum was obtained with either excitation wavelength, but the 420 nm excitation gave more intense luminescence. Two bands (H and L) were present in the emission spectra of these samples as shown in Fig. 26. As the concentration of MnO was increased (0.02 wt% to 5.33 wt%) the H band shifted from 550 to 608 nm while the L band shifted from 630 to 655 nm. The relative heights of the two bands (H/L) also changed with increasing MnO concentration: from 2.14 (MnO = 0.02 wt%) to 0.45 (MnO = 5.33 wt%), these results are summarized in Table IV.

It is clear that Mn^{2+} luminescence depends on the activator level and that increasing the Mn^{2+} concentration leads to quenching of the H band luminescent intensity relative to that of the L band (the H band being nearly completely quenched when the MnO concentration reaches *ca.* 5 wt%).

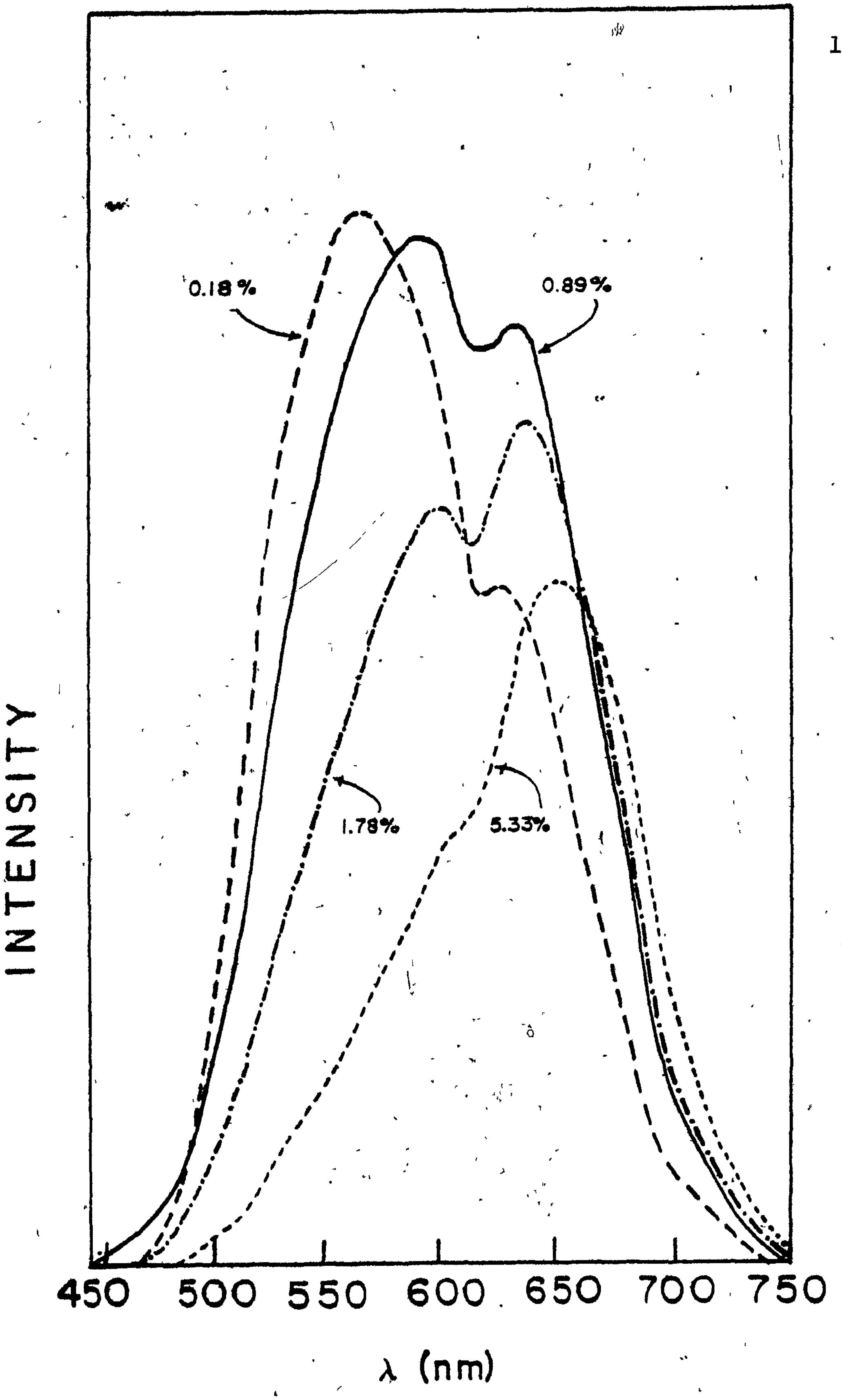

Fig. 26: Emission spectra of the consolute composition doped with different levels of MnO. Excitation wavelength: 420 nm.

Table IV: Band Positions and Relative Heights (H/L) as a Function of MnO Concentration (Consolute Point, Molar Composition : $6.30Na_2O \cdot 23B_2O_3 \cdot 70.70SiO_2$).

Sample	Weight% MnO	H band (nm)	L band (nm)	Relative Height H/L
MnCON-5	0.02	550	630	2.14
MnCON-4	0.04	550	630	2.08
MnCON-3	0.09	558	630	1.81
MnBS-2B	0.18	577	633	1.28
MnCON-2	0.35	580	635	1.28
MnCON-1	0.89	600	640	0.94
MnBS-2C	0.89	600	640	0.94
MnBS-2D	1.78	608	642	0.76
MnBS-2E	5.33	608	655	0.45

The doping material in MnCON-1 → 5 was introduced as $MnSO_4 \cdot H_2O$, while in MnBS-2B → 2E it was introduced as Mn_2O_3. No difference in the luminescence spectra of MnCON-1 and MnBS-2C was found. Excitation wavelength = 420 nm.

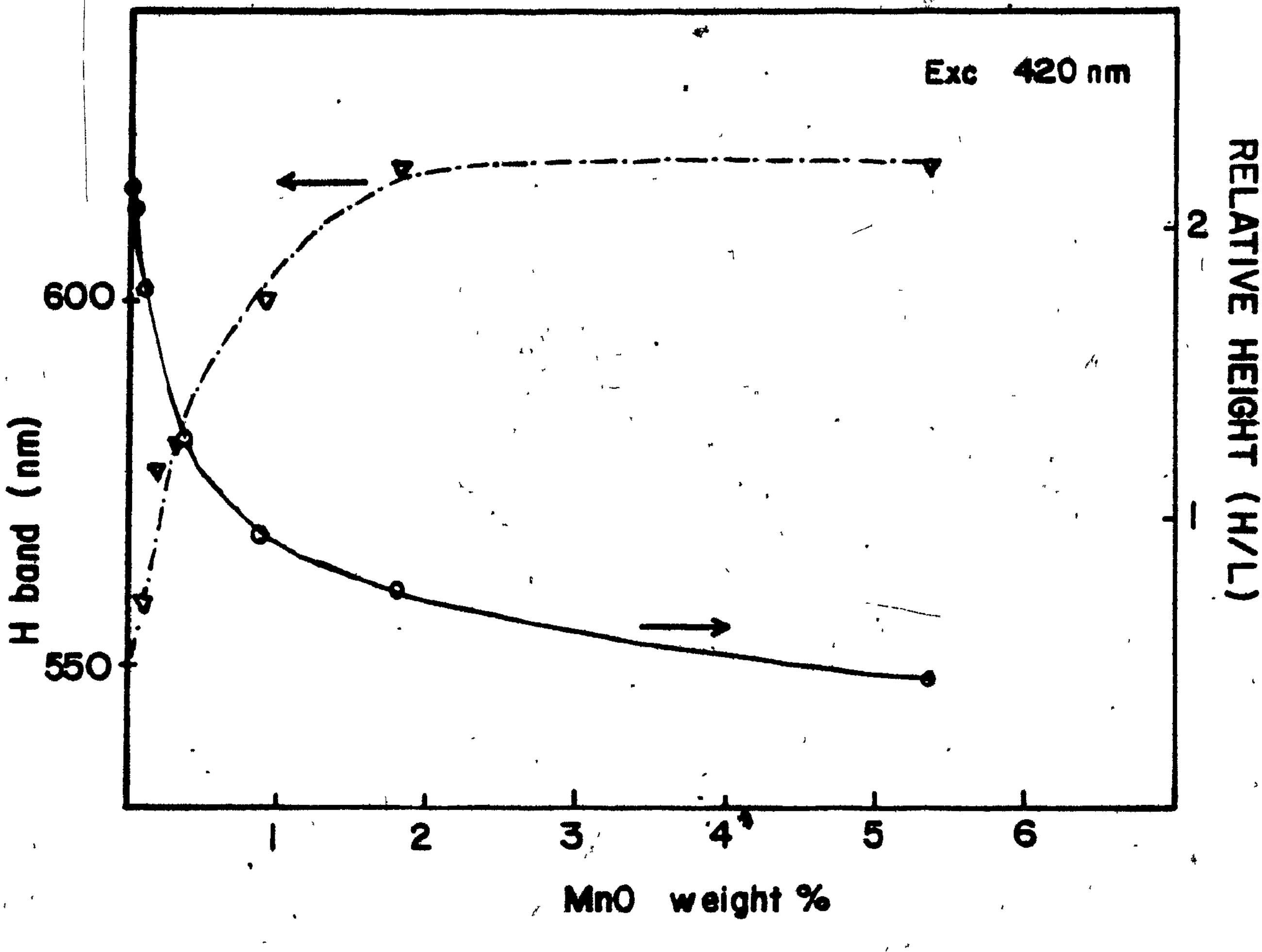

Fig. 27: Relative heights and positions of the H band of the consolute composition as a function of MnO concentration.

4.1.3 The Choice of MnO Doping Level

From the preceding discussion, there is an MnO concentration dependence for both the band peak positions and for their relative heights (H/L). The H band is more sensitive to the concentration of MnO than is the L band (Table IV). To best utilize these spectral changes for studying the glass, an optimum doping level should be determined. This optimum level will result from a balance between the shift and the dependence of H/L on concentration. Figure 27 shows how the most sensitive concentration range was established. The left-hand scale of Fig. 27 gives the dependence of the position of the H band on MnO concentration while the right-hand scale gives the relative heights (H/L) as a function of MnO concentration. Thus concentrations near the intersection of these two curves in the figure (∿ 0.2 to 0.6 wt%) will be optimal from the point of view of maximizing the spectral variations with respect to any morphological changes in the glass that would affect the Mn^{2+} concentrations.

4.1.4 Dependence of Mn^{2+} Luminescence Spectra on Glass Composition

Samples with compositions along the 650°C isotherm of the miscibility gap[17] (see Fig. 28) were prepared for this study because they allow large variations in glass compositions (Table V). Based on previous considerations,

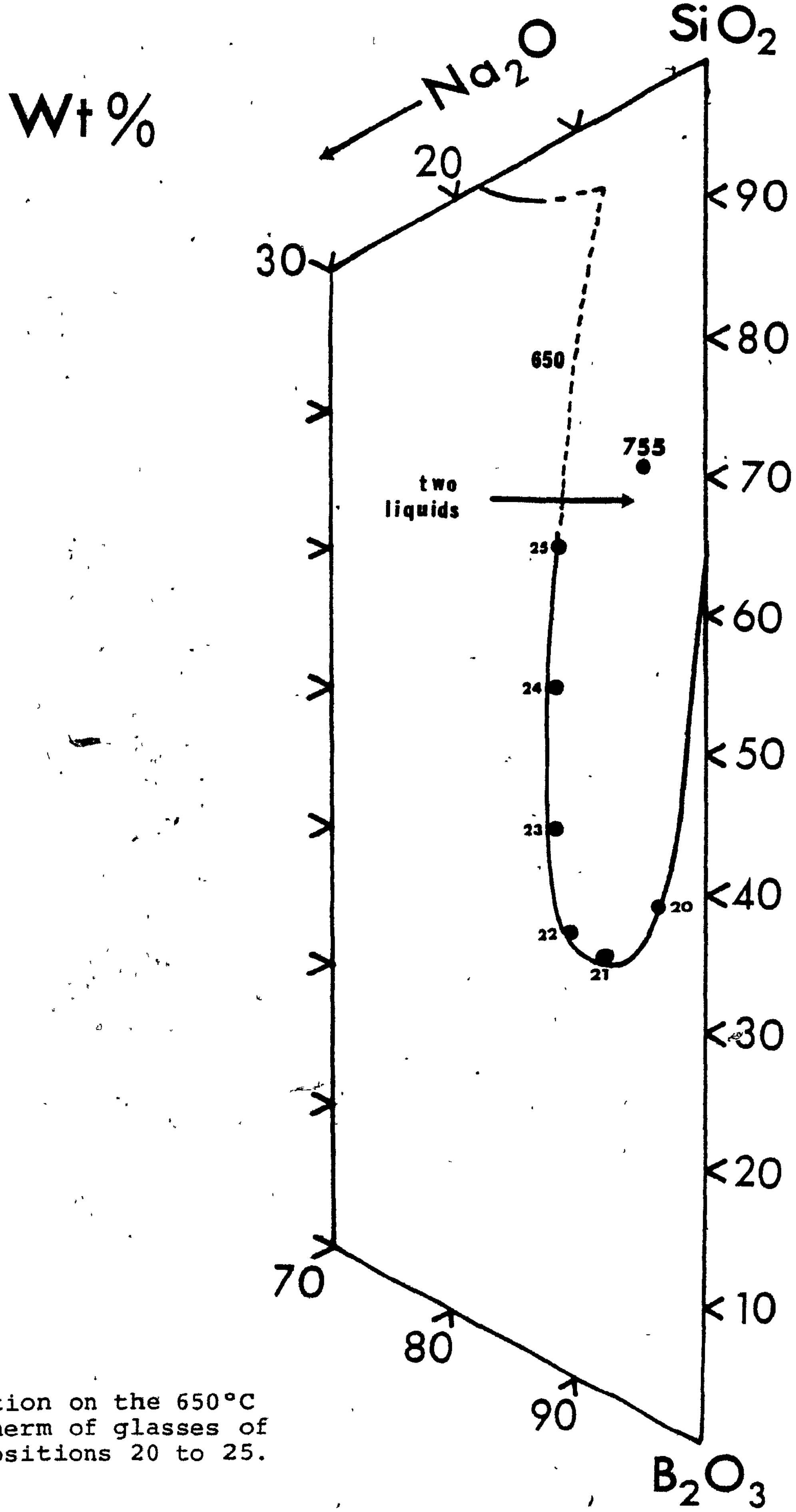

Fig. 28: Position on the 650°C isotherm of glasses of compositions 20 to 25.

Table V: Glass Compositions (in weight percent) of the Samples Shown in Figure 28.

Sample	Composition Weight%		
	Na_2O	B_2O_3	SiO_2
MnBS-20	4.19	58.88	36.93
MnBS-21	8.00	60.00	32.00
MnBS-22	11.00	57.00	32.00
MnBS-23	12.18	49.90	37.92
MnBS-24	12.18	39.92	47.90
MnBS-25	12.18	29.94	57.88

The samples MnBS-20 → 25 have 0.27 weight% MnO which was introduced in the glass as $MnSO_4 \cdot H_2O$.

the MnO doping level was fixed at 0.27 wt%. Here also, two bands (H and L) were observed (under 420 nm excitation). The high energy band centred at 593 nm (MnBS-20) shifted to 553 nm (MnBS-25) while the low energy band shifted from 638 nm (MnBS-20) to 627 nm (MnBS-25). These results are summarized in Table VI.

Figure 29 shows the emission spectra of three selected samples along the 650°C isotherm, showing that increasing the silica content shifts the H band toward higher energies and enhances its intensity. Thus we conclude that the Mn^{2+}

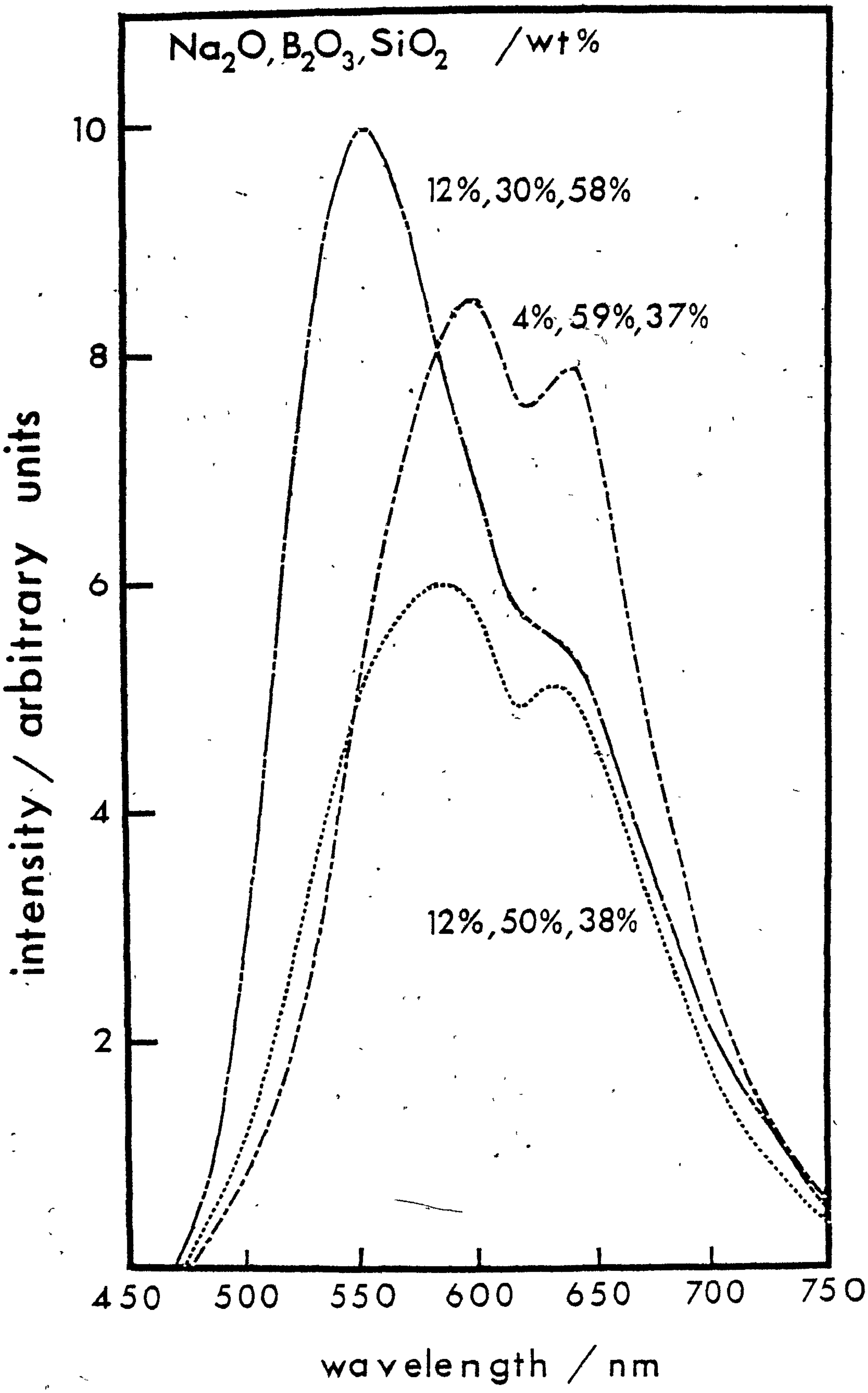

Fig. 29: Emission spectra of glasses of compositions 20, 23 and 25 doped with 0.27 wt% MnO. Excitation wavelength: 420 nm.

Table VI : Band Positions as a Function of Glass Composition 20 to 25 (MnO = 0.27 wt%).

Sample	H band (nm)	L band (nm)
MnBS-20	593	638
MnBS-21	593	638
MnBS-22	593	635
MnBS-23	588	635
MnBS-24	570	630
MnBS-25	553	627

Excitation wave length: 420 nm.

luminescence (for a given MnO concentration) depends on the glass composition.

4.2 MORPHOLOGICAL STUDY OF SAMPLES ALONG ONE TIE-LINE OF THE 700°C ISOTHERM

4.2.1 Introduction

From the previous discussion (Section 4.1) it is clear that Mn^{2+} luminescence in sodium borosilicate glasses depends on both the concentration of the activator for a given glass composition and on the composition of the glass for a particular activator level. To study the effect of phase separation on Mn^{2+} luminescence, the nature and

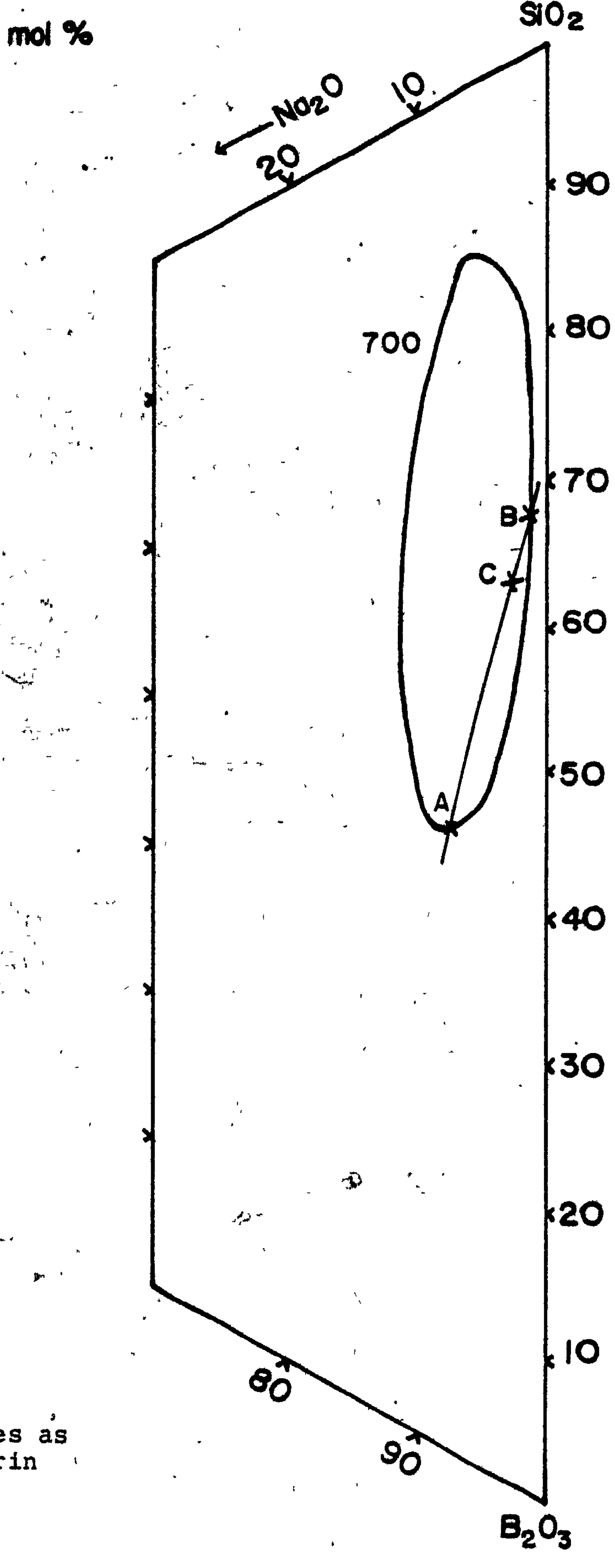

Fig. 30: One of the tie-lines as determined by Mazurin and Streltsina[20].

approximate composition of the separated phases must be known. Tie-lines provide the means for such studies. Indeed, any glass composition within the two-phase region bounded by a particular isotherm will, upon appropriate heat-treatment, separate into two phases with compositions given by the ends of its tie-line. The relative amounts of the two phases may be found from the lever rule (Section 2.5.2). Figure 30 shows one of the tie-lines of the 700°C isotherm[20]. Let, for example, point C represent the total glass composition, and let the ratio CB/CA = 1/4. At 700°C the glass will be composed of two phases, one of composition A, the other of composition B, their volume fraction being A/B = 20/80. Considering a doped glass, if Mn^{2+} remains uniformly distributed after phase separation, the luminescence spectrum of C, after heat-treatment, should be a composite of the two different spectra A and B in the ratio 20/80. If, on the other hand MnO concentrates in the boron-rich phase[†] upon heat treatment as in the case for ZnO[105] and CoO[112] in sodium borosilicate glasses, an effective increase in Mn^{2+} concentration will result. For example at 700°C the molar concentration of MnO (originally 1%) will become: $1\% \times \frac{100}{20} = 5\%$ in the boron-rich phase of the phase separated sample. The luminescence

---

[†] Since tie-lines cross the miscibility gap at a small angle to the $B_2O_3 \cdot SiO_2$ axis, the phase compositions are conveniently described as boron-rich and silica-rich. Note that sodium (like many other network modifiers[9,105]) tends to concentrate in the boron-rich phase.

spectrum of C should therefore be the same as one with five times the concentration of MnO and with the composition corresponding to that of the boron-rich end of the tie-line. Thus, both cases should result in an observable change in the fluorescence spectrum upon phase separation.

4.2.2 Glass Composition and MnO Concentration

One of the aims of this work was to study microstructural changes in glasses. We therefore undertook a careful morphological examination of MnO-doped glasses needed for the spectroscopic study.

Ten glass compositions (Table VII) were selected along one tie-line of the 700°C isotherm (Fig. 31) as determined by Mazurin and Streltsina[20]. Two MnO doping levels were chosen: 0.4 weight% (MnBS-30AC4 → MnBS-39AC4) and 0.6 weight% (MnBS-30 → MnBS-39). Four different glass compositions, two at each end of the tie-line (glasses 30 and 32, glasses 37 and 39) were doped with different levels of MnO (Table VIII). Since a correction was made to the weighed starting batches (Section 3.1), it was necessary to verify the glass compositions. The analysis was done by atomic absorption spectroscopy[†]. Five samples were selected for this purpose. The results of the analyses agree fairly well with the expected glass compositions (Table IX).

[†] The analyses were kindly performed by B. Sanipelli, Atomic Energy of Canada Ltd., Pinawa, Manitoba.

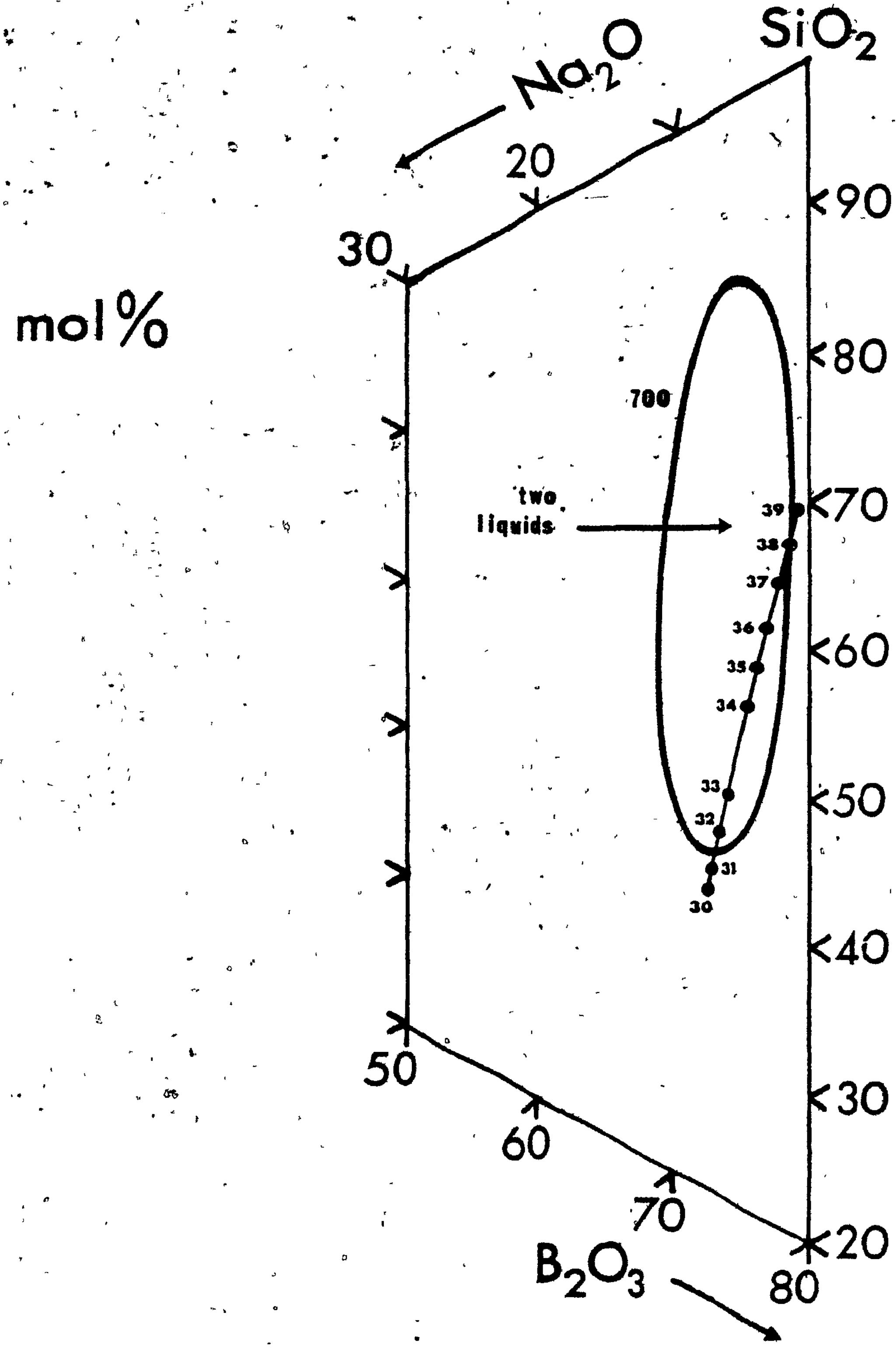

Fig. 31: Position on the tie-line of glasses of compositions 30 to 39.

Table VII: Glass Compositions Along the 700°C Isotherm (Figure 31).

Sample	Molar Composition		
	Na_2O	B_2O_3	SiO_2
MnBS-30 MnBS-30AC4	7.99	52.06	39.94
MnBS-31 MnBS-31AC4	7.43	50.28	42.29
MnBS-32 MnBS-32AC4	6.87	48.60	44.52
MnBS-33 MnBS-33AC4	6.25	46.53	47.22
MnBS-34 MnBS-34AC4	4.51	41.00	54.49
MnBS-35 MnBS-35AC4	3.79	38.77	57.44
MnBS-36 MnBS-36AC4	3.09	36.59	60.31
MnBS-37 MnBS-37AC4	2.40	34.43	63.18
MnBS-38 MnBS-38AC4	1.70	32.17	66.13
MnBS-39 MnBS-39AC4	1.01	29.96	69.03

The samples MnBS-30 → 39 have 0.6 weight% MnO which was introduced in the glass as $MnSO_4 \cdot H_2O$.

The samples MnBS-30AC4 → 39AC4 have 0.4 weight% MnO which was introduced in the glass as $Mn(CH_3COO)_2 \cdot 4H_2O$.

Table VIII: Glasses 30, 32, 37 and 39 (Molar Composition Given in Table XVII) With Different MnO Doping Levels.

Weight% MnO	MnBS-30	32	37	39
0.0	AC0	AC0	AC0	AC0
0.1	-	-	AC1	-
0.2	-	-	AC2	AC2
0.3	AC3	AC3	-	-
0.4	AC4	AC4	AC4	AC4
0.6	AC6	AC6	AC6	AC6
0.8	-	-	AC8	AC8
1.0	AC10	AC10	AC10	-
2.0	AC20	AC20	-	-
4.0	AC40	AC40	-	-
6.0	AC60	AC60	-	-

MnO was introduced in the glass as $Mn(CH_3COO)_2 \cdot 4H_2O$.

Table IX: Analysis Report of Mn-Doped Sodium Borosilicate Glasses.

Sample	Composition, weight%, observed/calculated			
	SiO_2	B_2O_3	Na_2O	MnO
MnBS-39AC4	64.6/65.88	31.4/33.13	0.9/0.99	0.4/0.4
MnBS-32AC60	37.5/41.23	48.6/52.14	6.3/6.56	5.4/6.0
MnBS-30AC0	35.9/36.81	56.3/55.59	7.8/7.60	-
MnBS-37AC10	60.2/59.86	35.3/37.79	1.7/2.34	1.0/1.0
MnBS-37AC0	61.0/59.86	35.4/37.79	1.7/2.34	-

The precision on the measurements is 5%.

4.2.3 Microstructural Study

4.2.3.1 Clearing temperature

Recently, Kawamoto, Clemens and Tomozawa[241] studied the effect of MoO_3 on phase separation of sodium borosilicate glasses. They concluded that the addition of small amounts of MoO_3 widen the miscibility gap of the system and raise the immiscibility temperature by 18°C for each mol% added. It was therefore necessary to determine at the outset whether the addition of small amounts of MnO also affects the process of phase separation, or the position of the immiscibility boundary of the sodium borosilicate system. To do this, the respective clearing temperatures of samples at the ends of the tie-line (glasses 30, 32, 37 and 39) with different MnO content were determined (Table X) following the procedures described previously (Section 3.3.2). The clearing temperatures (T_C) of the undoped samples were found to be more consistent with the 700°C miscibility gap of Galakhov and Alekseeva[18], than that of Haller *et al.*[17]. Upon doping with MnO, the clearing temperature increased steadily (Fig. 32). For low silica content (glasses 30 and 32) the increase was linear (at least up to 2.0 weight% of MnO) and the critical immiscibility temperature increased by approximately 14°C for each weight% MnO added. At the other end of the tie-line where the silica content was high (glasses 37 and 39) the increase in T_C was steep and non-linear. Even the addition of very small amounts of MnO (0.2 weight%) in glass 39 raised T_C by 140°C! Since the MnO has such a substantial effect on T_C, we need to consider the topography of the miscibility gap within the quaternary system, $Na_2O \cdot MnO \cdot B_2O_3 \cdot SiO_2$ (Fig. 33). Taylor and co-workers[105,107] described in detail the topography of some related quaternary systems. They reported that the miscibility gaps in a system of the type $X_2O \cdot MO \cdot (B_2O_3 + SiO_2)$, where X is an alkali ion and M a metal ion, change slightly when the fixed weight ratio of $SiO_2 : B_2O_3$ varies from one to five. Furthermore, a small one liquid region (the extent of which

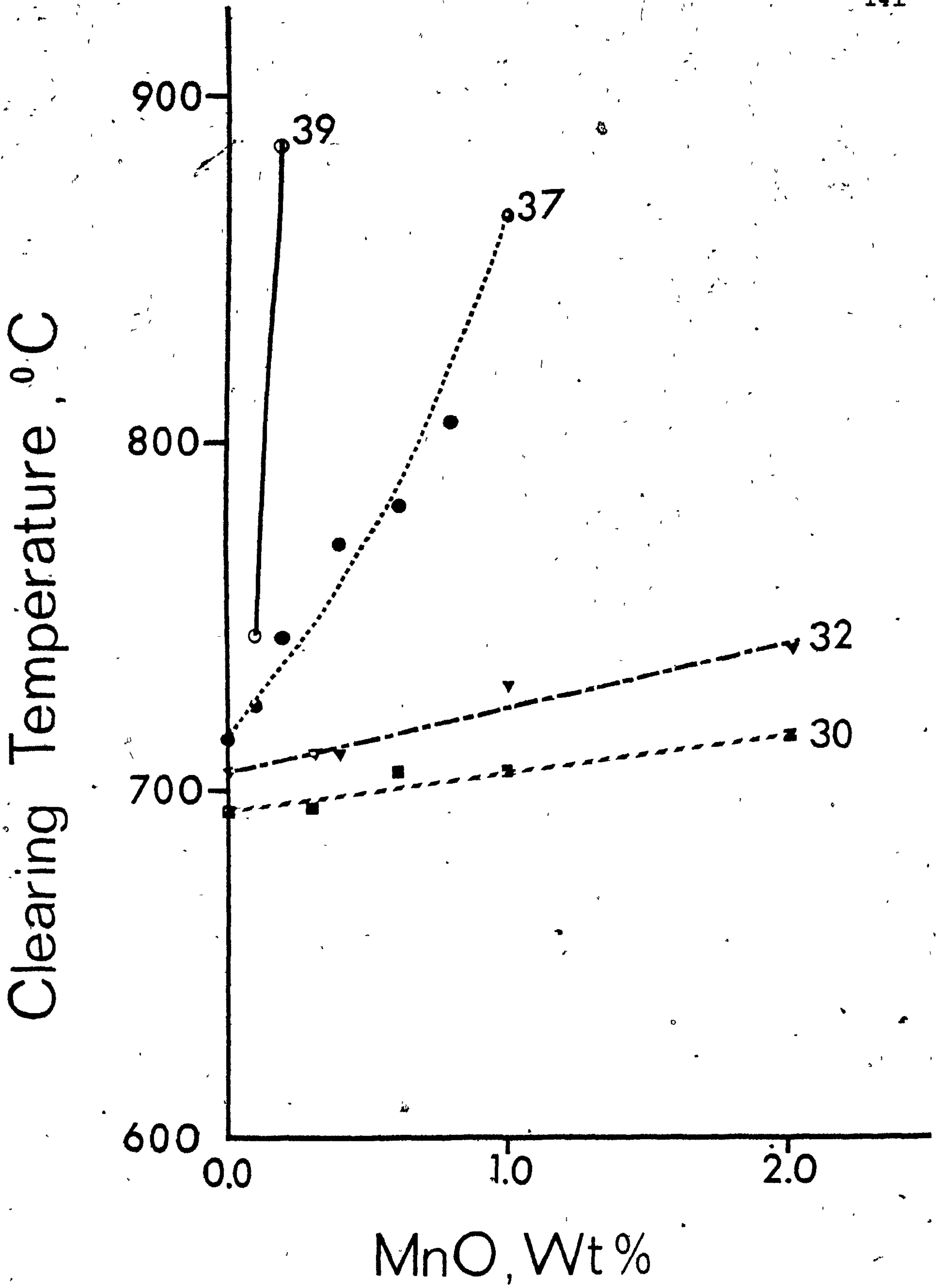

Fig. 32: Clearing temperature of glasses 30, 32, 37 and 39 as a function of MnO concentration.

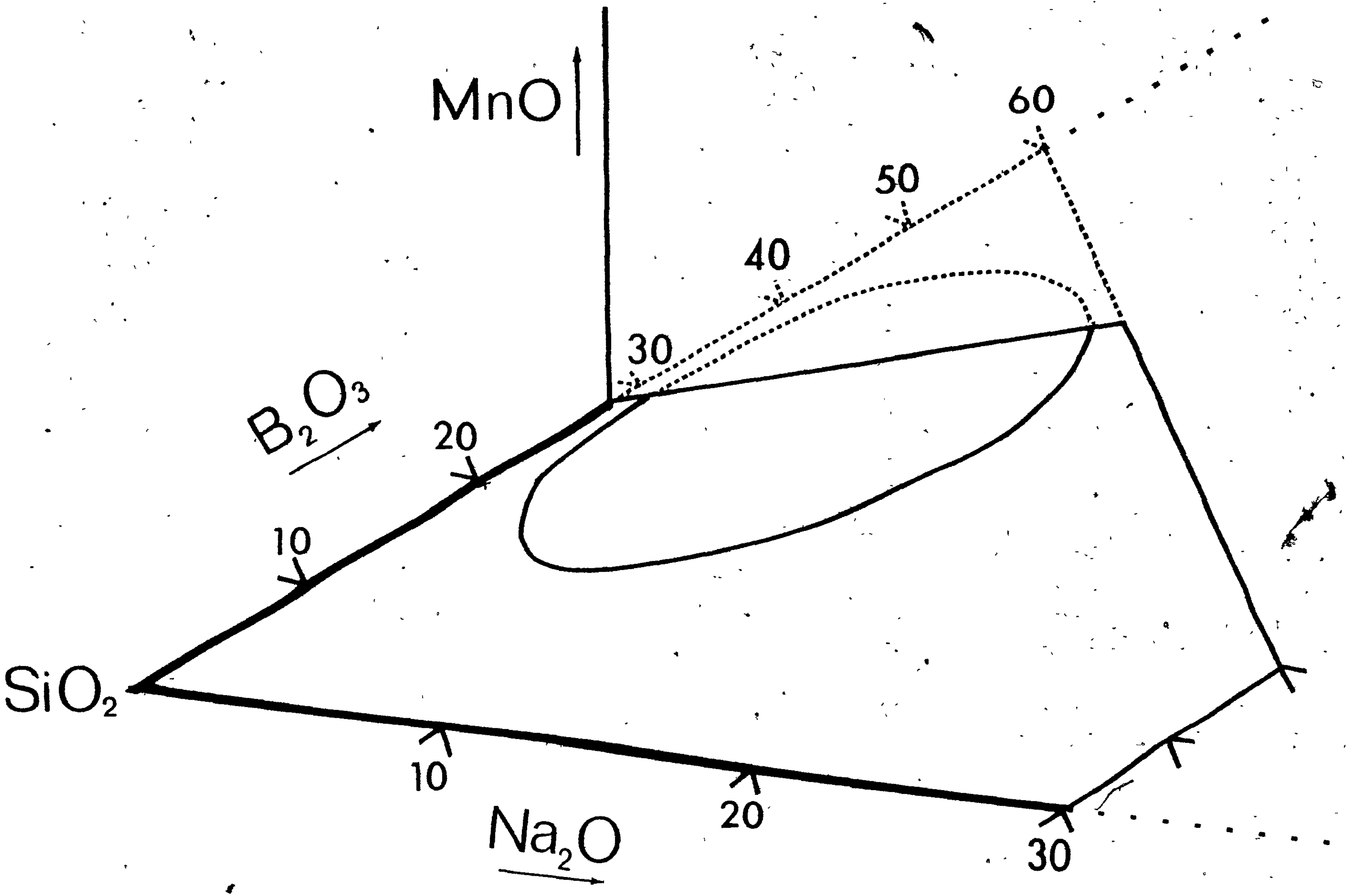

Fig. 33: Perspective drawing of the cross section which intersects the $Na_2O \cdot B_2O_3 \cdot SiO_2$ face, along the tie-line of interest.

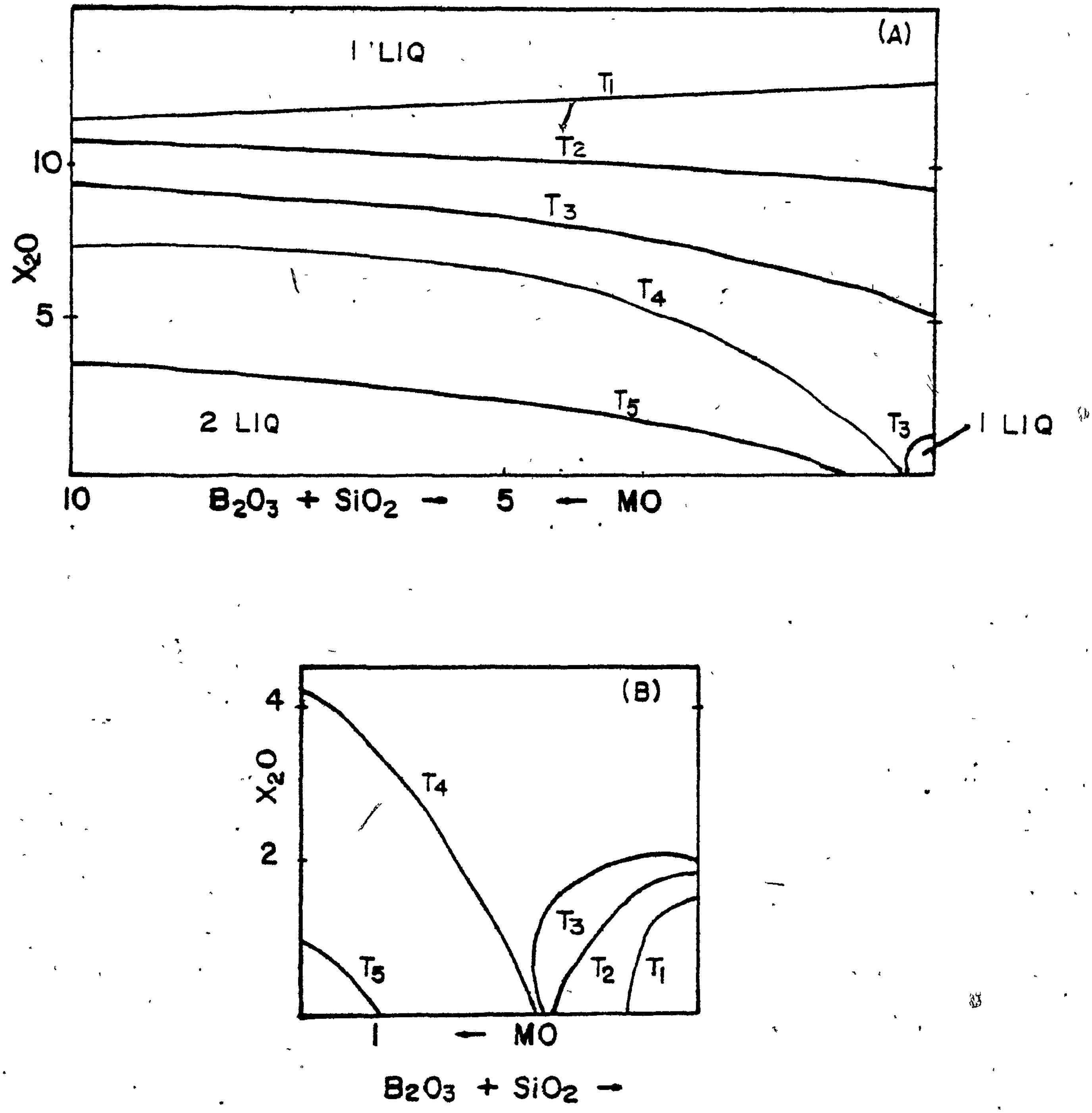

Fig. 34: Quaternary miscibility gaps for a fixed ratio of SiO_2:B_2O_3 in a system of the type $X_2O \cdot MO \cdot (B_2O_3+SiO_2)$, $T_5 > T_4 > T_3 > T_2 > T_1$.

(a) General representation (from Ref. 107).

(b) Expansion of the one liquid region adjacent to the $(B_2O_3+SiO_2)$ corner (from Ref. 242).

depends on the ratio of $SiO_2 : B_2O_3$) exists adjacent to the ($B_2O_3 + SiO_2$) corner (Fig. 34). For glasses 37 and 39 the weight ratio of $SiO_2:B_2O_3$ is approximately two, placing these samples within the limits of validity of the quaternary miscibility gaps as determined by Taylor *et al.*[104,105,107]. The rapid increase of T_c with increasing MnO content for these low-sodium compositions is consistent with the topography of the miscibility gaps in other systems of the type $X_2O{\cdot}MO{\cdot}B_2O_3{\cdot}SiO_2$, as determined by Taylor *et al.*[105,107].

To understand the behaviour of MnO-doped sodium borosilicate glasses a general description of the isotherms is needed. Rather than estimating the isotherms for a fixed ratio of $SiO_2:B_2O_3$, it is more appropriate here to delineate the perimeter of the isotherms for the cross-section which intersects the $Na_2O{\cdot}B_2O_3{\cdot}SiO_2$ face of the quaternary phase diagram along the tie-line of interest.

4.2.3.2 Estimation of the isotherms

The clearing temperatures of glasses 33, 34, 35 and 36 with 0.4 and 0.6 weight% MnO were determined (Table XI). The locus of the isotherms, as delineated by the data of Tables X and XI, is rather complex (Fig. 35).

The 800°C isotherm was above the 750°C (*i.e.* at higher MnO concentration for fixed $Na_2O{\cdot}B_2O_3{\cdot}SiO_2$ compositions), reflecting the enhancement of immiscibility by MnO. The 720°C

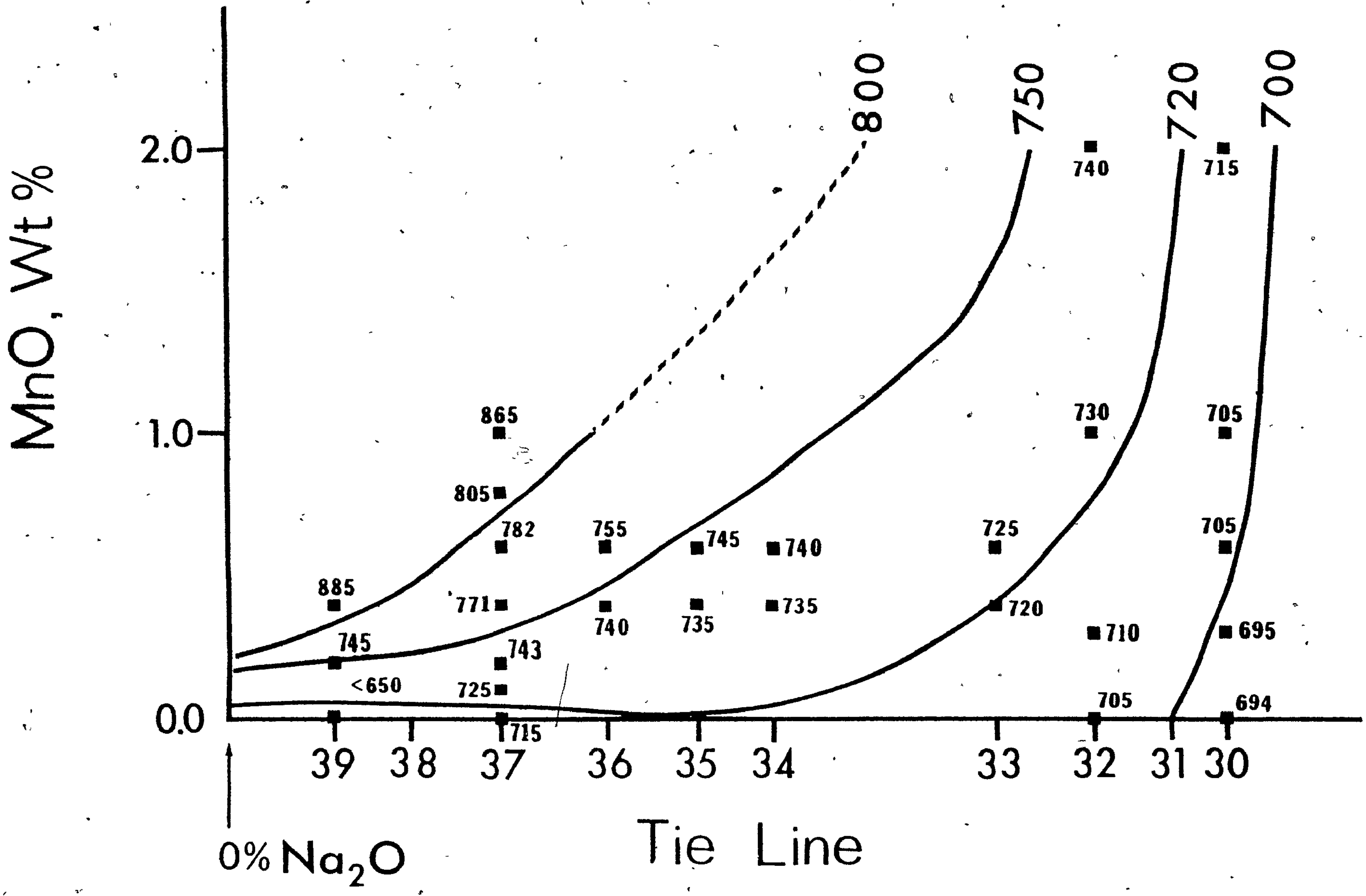

Fig. 35: Perimeter of the isotherms for the cross section represented in Fig. 33.

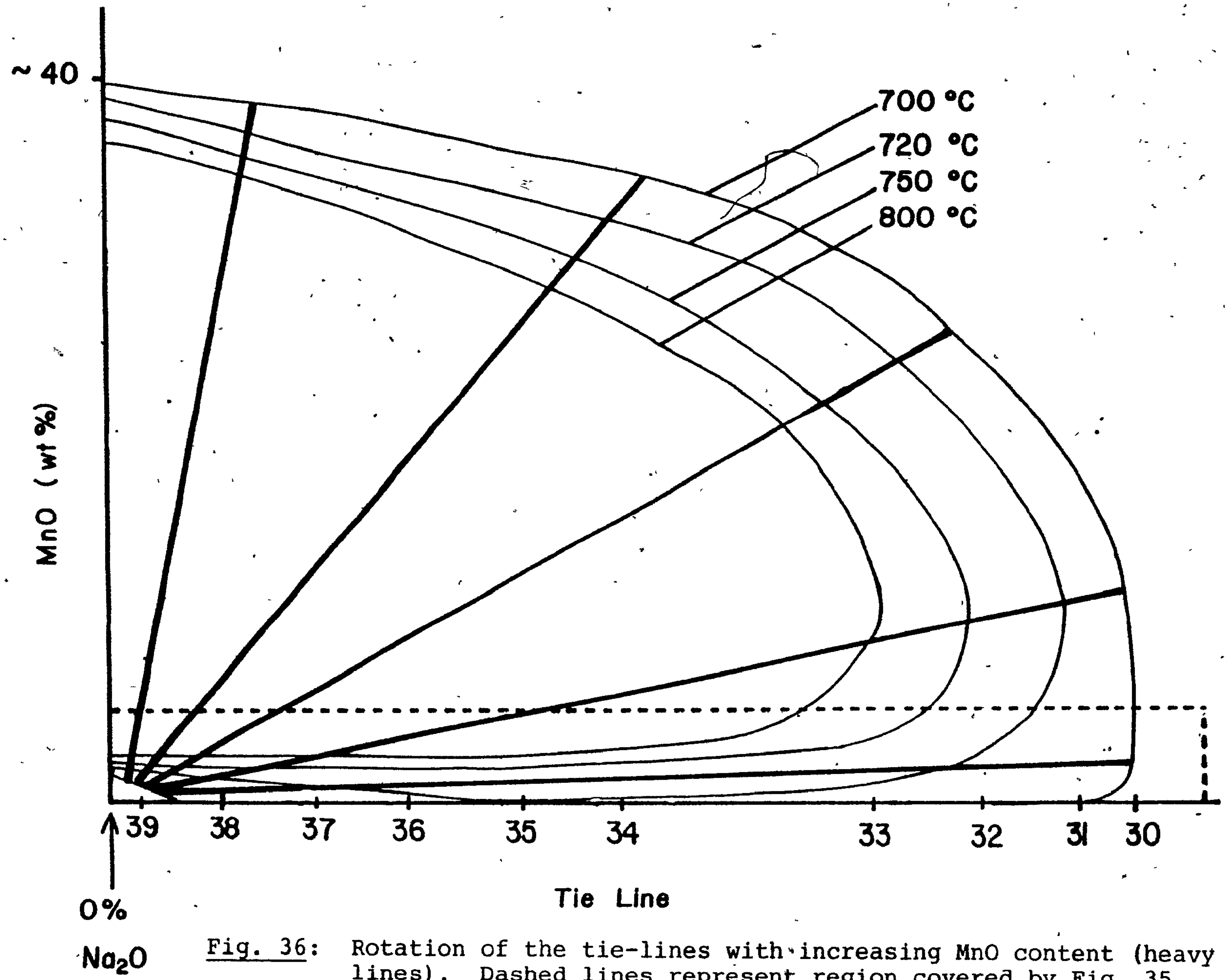

Fig. 36: Rotation of the tie-lines with increasing MnO content (heavy lines). Dashed lines represent region covered by Fig. 35. The figure is not to scale.

Table X: Clearing Temperatures (T_c) of Glasses 30, 32, 37 and 39 (Figure 31) With Different MnO Doping Levels.

Glass No.	Concentration MnO (Weight%)								
	0.00	0.10	0.20	0.30	0.40	0.60	0.80	1.00	2.00
No. 30	694°C	-	-	695°C	-	705°C	-	705°C	715°C
No. 32	705°C	-	-	710°C	-	-	-	730°C	740°C
No. 37	715°C	725°C	743°C	-	771°C	782°C	805°C	865°C	-
No. 39	<605°C	-	745°C	-	885°C	-	-	-	-

The precision on the measurements is $T_c \pm 5°C$.

Table XI: Clearing Temperatures (T_C) of Glasses 33, 34, 35 and 36 Doped with 0.4 and 0.6 Weight% MnO.

Glass No.	Concentration MnO (Weight%)	
	0.40	0.60
No. 33	720°C	725°C
No. 34	735°C	740°C
No. 35	735°C	745°C
No. 36	740°C	755°C

The precision on the measurements is $T_C \pm 5°C$.

Isotherm is tangent to the tie-line at glass 35 and continues at very low MnO content adjoining glasses 37, 38 and 39. At lower temperatures than 720°C, the one-liquid region is divided into two portions as represented in Fig. 35 (although these two portions are not entirely separate when represented on a full four-component diagram, see Ref. 107). Thus, one 700°C isotherm is approximately parallel to the MnO axis, intersecting the tie-line axis near composition 31, and a second 700°C isotherm delineates a minute one-liquid region at the lower left corner of the diagram (Fig. 35).

Thus, the system was actually found to behave like other quaternary systems of the type $X_2O \cdot MO \cdot B_2O_3 \cdot SiO_2$.

Figure 35 is the portion of the larger diagram shown in Fig. 36. The part of the x axis between glass composition 31 and 38 represents the tie-line at 700°C of the ternary $Na_2O \cdot B_2O_3 \cdot SiO_2$ system. On addition of MnO this tie-line rotates following the trend described in Fig. 36 and also twists out of the plane to some extent. At *ca.* 40 wt% MnO and 0% Na_2O the tie-line becomes coincident with the ternary $MnO \cdot B_2O_3 \cdot SiO_2$ system. The tie-line chosen for this work was specific to the ternary $Na_2O \cdot B_2O_3 \cdot SiO_2$ system. Since it was not clear what effect the addition of different doping levels of MnO would have on this conode (*i.e.* it may rotate) it was necessary to verify the tie-line. One way to do this in the quaternary $Na_2O \cdot MnO \cdot B_2O_3 \cdot SiO_2$ system is to study the micrographs of MnO-doped phase separated glasses along the presumed tie-line.

4.2.4 Tie-Line Verification

Any glass composition along the tie-line will, upon appropriate heat-treatment, separate into two phases (the amounts of which are given by the lever rule) with compositions represented by the ends of the tie-line (Section 2.5.2). One end is boron-rich (glass composition 31) and the other is silica-rich (glass composition 39). If the tie-line orientation does not change substantially on MnO addition, one would expect upon phase separation, a gradual

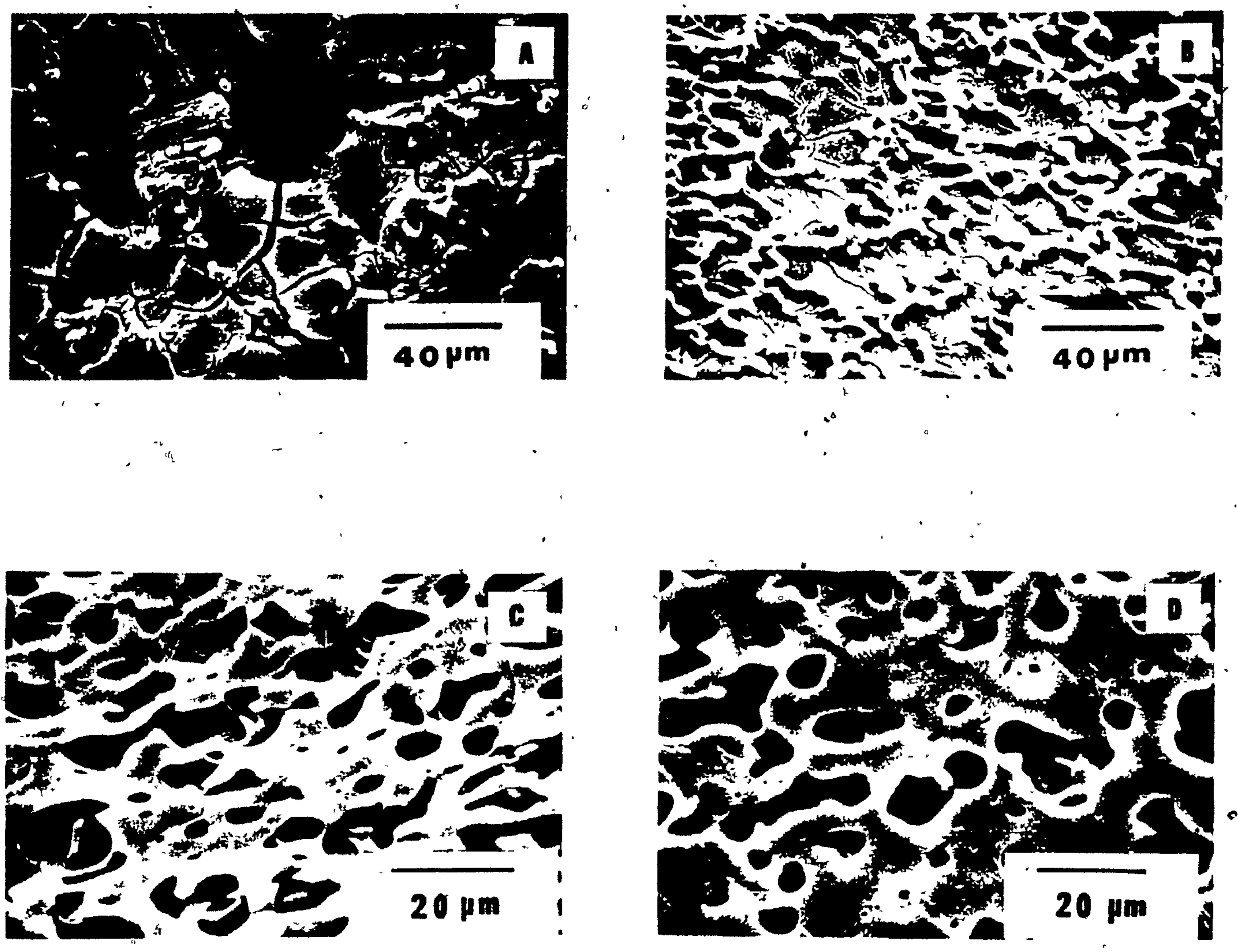

Fig. 37: Scanning electron micrographs of MnO-doped (0.6 wt%) samples along the tie-line (Fig. 31). (All micrographs in this figure are of HF-etched, freshly fractured surfaces). (A) Glass composition 31 after 6 h at 708°C, (B) Glass composition 33 after 6 h at 708°C, (C) Glass composition 34 after 12 h at 700°C, and (D) Glass composition 35 after 12 h at 700°C.

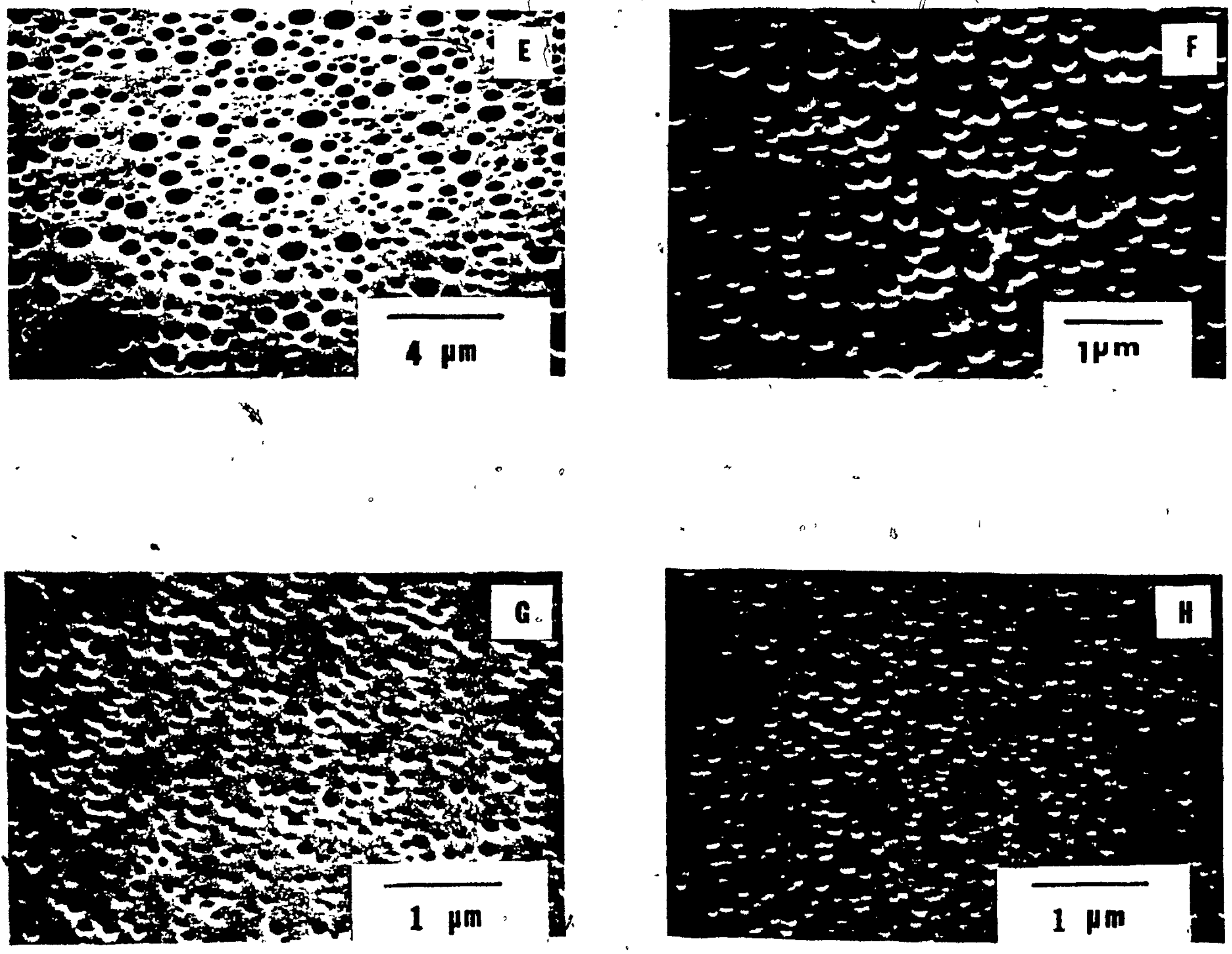

Fig. 37 (continued):

(E) Glass composition 36 after 16 h at 695°C,
(F) Glass composition 37 after 16 h at 710°C,
(G) Glass composition 38 after 16 h at 708°C,
(H) Glass composition 39 after 16 h at 708°C.

change in the relative amounts of the two phases (B-rich and Si-rich) on going from glass composition 31 to glass composition 39.

Figure 37 shows some scanning electron micrographs of MnO-doped (0.6 weight%) phase-separated samples along the tie-line of Fig. 31. Figure 37A (glass composition 31) shows a boron-rich matrix with few silica-rich particles. Figure 37B shows an increase in the volume fraction of the silica-rich particles (2-10 μm) leading to an interconnected microstructure†. Glass composition 34 lies approximately in the middle of the tie-line implying two coexisting phases in equal amounts (Fig. 37C). Glass composition 35 is closer to the Si-rich end of the tie-line than to the B-rich end. This is shown in the micrograph of Fig. 37D where the glass matrix is silica-rich with large holes (∿ 10 μm) of boron-rich phase. Between compositions 36 and 39, the more viscous silica-rich phase is continuous, with dispersed silica-poor holes a few tenths of a micrometer in diameter (Figs. 37E to 37H). The smaller scale of phase separation here is presumed to be due to the higher viscosity of the initial glasses, which are very low in alkali content (< 3.1% Na_2O). The progressive change in the microstructure on going from glass 31 to 39 is consistent with the tie-line orientation of Mazurin and Streltsina[20]. It can therefore be concluded

---

† The morphology of glass composition 32 will be examined in detail in the following section.

that the tie-line orientation is relatively insensitive to the addition of small amounts of MnO.

4.2.5 Distribution of Mn^{2+}, Cr^{3+} and Ti^{4+} in Phase-Separated Samples

4.2.5.1 Distribution of Mn^{2+}

The relatively large phase domains which occurred in compositions near the boron-rich end of the tie-line permitted examination by energy-dispersive X-ray microanalysis in conjunction with scanning electron microscopy. Composition 32 doped with 4 weight% MnO was phase separated by heating for 16 h at 695°C (Fig. 38A). Before examining this glass in detail several verifications were needed:

1) To ensure that 4 weight% MnO did not affect the volume fraction of the phases a similar undoped glass was subjected to the same thermal treatment (Fig. 38B). No major differences in the microstructure existed between the undoped composition 32 and the doped one (Figs. 38A and 38B).

2) To rule out any phase separation prior to heat-treatment, an unheated glass of composition 32 doped with 4 weight% MnO was investigated. Several locations on different faces were closely examined and no evidence of phase separation was detected (Fig. 38C). The particle in micrograph 38C is one of a small number of undissolved or precipitated particles present, and was included in the

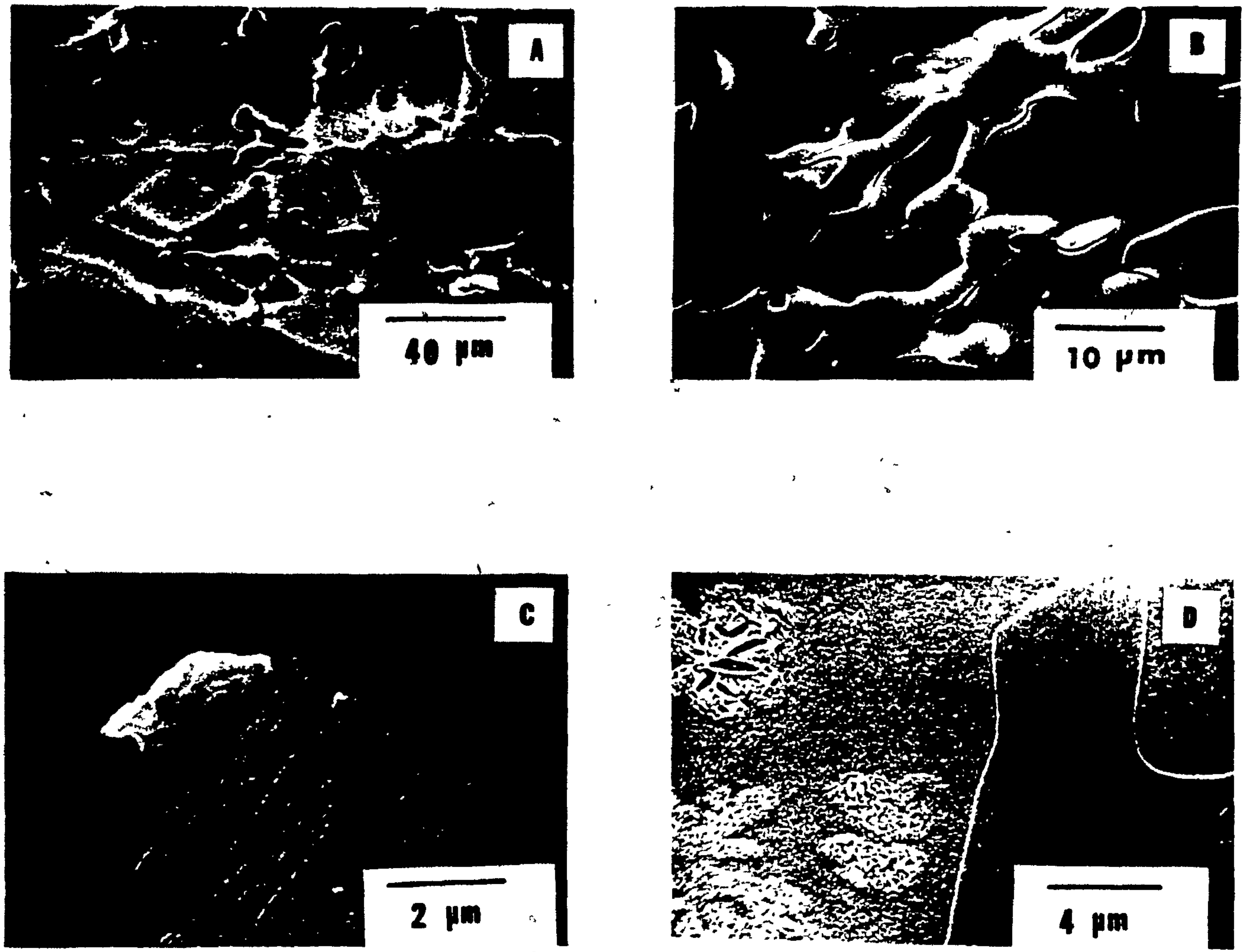

Fig. 38: Glass composition 32 (all micrographs in this figure are of water-etched freshly fractured surfaces). (A) Undoped after 16 h at 695°C, (B) Doped with 4 weight% MnO after 16 h at 695°C (*cf.* small volume fraction when compared to micrograph A), (C) Undoped showing no visible sign of phase separation prior to heat-treatment, (D) Undoped after 16 h at 695°C showing crystallization and phase separation.

micrograph to assure sharp focus.

3) To rule out the possibility that crystallization might interfere with the phase separation process, selected samples were checked to ensure only minimal (if any) crystallization had occurred. Figure 38D shows an example of the limited extent of crystallization found.

After these verifications, glass composition 32 doped with 4 weight% MnO was closely examined as shown in Fig. 39. Crosses in Fig. 39A represent points analyzed by EDAX spot analysis. The results of this EDAX spot analysis are shown in Figs. 39B and 39C where the two spectra are superimposed. Three major peaks representing three characteristic X-rays were found: 1.74 keV, Si; 2.12 keV, Au coating the sample and serving as a reference; 5.89 keV, Mn. The dotted spectrum (Fig. 39B) of the boron-rich (silica-poor) phase showed that the Mn was concentrated[†] in the boron-rich phase (Fig. 39C). The line scans (Figs. 39D and 39E) confirmed the identity of the separated phases (Si-rich and Si-poor) and the partition of manganese(II) into the silica-poor phase. The ratio of Si K_α X-ray intensities obtained from the two phases was about 1.65 uncorrected for matrix effect. This is in reasonable agreement with the mole percentage ratio

---

[†] Although Mn is concentrating in the B-rich phase, one cannot exclude the presence of very small quantities of Mn in the Si-rich phase which cannot be detected by EDAX, since spot analysis detection limit for Mn is approximately one percent as indicated by the signal to noise ratio of Fig. 39C.

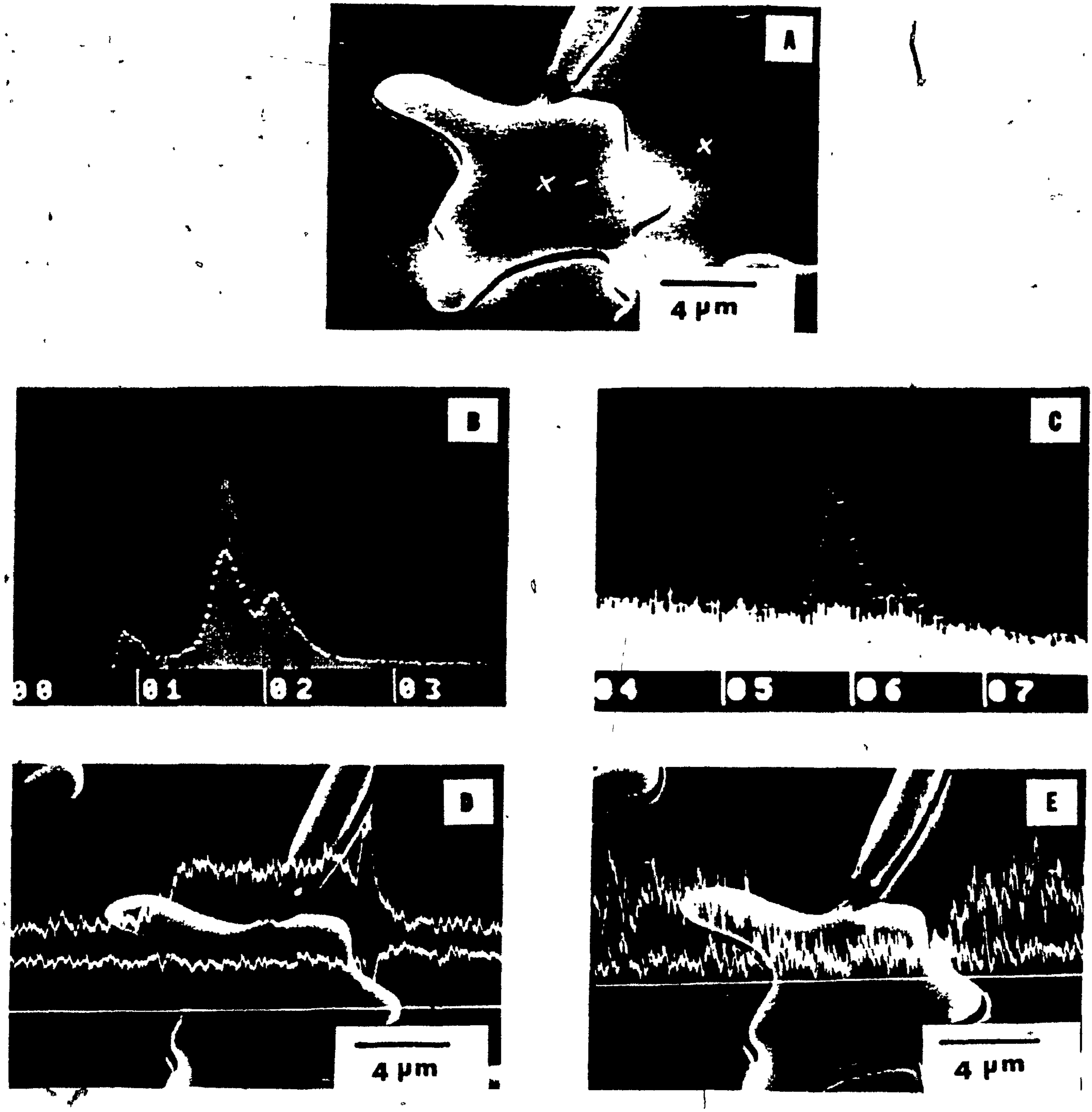

Fig. 39: (A) Glass composition 32, doped with 4 weight% MnO after 16 h at 695°C; water-etched fracture surface. Crosses represent points analyzed by EDAX spot analysis. (B) and (C) Spectra obtained from EDAX, spot analyses, demonstrating the concentration of Mn in the Si-poor phase (dotted spectrum) (peak identity: 1.74 keV, Si; 2.12 keV Au coating of sample; 5.89 keV Mn). (D) and (E) EDAX line scans showing the distribution of Si and Mn, respectively. Lower scan in (D) is on the Au peak that in (E) is on the background adjacent to the Mn peak. "Spikes" in (D) appear to be due to irregularity in the gold layer at the phase boundary.

of about 1.55 at 700°C, determined from the tie-line in Fig. 31. This offers further evidence that small quantities of MnO do not induce major rotation of the tie-line. These results are comparable to microprobe studies of similar CoO-doped glasses by Ehrt *et al.*[112], and studies of two undoped sodium borosilicate glasses by Scholes and Wilkinson[164].

4.2.5.2 Distribution of Cr^{3+} and Ti^{4+}

Energy-dispersive X-ray analysis does not differentiate between various possible oxidation states of the manganese ion. However, it is highly improbable that manganese exists in the prepared glasses in an oxidation state other than Mn^{2+} (a reducing agent was added to the last melt and heat-treatments were carried out in a nitrogen atmosphere). To complement this study of Mn^{2+} it would be desirable to study also the partition of a trivalent and of a quadrivalent transition metal ion in sodium borosilicate glasses. For this purpose glasses of composition 32 were prepared, one doped with 4 weight% Cr_2O_3 (introduced as the acetate) and another sample with 4 weight% TiO_2. The dissolution of Cr_2O_3 and TiO_2 into the glass was difficult even after the third melt, as indicated by the precipitation of Cr_2O_3 and TiO_2 in the bottom of the crucibles. This difficulty was encountered even with low doping levels

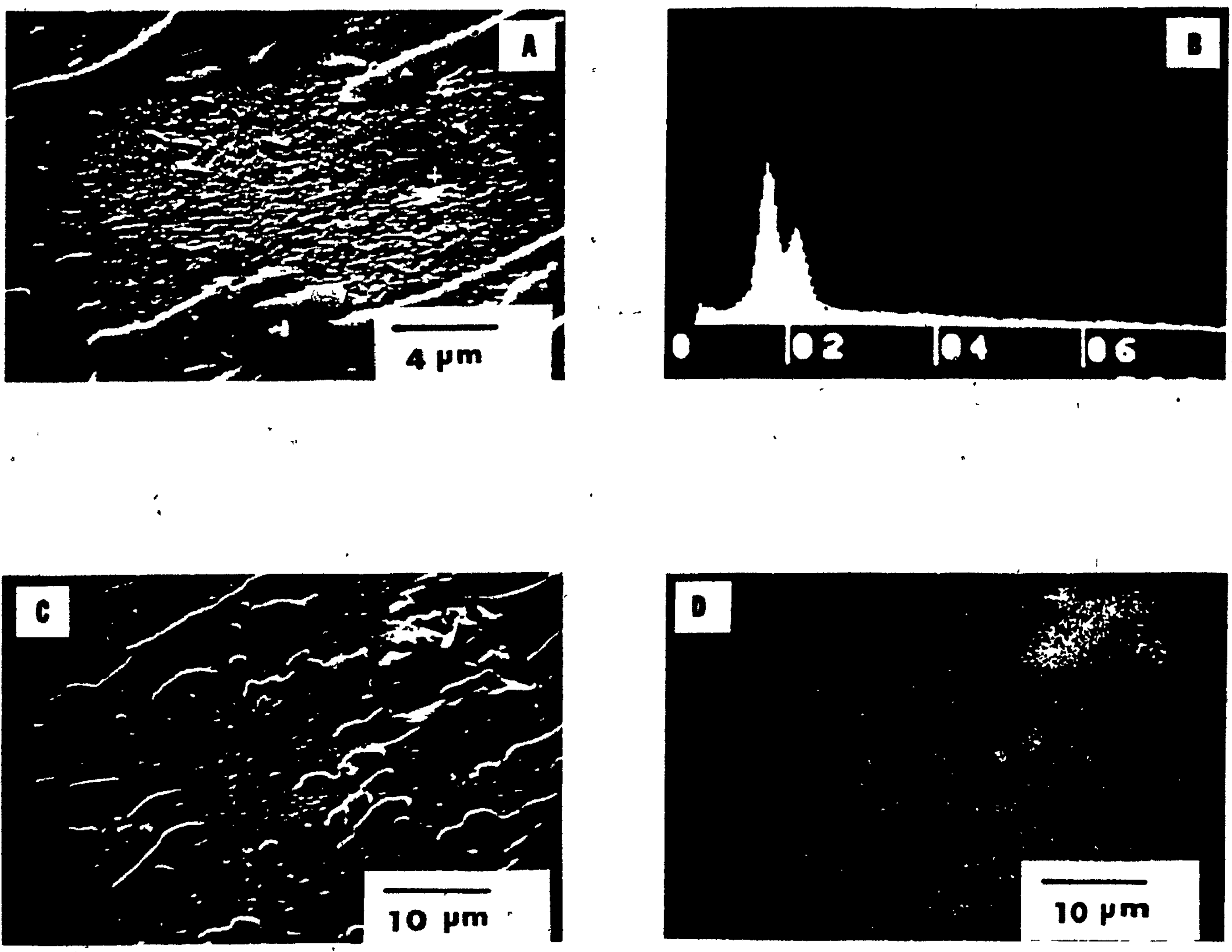

Fig. 40: (A) Glass composition 32 doped with 4 weight% Cr_2O_3 after 3 h at 695°C; water-etched fractured surface. Crosses represent points analyzed by EDAX spot analysis, (B) Spectra obtained from EDAX-spot analysis showing no visible partition of Cr in either phase (Cr K_α line: 5.41 keV), (C) Bright particles (probably undissolved Cr_2O_3) on the glass surface, (D) EDAX mapping (Cr K_α line) of micrograph (C) confirming the Cr identity of the bright particles.

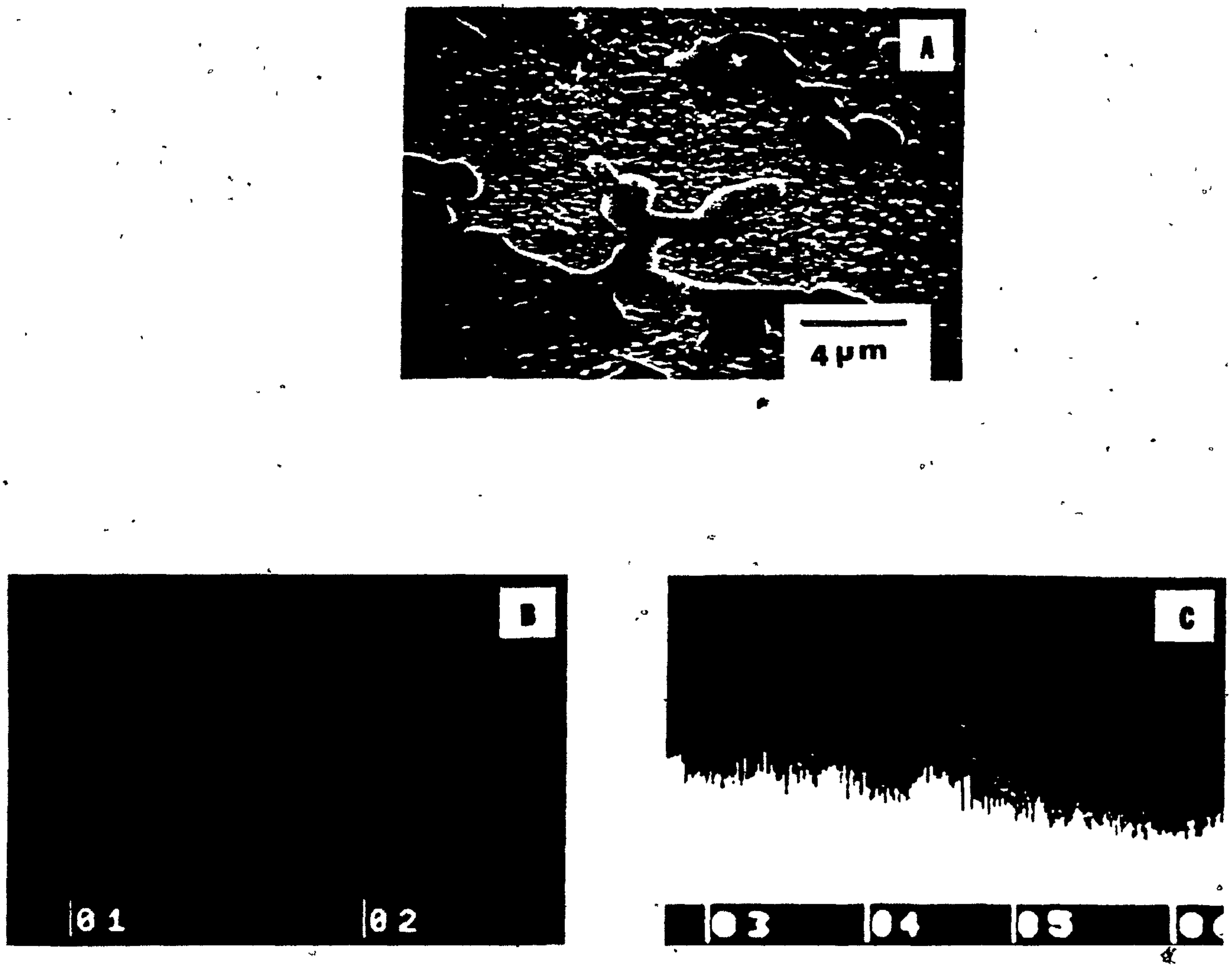

Fig. 41: (A) Glass composition 32, doped with 4 weight% TiO_2 after 3 h at 695°C; water-etched fractured surface. Crosses represent points analyzed by EDAX spot analysis, (B) and (C) Spectra obtained from EDAX spot analyses, demonstrating the concentration of Ti in the Si-poor phase (dotted spectrum) (peak identity: 1.74 keV, Si; 2.12 keV Au coating of sample, 4.51 keV Ti).

(0.6 weight%) of Cr_2O_3. The glasses obtained after the fourth melt were phase separated by heating for 3 h at 695°C, and examined in detail as shown in Figs. 40 and 41. The phase domains obtained (Figs. 40A and 41A) were comparable to MnO-doped composition 32 (Fig. 38A). Spot analyses of the Cr_2O_3-doped glass revealed the existence of the silica-poor and silica-rich phases, but failed to show any concentration of chromium in either phase. Some bright particles on the glass surface (Fig. 40C) were suspected to be undissolved Cr_2O_3 crystals. An X-ray mapping (Cr K_α line: 5.41 keV) confirmed that these bright particles indeed contained the Cr (Fig. 40D). Spot analyses (Figs. 41B and 41C) of TiO_2-doped composition 32 confirmed the identity of the silica-rich and silica-poor phases and showed that titanium(IV) was strongly partitioned into the latter phase. Si K_α X-ray intensities obtained from the two phases of the two samples (Cr_2O_3-doped and TiO_2-doped glasses) was about 1.45 uncorrected for matrix effects, in reasonable agreement with the results obtained for the MnO-doped glass of the same composition.

4.2.6 Conclusions

This morphological study showed that: 1) MnO-doped sodium borosilicate glasses behave similarly to glasses in other quaternary systems of the type $X_2O \cdot MO \cdot B_2O_3 \cdot SiO_2$; 2) the tie-line orientation (in the ternary $Na_2O \cdot B_2O_3 \cdot SiO_2$ system) is insensitive to the addition of small quantities of MnO and thus could still be used in the quaternary system with low doping levels of MnO; 3) Manganese(II) and titanium(IV) both concentrate in the silica-poor phase while chromium(III) remained essentially undissolved in this glass composition.

Partitioning of the manganese(II) preferentially into the silica-poor phase upon phase separation, leads to an effective increase in the concentration of MnO as discussed earlier in Section 4.2.1. The manganese(II) luminescence spectrum in sodium borosilicate glasses was shown to be sensitive to MnO concentrations (Section 4.1.2). Upon phase separation, manganese(II) in glass composition 37 will concentrate in the boron-rich phase with a composition approximately that of glass 30. This partition of Mn^{2+} into the borate phase will lead to an increase in the activator level in this phase. Therefore, upon heat-treatment, a correlation between the luminescence spectra of glass composition 37 with low doping levels of MnO and that of the unheated composition 30 with high doping levels of MnO is expected[†]. In fact similar correlations between the samples shown on the left-hand side of Fig. 41' and those on the right-hand side are expected.

[†] Actually the correlation is expected with the boron-rich end of the tie-line, that is a composition between glass 31 and glass 32. On addition of MnO the miscibility gap widens (Section 4.2.3.1) and glass composition 30 is probably closer to the end of the tie-line than glass composition 32.

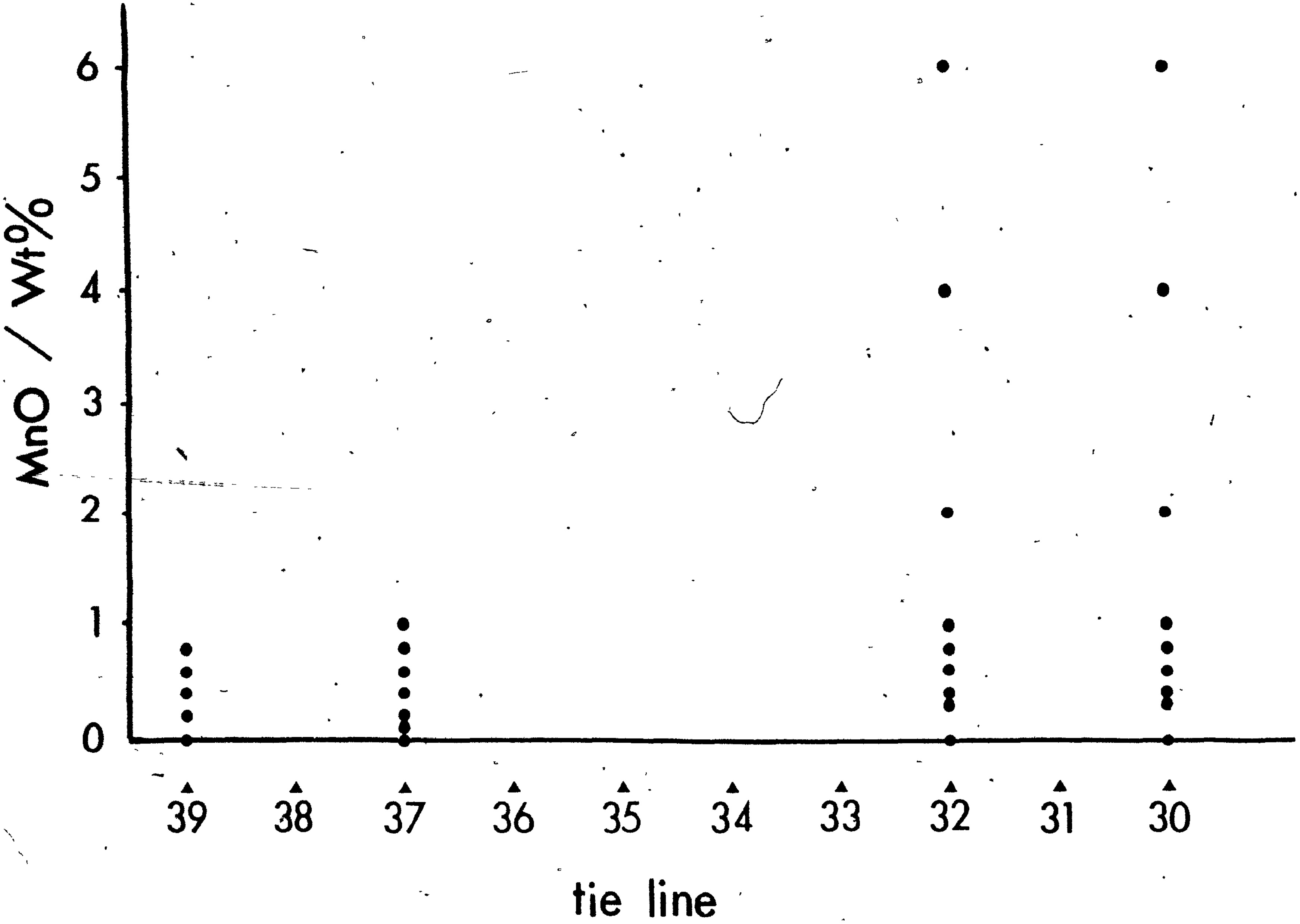

Fig. 41: Position of the tie-line of glasses of compositions 30, 32, 37 and 39 with different MnO content.

4.3 LUMINESCENT SPECTRA ALONG ONE TIE-LINE OF THE 700°C ISOTHERM

4.3.1 Unheated Samples Along the Tie-Line

Ten samples along the tie-line (Fig. 31) doped with 0.4 weight% MnO were excited with 420 nm light. Two bands (H and L) were present in all the spectra. The high energy band centred at 595 nm (MnBS-30AC4) shifted to 610 nm (MnBS-38AC4) while the low energy band shifted from 638 nm (MnBS-30AC4) to 646 nm (MnBS-38AC4). The relative height (H/L) also changed on going from one end of the tie-line to the other. The value of H/L decreased from 1.03 (MnBS-30AC4) to 0.73 (MnBS-38AC4). These results are summarized in Table XII. Glass composition 39 did not follow the general trend of the series (*i.e.* a gradual shift of the H band toward longer wavelength and a decrease in H/L, on going from the boron-rich end to the silica-rich end of the tie-line). This was probably due to the poor glass quality obtained with the high-silica low-sodium composition. For this reason glass composition 39 is not included in this discussion. It is clear from Table XII that the relative heights of the two bands [H/L = 1.03 (MnBS-30AC4) to H/L = 0.73 (MnBS-38AC4)] is more affected by glass composition than the change in the band positions (595 nm to 610 nm for the H band and 638 to 646 nm for the L band). Nevertheless the luminescent spectrum of MnBS-31AC4 at the

Table XII: Band Positions and Relative Heights (H/L) as a Function of Glass Composition. (0.4 Weight% MnO).

Sample	H band (nm)	L band (nm)	Relative Height H/L
MnBS-30AC4	595	638	1.03
MnBS-31AC4	595	638	1.02
MnBS-32AC4	598	640	1.00
MnBS-33AC4	598	640	0.99
MnBS-34AC4	600	640	0.95
MnBS-35AC4	603	643	0.87
MnBS-36AC4	605	643	0.85
MnBS-37AC4	608	646	0.75
MnBS-38AC4	610	646	0.73
MnBS-39AC4	608	648	0.75

Excitation wavelength = 420 nm.

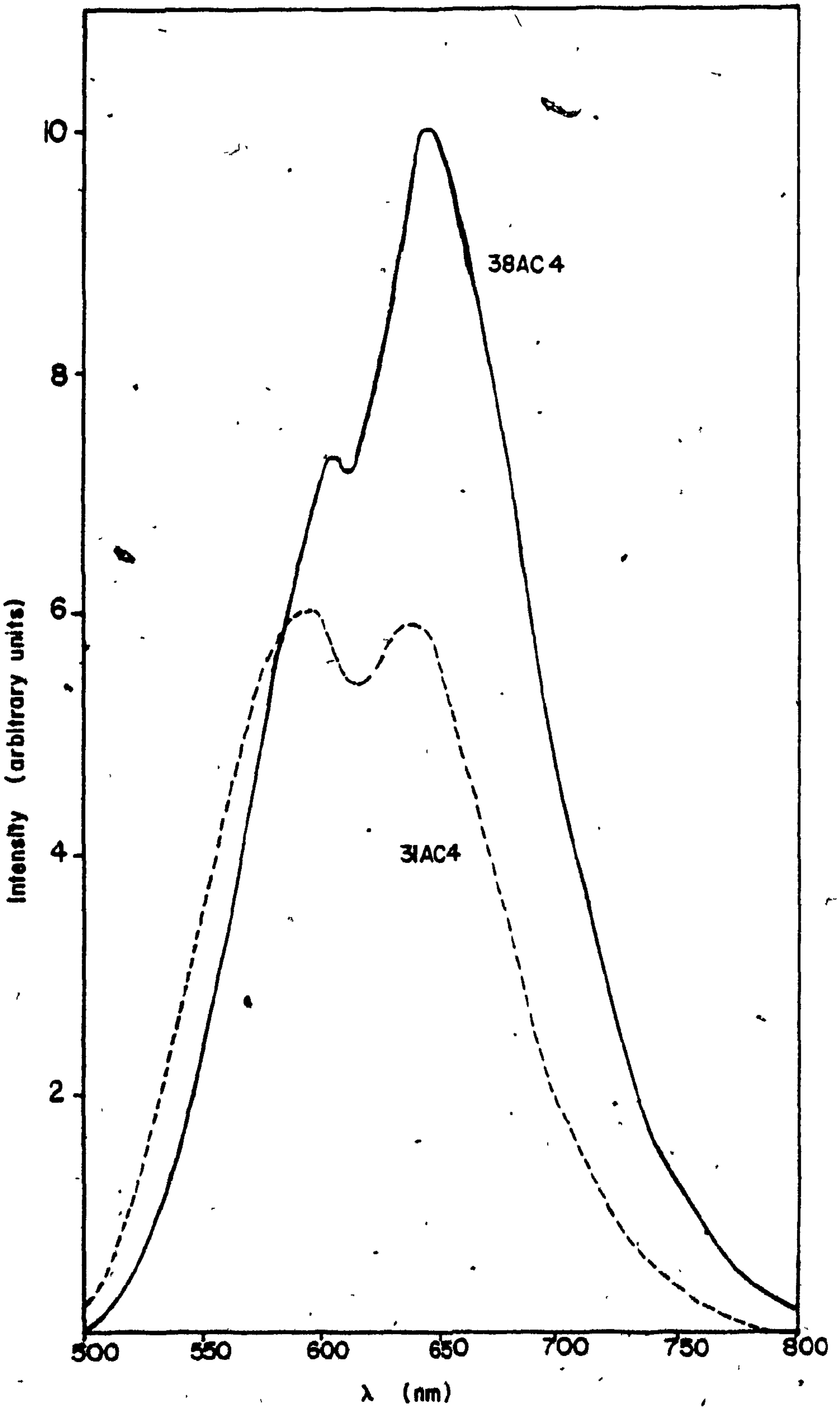

Fig. 42: Emission spectra of glasses of compositions 31AC4 and 38AC4. Excitation wavelength: 420 nm.

boron-rich end of the tie-line was found to be noticeably different from that of MnBS-38AC4 at the silica-rich end of the tie-line (Fig. 42). Another series of samples along the tie-line, but doped with 0.6 weight% MnO (MnBS-30 to MnBS-39), was excited with 420 nm light. The changes in their luminescent characteristics showed the same trends as those doped with 0.4 weight% MnO, again excepting glass composition 39. The results are summarized in Table XIII.

4.3.2 Unheated Samples at the Extremities of the Tie-Line

4.3.2.1 Boron-rich end

Glasses of composition 30 and 32 doped with different levels of MnO (0.3 to 6.0 weight%) were excited at 420 nm. Two bands (H and L) were present in all the spectra.

(i) Glass composition 30

The high energy band centred at 593 nm (0.3 weight% MnO) shifted to 613 nm (6.0 weight% MnO) while the low energy band shifted from 635 nm (0.3 weight% MnO) to 667 nm (6.0 weight% MnO). The relative heights (H/L) decreased from 1.08 (0.3 weight% MnO) to 0.32 (6.0 weight% MnO). These results are summarized in Table XIV. A nearly complete quenching of the H band relative to the L band was observed when MnO concentrations

Table XIII: Band Positions and Relative Heights (H/L) as a Function of Glass Composition (0.6 Weight% MnO).

Sample	H band (nm)	L band (nm)	Relative Height H/L
MnBS-30	598	639	0.96
MnBS-31	600	640	0.96
MnBS-32	603	642	0.89
MnBS-33	603	642	0.88
MnBS-34	605	643	0.86
MnBS-35	605	643	0.84
MnBS-36	608	644	0.77
MnBS-37	609	648	0.72
MnBS-38	610	649	0.70
MnBS-39	609	649	0.74

Excitation wavelength = 420 nm.

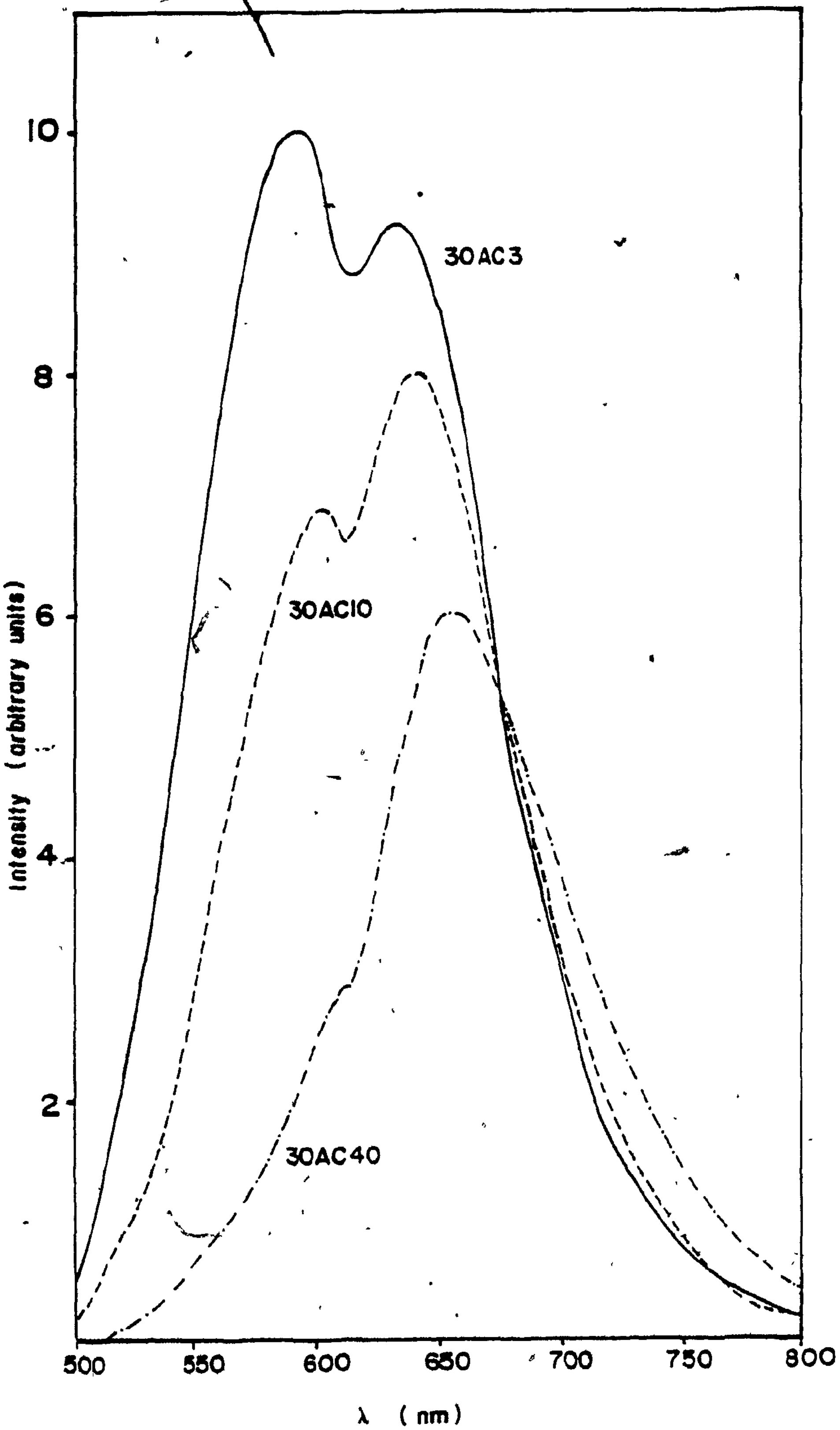

Fig. 43: Emission spectra of glasses of compositions 30AC3, 30AC10 and 30AC40. Excitation wavelength: 420 nm.

Table XIV: Band Positions and Relative Heights (H/L) as a Function of MnO Concentration (Glass Composition 30).

Weight% MnO	H band (nm)	L band (nm)	Relative Height H/L
0.30	593	635	1.08
0.40	595	638	1.03
0.60	598	639	0.96
1.00	603	642	0.85
2.00	608	647	0.69
4.00	610	655	0.48
6.00	613	667	0.32

Excitation wavelength = 420 nm.

reached *ca.* 4 weight%. This is comparable with the dependence of Mn^{2+} luminescence on MnO concentrations (Section 4.1.2). Figure 43 shows the luminescence spectra of glass composition 30 with different concentrations of MnO.

(ii) Glass composition 32

Here also, a change in the band positions as a function of MnO concentration was observed. The H band shifted

Table XV: Band Positions and Relative Heights (H/L) as a Function of MnO Concentration (Glass Composition 32).

Weight% MnO	H band (nm)	L band (nm)	Relative Height H/L
0.30	593	637	1.12
0.40	598	640	1.00
0.60	598	640	0.99
1.00	605	643	0.85
2.00	608	648	0.67
4.00	612	660	0.42
6.00	615	667	0.35

Excitation wavelength = 420 nm.

from 593 nm (0.3 weight% MnO) to 615 nm (6.0 weight% MnO and the L band from 637 nm (0.3 weight% MnO) to 667 nm (6.0 weight% MnO). A nearly complete quenching of the high energy band relative to the low energy one was again observed when MnO observations reached *ca.* 4 weight%. The relative height (H/L) decreased on addition of MnO from 1.12 (0.3 weight% MnO) to 0.35 (6.0 weight% MnO). These results are summarized in Table XV above. Figure 44 shows selected luminescence spectra of glass composition 32 with different doping levels of MnO.

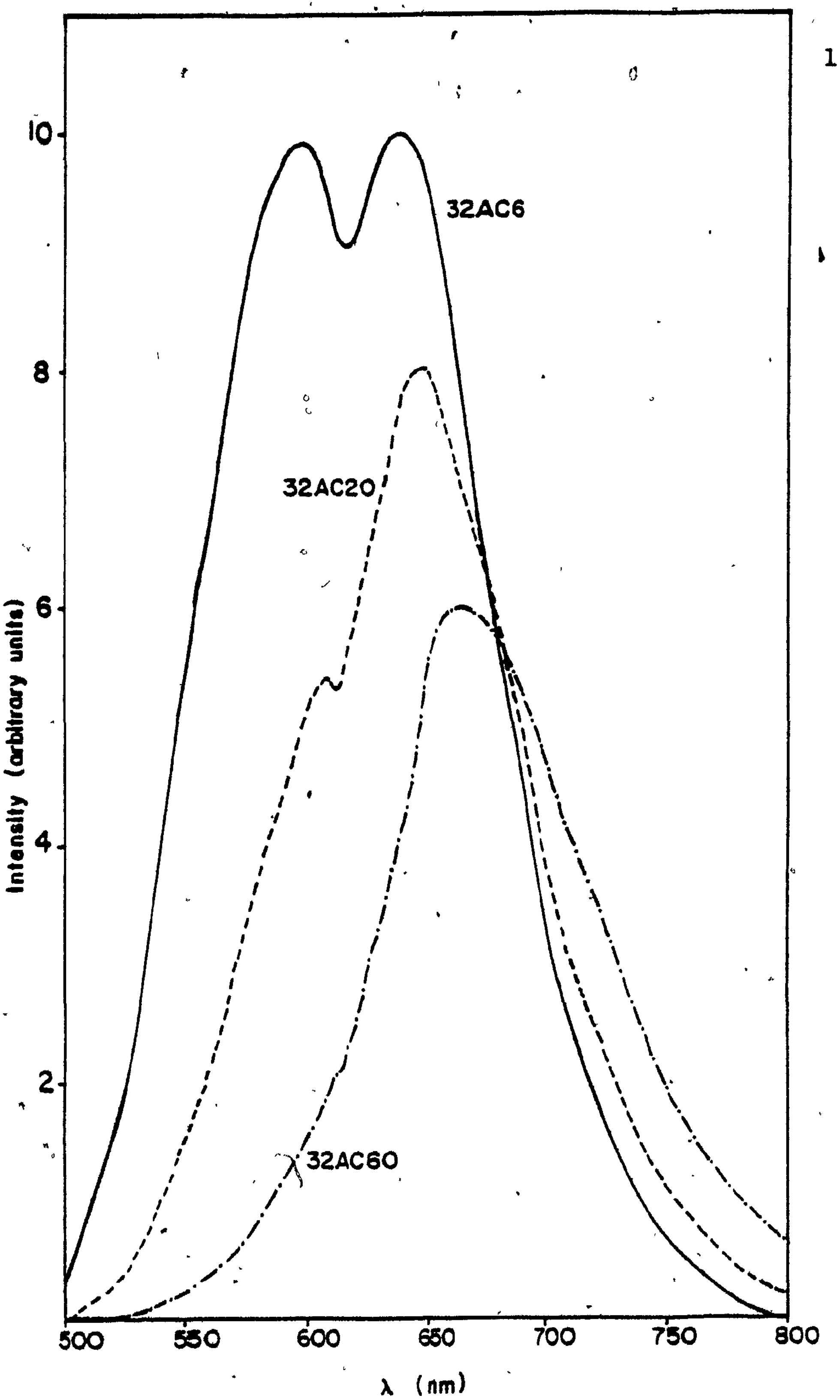

Fig. 44: Emission spectra of glasses of compositions 32AC6, 32AC20 and 32AC60. Excitation wavelength:- 420 nm.

The results also are comparable to those of glass composition 30 with different activator concentrations.

4.3.2.2 Silica-rich end

Glasses of composition 37 and 39 doped with different levels of MnO (0.1 to 1.0 weight%) were excited at 420 nm. Two bands, H and L, were present in all the spectra.

(i) Glass composition 37

The high energy band centred at 595 nm (0.1 weight% MnO) shifted to 612 nm (1.0 weight% MnO) and the low energy band shifted from 638 nm (0.1 weight% MnO) to 653 nm (1.0 weight% MnO). The relative height (H/L) decreased from 1.05 (0.1 weight% MnO) to 0.51 (1.0 weight% MnO). The results are summarized in Table XVI. At a concentration of 1.0 weight% MnO the intensity of the high energy band decreased considerably compared to that of the low energy band. Figure 45 shows selected luminescence spectra of glass composition 37 doped with different levels of MnO.

(ii) Glass composition 39

For the same doping levels, the changes in the luminescent characteristics of glass composition 39 were small

Table XVI: Band Positions and Relative Heights (H/L) as a Function of MnO Concentration (Glass Composition 37).

Weight% MnO	H band (nm)	L band (nm)	Relative Height H/L
0.10	595	638	1.05
0.20	600	641	0.95
0.40	608	646	0.74
0.60	608	646	0.72
0.80	610	651	0.61
1.00	612	653	0.51

Excitation wavelength = 420 nm.

when compared to those of glass composition 37. The H band shifted from 601 nm (0.2 weight% MnO) to 608 nm (0.8 weight% MnO) and the L band from 641 nm (0.2 weight% MnO) to 648 nm (0.8 weight% MnO). The relative height (H/L) of the two bands decreased slightly from 0.88 (0.2 weight% MnO) to 0.75 (0.8 weight% MnO). These results are summarized in Table XVII. Figure 46 shows the luminescence spectra of two glasses of composition 39 doped respectively with 0.2 and 0.8 weight% MnO.

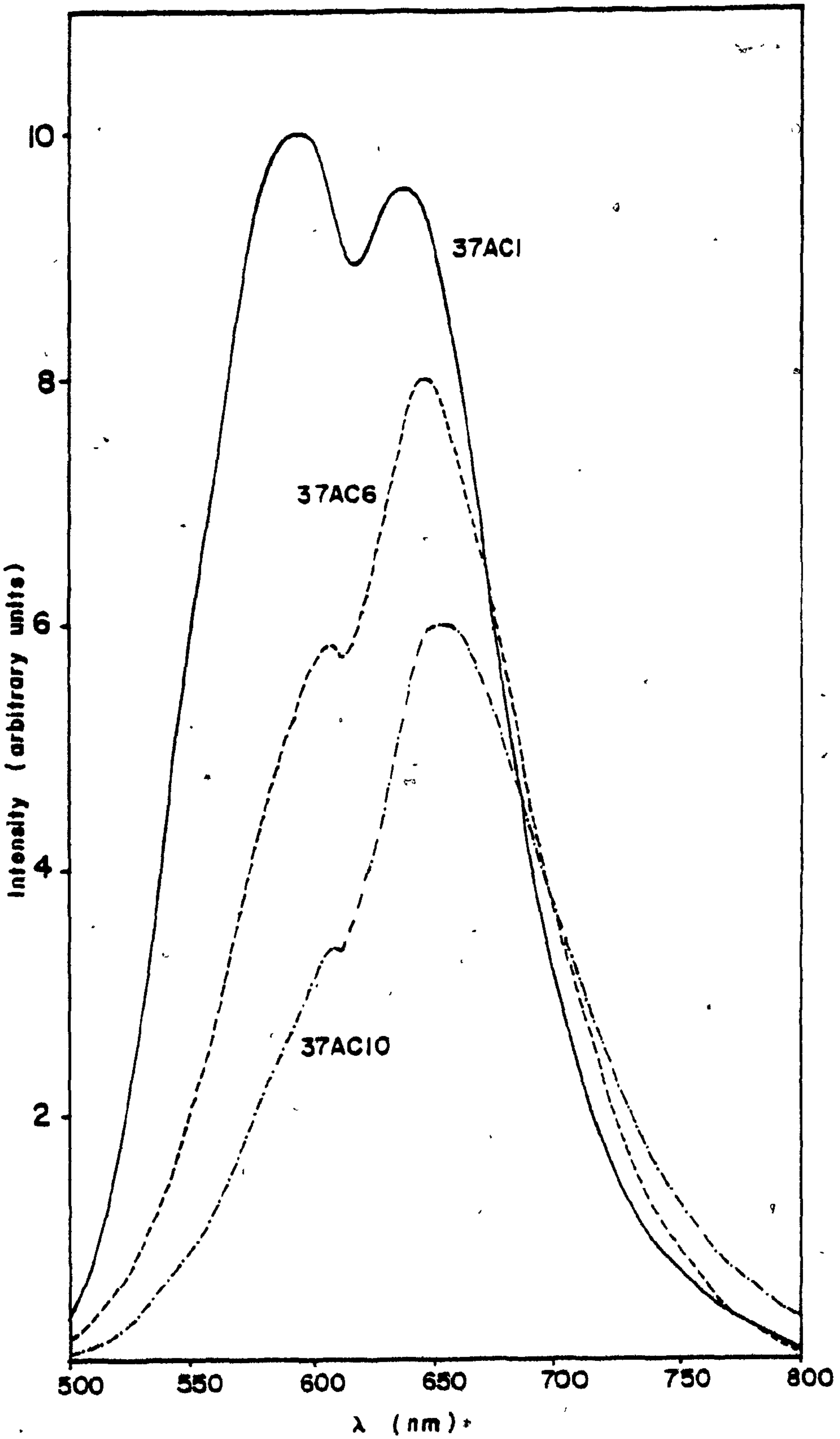

Fig. 45: Emission spectra of glasses of compositions 37ACl, 37AC6 and 37AC10. Excitation wavelength: 420 nm.

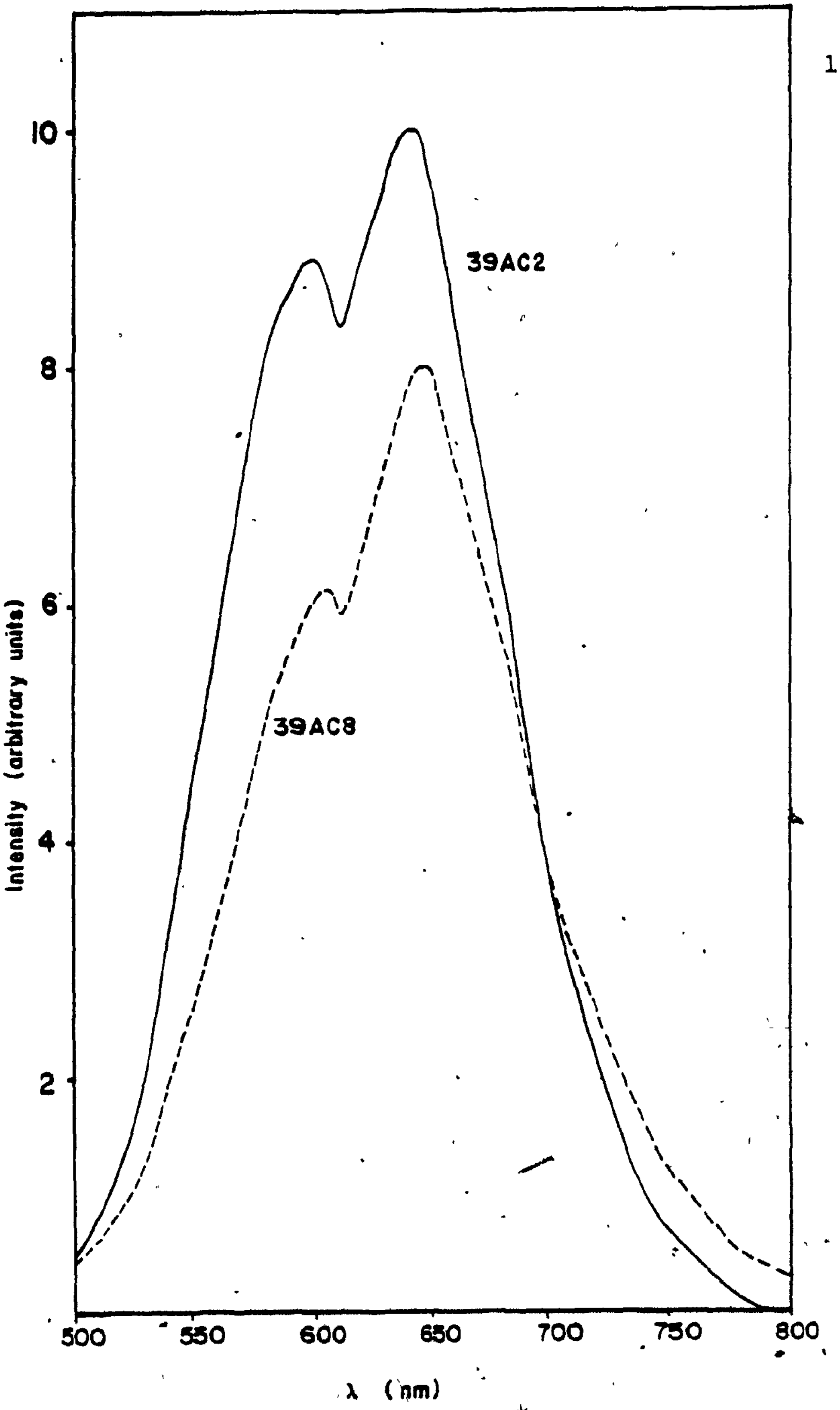

Fig. 46: Emission spectra of glasses of compositions 39AC2 and 39AC8. Excitation wavelength: 420 nm.

Table XVII: Band Positions and Relative Heights (H/L) as a Function of MnO Concentration (Glass Composition 39).

Weight% MnO	H band (nm)	L band (nm)	Relative Height H/L
0.20	601	641	0.88
0.40	608	648	0.76
0.60	608	648	0.76
0.80	608	648	0.75

Excitation wavelength = 420 nm.

4.3.3 Heated Samples at the Silica-Rich End of the Tie-Line

Glasses of composition 37 doped with various levels of MnO (Table IX) were phase separated by heating for 4 h at 690°C. They were then excited at 420 nm. Two bands (H and L) were present. As the concentration of MnO increased (from 0.1 to 1.0 weight%), the H band shifted from 595 to 612 nm, and the relative height (H/L) decreased from 1.04 to 0.50. These results are listed in Table XVIII. Figure 47 shows the luminescence spectra of phase-separated glass composition 37 with different concentrations of MnO.

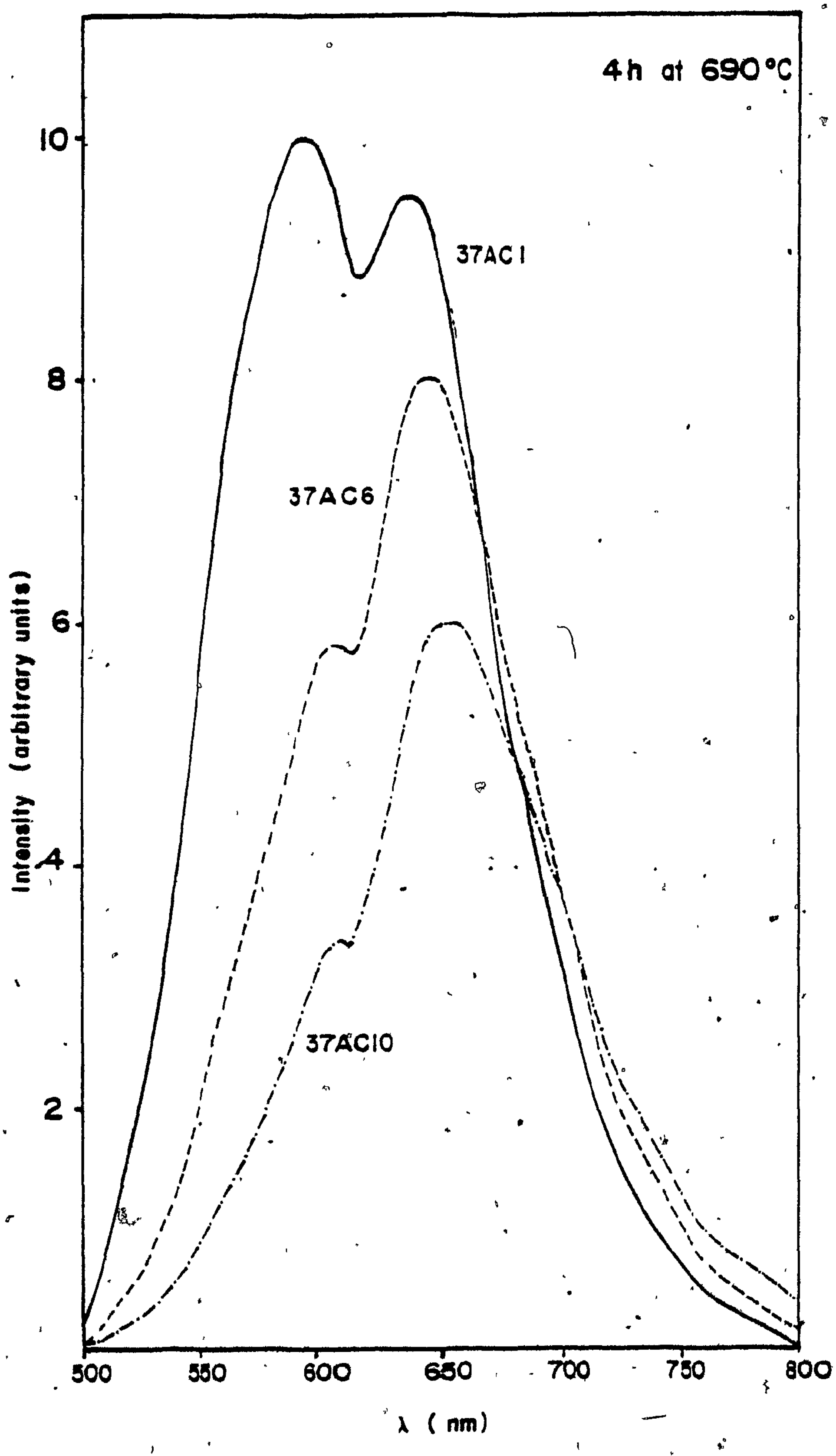

Fig. 47: Emission spectra of heat-treated glasses of compositions 37AC1, 37AC6 and 37AC10. Excitation wavelength: 420 nm.

Table XVIII: Band Positions and Relative Heights (H/L) as a Function of MnO Concentration (Glass Composition 37 Phase-Separated by Heating for 4 h at 690°C).

Weight% MnO	H band (nm)	L band (nm)	Relative Height H/L
0.10	595	638	1.04
0.20	600	641	0.96
0.40	608	646	0.75
0.60	608	646	0.70
0.80	610	651	0.63
1.00	612	653	0.50

Excitation wavelength = 420 nm.

4.3.4 Comparison and Discussion

Previous discussions (Sections 4.1 and 4.2) led to the conclusions that the Mn^{2+} luminescence spectrum was sensitive to MnO concentrations (Section 4.1.2) that, upon phase separation, manganese(II) was preferentially partitioned into the boron-rich phase (Section 4.2.3.1) leading to an effective increase in the MnO concentration within this phase (Section 4.2.1). Thus, if a glass of composition 37 doped with MnO is phase-separated, the MnO concentration will be increased and its luminescence spectrum must be altered as compared to the spectrum prior to heat-treatment. This was not found to be the case. A comparison between the unheated glasses of composition 37 (0.1 to 1.0 weight% MnO) and the heated ones did not show any difference in their respective luminescent characteristics (compare Table XVIII and Table XVI, and Figure 47 and Figure 45). This constancy in the characteristics of the luminescence upon heat-treatment, of glass composition 37, suggests that the glass was already phase-separated when it was first formed. In that case, a correlation satisfying the lever rule ought to exist between the luminescent characteristics of a given sample (with low doping levels of MnO) on the tie-line and that of glass composition 30 (with higher doping levels of MnO) as discussed in Section 4.2.1.

If one takes the length of the tie-line as extending from glass composition 30 to glass composition 39†, then the effective concentration of MnO in glass composition 37 has to be increased by a factor of about 4.5 (Section 4.2.1). Thus, the luminescent characteristics of a glass of composition 37 doped with 0.1, 0.2, 0.6 and 1.0 weight% MnO ought to correspond to, respectively, those of glasses of composition 30 doped with 0.4, 1.0, 2.0 and 4.0 weight% MnO. This is indeed the case (compare Tables XIV and XVI). Figure 48 shows

---

†A reasonable assumption, since on addition of MnO the miscibility gap widens (Section 4.2.3.1).

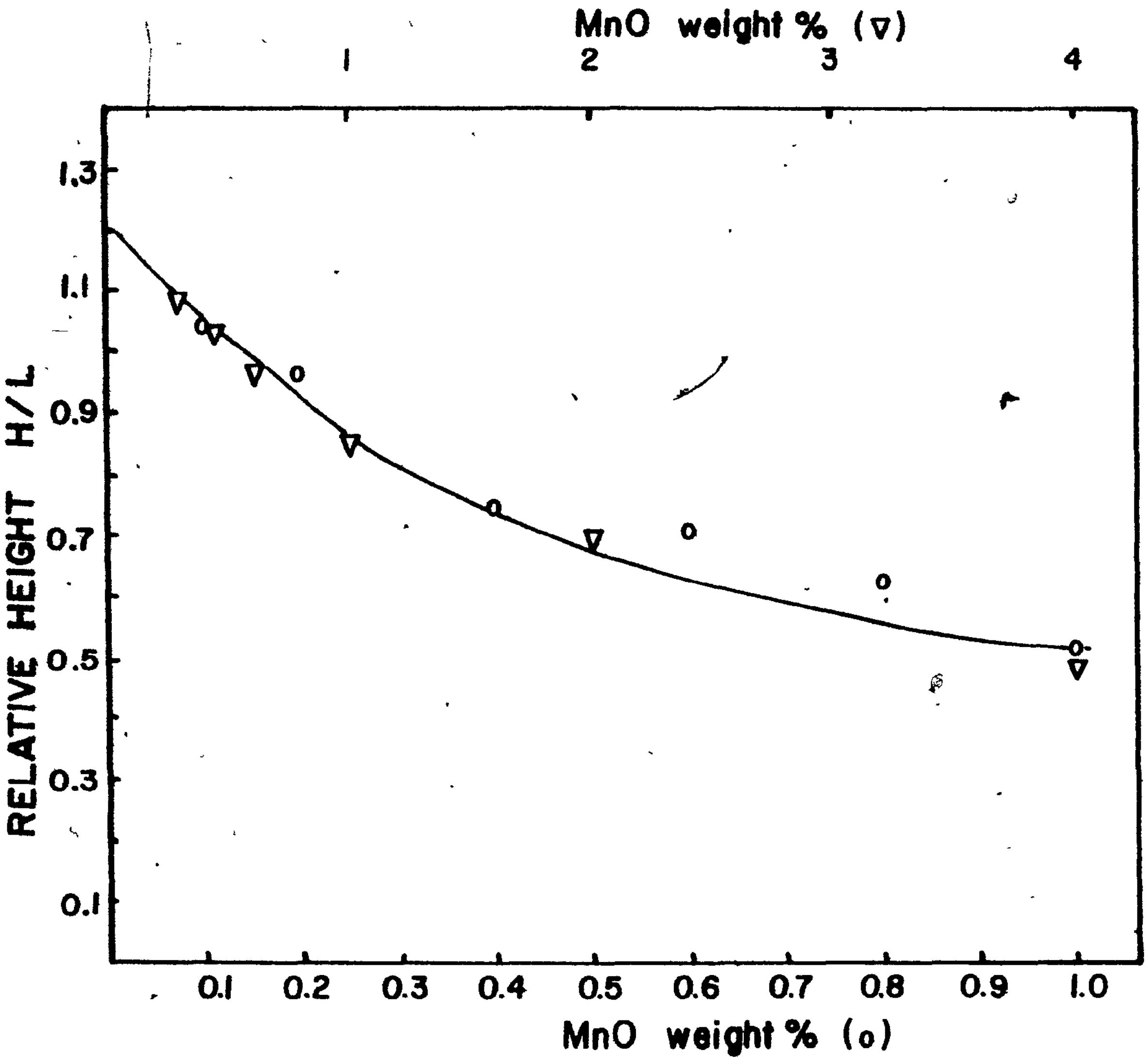

Fig. 48: Relative heights (H/L) as a function of MnO concentration for glasses of composition 30 (upper scale) and composition 37 (lower scale).

the dependence of H/L on MnO concentrations for glasses of compositions 30 and 37. MnO concentration scales were chosen in such a way that 4.0 weight% MnO in glass composition 30 match 1.0 weight% MnO in glass composition 37. The correspondence between the set of data of Fig. 48 is striking. The same should be true for any given glass composition on the tie-line. The concentration factor for glass composition 38 as given by its position on the tie-line is about 6. Thus, the luminescent characteristics of glass composition 38 with 0.4 weight% MnO ought to be comparable with those of glass composition 30 with 2.0 weight% MnO. Again, this is found to be the case (compare line 9 of Table XII with line 5 of Table XIV). The concentration factor for glass 35 as given by its position on the tie-line is about 2.33 implying a correspondence of the luminescent characteristics of glass composition 35 with 0.4 weight percent MnO and those of glass composition 30 with 1.0 weight% MnO. The similarity again is evident (compare line 6 of Table XII with line 4 of Table XIV). The concentration factors of glasses lying in the vicinity of the boron-rich end of the tie-line is low, only about 1.17 for glass composition 32. This explains the very small changes observed in their respective luminescent characteristics (compare Table XIV and Table XV).

The important conclusion to be drawn from the preceding discussion is that inside the miscibility gap, sodium borosilicate glasses are phase separated from the start (*i.e.* when the glass is first formed). This phase separation which is on a sub-microscopic scale, probably occurs during the quenching of the melt to room temperature. The melting temperatures of 1200°C or more lie far above the two-liquid region, but during quenching these glasses probably spend a few seconds cooling between the critical miscibility temperature, T_c, and the glass transition temperatures, T_g. No further molecular rearrangement is expected to occur below T_g. It is during this quenching time ($\sim$ 2 s) that phase separation occurs. The possibility of preparing a non-phase separated glass (inside the miscibility gap) can not be ruled out if faster quenching times can be achieved or by using other preparation methods such as vapor deposition on a cold substrate or dehydration. Nonetheless, in our case phase separation probably occurs during the quenching of the melt at room temperature, which strongly suggests a spinodal decomposition mechanism. Although no rigorous proof for this mechanism can be inferred from the above, the rapidity by which phase separation would have to occur does not favour nucleation and growth of second phase particles (where the kinetics of phase separation are slow - see Chapter 2).

4.4 LUMINESCENT DECAY ANALYSIS

4.4.1 Introduction

Non-exponential luminescent decay of Mn^{2+} in glasses has been reported[31,40,158] ranging from 1 to 24 ms, depending on the glass composition and on the activator concentration. For a given sample, Mn^{2+} luminescent decay was found to decrease with increasing activator concentrations. This is reasonable in terms of concentration quenching especially when one considers the likelihood of exchange and superexchange interactions occurring between Mn^{2+} ions, which would relax the spin selection rule.

It was shown earlier that sodium borosilicate glasses, inside the miscibility gap, were phase separated as prepared (Section 4.3) and that Mn^{2+} was preferentially partitioned (almost entirely) in the boron-rich phase (Section 4.2.5.1) leading to an effective increase of MnO concentrations within this phase. Manganese(II) luminescent decay, which is sensitive to MnO concentrations, may therefore be used as further evidence that the activator partitions into the boron-rich phase.

4.4.2 Dependence of the Luminescent Decay on the Activator Concentration

Glasses having the consolute composition and doped with different levels of MnO (0.18, 0.89, 1.78 and 5.33 weight%) were excited with a pulsed nitrogen laser

(λ = 337.1 nm) as described in Section 3.4.3.2. The high energy band was observed at 550 nm and the low energy band at 650 nm (the luminescence characteristics of these samples were described in Table IV and Fig. 26). Calculations were carried out following the scheme described in Section 2.6.6.2. An estimation of the relative error on the measurements was calculated from: $t(S/\sqrt{n})/\bar{X}$, where t is the student t-test value, S is the standard deviation, n is the number of measurements and $\bar{X}$ is the mean value of the measurements. Five decay parameters ($\bar{t}$) were computed[†] from three different[§] glass compositions, The relative error at the 95% confidence level in each case was found to be less than 5%. All the experiments were repeated and the results[¶] were in agreement.

4.4.2.1 Unheated glasses

The decay parameter ($\bar{t}$) of the high energy band decreased from 8.7 ms (0.18 weight% MnO) to 4.4 ms (5.33 weight% MnO). Similarly $\bar{t}$ for the low energy band decreased from 7.9 ms (0.18 weight % MnO) to 3.7 ms (5.33 weight% Mn). The results are summarized in Table XIX. It is clear from

---

[†] Each result must be statistically independent therefore, after each measurement the sample was moved and the experiment was repeated.

[§] Glass compositions 6, 9 and 10 (Table XXI) doped with 0.27 weight% MnO.

[¶] The results presented in this section are from one set of experimental data.

Table XIX: Decay Parameter ($\bar{t}$) as a Function of MnO Concentration (Consolute Composition).

Sample	Weight% MnO	$\bar{t}$ (ms)	
		λ = 550 nm	λ = 650 nm
MnBS-2B	0.18	8.7	7.9
MnBS-2C	0.89	7.3	7.0
MnBS-2D	1.78	5.6	5.3
MnBS-2E	5.33	4.4	3.7

Excitation wavelength: 337.1 nm. Relative error: 5%.

this table that the Mn^{2+} luminescent decay parameter for both bands (H and L) decreases with increasing activator concentrations and that $\bar{t}$ of the L band is slightly shorter than that of the H band. There was no temperature dependence of the decay parameter $\bar{t}$ for sample MnBS-2C down to 8.8°K. For this reason the other samples were not studied at low temperature.

4.4.2.2 Phase-separated glasses

The samples (MnBS-2B to MnBS-2E) were phase-separated by dry thermal treatment in a nitrogen atmosphere (1 h at 750°C). Their respective $\bar{t}$ were equal to those of the unheated samples within experimental error. The decay parameter of the H band decreased from 9.0 ms (0.18 weight% MnO) to 6.1 ms (1.78 weight% MnO)[†] and that the L band from 8.1 ms (0.18 weight% MnO) to 5.8 ms (1.78 weight% Mn). Furthermore, two phase-separated samples (0.18 and 1.78 weight% MnO) were cleared by successive heating (1 h at 851°C and 1/2 h at 850°C). No change in their respective decay parameters, relative to the unheated and/or phase-separated samples, were found. The results are summarized in Table XX.

4.4.3 Dependence of the Luminescent Decay on the Glass Composition

4.4.3.1 Glass composition and luminescence spectra

Five glasses with compositions lying at the extremities of the 750°C, 700°C, 650°C and 600°C isotherms and one glass having the consolute composition (Table XXI and Fig. 49) were doped with 0.27 weight% MnO. They were excited at a wavelength of 420 nm. Two bands (H and L) were present in the emission spectra of these samples. The high energy band centred at 533 nm (glass composition 7) shifted to 635 nm (glass composition 11). The relative height (H/L) decreased from 3.84 (glass composition 7) to 1.29 (glass

---

[†] The sample MnBS-2E (5.33 weight% MnO) was heavily phase-separated. It was not possible to measure its luminescent decay.

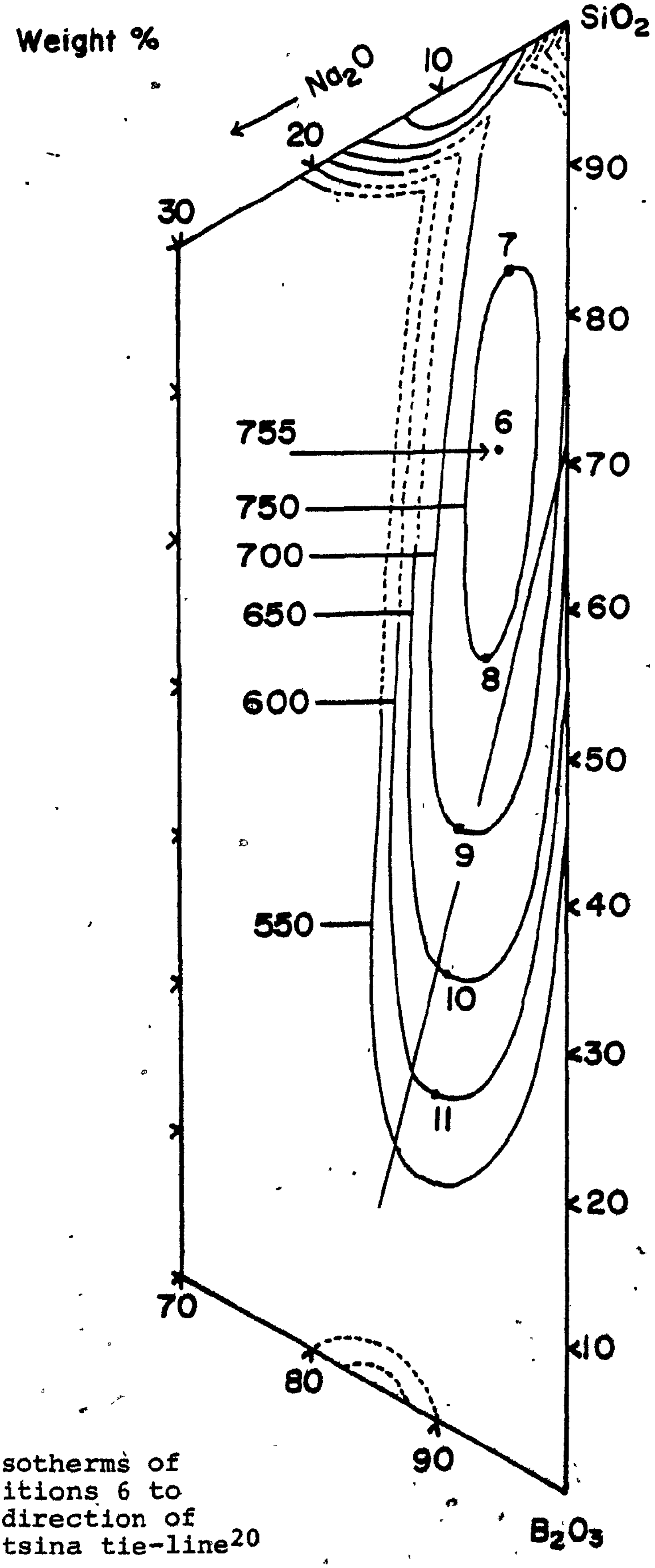

Fig. 49: Position on the isotherms of glasses of compositions 6 to 11. The general direction of Mazurin and Streltsina tie-line[20] is also shown.

Table XX: Decay Parameter ($\bar{t}$) After Heat-Treatment as a Function of MnO Concentration (consolute Composition).

Sample	Weight% MnO	$\bar{t}$ (ms)	
		λ = 550 nm	λ = 650 nm
MnBS-2B, 1h/750°C	0.18	9.0	8.1
MnBS-2C, 1h/750°C	0.89	7.9	7.6
MnBS-2D, 1h/750°C	1.78	6.1	5.8
MnBS-2B, 1h/851°C	0.18	9.1	8.2
MnBS-2D, ½h/850°C	1.78	-	5.6

Excitation wavelength: 337.1 nm. Relative error: 5%.

composition 8) and remained within this range for glasses of composition 9, 10 and 11. The results are summarized in Table XXII. They are consistent with those of Section 4.1.4 and Section 4.3.2 (compare line 3 in Table VI with line 5 in Table XXII and line 1 in Table XV with line 4 in Table XXIII). Figure 50 shows the luminescent spectra of glasses 6, 7 and 8 doped with 0.27 weight% MnO. Different glasses of composition 6 (0.27 weight% MnO) were phase-separated in a nitrogen atmosphere by successive heatings (1 h at 750°C, 18 h at 701°C, 20 h at 650°C and 4 days at 600°C) and excited at 420 nm. Their luminescent spectra were identical to the

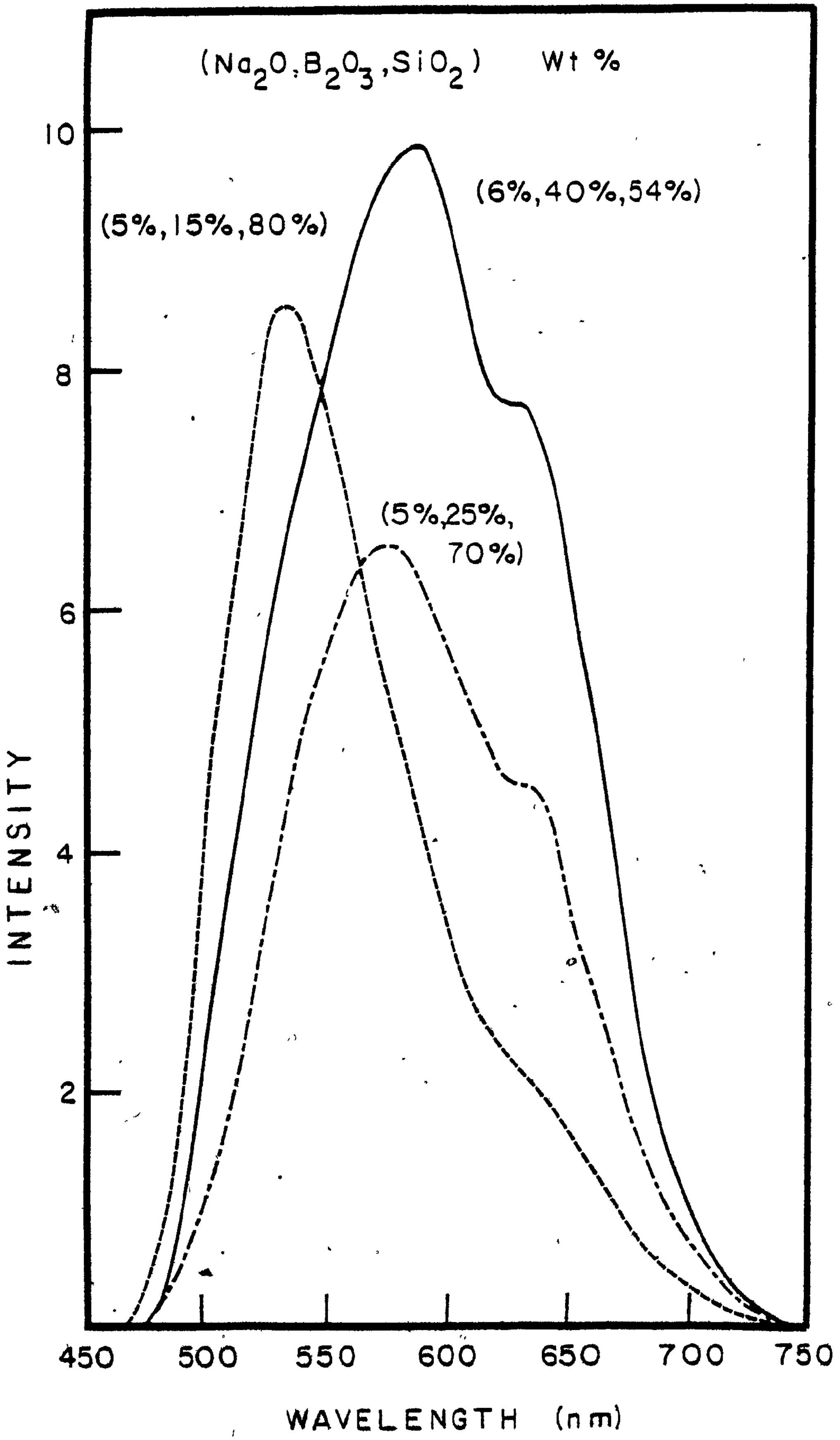

Fig. 50: Emission spectra of glasses of compositions 6, 7 and 8 doped with 0.27 wt% MnO. Excitation wavelength: 420 nm.

Table XXI: Glass Compositions (in weight percent) of the Samples Shown in Figure 49.

Sample	Composition weight%		
	Na_2O	B_2O_3	S_iO_2
MnBS-6	5.38	24.9	69.72
MnBS-7	5.38	14.94	79.68
MnBS-8	6.19	38.92	54.89
MnBS-9	8.18	49.90	41.92
MnBS-10	9.00	60.00	31.00
MnBS-11	9.82	67.13	23.05

The samples MnBS-6 to MnBS-11 have 0.27 weight% MnO which was introduced in the glass as Mn_2O_3.

unheated glasses of composition 6 (0.27 weight% MnO), confirming that the glass was phase separated from the start (Section 4.3).

4.4.3.2 Luminescent decay

Glasses of compositions 6 to 11 (0.27 weight% MnO) were excited with a pulsed nitrogen laser. The high energy band was observed respectively at 550 nm and then at 525 nm (to minimize the contribution of the L band). The low energy

Table XXII: Band Positions and Relative Heights (H/L) as a Function of Glass Composition (0.27 weight% MnO).

Sample	H band (nm)	L band (nm)	Relative Height H/L
MnBS-7	533	628	3.84
MnBS-8	578	629	1.29
MnBS-9	591	633	1.20
MnBS-10	592	635	1.25
MnBS-11	592	635	1.32

Excitation wavelength: 420 nm.

band was observed at 670 nm. The results (Table XXIII) showed that $\bar{t}$ of the H band remained constant within experimental error from glass composition 7 to glass composition 11 and that $\bar{t}$ of the L band increased steadily from 6.0 ms (glass composition 7) to 7.9 ms (glass composition 11). In addition, glasses of composition 6, 7 and 9 were also excited with the nitrogen-pumped dye-laser (λ = 420 nm). The same values of $\bar{t}$ (Table XXIV) were obtained with the 420 nm excitation (within error) as with the 337.1 nm excitation[†] implying that both emission bands arise from the same level probably ($^4T_1$). Finally, the

---

[†] It was easier to excite with the N_2 laser since the optics alignment of the dye-laser were tedious.

Table XXIII: Decay Parameters ($\bar{t}$) as a Function of Glass Composition (Compositions 6 to 11 Doped with 0.27 Weight% MnO).

Sample	$\bar{t}$ (ms)		
	λ = 525 nm	λ = 550 nm	λ = 670 nm
MnBS-7	7.9	7.7	6.0
MnBS-6	8.1	7.4	6.4
MnBS-8	8.0	7.6	6.7
MnBS-9	7.9	7.6	7.3
MnBS-10	7.8	7.3	7.8
MnBS-11	7.5	7.1	7.9

Excitation wavelength: 337.1 nm. Relative error: 5%.

luminescent decay parameter of the phase-separated glasses of composition 6 (Section 4.4.3.1) were examined. The results showed that $\bar{t}$ was unaffected by the temperature/ duration of heat-treatment (Table XXV). Moreover, $\bar{t}$ of the heated samples was within experimental error of that of the unheated glass of composition 6.

4.4.4 Conclusions

Manganese(II) luminescent decay in sodium borosilicate

Table XXIV: Decay Parameter ($\bar{t}$) of Glasses 6, 7 and 9 (0.27 Weight% MnO).

Sample	$\bar{t}$ (ms)	
	λ = 550 nm	λ = 670 nm
MnBS-7	-	6.5
MnBS-6	8.1	6.8
MnBS-9	8.1	-

Excitation wavelength: 420 nm. Relative error: 5%.

Table XXV: Decay Parameter $\bar{t}$ as a Function of Temperature/ Duration of Heat Treatment (Consolute Composition Doped with 0.27 Weight% MnO).

Consolute Composition MnBS-6	$\bar{t}$ (ms)	
	λ = 550 nm	λ - 670 nm
1 h at 750°C	8.1	-
18 h at 701°C	7.8	6.7
20 h at 750°C	7.8	-
4 days at 600°C	8.0	7.0

Excitation wavelength: 337.1 nm. Relative error: 5%.

glasses, for both bands (H and L), decreased with increasing MnO concentrations (Section 4.4.2). Inside the miscibility gap these glasses were found to be phase separated from the start (Section 4.3.4), a result which was further confirmed by the fact that $\bar{t}$ of the consolute composition (with different doping levels of MnO) did not change with heat treatment (Sections 4.4.2.2. and 4.4.3.2). Although these glasses (composition 6, 7, 8, 9, 10 and 11) are not all on the same tie-line, every glass composition within the miscibility gap must lie on some tie-line. If one considers that phase separation occurs during quenching from the melt and is completed when the glass transition temperature is reached (< 500°C depending on the glass composition), then the tie-lines will join compositions at extremities of the 550°C isotherm (the closest one to T_g). From the previous study the general direction of the tie-lines as determined by Mazurin and Streltsina[20] were found to be consistent with the morphological study of glasses 30 to 39. They are used here for glasses of composition 6, 7, 8, 9, 10 and 11. For dilute ideal solutions at equilibrium (at constant T and P), the ratio of concentration of a component partitioned between two immiscible phases is constant and is given by the Nernst distribution law†. This can be expressed as:

---

†No precipitation was observed in the micrographs of the Mn-doped glasses studied, so it is safe to assume that neither phase is saturated with MnO. Note that this was not the case for the Cr-doped glasses in which precipitation was clearly detected by SEM and EDAX (*cf*. Section 4.2.5.2). Naturally the application of this law to phase separated glasses is only as valid as the solutions are ideal.

$$\frac{C_B}{C_{Si}} = k$$

where k is the Nernst partition coefficient, C_B the MnO concentration in the B-rich phase and C_{Si} that in the Si-rich phase. It can be shown (Appendix) that for large values of k, C_{Si} and C_B are determined by:

$$C_{Si} \cong \frac{X}{kV_B} \qquad C_B \cong \frac{X}{V_B}$$

where X is the total number of moles added to the glass, V_B is the volume of the B-rich phase. Assuming that the Nernst distribution law holds for the glasses studied then any increase in the effective concentration of MnO in one of the phases on going from one end of the tie-line to the other end must be accompanied by a corresponding increase in the effective concentration of MnO in the other phase. Since most of the manganese concentrates in the B-rich phase concentration factors determined from the tie-line by the lever rule were calculated with respect to that phase. Table XXVI summarizes the approximate composition at the Si-rich and B-rich ends of each tie-line as well as the concentration factors and the effective concentration of MnO in the B-rich phase. Note that as mentioned earlier (footnote in Section 4.2.1) the phases denoted "Si-rich" and "B-rich" are those showing greater and lesser resistance, respectively, to the etching in water or dilute HF.

The parameter $\bar{t}$ of the L band decreased steadily from glass composition 11 to glass composition 7 (Table XXIII) reflecting an increase of the effective MnO concentration in one of the phases. Since most of the manganese concentrates in the B-rich phase and within this phase, the effective MnO concentration increases from 0.35 wt% (glass composition 11) to 1.20 wt% (glass composition 7), we may conclude that the L band arises predominantly from Mn^{2+} ions in the B-rich phase.

The analysis of the data of $\bar{t}$ of the H band is rather complex. If the H band arose from the sizeable amount of silica present in the B-rich phase (Table XXVI) then the effective increase of MnO concentration within the B-rich phase should affect $\bar{t}$ of the H band and a decrease in $\bar{t}$ would be expected on going from glass composition 11 to glass composition 7. This was not found to be the case, the decay parameter $\bar{t}$ of the H band being essentially constant for the glasses studied. If on the other hand the H band arises from the very small quantities of Mn^{2+} in the Si-rich phase, the effective increase in the MnO concentration within this phase would still result in rather low levels of MnO. At sufficiently low concentrations (0.1-0.2 wt% MnO), the change in $\bar{t}$ should be less than the experimental error. This case is illustrated in Fig. 51 where $\bar{t}$ is plotted *versus* MnO concentrations (for the consolute composition) the parameter

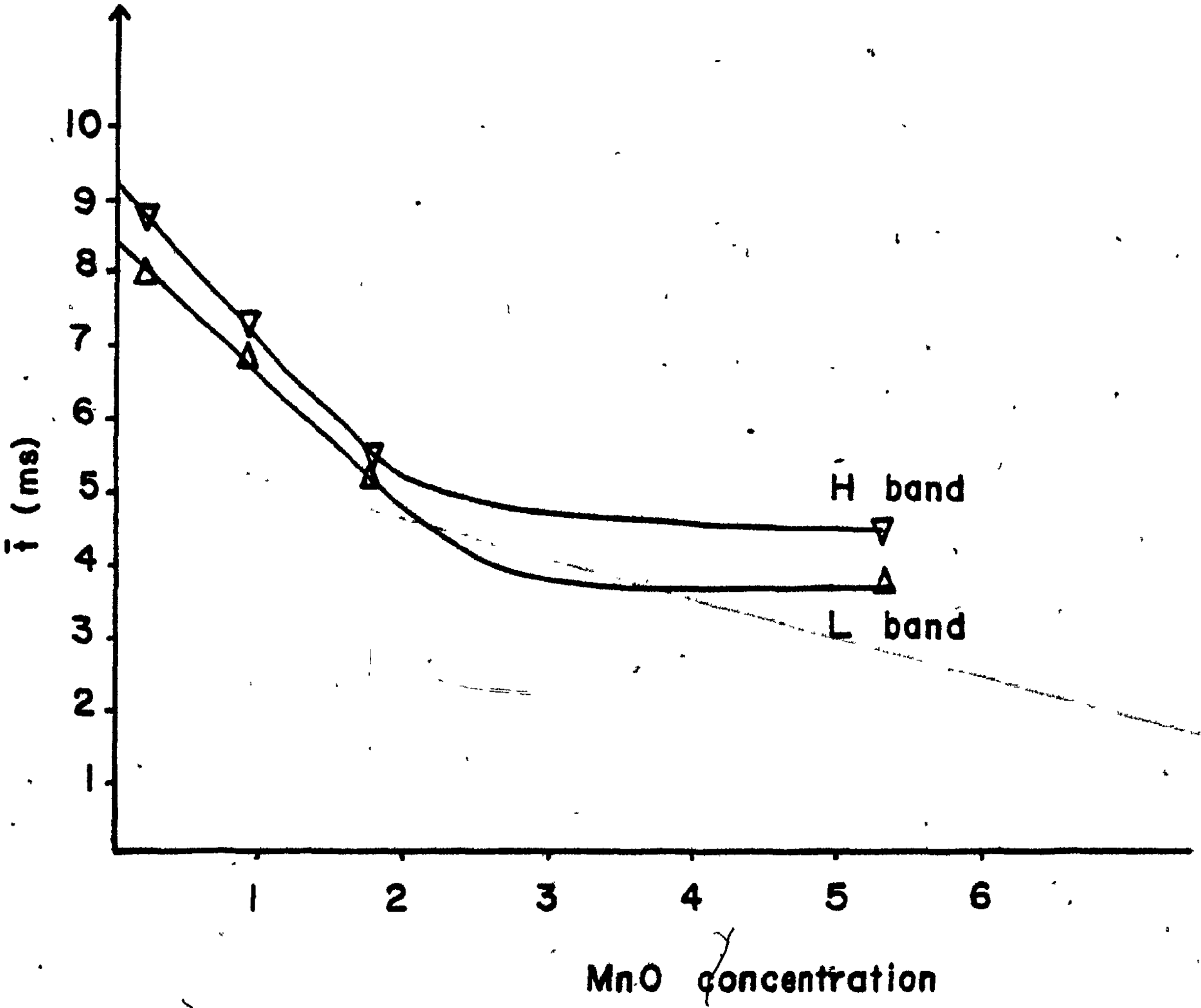

Fig. 51: Variation of $\bar{t}$ as a function of MnO concentrations.

Table XXVI: Approximate Compositions at the Si-rich and B-Rich End of the Tie-Lines Passing Through Glasses 6, 7, 8, 9, 10 and 11 (MnO = 0.27 wt%). The Concentration Factors and the Effective Concentrations of MnO in the B-Rich Phase are also Shown.

Sample	Si-rich (wt%)			B-rich (wt%)			Concentration factor	Effective MnO concentration in the B-rich phase (wt%)
	SiO_2	B_2O_3	Na_2O	B_2O_3	SiO_2	Na_2O		
MnBS-7	94	5	<1	40	45	15	4	1.20
MnBS-6	86	13	<1	54	33	13	3	0.9
MnBS-8	76	23	<1	60	24	16	2.5	0.75
MnBS-9	70	28	≅2	70	19	11	1.6	0.48
MnBS-10	70	28	≅2	70	19	11	1.35	0.41
MnBS-11	58	41	<1	72	16	12	1.15	0.35

The effective MnO concentration was calculated on the basis that all Mn is concentrating into the B-rich phase.

$\bar{t}$ changes from ≅ 9.1 ms extrapolated to 0 wt% MnO to 8.7 ms at 0.18 wt% MnO (9.1 ms and 8.7 ms are within experimental error). These considerations indicate that the H band arises predominantly from the small amounts of Mn^{2+} in the silica-rich phase.

We cannot exclude the possible presence of small quantities of Mn^{2+} which may be associated with both the Si in the B-rich phase or with B in the Si-rich phase. However, from the decay parameter ($\bar{t}$) data it appears that the L band arises predominantly from Mn^{2+} ions in the B-rich phase (which is also Na-rich) while the H band is primarily due to Mn^{2+} ions in the Si-rich phase (which is also Na-poor).

4.5 MANGANESE(II) IN SODIUM BOROSILICATE GLASSES

4.5.1 Excitation Spectra

The previous discussion led to the conclusion that the H band emission comes from Mn^{2+} in the silica-rich phase while the L band is associated with Mn^{2+} in the boron-rich phase. The excitation spectra of divalent manganese in each phase may thus be obtained separately by monitoring each of the emission bands. Two samples were selected for this purpose. The first one (glass composition 25, Table V) with the high energy band centred at 553 nm and a relative height (H/L) of 1.77 [*i.e.* the luminescent intensity of the L band is small compared to that of the H band (Fig. 29)]. The

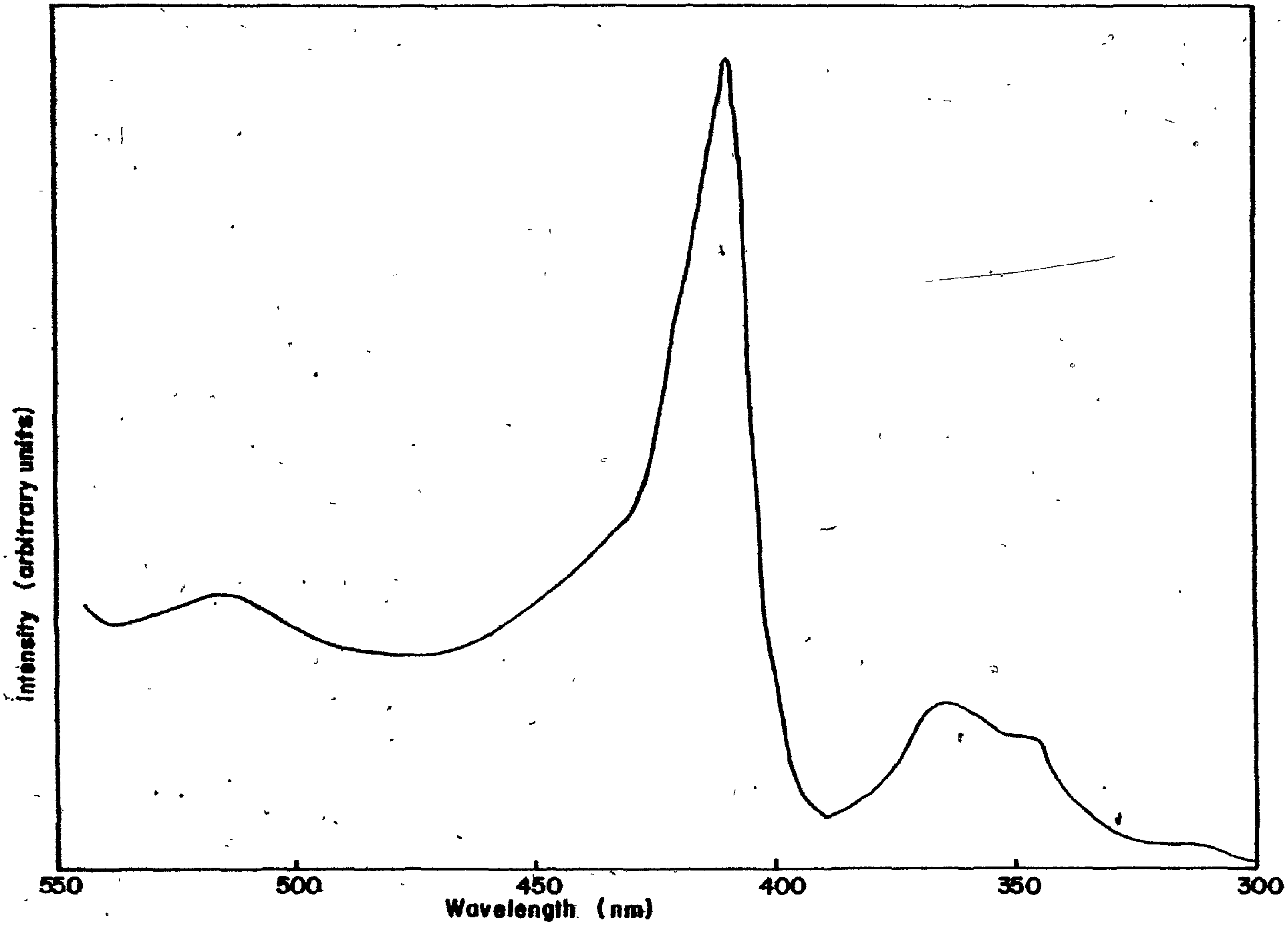

Fig: 52: Excitation spectrum of glass of composition 32AC60. Observation wavelenth: 650 nm.

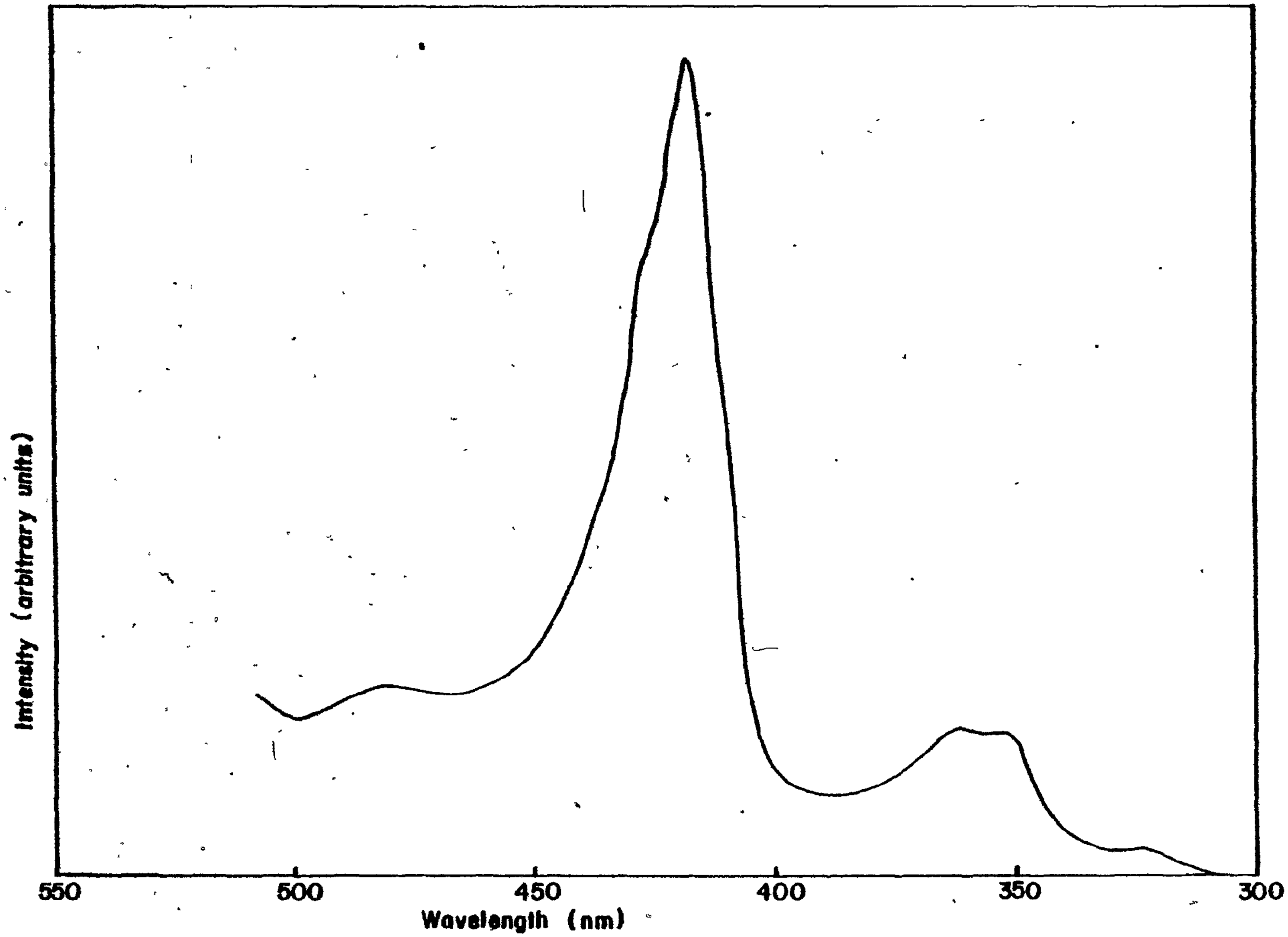

Fig. 53: Excitation spectrum of glass of composition 25 doped with 0.27 wt% MnO. Observation wavelength: 550 nm.

second sample (glass composition 32 AC60, Table XVIII) with the low energy band centred at 667 nm and a relative height (H/L) of 0.35 [H band intensity much weaker than that of the L band (Fig. 44)]. It was thus possible to monitor the luminescence of Mn^{2+} in each of the two phases separately without any significant contribution from the emission of Mn^{2+} in the other. The excitation spectra obtained in this way are representative of Mn^{2+} centres in either a silica-rich or a boron-rich environment.

The excitation spectrum of glass composition 25 was observed at 550 nm (Fig. 52) and that of glass composition 32AC60 at 650 nm (Fig. 53). Six bands were present in each spectrum, and these results are summarized in Table XXVII.

4.5.2 Energy Level Diagrams

The Racah parameters (B and C) and the energy level diagrams were derived following the scheme described earlier (Section 2.6.5).

4.5.2.1 $\lambda_{obs} = 550$ nm

The excitation band at 28 329 cm^{-1} can be assigned to the $^6A_1(S) \rightarrow {}^4E(D)$ transition and that at 23 923 cm^{-1} to the $^6A_1(S) \rightarrow {}^4E(G)$ transition (Section 2.6.5). This results in a value of $B = 629.4$ cm^{-1} and $C = 3525.8$ cm^{-1}. The ratio of C/B is found to be 5.6. The calculated energy levels as a function of Δ/B for C/B = 5.6 are shown in Fig. 54. The observed excitation energies fit this energy level diagram best for the value $\Delta/B = 6.25$ corresponding to $\Delta = 3934\ \mathrm{cm}^{-1}$.

4.5.2.2 $\lambda_{obs} = 650$ nm

The excitation bands at 28 818 cm^{-1} and 24 390 cm^{-1} can be identified as the ${}^6A_1(S) \rightarrow {}^4E(D)$ and ${}^6A_1(S) \rightarrow {}^4E(G)$ transitions, respectively (Section 2.6.5). The Racah parameters B and C obtained from this assignment are $B = 632.6\ \mathrm{cm}^{-1}$ and $C = 3612.8\ \mathrm{cm}^{-1}$. Thus the ratio of C/B is 5.71. The calculated energy levels as a function of Δ/B for C/B = 5.71 are shown in Fig. 55. Here, the excitation energies were best fit for $\Delta/B = 10$, corresponding to a value of $\Delta = 6326\ \mathrm{cm}^{-1}$. All of these assignments are summarized in Table XXVII.

4.5.3 Conclusions

The foregoing results show that the Mn^{2+} ions in the silica-rich phase experience a different crystal field than do those in the boron-rich phase. It is interesting to compare the results obtained above with those of Bingham and Parke[154] on the absorption spectra of Mn^{2+} in sodium borate and sodium silicate glasses. By comparison of the

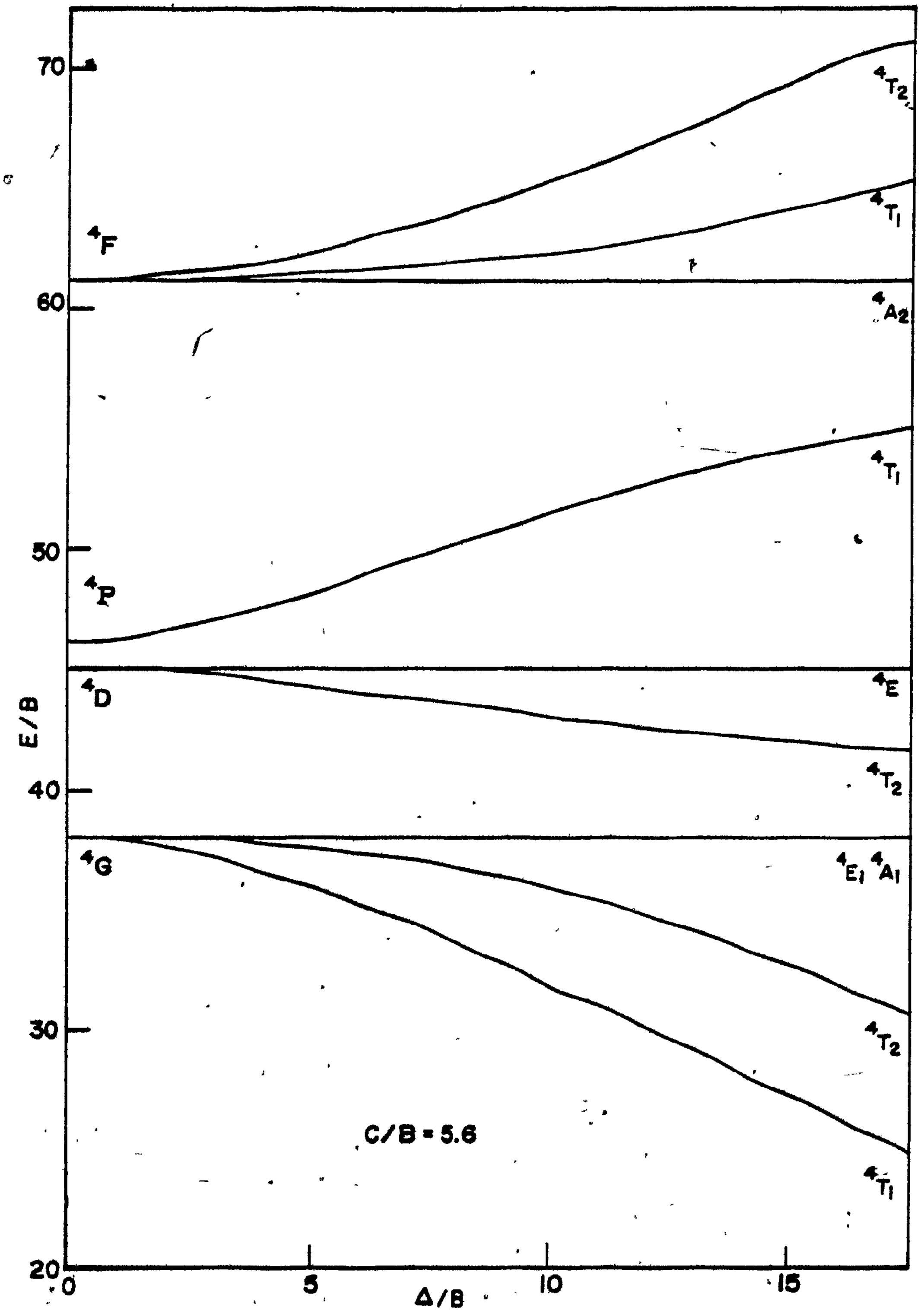

Fig. 54: Energy level diagram of Mn^{2+} in glass of composition 25 doped with 0.27 wt% MnO.

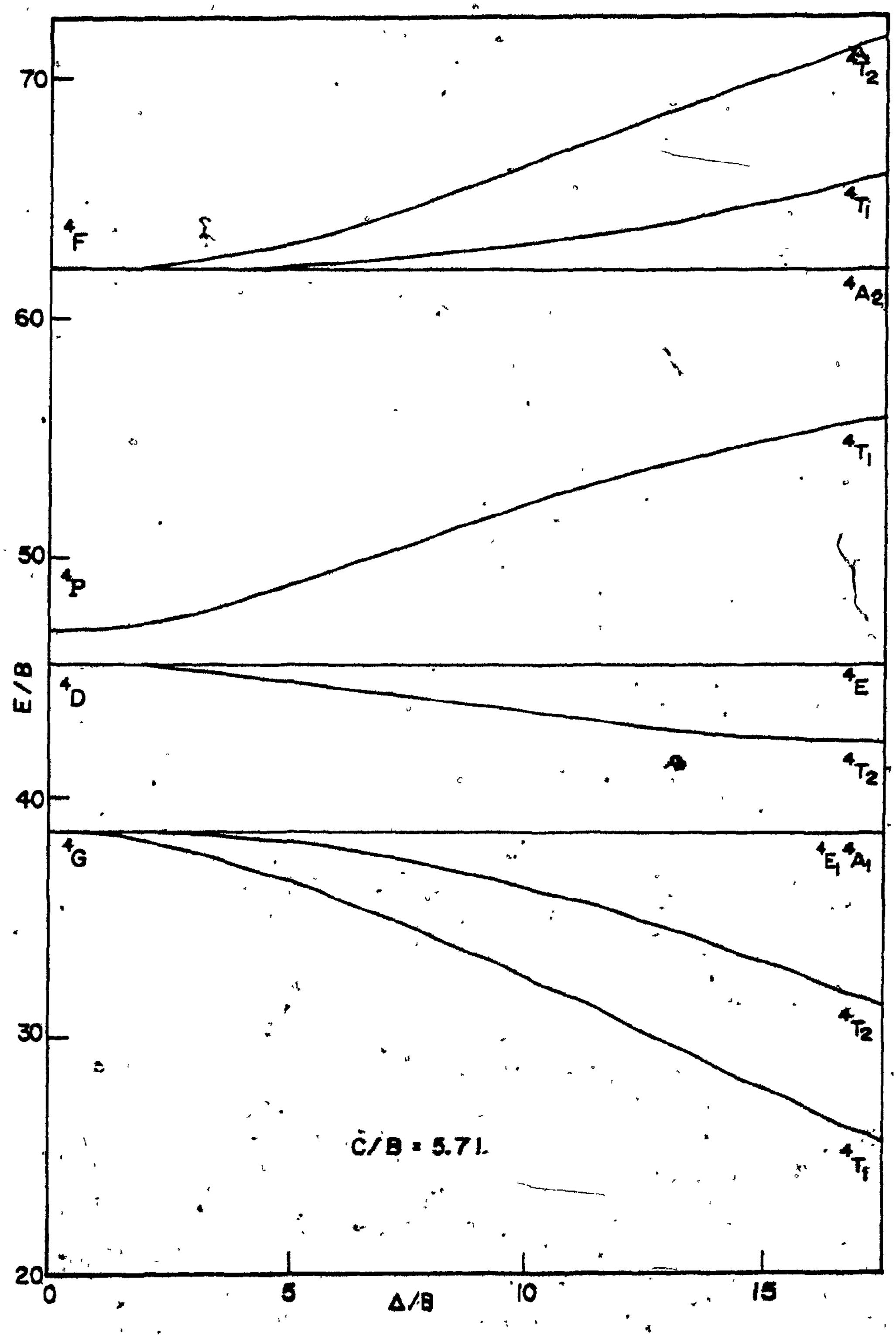

<u>Fig. 55</u>: Energy level diagram of Mn^{2+} in glass of composition 32AC60.

Table XXVII: Assignments of the Excitation Bands. The Excitation Transitions are in (nm) and in cm^{-1}.

	$^4T_1(P)$	$^4E(D)$	$^4T_2(D)$	$^4A_1$, $^4E(G)$	$^4T_2(G)$	$^4T_1(G)$
MnBS-25 λ_{obs} = 550 nm	(324) 30864	(353) 28329	(362) 27624	(418) 23923	(427) 23419	(480) 22026
MnBS-32AC60 λ_{obs} = 650 nm	(310) 32258	(347) 28818	(364) 27473	(410) 24390	(436) 22936	(513) 19493

crystal field strength (Δ) obtained for their glasses with those of Mn^{2+} in crystals and solutions, they concluded that Mn^{2+} ions in sodium silicate glasses were in tetrahedral sites while in sodium borate glasses the coordination was octahedral. Our value of Δ in the Si-rich phase ($\Delta = 3934\ cm^{-1}$) is quite comparable with that of Bingham and Parke for the sodium silicate glass ($\Delta = 4100\ cm^{-1}$) and that of the B-rich phase ($\Delta = 6326\ cm^{-1}$) with that of the sodium borate glass ($\Delta = 6800\ cm^{-1}$). Moreover, the crystal field strength Δ found for the Si-rich phase differs from that found for the B-rich phase by a factor of 5.6/9; just a little larger than the 4/9 factor relating tetrahedral and octahedral crystal fields: $\Delta_t = 4/9\ \Delta_o$. It is quite understandable for the experimental factor to be larger than the theoretical one (5.6/9 as compared to 4/9) when one considers that the factor of 4/9 results from the assumption that equal point charges are located at equal distances from the central ion in either an octahedron or a tetrahedron. In fact the surrounding oxygen ions are expected to be at a greater distance from the Mn^{2+} in an octahedral site than in tetrahedral[30]. The weight of this evidence leads to the conclusion that in sodium borosilicate glasses Mn^{2+} ions occupy two different sites, tetrahedral and octahedral, and furthermore, that the H band arises from Mn^{2+} in tetrahedral coordination, while the L band comes from octahedrally coordinated Mn^{2+}. This interpretation also agrees with that of Linwood and Weyl[30] that in silicate glasses Mn^{2+} ions replace Si^{4+} ions (tetrahedral coordination) and in borate glasses they occupy interstitial positions of approximately octahedral symmetry. Further evidence for this view is provided by the dependence of the L band intensity on temperature. Figure 56 shows the emission spectra of Mn^{2+} in glass composition 32AC6 at room temperature and at 77°K. The relative height (H/L) decreased from 0.99 (room temperature) to 0.86 (77°K). It is possible to understand this temperature dependence if the L band arises from Mn^{2+} in rather loosely bound interstitial positions which are more influenced by thermal vibrations than are the more rigidly bounded tetrahedrally coordinated Mn^{2+}.

Raman and N.M.R. spectroscopic investigations of sodium borosilicate glasses[109-111] showed that the silicate structural unit was the silicon-oxygen tetrahedron while the borate structural units were more complex including diborate, tetraborate and boroxol rings. It is thus perhaps more realistic to consider Mn^{2+} in the B-rich phase as being the centres occupying a distribution of distorted octahedral sites. In this scheme the Laporte selection rule would be relaxed for Mn^{2+} in octahedral sites and this may well account for the comparable luminescent intensities of the H and L bands (the H band being Laporte allowed) observed in glasses with low levels of MnO.

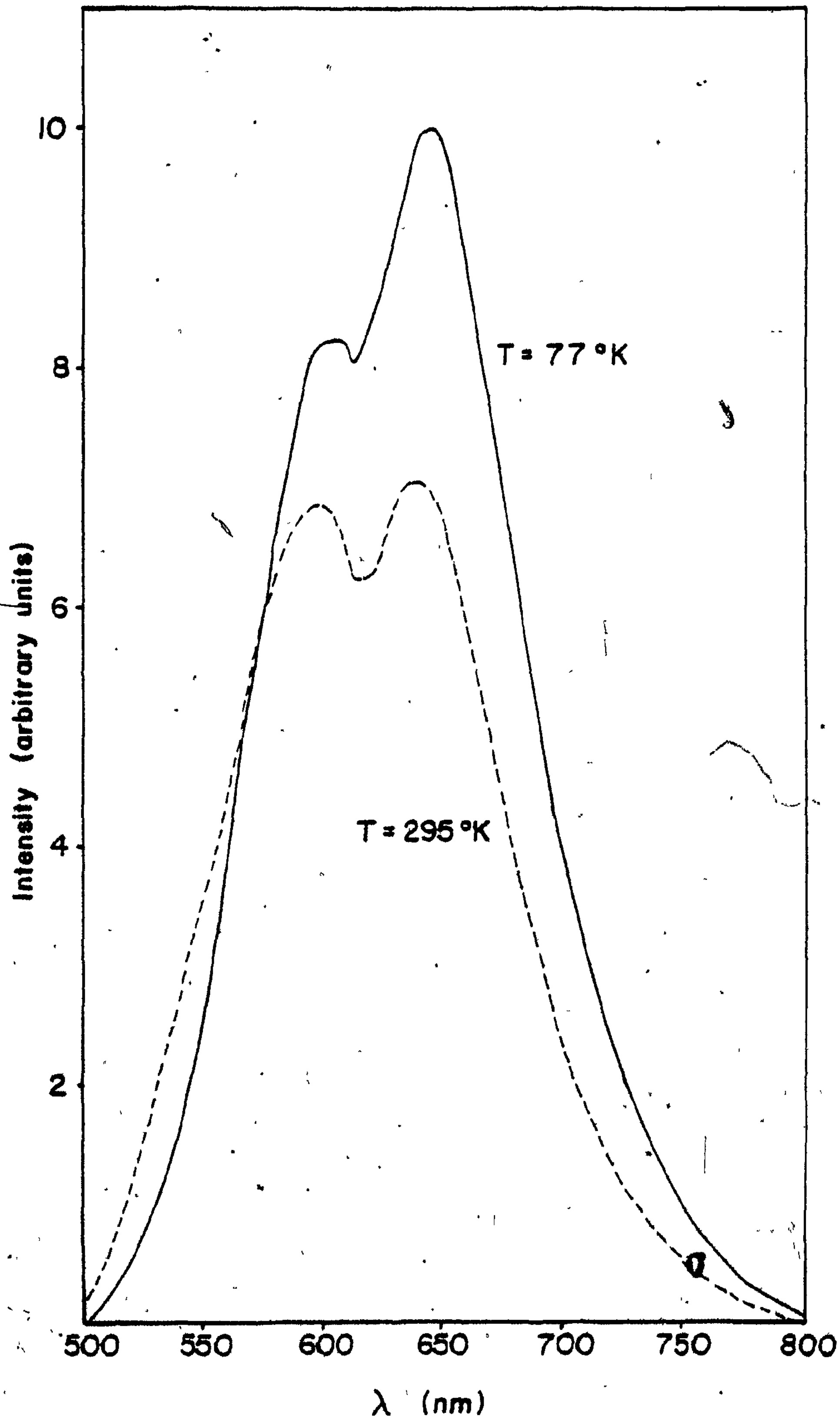

Fig. 56: Emission spectra at 77°K and 295°K of glass of composition 32AC6. Excitation wavelength: 420 nm.

Both Mn^{2+} emission bands shift toward longer wavelengths with increasing MnO content for a given glass composition. This red shift may be related to the reduction of the energy of the $^4T_1$ emitting level of Mn^{2+} with increasing crystal field strength. Hence an effective crystal field parameter Δ' may be obtained from the emission band maxima, and can be used to estimate the quantitative effect of increasing MnO concentration on the magnitude of the crystal field. Nine glass compositions (glasses 30 to 38, the molar compositions of these glasses were given in Table VII) with different MnO concentrations will be compared. The values of Δ' calculated from the emission band maxima are presented in Tables XXVIII to XXXI. In Fig. 57, Δ' is plotted as a function of MnO concentrations. Concentration factors (obeying the lever rule) of *ca.* 1.20 for glass 32, *ca.* 1.40 for glass 33, *ca.* 1.90 for glass 34, *ca.* 2.33 for glass 35, *ca.* 3.15 for glass 36, *ca.* 4.5 for glass 37 and *ca.* 6 for glass 38 were taken into consideration for both phases. The parameter Δ' for the H band increases with increasing MnO content until a concentration of *ca.* 2.5 wt% after which there is a plateau region where Δ' is essentially independent of concentration. For the L band, Δ' increases sharply up to an MnO concentration of 1 wt% and then continues to increase, but much more gradually. To understand this behaviour, it is useful to consider the result of the recent Raman study of sodium borosilicate glasses[111]. For a ratio

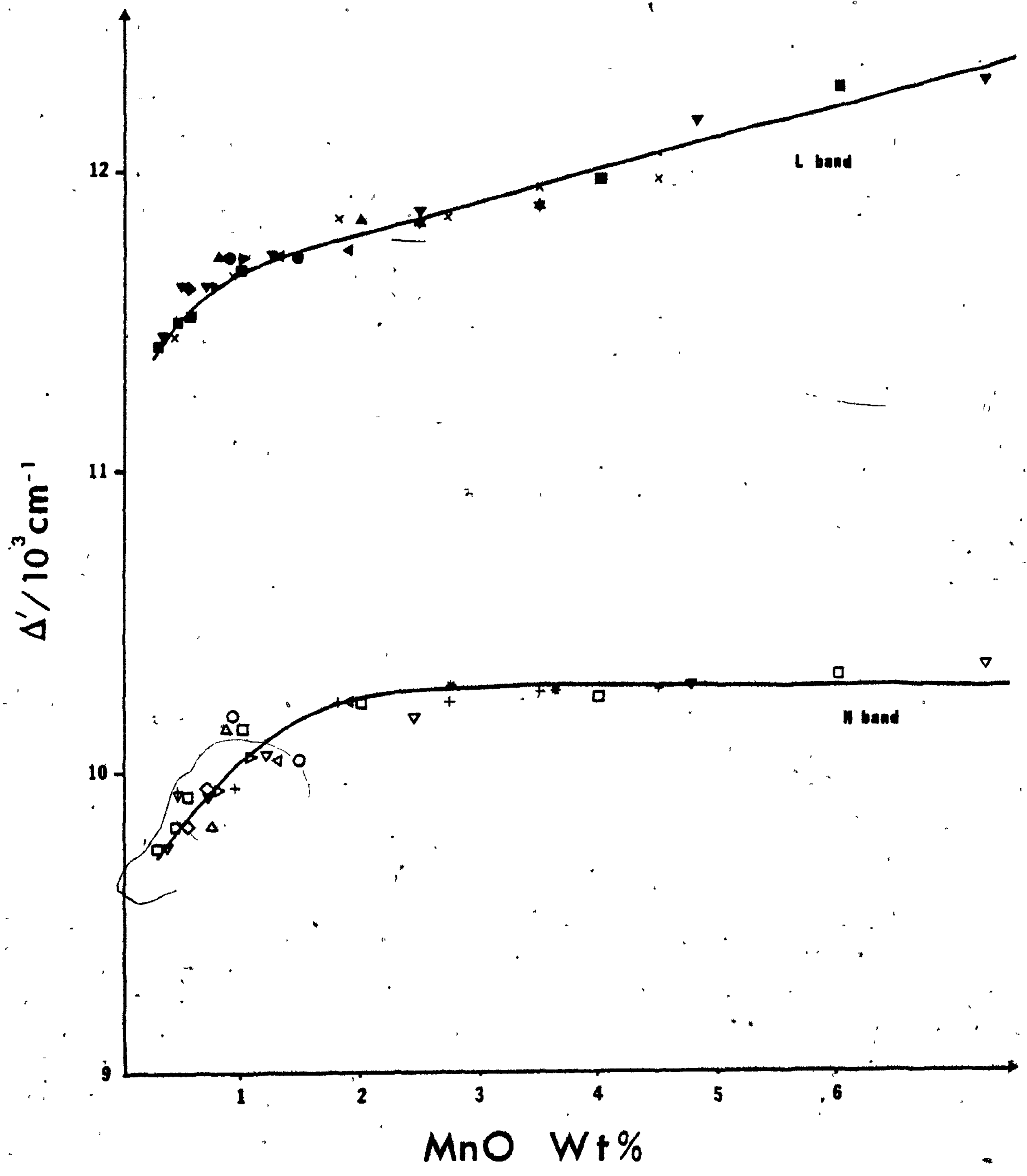

M band : 30(□),31(◇),32(▽),33(△),34(▷),35(○),36(◁),37(+),38(*).

L band : 30(■),31(◆),32(▼),33(▲),34(▶),35(●),36(◀),37(×),38(✱).

Fig. 57: Variation of Δ' as a function of MnO concentration.

Table XXVIII: Dependence of the Parameter Δ' as a Function of MnO Concentration (Glass Composition 30).

MnO (wt%)	H band (cm^{-1})	E/B	Δ'/B	Δ'
0.30	16863	26.79	15.50	9755
0.40	16807	26.70	15.60	9819
0.60	16722	26.57	15.75	9913
1.00	16584	26.35	16.15	10165
2.00	16447	26.13	16.25	10228
4.00	16393	26.04	16.29	10253
6.00	16313	25.92	16.40	10322
-	L band (cm^{-1})	-	-	-
0.30	15748	24.89	18.07	11431
0.40	15674	24.78	18.15	11482
0.60	15649	24.74	18.20	11513
1.00	15576	24.62	18.45	11672
2.00	15456	24.43	18.72	11842
4.00	15267	24.13	18.90	11956
6.00	14993	23.70	19.40	12276

The values of Δ'/B for the H band were taken from Fig. 54 ($B = 629.4\ cm^{-1}$) and those for the L band from Fig. 55 ($B = 632.6\ cm^{-1}$).

Table XXIX: Dependence of the Parameter Δ' as a Function of MnO Concentration (Glass Composition 32).

MnO (wt%)	H band (cm^{-1})	E/B	Δ'/B	Δ' (cm^{-1})
0.30	16863	26.79	15.5	9756
0.40	16722	26.57	15.75	9913
0.60	16722	26.57	15.75	9913
1.00	16529	26.26	16.00	10070
2.00	16447	26.13	16.25	10228
4.00	16340	25.96	16.35	10291
6.00	16260	25.83	16.45	10354
-	L band (cm^{-1})	-	-	-
0.30	15699	24.82	18.10	11450
0.40	15625	24.70	18.35	11608
0.60	15625	24.70	18.35	11608
1.00	15552	24.58	18.50	11703
2.00	15432	24.39	18.75	11861
4.00	15152	23.95	19.20	12146
6.00	14993	23.70	19.40	12276

The values of Δ'/B for the H band were taken from Fig. 54 ($B = 629.4\ cm^{-1}$) and those for the L band from Fig. 55 ($B = 632.6\ cm^{-1}$).

Table XXX: Dependence of the Parameter Δ' as a Function of MnO Concentration (Glass Composition 37).

MnO (wt%)	H band (cm^{-1})	E/B	Δ'/B	Δ' (cm^{-1})
0.1	16807	26.70	15.6	9919
0.2	16667	26.48	15.8	9944
0.4	16447	26.13	16.25	10228
0.6	16447	26.13	16.25	10228
0.8	16393	26.05	16.30	10259
1.00	16340	25.96	16.35	10291
-	L band (cm^{-1})	-	-	-
0.1	15674	24.78	18.15	11482
0.2	15600	24.66	18.40	11640
0.4	15480	24.47	18.70	11830
0.6	15480	24.47	18.70	11830
0.8	15361	24.28	18.85	11924
1.0	15314	24.21	18.90	11956

The values of Δ'/B for the H band were taken from Fig. 54 ($B = 629.4\ cm^{-1}$) and those for the L band from Fig. 55 ($B = 632.6\ cm^{-1}$).

Table XXXI: Dependence of the Parameter Δ' as a Function of MnO Concentration (0.4 and 0.6 wt%) for Glasses of Compositions 31, 33, 34, 35, 36 and 38.

Sample	H band (cm^{-1})	E/B	Δ'/B	Δ'
MnBS-31AC4	16807	26.70	15.60	9819
MnBS-31	16667	26.48	15.80	9944
MnBS-33AC4	16722	26.57	15.75	9913
MnBS-33	16584	26.35	16.15	10165
MnBS-34AC4	16667	26.48	15.80	9944
MnBS-34	16529	26.26	16.00	10070
MnBS-35AC4	16584	26.35	16.15	10165
MnBS-35	16529	26.26	16.00	10070
MnBS-36AC4	16529	26.26	16.00	10070
MnBS-36	16447	26.13	16.25	10228
MnBS-38AC4	16393	26.05	16.28	10247
MnBS-38	16393	26.05	16.28	10247
-	L band (cm^{-1})	-	-	-
MnBS-31AC4	15674	24.78	18.15	11482
MnBS-31	15625	24.70	18.35	11608
MnBS-33AC4	15625	24.70	18.35	11608
MnBS-33	15576	24.62	18.45	11672
MnBS-34AC4	15625	24.70	18.35	11608
MnBS-34	15552	24.58	18.50	11703
MnBS-35AC4	15552	24.58	18.50	11703
MnBS-35	15552	24.58	18.50	11703
MnBS-36AC4	15552	24.58	18.50	11703
MnBS-36	15530	24.55	18.53	11722
MnBS-38AC4	15480	24.47	18.70	11830
MnBS-38	15408	24.36	18.79	11887

The values Δ'/B for the H band were taken from Fig. 54 ($B = 629.4\ cm^{-1}$) and those for the L band from Fig. 55 ($B = 632.6\ cm^{-1}$).

of $Na_2O/B_2O_3 \leq 1$ (all the glass compositions in this work fall within this range), most of the Na_2O was found to transform the structural units $(BO_3)^{3-}$ into $(BO_4)^{5-}$ units; at the same time only a few Si-O^- non-briding bonds were present. On the one hand the MnO can act as a network modifier (when Mn^{2+} occupies interstitial positions) and will assist the Na_2O in transforming the structural $(BO_3)^{3-}$ units into $(BO_4)^{5-}$ units, thus increasing the ionic character of Mn^{2+} environment. This would result in an increased crystal field (Δ') at the octahedral sites and hence the observed red shift of the L band. On the other hand, when the MnO acts as a network former by replacing Si^{4+} ions in tetrahedral coordination, by increasing the MnO concentration Mn^{2+} would replace the small number of silicon atoms in the Si-O^- non-briding bonds as well as some silicon atoms in the regular tetrahedron. This would lead to an increase in crystal field strength (Δ') for the tetrahedral Mn^{2+} ions and a red shift of the H band. But when the concentration of MnO reaches *ca.* 2.5 wt% no further increase in Δ' is observed, which implies that at that point presumably an equilibrium is reached where additional MnO will preferentially go to the more ionic B-rich phase.

4.6 CONCLUDING REMARKS

Each of the preceding sections led to conclusions that were used in the arguments of the succeeding sections. It seems appropriate to summarize these results and also to comment on some of the aspects that may still need clarification.

Manganese(II) luminescence in sodium borosilicate glasses exhibits two bands, the positions and relative intensities of which depend on both the concentration of the activator for a given glass composition and on the composition of glass for a particular activator level. Morphological studies of the MnO-doped samples showed that the MnO concentrates in the B-rich phase, leading to an effective increase in the MnO concentration within that phase. This, in turn, affects the luminescent characteristics of the doped glasses along the tie-line. The luminescence study of these samples led to the conclusion that the glasses inside and around the miscibility gaps were submicroscopically phase separated as formed. The decay-time analysis indicated that the H band was mainly due to Mn^{2+} centres in the Si-rich phase while the L band was principally due to Mn^{2+} in the B-rich phase. The excitation spectra of each of the two emission bands were used to determine the energy level diagrams of Mn^{2+} in these glasses. The resulting crystal field parameters then showed that in these glasses Mn^{2+} occupies two sites, one octahedral and the other tetrahedral. The high energy band was associated with tetrahedral manganese, the low energy band with octahedral manganese. This together with the conclusions drawn from the decay times, imply that the H emission band arises from tetrahedral manganese mainly in the Si-rich phase and the L band from octahedrally coordinated manganese located primarily in the B-rich phase.

Throughout this work the two phases have been designated as either B-rich or Si-rich. It should be emphasized that the network modifier, Na_2O, concentrates in the B-rich phase. It is probably this network modifier that affects the partitioning of MnO between the two phases. It is the Na_2O which supplies the oxygens needed to transform the $(BO_3)^{3-}$ structural units into the $(BO_4)^{5-}$ and other more ionic structural units and also to form the small number of $Si\text{-}O^-$ non-bridging oxygens associated with the silicon atoms. It is still, however, not clear to what extent this network modifier affects the magnitude of the Nernst partition coefficient, especially when MnO, which can also act as a network modifier, is added to the glass. For a fixed MnO concentration, and on going from one end of the tie-line to the other end, the effective manganese concentration inside the two phases changes and hence the relative solubility, of MnO in these two phases, may also change. The B-rich phase is probably more affected than the Si-rich phase, since it is within this phase that most of the sodium and manganese concentrates. The more the MnO concentration increases, the more ionic the B-rich phase becomes and thus the more attractive it will be to the Mn^{2+} ions. In other words, when one considers the effect of the dissolved MnO on the chemistry of the B-rich phase, one is led to conclude that the Nernst partition coefficient increases with increasing MnO content. Figure 57 shows that for the concentration range studied this may indeed be happening. The fact that Δ' (the effective crystal field parameter) becomes essentially constant for the H-band (Si-rich phase) but not for the L band (B-rich phase) implies an increasing preference of the added MnO for the B-rich phase. One cannot, of course, assume that this would necessarily be true for still higher concentrations.

CONTRIBUTIONS TO KNOWLEDGE

On addition of MnO the ternary $Na_2O \cdot B_2O_3 \cdot SiO_2$ system was shown to behave like quaternary systems of the type $X_2O \cdot B_2O_3 \cdot SiO_2$ (X = Na, K; M = Mg, Ca, Ba, Zn). The perimeters of the isotherms for the cross section which intersects the $Na_2O \cdot B_2O_3 \cdot SiO_2$ face of the quaternary phase diagram along one tie-line (Tg = 400°C) were determined.

Clearing temperature measurements were made with results that were consistent with the 700°C isotherms as determined by Mazurin and Streltsina[20] than that of Haller *et al.*[17].

It was shown that the addition of small quantities of MnO does not induce major rotation of the tie-lines in the sodium borosilicate system.

Both manganese and titanium were found to concentrate in the B-rich phase of phase separated sodium borosilicate glasses, while very little chromium dissolved.

Sodium borosilicate glasses inside the miscibility gaps were found to be submicroscopically phase separated as formed. The rapidity by which phase separation must have occurred suggests a spinodal decomposition.

Manganese(II) luminescence in sodium borosilicate glasses exhibits two emission bands: a high energy band which was attributed to Mn^{2+} in tetrahedral sites mainly from the silica-rich phase, and a low energy band assigned to Mn^{2+} in octahedral positions and principally in the boron-rich phase.

SUGGESTIONS FOR FURTHER WORK

Morphological and glass transition temperature studies of glasses of the ternary $MnO \cdot B_2O_3 \cdot SiO_2$ system would determine the miscibility gaps and the tie-lines of that system. Then luminescence spectroscopy may be used to determine the number of manganese ions that play the role of network formers and/or network modifiers in that system.

When the separated phases are large enough (∼ 10 μm), it should be possible to excite Mn^{2+} ions separately in each phase. Since the detection limit for luminescence is much better than that of EDAX it should be possible to determine the actual distribution of Mn^{2+} between the two phases. Note that from the excitation spectra obtained for both bands, the 514.5 nm laser line would excite only Mn^{2+} in octahedral sites while the 488.0 nm laser line would excite Mn^{2+} ions in both sides (octahedral and tetrahedral).

With a tunable dye laser it should be possible to excite Mn^{2+} ions occupying a particular site in the glass. This hopefully would yield a single decay exponential representative of a particular site, and may thus elucidate the site distribution.

It would be interesting to investigate the effect of heat-treatment on the luminescence and luminescent decay-times of Mn^{2+} in glasses of the ternary $Cs_2O \cdot B_2O_3 \cdot SiO_2$ system. Because this system has very small miscibility gaps, it is likely that single phase glasses could be prepared.

APPENDIX

Let X be the total number of moles of Mn added to a given glass and C_B and C_{Si} the respective concentrations of Mn in the B-rich and Si-rich phases. The Nernst partition coefficient may be written as:

$$k = \frac{C_B}{C_{Si}} \qquad (A.1)$$

If V_B and V_{Si} designate the respective volumes in the B-rich and Si-rich phases, then X is given by:

$$X = V_B C_B + V_{Si} C_{Si} \qquad (A.2)$$

Replacing C_B from equation (A.1) in equation (A.2) yields:

$$X = V_B k C_{Si} + V_{Si} C_{Si} \qquad (A.3)$$

Expression (A.3) may be rearranged to give:

$$C_{Si} = \frac{X}{kV_B + V_{Si}} \qquad (A.4)$$

If k is large then equation (A.4) becomes approximately:

$$C_{Si} \sim \frac{X}{kV_B} \qquad \text{(A.5)}$$

The same calculations may be carried out for C_B to get:

$$C_B = \frac{X}{V_B + V_{Si}/k} \qquad \text{(A.6)}$$

Again, if k is large, then

$$C_B \sim \frac{X}{V_B} \qquad \text{(A.7)}$$

REFERENCES

1. Levin, E.M., *Phase Diagrams: Material Science and Technology*, Vol. 3, Chap. 5, Ed. A.M. Alper, Academic Press, N.Y. (1970).

2. Morey, G.W., *The Properties of Glass*, 2nd Ed., p. 1, Reinhold, N.Y. (1954).

3. Weyl, W.A. and Marboe, E.C., *The Constitution of Glasses*, Vols. I and II, Wiley, N.Y. (1964-1967).

4. Mackenzie, J.D., Ed., *Modern Aspects of the Vitreous State*, Vols. I to III, Butterworths, London (1960-1964).

5. James, P.F., J. Mater. Sci. 10, 1802 (1975).

6. Uhlman, D.R. and Kolbeck, A.G., Phys. Chem. Glasses 17, 146 (1976).

7. Seward III, T.P., *Phase Diagrams*, Vol. I, Ed. A.M. Alper, p. 295, Academic Press, N.Y. (1970).

8. Porai-Koshits, E.A., The Structure of Glass, Vol. I, p. 112, Consultants Bureau, N.Y. (1973).

9. Vogel, W., J. Non-Cryst. Solids 25/26, 170 (1977).

10. Tomozawa, M., Treatise Mater. Sci. Technol. 17, 71 (1979).

11. Andreev, N.S. and Porai-Koshits, E.A., Disc. Faraday Soc. 50, 135 (1970).

12. Shelby, J.E., J. Non-Cryst. Solids 49, 287 (1982).

13. Wong, J. and Angell, C.A., *Glass Structure by Spectroscopy*, p. 191, Marcel Dekker Inc., N.Y. (1976).

14. Gordon, D.E., Proceedings of the Workshop on Alternate Nuclear Waste Fuel Forms and Interactions in Geologic Media, Gatlinburg, Tennesse, (CONF-8005107), p. 355 (1980).

15. Strathdee, G.G., McIntyre, N.S. and Taylor, P., Proceedings of the International Symposium on Nuclear Waste Management, Cincinnati, Ohio, (CONF-790420), p. 243 (1979).

16. Ross, W.A., Tech. Rept. No. PNL-2625, Pacific Northwest Laboratory, Richland, Washington (1979).

17. Haller, W., Blackburn, D.H., Wagstaff, F.E. and Charles, R.J., J. Am. Ceram. Soc. 53(1), 34 (1970).

18. Galakhov, F.Ya. and Alekseeva, O.D., Dokl. Akad. Nauk SSSR 184(5), 1102 (1969).

19. Srinivasan, G.R., Tweer, I., Macedo, P.B. and Sarkar, A., J. Non-Cryst. Solids 6(3), 221 (1971).

20. Mazurin, O.V., and Streltsina, M.V., *ibid.* 11(3), 199 (1972).

21. Makishima, A., Mackenzie, J.D. and Hammel, J.J., J. Non-Cryst. Solids 31, 377 (1979).

22. Tomozawa, M., Kawamoto, Y. and Takamori, T., *ibid.* 37, 437 (1980).

23. Takamori, T. and Tomozawa, M., J. Am. Ceram. Soc. 61, 509 (1978).

24. Howell, B.F., Simmons, J.H. and Haller, W., Ceram. Bull. 54, 707 (1975).

25. Tomozawa, M. and Takamori, T., J. Am. Ceram. Soc. 60, 301 (1977).

26. Toyuki, H., Yogyo Kyokai-shi 86, 536 (1978).

27. Labutina, L.V., Pavlushkin, N.M. and Artamonova, M.V., Structure of Glass, Vol. 8, p. 170, Ed. E.A. Porai-Koshits, Consultants Bureau, N.Y. (1973).

28. Tisher, R.E., J. Chem. Phys. 48(9), 4291 (1968).

29. Lunter, S.G., Karapetyan, G.O., Bokin, N.M. and Yudin, D.M., Sov. Phys. Solid State 9(10), 2259 (1968).

30. Linwood, S.H. and Weyl, W.A., J. Opt. Soc. Amer. 32, 443 (1942).

31. Turner, W.H. and Eastman-Turner, J., J. Am. Ceram. Soc. 53(6), 329 (1970).

32. Lunter, S.G., Karapetyan, G.O. and Yudin, D.M., Izv. Akad. Nauk SSSR Neorg. Mater. 5(2), 325 (1969).

33. Lunter, S.G., Karapetyan, G.O. and Yudin, D.M., Izv. Akad. Nauk SSSR Ser. Fiz. 31(5), 811 (1967).

34. Margaryan, A.A., Manvelyan, M.G., Karapetyan, S.S., Grigoryan, A.L. and Kozmanyan, A.A., Dokl. Akad. Nauk SSSR 221(3), 665 (1975).

35. Lunter, S.G., Karapetyan, G.O. and Yudin, D.M., Izv. Sib. Otd. Akad. Nauk SSSR, Ser. Khim. Nauk 4, 46 (1967).

36. Kuz'menkov, M.I. and Rzhevski, M.B., Structure of Glass, Vol. 8, p. 183, Ed. E.A. Porai-Koshits, Consultants Bureau, N.Y. (1973).

37. Mack, H., Boulon, G. and Reisfeld, R., J. Lumin. 24/25, 111 (1981).

38. Tsurikova, G.A., Opt. Spektrosk. 24(2), 290 (1968).

39. Kreidl, N.J., J. O. S. A., 35(4), 249 (1945).

40. Simkin, D., Oyama-Gannon, K., Ménassa, P. and Taylor, P., J. Lumin. 24/25, 107 (1981).

41. Margaryan, A.A., Manvelyan, M.G. and Karapetyan, S.S., Dokl. Akad. Nauk SSSR 228(4), 881 (1974).

42. The New Encyclopedia Britannica, 15th Ed., Vol. 8, p. 181 (1981), and references therein.

43. Faraday, M., Phil. Trans. Roy. Soc., 49 (1830).

44. Faraday, M., Phil. Mag. 14, 401 (1857).

45. Faraday, M., Experimental Researches in Electricity, reprinted by J.M. Dent, London, 1914, pp 38 and 115.

46. Buff, H., Leipzig Ann. 90, 257 (1854).

47. Zschimmer, E.: Die Glasindustrie in Jena, E. Diederichsverlag, Jena (1912), as quoted in Ref. 9, p. 172.

48. Warburg, E., Ann. Phys. 21, 622 (1884).

49. Warburg, E. and Tegetmeier, F., *ibid.* 35, 455 (1888).

50. Schulz, G., *ibid.* 40, 335 (1913).

51. Tamman, G., Der Glaszustand, Voss, Leipzig (1933).

52. Guertler, W., Z. Anorg. Chem. 40, 225 (1904).

53. Greig, J.W., Am. J. Sci., Ser. 5 13, 1 (1927).

54. Greig, J.W., *ibid.*, Ser. 5 13, 133 (1927).

55. Lebedev, A.A., Arb. Staatl. Opt. Inst. 2(10), 1 (1921).

56. Valenkov, N. and Porai-Koshits, E.A., Z. Kristallogr. Kristallogeom. 95, 195 (1936).

57. Markin, B.J., Technologie des Glases, Kitaigorodski, VEB Verlag Technik, Berlin, and Oldenburg Verlag, Munich.

58. Botwinkin, O.K., Mitt. Akad. Wiss. UdSSR, Phys. Serie 4, 600 (1940).

59. Zachariasen, W.H., J. Am. Chem. Soc. 54, 3841 (1932).

60. Warren, B.E., *ibid.* 19, 202 (1936).

61. Hartleif, G., Zeitschr. Anorg. Chem. 238, 353 (1938).

62. Dietzel, A., Glastechn. Ber. 22, 40 (1948/49).

63. Dietzel, A., *ibid.* 22, 212 (1948/49).

64. Warren, B.E. and Pincus, A.G., J. Am. Ceram. Soc. 23, 301 (1940).

65. Warren, B.E., J. Appl. Phys. 8, 645 (1937).

66. Warren, B.E. and Biscoe, J., J. Am. Ceram. Soc. 21, 49 (1938).

67. Weinberg, D.L., J. Appl. Phys. 33, 1012 (1962).

68. Levelut, A.M. and Guinier, A., Bull. Soc. Franc. Miner. Crist. 90, 445 (1967).

69. Bienenstock, A. and Bagley, B.G., J. Appl. Phys. 37, 4840 (1966).

70. Wright, A.C., Adv. Struct. Res. Diff. Meth. 5 (1974).

71. Slayter, G., Am. Ceram. Soc. Bull. 31, 276 (1952).

72. Prebus, A.F. and Michener, J.W., Ind. Eng. Chem. 46, 147 (1953).

73. Shelyubsky, V.Y., Steklo i Keramika 11, No. 11, 19 (1954).

74. Oberlies, F., Naturwissenschaften 43, 224 (1956).

75. Vogel, W. and Gerth, K., Glastechn. Ber. 31, 15 (1958).

76. Vogel, W. and Gerth, K., Silikattechnik 9, 353 (1958).

77. Vogel, W. and Gerth, K., *ibid.* 9, 495 (1958).

78. Doremus, R.H., *Glass Science*, p. 1, Eds. J.E. Burke, B. Chalmers and J.A. Krumhansl, Wiley, N.Y. (1973).

79. Cahn, J.W., Acta Metall. 9, 795 (1961).

80. Cahn, J.W., *ibid.* 10, 179 (1962).

81. Hillert, M., *ibid.* 9, 525 (1961).

82. Shaw, R.R. and Uhlman, D.R., J. Am. Ceram. Soc. 51(7), 377 (1968).

83. Golubkov, V.V., Titov, A.P., Vasilevskii, T.N. and Porai-Koshits, E.A., Fiz. Khim. Stekla 3(4), 306 (1977).

84. Moriya, Y., Warrington, D.H. and Douglas, R.W., Phys. Chem. Glasses 8, 19 (1967).

85. Haller, W., Blackburn, D.H. and Simmons, J.H., J. Am. Ceram. Soc. 57, 120 (1974).

86. Charles, R.J., *ibid.* 49, 55 (1966).

87. Seward III, T.P., Uhlman, D.R. and Turnbull, D., *ibid.* 51, 278 (1968).

88. Levin, E.M. and Block, S., *ibid.* 40, 113 (1957).

89. Charles, R.J. and Wagstaff, R.E., *ibid.* 51, 16 (1968).

90. Geller, R.F. and Bunting, E.N., J. Res. Natl. Bur. Stan. 18, 585 (1937).

91. Liedberg, D.J., Ruderrer, C.G. and Bergeron, G.G., J. Am. Ceram. Soc. 48, 440 (1965).

92. Zarzycki, J. and Naudin, F., C.R. Acad. Sci. Ser. B265, 1456 (1967).

93. Simmons, J.H., J. Am. Ceram. Soc. 56, 284 (1973).

94. MacDowell, J.F. and Beall, G.H., *ibid.* 52, 17 (1969).

95. Takamori, T. and Roy, R., *ibid.* 56, 639 (1973).

96. de Neuville, J.P. and Turnbull, D., Discuss. Faraday Soc. 50, 182 (1970).

97. Hammel, J.J., J. Chem. Phys. 46, 2234 (1967).

98. Burnett, D.G. and Douglas, R.W., Phys. Chem. Glasses 11, 125 (1970).

99. Krupkin, S.Yu., Milyukov, E.M. and Ushakov, D.F., Izv. Akad. Nauk SSSR, Neorg. Mater. 6, 1490 (1970).

100. Nagawaka, K. and Izumitani, T., J. Non-Cryst. Solids 7, 168 (1972).

101. Varshal, B.G., Vaisfel'd, N.M., Keshishyan, T.N., Malakhovskaya, N.M. and Naumkin, A.P., Izv. Akad. Nauk SSSR, Neorg. Mater. 6, 1494 (1970).

102. Topping, J.A., Fuchs, P. and Murthy, M.K., J. Am. Ceram. Soc. 57, 205 (1974).

103. Hummel, F.A., Tien, T.Y. and Kim, K.H., *ibid.* 43, 192 (1960).

104. Taylor, P. and Owen, D.G., J. Non-Cryst. Solids 42, 143 (1980).

105. Taylor, P. and Owen, D.G., J. Am. Cera. Soc. 64(6), 360 (1981).

106. Taylor, P. and Owen, D.G., *ibid.* 64(11), C-158 (1981).

107. Taylor, P., Campbell, A. and Owen, D.G., *ibid.* 66, 347 (1983).

108. Kawazoe, H., Hosono, H. and Kanazawa, T., J. Non-Cryst. Solids 29, 249 (1978).

109. Berthous, J.C., Levasseur, A., Villeneuve, G., Echegut, P., Hagenmuller, P. and Couzi, M., J. Solid State Chem. 39, 199 (1981).

110. Konijnendijk, W.L. and Stevels, J.M., J. Non-Cryst. Solids 20, 193 (1976).

111. Furukawa, T. and White, W.B., J. Mat. Sci. 16, 2689 (1981).

112. Ehrt, D., Reiss, H. and Vogel W., Silikattechnik 28, 359 (1977).

113. Bando, Y., Iijima, S., Kawamoto, Y. and Tomozawa, M., J. Non-Cryst. Solids 42, 151 (1980.

114. Bando, Y., Iijima, S., Kawamoto, Y. and Tomozawa, M., *ibid.* 43, 379 (1981).

115. Weyl, W.A., Coloured Glasses, p. 1, Society of Glass Technology, Sheffield, England (1951).

116. Bates, T., *Modern Aspects of the Vitreous State*, Vol. 2, p. 195, ed. J.D. Mackenzie, Butterworth Inc., Washington D.C. (1962).

117. Bamford, C.R., Phys. Chem. Glasses 3(6), 189 (1962).

118. Smith, H.L. and Cohen, A.J., *ibid.* 4(5), 173 (1963).

119. Bamford, C.R., *Colour Generation and Control in Glass*, p. 1, Elsevier North-Holland Inc., N.Y. (1971).

120. Steele, F.N. and Douglas, R.W., Phys. Chem. Glasses 6, 246 (1965).

121. Brawer, S.A. and White, W.B., J. Chem. Phys. 67(5), 2043 (1977).

122. Andrews, L.J., Lempicki, A. and McCollum, B.C., J. Chem. Phys. 74(10), 5526 (1981).

123. Lell, E., Kreidl, N.J. and Hensler, J.R. in: *Progress in Ceramic Science*, Vol. 4, ed. J. Burke, Pergamon, Oxford (1966).

124. Yokota, Y., Phys. Rev. 95, 1145 (1954).

125. Bishay, A., J. Non-Cryst. Solids 3, 54 (1970).

126. Menassa, P., Simkin, D., Oyama-Gannon, K. and Taylor, P., unpublished results.

127. Reisfeld, R. and Bochm, L., J. Solid State Chem. 4, 417 (1972).

128. Martin, J.P., Thèse de doctorat, Université McGill, Département de Chimie, Novembre (1979).

129. Sauvagé, F., French Pat. No. 579,284 (1923).

130. Guntz, A., French Pat. No. 582,407 (1923).

131. Rindone G.E. in: *Luminescence of Inorganic Solids*, p. 419, ed. P. Goldberg, Academic Press, N.Y. (1966).

132. Buzhinzkii, I.M. and Bodrova, N.I., Opt. Spectrosk. English translation 12(3), 212 (1962).

133. Hunter, T.F. and Wyatt, R.F., Chem. Phys. Lett. 6, 221 (1970).

134. Reisfeld, R. and Kalisky, Y., Nature 283, 281 (1980).

135. Ostermayer, F.W. Jr., Metall. Trans. 2, 747 (1971).

136. Harper, D.W., Phys. Chem. Glasses 5(1), 11 (1964).

137. Snitzer, E., Phys. Rev. Lett. 7, 444 (1961).

138. Reisfeld, R., Structure and Bonding, Vol. 22, p. 123, Springer-Verlag, Berlin (1975).

139. Snitzer, E., Bull. Am. Phys. Soc., II 9, 447 (1964).

140. Snitzer, E., Am. Ceram. Soc. Bull. 52, 516 (1973).

141. Szabo, A., Phys. Rev. Lett. 25, 924 (1970).

142. Riseberg, L.A., *ibid.* 28, 789 (1972).

143. Riseberg, L.A., Solid State Commun. 11, 469 (1972).

144. Riseberg, L.A., Phys. Rev. A7, 671 (1973).

145. Yen, W.M., J. Lumin. 18/19, 639 (1979).

146. Rodriguez, A.R., Parmelee, C.W. and Badger, A.E., J. Am. Ceram. Soc. 26, 137 (1943).

147. Parke, S. and Webb, R.S., Phys. Chem. Glasses 13, 157 (1972).

148. Lunkin, S.I., Milyukov, E.M. and Mokeeva, G.A., Zh. Prikl. Spectrosk. 32(1), 62 (1980).

149. de Boisbaudran, L., Compt. Rend. 103, 1107 (1887).

150. Urbain, G., Ann. Chim. Phys. 18, 222 (1909).

151. Lunter, S.G. and Margaryan, A.A., Spektrosk. Tverd. Tela, 221 (1969).

152. Margaryan, A.A., Bohun, A., Janatova, J., Zavada, P., Bryknar, Z. and Trinkler, M.F., Arm. Khim. Zh. 22(11), 969 (1969).

153. Parke, S., J. Phys. Chem. Solids 32, 669 (1971).

154. Bingham, K. and Parke, S., Phys. Chem. Glasses 6(6), 224 (1965).

155. Margaryan, A.A., Arm. Khim. Zh. 33(9), 707 (1980).

156. Bohun, A., Mararyan, A.A., Grigoryan, A.L., and Kuradzhyan A.M., Czech. J. Phys. B24, 1057 (1974).

157. Bohun, A. and Polecha, J., *ibid.* B29, 939 (1979).

158. Parke, S., Watson, A.I. and Webb, R.S., J. Phys. D3, 763 (1970).

159. Szörenyl, T., Szöllösy, L. and Szanka, K., Phys. Chem. Glasses 17(4), 104 (1976).

160. Egorova, V.F., Zubkova, V.S. and Karapetyan, G.O., Spektrosk. Krist., Mater. Simp. 2nd, ed. S.V. Grum-Gryhimalio, 219 (1970).

161. Zarubina, T.V., MokeevaG.A. and Stepanov, S.A., Opt. Spektr. Svoistra Stekol, Tezisy Dokl., Vses. Simp. 4th, 60 (1977).

162. Kumar, S. and Nath, P., Trans. Ind. Ceram. Soc. 25(1), 12 (1966).

163. Scholes, S., J. Non-Cryst. Solids 12, 266 (1973).

164. Scholes, S. and Wilkinson, F.C.F., Disc. Faraday Soc. 50, 175 (1970).

165. Elmer, T.H., Nordberg, M.E., Carrier, G.B. and Korda, E.J., J. Am. Ceram. Soc. 53, 171 (1970).

166. Makishima, A. and Sakaino, T., J. Am. Ceram. Soc. 53, 64 (1970).

167. Baron, J. and Wey, R., Verres et Refractaires 28, 16 (1974).

168. Webster's new collegiate dictionary, William Collins, Cleveland, Ohio (1979).

169. Sugisaka, M., Suga, H. and Seki, S., Bull. Chem. Soc. Jap. 41, 2591 (1968).

170. Onodera, N., Suga, H. and Seki, S., *ibid.* 41, 2222 (1968).

171. Shen, M.C. and Eisenberg, A., Prog. Solid State Chem. 3, 407 (1966).

172. Materials Advisory Board, Nat. Acad. Sci. Res. Council MAB, 243 (1968), as quoted in Ref. 13, p. 2.

173. Turnbull, D., Contemp. Phys. 10(5), 473 (1969).

174. Turnbull, D., in: *Physics of Non-Crystalline Solids*, p. 41, North-Holland, Amsterdam (1965).

175. Wagstaff, F.E., J. Am. Ceram. Soc. 52, 650 (1969).

176. Vergano, P.J. and Uhlmann, D.R., Phys. Chem. Glasses 11, 30 (1970).

177. Cormia, R.L., Mackenzie, J.D. and Turnbull, D., J. Appl. Phys. 34, 2239 (1963).

178. Scott, W.D. and Pask, J.A., J. Am. Ceram. Soc. 44, 181 (1961).

179. Meiling, G.S. and Uhlmann, D.R., Phys. Chem. Glasses 8, 62 (1967).

180. Leontewa, A., Acta Physicochem., USSR 16, 97 (1942).

181. Laird, J.A. and Bergeron, C.G., J. Am. Ceram. Soc. 53, 482 (1970).

182. DeLuca, J.P., Eagan, R.J. and Bergeron, C.G., *ibid.* 52, 322 (1969).

183. Fulcher, G.S., *ibid.* 6, 339 (1925).

184. Hetherington, G., Jack, K.H. and Kennedy, J.C., Phys. Chem. Glasses 5, 130 (1964).

185. Fontana, E.H. and Plummer, W.A., *ibid.* 7, 139 (1966).

186. Cohen, M.H. and Turnbull, D., J. Chem. Phys. 31, 1164 (1959).

187. Turnbull, D. and Cohen, M.H., *ibid.* 29, 1049 (1958).

188. Stanworth, J.E., J. Am. Ceram. Soc. 54, 61 (1971).

189. Levin, E.M. and Block, S., *ibid.* 40(3), 95 (1957).

190. Kawamoto, Y. and Tomozawa, M., *ibid.* 64(5), 289 (1981).

191. Charles, R.J., *ibid.* 50(12), 631 (1967).

192. Kawamoto, Y. and Tomozawa, M., Phys. Chem. Glasses 22(1), 11 (1981).

193. Kawamoto, Y. and Tomozawa, M., J. Non-Cryst. Solids 43, 417 (1981).

194. Meijering, J.L., Philips Res. Rep. 5, 333 (1950).

195. Meijering, J.L., *ibid.* 6, 183 (1951).

196. Zarzycki, J., Disc. Faraday Soc. 50, 122 (1970).

197. Charles, R.J., Phys. Chem. Glasses 10(5), 169 (1969).

198. Macedo, P.B. and Simmons, J.H., J. Res. Nat. Bur. Stand. A78(1), 53 (1974).

199. Darken, L.S. and Burry, R.W., *Physical Chemistry of Metals*, p. 1, McGraw Hill, N.Y. (1953).

200. Gibbs, J.W., Scientific Papers, p. 254, Dover, N.Y. (1961).

201. Lumsden, J., Thermodynamics of Alloys, Institute of Metals, p. 335, London (1952).

202. Frank, F.C., Proc. Roy. Soc. London A201, 586 (1950).

203. Turnbull, D., Solid State Phys. 3, 225 (1956).

204. Hillert, M., Acta Metall. 9, 525 (1961).

205. Cahn, J.W., *ibid.* 9, 795 (1961).

206. Cahn, J.W., J. Chem. Phys. 42(1), 93 (1965).

207. Jantzen, C.M.F. and Herman, H., *Phase Diagrams Materials Science and Technology*, Vol. V, p. 127, ed. A.M. Alper, Academic Press, N.Y. (1978).

208. Cahn, J.W., Acta Metall. 14, 1685 (1966).

209. Cook, H.E. and Hilliard, J.E., Trans. Amer. Inst. Metall. Eng. 223, 142 (1965).

210. Cahn, J.W. and Charles, R.J., Phys. Chem. Glasses 6(5), 181 (1965).

211. Haskell, R.W., J. Am. Ceram. Soc. 56(7), 355 (1973).

212. Rundman, K.B. and Hilliard, J.E., Acta Metall. 15, 1025 (1967).

213. Neilson, G.F., Phys. Chem. Glasses 10, 54 (1969).

214. Srinivasan, G.R., Sarkar, A., Gupta, P.K. and Macedo, P.B., J. Non-Cryst. Solids 20, 141 (1976).

215. Tomozawa, M., J. Am. Ceram. Soc. 51, 444 (1978).

216. Levin, E.M., *Phase Diagrams for Ceramists*, Am. Ceram. Soc., p. 5 (1964).

217. Francis, A.W., *Liquid-Liquid Equilibriums*, p. 26, Wiley, N.Y. (1963).

218. Alexander, F., *The Phase Rule and its Applications*, p. 1, 9th ed., by A.N. Campbell and N.O. Smith, Dover Publications, N.Y. (1951).

219. Taylor, P., Campbell, A., Owen, D.G., Simkin, D. and Ménassa, P., Proceedings on *Advances in Materials Characterization*, Alfred, N.Y. to be published in "Advances in Materials Research" (1982).

220. Trash-Lan, T., Verres et Refractaires 19, 416 (1965).

221. Bondi, A., *Physical Properties of Molecular Crystals, Liquids and Glasses*, p. 381, Wiley, N.Y. (1968).

222. Handbook of Chemistry and Physics, 51st ed. by R.C. Weast, CRC, Cleveland, Ohio (1970).

223. Terai, R. and Kosaka, E., Osaka Kogyo Gijutsu Shikensho Kiho 27(3), 150 (1976). English translation available from Oak Ridge National Laboratory, Rept. No. ORNL-tr-4629, 1976.

224. Wilds, G.W., Tech. Rept. No. DP-1504, Savannah River Laboratory, Aiken, S.C. 1978.

225. Knoll, M., Z. Tech. Phys. 11, 467 (1935).

226. Stewart, A.D.G. and Snelling, M.A., *A New Scanning Electron Microscope*, pp 55-56 in Titleback (1965).

227. Everhart, T.E. and Thornley, R.F.M., J. Sci. Instrum. 37, 246 (1960).

228. Swift, J.A., *Electron Microscopes*, p. 64, eds. M.M. Breuer and A.D. Jenkins, Barnes and Noble, N.Y. (1970).

229. Oatley, C.W., *The Scanning Electron Microscope*, Part 1, The Instrument, p. 28, eds. M.M. Woolfson and J.M. Ziman, Cambridge University Press, Cambride (1972).

230. Wells, O.C., *Scanning Electron Microscopy*, p. 1, eds. J. Robinson, G. Ryan and R. Braine, McGraw-Hill, N.Y. (1974).

231. Hearle, J.W.S., Sparrow, J.T. and Cross, P.M., *The Use of the Scanning Electron Microscope*, p. 1, Pergamon Press, N.Y. (1972).

232. Brooker, G.R., *Modern Diffraction and Imaging Techniques in Material Science*, p. 553, eds. S. Amelinchn, R. Gevers, G. Remant and J. Van Landuyt, North-Holland, Amsterdam (1970).

233. Goldstein, J.I., Newbury, D.E., Echlin, P., Joy, D.C., Fiori, C. and Lifshin, E., *Scanning Electron Microscopy and X-Ray Microanalysis*, p. 1, Plenum, N.Y. (1981).

234. Deutch, T.D. and Bass, M., IEEE J. Quantum Electron., QE-5, 260 (1969).

235. Warden, J.T. and Gough, L., Appl. Phys. Letters, 19(9), 345 (1971).

236. Srinivasan, R, IEEE J. Quantum Electron., QE-5, 522 (1969).

237. Furumato, H. and Cesson, H., IEEE J. Quantum Electron., QE-6, 262 (1970).

238. Broida, H.P. and Haydon, S.C., Appl. Phys. Lett. 16, 142 (1970).

239. Furumato, H. and Cesson, H., J. Appl. Phys. 40, 4204 (1969).

240. Reynolds, G.A. and Drexhage, Opt. Commun. 13(3), 222 (1975).

241. Kawamoto, Y., Clemens, K. and Tomozawa, M., J. Am. Ceram. Soc. 64(5), 292 (1981).

242. Taylor, P., private communication.

243. Medlin, W.L., J. Opt. Soc. Amer. 53, 1963 (1963).

244. Figgis, B.N., *Introduction to Ligand Fields*, Chapter 3, Interscience Publishers, N.Y. (1966).

245. Tanabe, Y. and Sugano, S., J. Phys. Soc. Japan 9, 753 (1954).

246. Orgel, L.E., J. Chem. Phys. 23, 1004 (1955).

247. Imbush, G.F. in: *Luminescence Spectroscopy*, p. 25, ed. M.D. Lumb, Academic Press, N.Y. (1978).

248. Dictionary of Mining, Minerals and Related Terms, ed. P.W. Thrush, U.S. Department of Interior, Washington, D.C. (1968).

249. Bethe, H., Ann. Physik. 3, 133 (1929).

250. ASTM Standard C-162-80.